UNIVERSITY OF BIRMINGHAM

EVALUATION OF CERAMICS AS A MATERIAL FOR TOTAL DISC REPLACEMENTS

By

NAOMI CHAROTTE GREEN

A thesis submitted to the

University of Birmingham

for the degree of

DOCTOR OF PHILOSOPHY

School of Engineering

Department of Mechanical Engineering

University of Birmingham

September, 2016

Abstract

Total Disc Replacement aims to maintain the natural movement of the spine by replacing the intervertebral disc with an articulating or flexible implant. One reason Total Disc Replacements fail is aseptic loosening of the implant, caused by osteolysis, an inflammatory response to the wear debris produced by the articulating surfaces of the implant. Therefore, it is important to understand the wear performance of different designs and materials. The overall aim of this thesis was to investigate the use of ceramics in Total Disc Replacements and evaluate their tribological performance.

This was achieved through the manufacture of alumina cervical implants, which were then used for in vitro wear and friction tests. Despite high wear rates, caused by chipping and a high surface roughness on the articulating surfaces, there were some issues with measuring the wear using the gravimetric method. Therefore, the rest of the thesis was focused on developing and validating new methods for measuring volumetric wear using non-contacting optical microscopy. The results showed that the new optical method had several advantages over the traditional gravimetric method, including better measurement precision and the ability to visualise the location of the wear damage.

For Mum and Dad

Acknowledgments

Firstly I must thank my supervisors Profs. Duncan Shepherd and David Hukins. Without their inspiration, expertise and support, this thesis would not have been completed.

I wish to acknowledge the generous support of the Institution of Mechanical Engineers and the University of Birmingham in funding my PhD. Without which I may not have had the bravery to leave industry and join academia.

I am also grateful to Universitas 21 for funding my study period at University College Dublin, and to Dr Eamonn Aherne and Dr Shane Keaveney for welcoming me into their research group. I would also like to thank my landlady, Melissa Curry, for making me part of her family during my stay.

I would like to thank the academic and technical staff of Mechanical Engineering for their technical and moral support, including: Dr Daniel Espino, Dr Aziza Mahomed, Dr Richard Hood, Dr James Bowen, Carl Hingley, Peter Thorton, Simon Rowan, Lee Gauntlet, and Adam Sheward.

My friends in the biomedical engineering laboratory have provided support and distraction in equal measure. Thank you for all the laughter, without which I may not have got through this. Particular thanks must go to Dr David Eckold for his patience in teaching me how to write MATLAB code.

Last, but most definitely not least, I want to thank my family. Mum and Dad, your love and support are unfaltering in both the best and worst of times. Thank you, is not enough. Ben, thanks for teasing me, as every big brother should, and reminding me to get on and finish it. Edward and Isobel, our video calls have brightened up many an afternoon working on this thesis. I hope you grow up to be as inquisitive and fascinated by the world as me.

Table of Contents

List of Figures

List of Tables

Chapter 1

Introduction

Back pain is a significant public health issue in developed societies and it has a substantial social and economic impact (Maniadakis and Gray, 2000). One cause of back pain is degenerative disc disease, which can cause painful intervertebral disc bulges and herniations, and spinal stenosis. If conservative treatment of these conditions fails, then patients may need surgical intervention to improve their symptoms. The gold standard treatment is spinal fusion, however, it can change the biomechanics of the spine and lead to adjacent segment degeneration (Mannion et al., 2014).

Total Disc Replacement is an alternative treatment, which aims to maintain the natural movement in the spine. The implants use either an articulating ball and socket joint or a flexible elastomer insert. Clinical trials have shown that Total Disc Replacement is equivalent to, and in some areas superior to fusion (Blumenthal et al., 2005; McAfee et al., 2005; Zigler et al., 2007). However, a number of failure modes have been found in explanted Total Disc Replacements. One such failure mode is aseptic loosening of the implant, which is caused by osteolysis, an inflammatory response to wear debris produced by the articulating surfaces of the implant (Ingham and Fisher, 2000; Punt et al., 2009). Subsidence, migration, impingement, poor implant positioning and rim fracture have also been identified as reasons for Total Disc Replacement failure (Kurtz et al., 2012).

Further research and development of Total Disc Replacement designs is needed to reduce the incidence of these failure modes. This is particularly important because patients requiring spinal surgery tend to be active and middle aged, which places extra demands on the longevity of the devices (van Ooij et al., 2003; Guyer et al., 2009). *In vitro* experiments can simulate the conditions under which Total Disc Replacements perform in the body. Friction and wear testing

can provide valuable information about the tribological performance of different implant designs and materials. The results of these tests can be used to compare different materials, identify failure modes and improve future designs.

Ceramic materials are beginning to be used in Total Disc Replacement designs and their tribological performance needs to be better understood in this context. Ceramic Total Hip Replacements have produced very low wear rates compared to other materials (Clarke et al., 2000) and it is expected that Total Disc Replacements will produce similar results. The gravimetric method is normally used for measuring wear rates. However, some studies have concluded that it has reached the limit of its resolution, particularly when used with ceramic implants (Bills et al., 2005; Blunt et al., 2009; Sagbas and Durakbasa, 2012). Therefore, new methods need to be developed, which can accurately measure the low wear rates associated with ceramic bearings.

The overall aim of this thesis was to investigate the use of ceramics in Total Disc Replacements and evaluate their tribological performance. The objectives were to:

- Manufacture alumina cervical Total Disc Replacements using ultra-precision grinding techniques to produce a high quality surface finish.
- Conduct a tribological assessment of alumina Total Disc Replacements, using *in vitro* testing.
- Carry out a preliminary study into the use of non-contacting optical microscopy to measure the low wear rates associated with ceramic bearings.
- Develop a new optical method for measuring the volumetric wear of ceramic Total Disc Replacements and compare the results to the traditional gravimetric method.

Chapter 2 outlines and reviews the background research which is relevant to this thesis. The anatomy of the spine is described, including the characteristics and material properties of the vertebrae and intervertebral discs. The effects of degenerative disc disease on these key structures and how it can be treated is explored. This is followed by a description of Total Disc Replacement devices and how they can fail. Lastly, the key aspects of tribology and their relevance to the performance and failure of Total Disc Replacements are explained.

Chapter 3 investigates the use of ultra-precision grinding techniques to produce the articulating surfaces of alumina cervical Total Disc Replacements. The aim of the study was to explore if the high quality surface finish and dimensional tolerance specification could be achieved using grinding tools alone, with no polishing.

In Chapter 4 a tribological assessment of the alumina cervical Total Disc Replacements, made in Chapter 3, was carried out. *In vitro* testing determined the frictional torques produced, the lubrication regime, and the wear rates of the implants. The results were compared with similar tests conducted on Total Disc and Hip Replacements manufactured from other materials.

Chapter 5 presents a preliminary study which uses non-contacting optical microscopy to measure the low volumetric wear rates produced by ceramic bearings. A series of alumina-on-alumina, ball-on-disc tests were conducted with test conditions approximating those of cervical Total Disc Replacement wear tests. The volumetric wear was determined using scan data from a white light interferometer.

Chapter 6 builds on the work in Chapter 5. A new optical method, using focus variation technology, was developed to calculate the volumetric wear loss of the alumina Total Disc Replacements wear tested in Chapter 4. The optical

method was also used to obtain images of the surface damage and identify changes in surface roughness. The precision and accuracy of the optical method was compared to that of the gravimetric method.

Chapter 7 contains the overall discussion and conclusions to the thesis and gives recommendations for further research.

Chapter 2

Background

Overview

This chapter presents and reviews background information and research pertinent to this thesis. Section 2.1 describes the anatomy of the spine and its key structures, as well as their characteristics and material properties. Section 2.2 explains the effects of degenerative disc disease, one of the leading causes of back pain, and how it can be treated. In Section 2.3 one of these treatments, Total Disc Replacement, is explained in detail and also why the devices can fail. Finally, Section 2.4 describes the key aspects of tribology and their relevance to the performance of Total Disc Replacements.

2.1 Anatomy of the Spine

2.1.1 Anatomical Directions

Anatomical directions are used to describe the position of structures relative to other structures in the human body (Figure 2.1) (Moreau et al., 2002). Superior refers to a position above another body part, and inferior refers to a position below. Anterior defines the front of the body and posterior defines the rear. Medial describes a point which is closer to the centre of the body and lateral describes a point nearer the side of the body. Proximal and distal describe a position which is close or distant from the main mass of the body, respectively. When referring to the spine, cranial describes a location towards to the skull and caudal a location towards the coccyx.

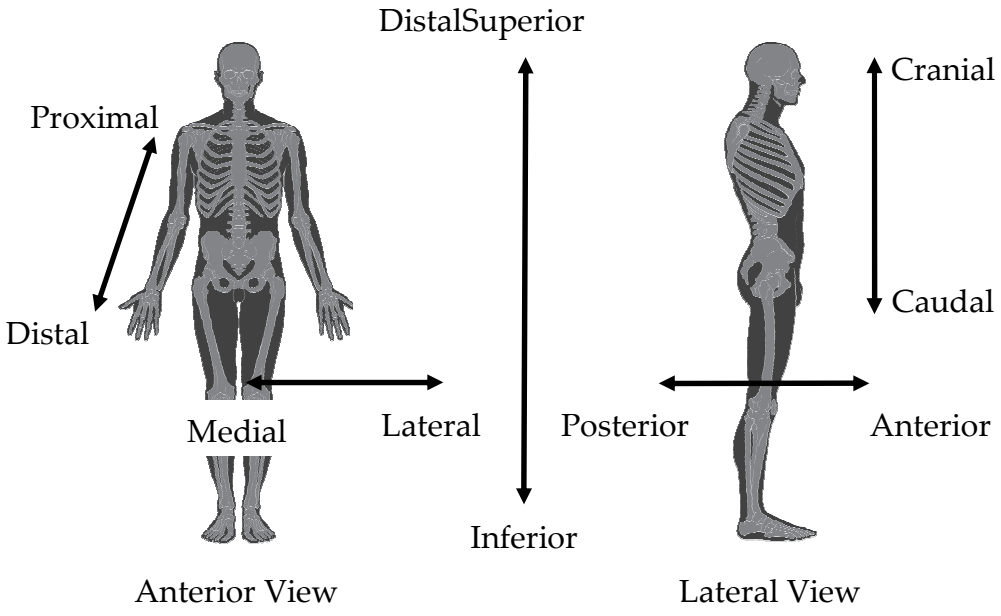

Figure 2.1: Anatomical directions (Lynch and Jaffe, 2006)

2.1.2 Regions of the Spine

The purpose of the spine is to support the body, whilst allowing movement, and to protect the spinal cord from damage. It is comprised of 33 bones, called vertebrae, which are attached to 24 soft tissue structures, known as intervertebral discs (Figure 2.2). The intervertebral discs allow flexibility and movement, but they also have to withstand and transmit large loads.

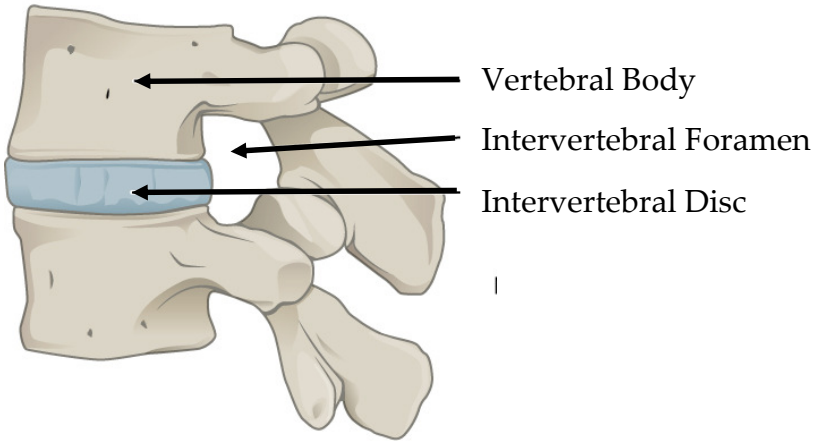

Figure 2.2: Lateral view of a spinal segment (OpenStax, 2014)

The spine is split into five regions, cervical, thoracic, lumbar, sacral and the coccyx (Figure 2.3) (Aiello et al., 2002). There are seven cervical vertebrae in the neck, C1-7, which support the head and provide a high degree of flexibility. Cervical vertebrae and intervertebral discs are the smallest in the spine because they only have to carry the load of the head. It is estimated that the compressive load on the cervical spine ranges from 120 to 1200 N (Patwardhan et al., 2000). The twelve thoracic vertebrae, T1-12, support the rib cage and, therefore, have limited flexibility. The five lumbar vertebrae, L1-5, and intervertebral discs experience the highest loads and moments because they support the load of the upper body. Dolan et al. (1994) demonstrated that during bending and lifting operations compressive loads in the lumbar spine range from 2500 to 5000 N.

As such they are the largest vertebrae and intervertebral discs in the spine. The sacrum is made up from five fused vertebrae. Its purpose is to connect the spine to the pelvis via the sacroiliac joints. The coccyx is also comprised of fused vertebrae and is a vestigial tail, but still has a function as an attachment point for muscles and ligaments (Cramer and Darby, 2013).

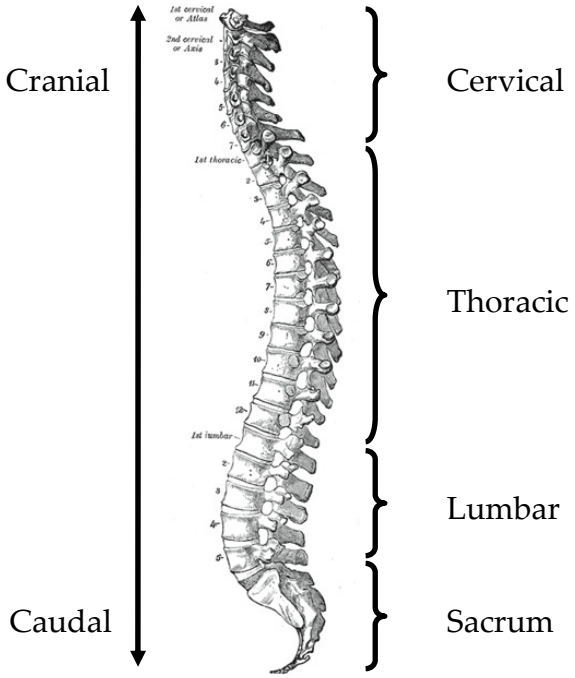

Figure 2.3: Regions of the spine (Gray, 1918)

2.1.3 Spinal Movements

The movement allowed by an individual intervertebral disc between two adjacent vertebrae is small. However, when the many small movements of each spinal segment are combined along the length of the spinal column the result is a substantial amount of movement (Cramer and Darby, 2013). Spinal movements are described using the following anatomical terms (Figure 2.4) (Kurtz and Edidin, 2006). Flexion and extension describes bending anteriorly and posteriorly, respectively. Lateral bending refers to side bending and axial rotation to a twisting motion.

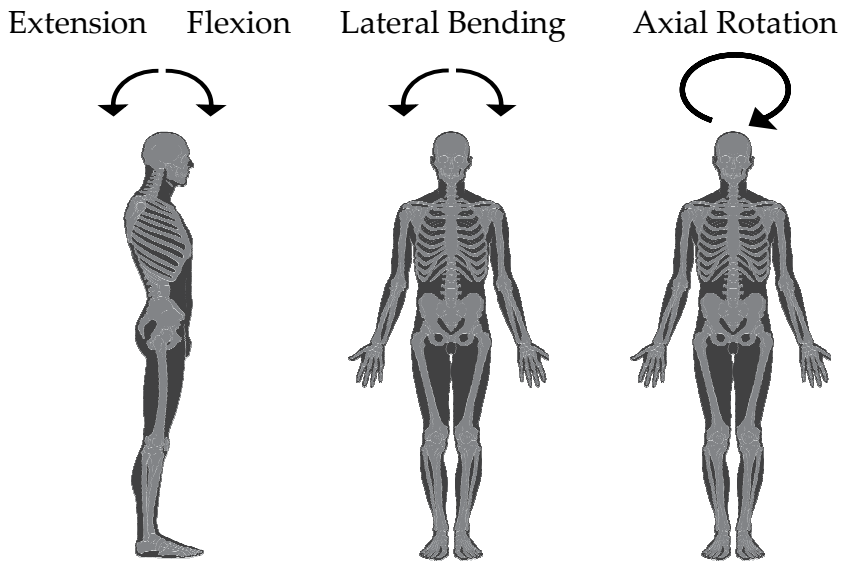

Figure 2.4: Anatomical terms for spinal motions (Lynch and Jaffe, 2006)

2.1.4 Vertebrae

A vertebra is comprised of a vertebral body and a vertebral arch, which forms the posterior section of each vertebrae (Cramer and Darby, 2013) (Figure 2.5). The vertebral arch is formed from two pedicles, directly attached to the posterior of the vertebral body, and two lamina, which connect to the pedicles to form the posterior of the arch. The space between the vertebral body and the arch is known as the vertebral foramen, and is the structure through which the spinal cord passes (Aiello et al., 2002). The posterior elements project from the vertebral arch, including the articular, spinous and transverse processes. The spinous process protrudes posteriorly from the midline of the arch. The two transverse processes project laterally from the intersection between the pedicle and the lamina. The spinous and transverse processes are attachment points for important muscles, which control the movement of the spine (OpenStax, 2014). There are also four articular processes: two superior articular processes, which face upwards, and two inferior articular processes, which face downwards. At each pair of adjacent vertebrae, the superior articular processes of one vertebra

will meet with the inferior articular processes of the other, to form two facet joints. The facet joints vary in size and shape at each level, and play an important role in determining the possible range and direction of motion (Aiello et al., 2002).

The outer surface of the vertebra is comprised of cortical, or compact bone. The interior is made from cancellous bone, which has a lower elastic modulus, is more flexible, and is also less dense than cortical bone (Hukins and Meakin, 2000). Cancellous bone is made up from trabeculae, rod shaped structures, which are oriented along the lines of largest stress (Smit et al., 1997; Feltrin et al., 2001). The main function of the vertebral body is to carry load and it is designed to have the greatest strength for the least bone mass (Feltrin et al., 2001). Vertical trabeculae predominate in the vertebral body and they are supported by horizontal trabeculae, which act as struts (Smit et al., 1997; Feltrin et al., 2001).

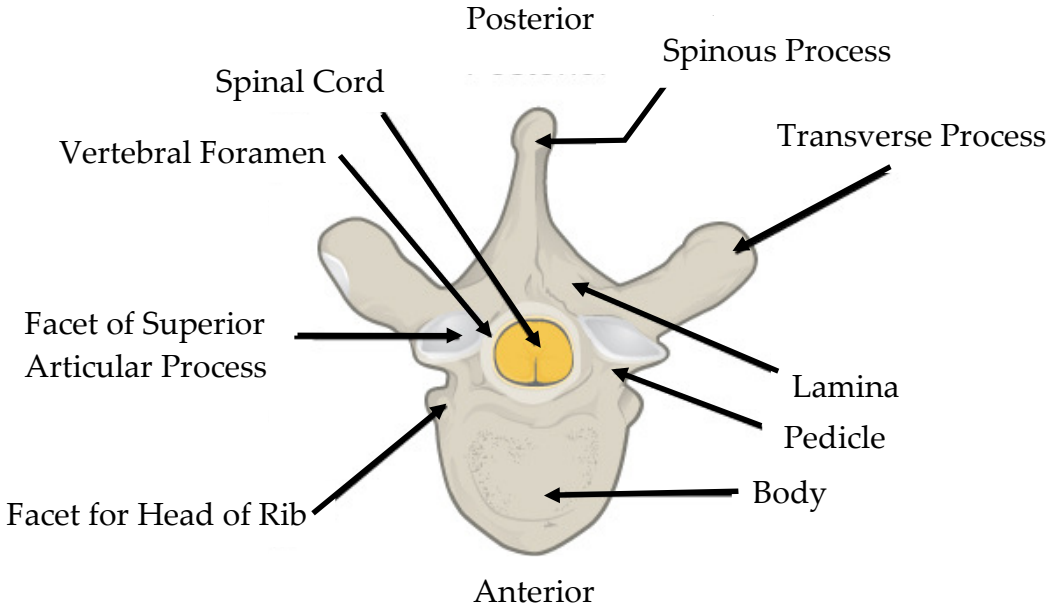

Figure 2.5: Superior view of a typical vertebra (OpenStax, 2014)

2.1.5 Intervertebral Disc

The intervertebral discs are soft tissue structures, which form flexible joints between each of the vertebrae, capable of withstanding the loads applied by the spinal column (Lyons et al., 1981). The intervertebral disc is comprised of water, cells, proteoglycans and collagen fibres, and the proportions of each vary in the different structures. They have three elements: the annulus fibrosus, the nucleus pulposus and the vertebral end plates (Cramer and Darby, 2013) (Figure 2.6). The annulus fibrosus is a fibrous ring, which encloses the nucleus pulposus, the highly hydrated and gelatinous centre of the disc. They are typically described as two distinct types of tissue, however, there is no clear anatomical boundary between them (Hukins, 1992). The vertebral end plates are cartilaginous plates, which join the vertebrae to the superior and inferior surfaces of the intervertebral disc (Cramer and Darby, 2013).

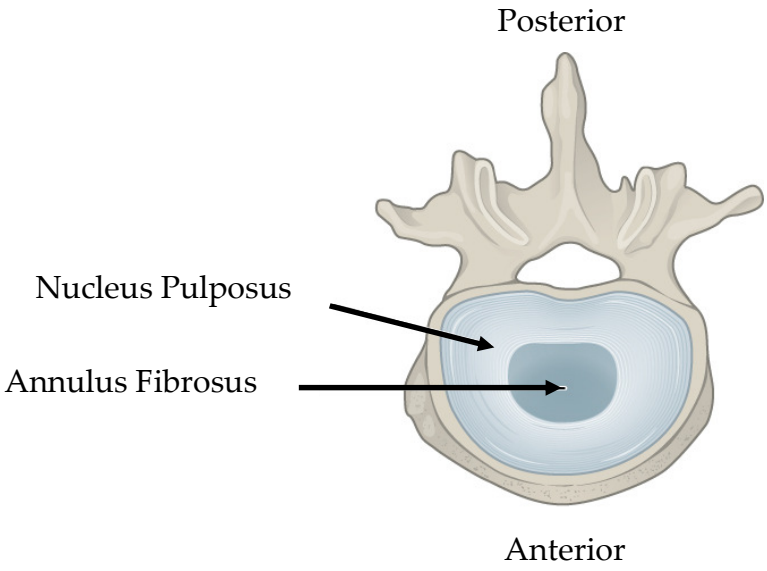

Figure 2.6: Superior view of a typical intervertebral disc (OpenStax, 2014)

Like vertebrae, intervertebral discs vary in size and shape depending on their position in the spinal column. They are thickest in the lumbar region and

thinnest in the thoracic region (Cramer and Darby, 2013). In the cervical region of the spine the discs have an elliptical shape, in the thoracic spine this transforms to more of a heart shape and then into a kidney shape in the lumbar spine (Hukins, 1988).

The intervertebral disc is adapted to withstand compressive axial loads, as well as loads from bending and torsion. The axial loads are comprised of body weight, muscle contraction and external loads (Nachemson, 1987). The nucleus pulposus acts like a fluid in a thick-walled pressure vessel, because it is constrained by the annulus fibrosus and end plates (Hukins, 1992). This enables the intervertebral disc to withstand the compressive loads applied to it. A study by McNally and Adams (1992) measured the pressure in human cadaveric lumbar discs using a transducer. They found the pressure in the nucleus pulposus increased with compressive load, which supports the pressure vessel theory. A maximum compressive force of 2000 N resulted in a pressure in the disc of 2 MPa.

2.1.5.1 Nucleus Pulposus

The nucleus pulposus is made up of water, cells, collagen and proteoglycans. In a healthy disc roughly 80% of its mass is water, however, this water content varies with age and degeneration (Lyons et al., 1981).

Proteoglycans account for 30-50% of the dry weight of the nucleus and is the second most abundant constituent after water (Guerin and Elliott, 2006). The main proteoglycan, aggrecan, is negatively charged and attracts positive ions to the nucleus. The ion concentration in the nucleus is, therefore, higher than the surrounding tissue. This causes osmotic pressure, and water is attracted into the nucleus to balance the ion concentration with the surrounding annulus and end

plates (Johannessen and Elliott, 2005). This is why the nucleus pulposus has such a high water content. The high water content and the osmotic pressure, described above, contribute to the swelling pressure within the nucleus, which supports the compressive loads of the spine. The theory that the nucleus behaves like a pressurised fluid is supported by the fluid-like mechanical properties of the nucleus. The compressive modulus of the nucleus is 1 MPa (Johannessen and Elliott, 2005) and the shear modulus is 6 kPa (Iatridis et al., 1997).

Collagen constitutes 20% of the dry weight of the nucleus pulposus, most of which is Type II and found in other compressive load bearing tissues in the body (Guerin and Elliott, 2006). Collagen fibres give tensile strength and reinforcement to tissues (Hukins and Aspden, 1985). In the nucleus pulposus these fibres are disorganised and randomly dispersed throughout the tissue (Hukins, 1992). Hence, the isotropic pressure in the nucleus, measured by McNally and Adams (1992).

2.1.5.2 Annulus Fibrosus

The annulus fibrosus, of lumbar and thoracic intervertebral discs, is made up from a series of layers of fibrocartilage called lamellae, which encompass the nucleus pulposus (Cramer and Darby, 2013). There are between 15 and 25 lamellae in the annulus (Marchand and Ahmed, 1990), with more layers anteriorly than posteriorly (Guerin and Elliott, 2006). In cervical discs the annulus is a crescent shaped mass of collagen, which is thickest anteriorly and thins laterally (Mercer and Bogduk, 1999). At the posterior of the annulus the nucleus is only constrained by a single thin lamella.

When the intervertebral disc is compressed, the inner and outer edges of the annulus bulge outwards in response to the increased pressure in the nucleus. The annulus must withstand both a compressive radial stress and a tensile tangential stress, which reduce towards the outer lamellae (Hukins and Meakin, 2000; Guerin and Elliott, 2006). The annulus fibrosus can withstand the tensile forces placed on it due to the highly organised collagen fibres in each of the lamellae. It has been shown experimentally that within each lamella the fibres are parallel to one another and tilted at an angle to the axis of the disc of around 60 to 65° (Hukins, 1988; McNally and Arridge, 1995). The tilt of the fibres alternates between adjacent lamellae. This arrangement of layers and alternating collagen fibres is what makes the disc capable of withstanding large, multidirectional loads (Guerin and Elliott, 2006).

The water content of the annulus reduces as the radius of the disc increases, with the inner lamellae being similar to the nucleus at 80%, and falling to 70% in the outer lamellae (Lyons et al., 1981). The annulus can withstand some axial compression because it also has a swelling pressure, due to the presence of proteoglycans (Hukins and Meakin, 2000). The proteoglycan content and, therefore, the water content, is higher in the inner lamellae than the outer lamellae (Lyons et al., 1981). Hukins (1992) predicted that, like the water content, the radial stress in the annulus decreases with radius. This was shown experimentally by McNally and Adams (1992) who measured the pressure in cadaveric discs.

The mechanical properties of the annulus fibrosus are highly anisotropic and inhomogeneous (Guerin and Elliott, 2006). This is because the proportions of water, cells, collagen and proteoglycans vary both radially and from the anterior of the annulus to the posterior. For example, outer lamellae have the

highest collagen content because they are placed under the most tensile stress during bending and torsion (Hukins and Meakin, 2000). The structure of the annulus also changes from the anterior to posterior of the disc. The anterior is characterised by highly organised collagen fibres and more defined lamellae. However, the posterior is characterised by incomplete lamellae and loosely connected fibres (Marchand and Ahmed, 1990).

2.1.5.3 Vertebral End Plates

The vertebral end plates are cartilaginous structures which connect the intervertebral discs to the adjacent vertebrae. The end plates help to evenly distribute loads across the intervertebral disc and also play an important role in the nutrition of the disc (Guerin and Elliott, 2006; Cramer and Darby, 2013). After the first decade of life there is no vascular supply to the disc, so it receives all of its fluid flow and nutrition through diffusion across the end plates (Boos et al., 2002).

2.2 Back Pain

Back pain is a major public health problem in developed societies, which causes chronic pain and disability, and has a significant economic impact. It is estimated that one third of the UK population will have back pain in any one year (Savigny et al., 2009). The last major study into the cost of back pain in the UK in 1998 estimated that it cost the economy £3,440 M to £9,090 M a year in lost working time. Costs to the UK's National Health Service and community care are estimated at £1,067 M per year (Maniadakis and Gray, 2000). Due to economic factors and inflation the current costs will be significantly higher than these figures (National Institute for Health and Clinical Excellence, 2009).

2.2.1 Degenerative Disc Disease

Degeneration of the intervertebral disc is a complex combination of biochemical, cellular and mechanical changes (Johannessen and Elliott, 2005). It can be difficult to discern the difference between normal ageing and degenerative disc disease because they are very similar processes. Indeed a young person can have the level of degeneration in their discs you would expect in an elderly person, and the converse can be equally true (Boos et al., 2002). Although degenerative disc disease is associated with back pain, the precise source and mechanism for the pain is not confirmed (Guerin and Elliott, 2006).

One of the first degenerative changes in the disc is the reduction of the main proteoglycan in the nucleus pulposus, aggrecan (Johannessen and Elliott, 2005). This causes a reduction in the water content and the swelling pressure drops with degeneration (Adams et al., 1996). The collagen fibres in the nucleus also become denatured (Guerin and Elliott, 2006). These changes lead to the nucleus becoming stiffer, more fibrous and changing colour from white to yellow to brown (Adams et al., 1996). It has been shown that in a degenerated nucleus the shear modulus is higher and it acts more like a solid than a fluid (Iatridis et al., 1997).

These degenerative changes in the nucleus pulposus affect the annulus fibrosus. The reduction in pressure in the nucleus makes it less able to withstand compressive loads, which are then transferred to the annulus. The lack of pressure can cause the inner lamellae to bulge inwards under compression, rather than outward (Hukins and Meakin, 2000). Degeneration of the annulus results in the lamellae becoming disorganised and less distinct (Marchand and Ahmed, 1990). Combined with the change in loading patterns, this can cause an

increase in stress concentrations and lead to tears and fissures in the annulus (Adams et al., 1996).

2.2.2 Effects of Degeneration

One effect of degeneration is that the intervertebral discs lose height (Cramer and Darby, 2013). This reduction in thickness leads to increased loading of the facet joints, which can cause osteoarthritis and pain (Adams and Hutton, 1980). The changes in the mechanical properties and loading of the degenerated intervertebral disc can lead to disc bulges and herniations (Figure 2.7). Tissue protrudes through a fissure in the annulus fibrosus and compresses the nerve roots or spinal cord causing pain, which can radiate to other parts of the body (Cramer and Darby, 2013). Degeneration can also lead to spinal stenosis, which is a narrowing of the vertebral foramen. It is caused by the surrounding disc, facet joints, vertebrae and ligaments changing shape, due to degeneration (Guerin and Elliott, 2006).

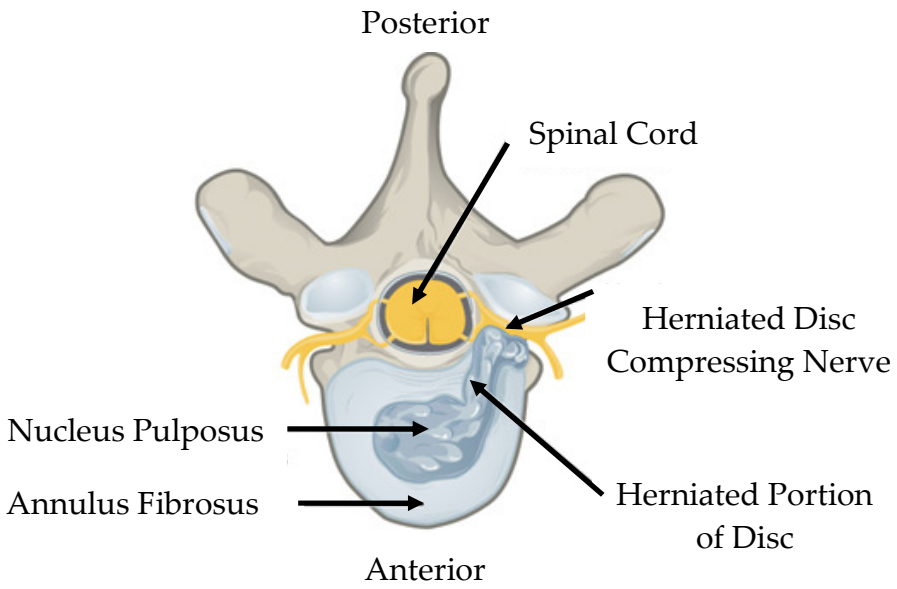

Figure 2.7: Superior view of a herniated intervertebral disc (OpenStax, 2014)

2.2.3 Types of Treatment

The majority of back pain cases are treated conservatively and resolve within three months. Conservative treatment involves rest, pain management, physiotherapy, and activity modification. However, around 10 -15% of patients require surgical intervention (Guerin and Elliott, 2006). Discectomy removes herniated tissue from a degenerated disc and decompresses the nerve root to reduce the pain. Although effective at alleviating pain in the short term, this procedure has been shown to advance degeneration by altering the segment's biomechanics (O'Connell et al., 2011).

Patients with severe degeneration and chronic pain may need to undergo a spinal fusion operation. The affected disc is removed and a fusion cage is fitted between the adjacent vertebrae, together with a bone graft, to fuse the spinal segment. Spinal fusion is considered the "gold standard" surgical intervention (van den Eerenbeemt, 2010) but there is continuing debate over the effectiveness of spinal fusion (Gibson et al., 1999; Gibson and Waddell, 2005: Willems et al., 2011). The biomechanics of the spine are altered by immobilising the intervertebral joint, which may affect the adjacent discs. Indeed, long term follow up of patients, who have undergone fusion surgery, has shown increased degeneration in the adjacent segments (Mannion et al., 2014).

Nucleus replacement is a less invasive procedure than fusion designed for patients with early degenerative disc disease (Marcolongo et al., 2006). The degenerated nucleus is replaced with an implant, which mimics the mechanical properties of a healthy nucleus. The hope being that if normal biomechanical behaviour is restored, degeneration of the annulus fibrosus will be halted.

An alternative surgical intervention to fusion is Total Disc Replacement or Arthroplasty. The patient's intervertebral disc is removed and replaced with an implant, which is designed to enable movement at that spinal segment. It is expected that by maintaining the natural motion of the spine there will be improved clinical outcomes for these patients.

2.3 Total Disc Replacement

The primary aim of Total Disc Replacement is to restore the natural biomechanics of a degenerated intervertebral disc. It has been shown that patients recover faster from Total Disc Replacement surgery than fusion surgery (Blumenthal et al., 2005; Sasso et al., 2008; Pan et al., 2016). Clinical trials have also demonstrated that the flexibility and range of motion of the spinal segment is maintained (McAfee et al., 2005; Zigler et al., 2007; Sasso et al., 2008). This is expected to reduce the frequency of adjacent segment degeneration, however, the evidence for this is mixed. Some trials have found no significant difference in the rate of adjacent segment disease after Total Disc Replacement and fusion (Sasso et al., 2008; Guyer et al., 2009). Others have concluded that Total Disc Replacement does reduce the incidence of adjacent segment disease (Pan et al., 2016; Janssen et al., 2015). It has also been suggested that adjacent segment disease is just the natural progression of degenerative disease and is not caused by surgical intervention (Radcliff et al., 2013).

There have been several randomised clinical trials and follow up studies, which compare the clinical outcomes of Total Disc Replacement procedures with those of spinal fusion (Blumenthal et al., 2005; McAfee et al., 2005; Zigler et al., 2007; Sasso et al., 2008; Murrey et al., 2009). These studies show that Total Disc Replacement is equivalent to, and in some areas superior to fusion. However, Jacobs et al. (2013) reviewed the evidence from these studies and concluded that

any improvements over fusion were so small they were not clinically relevant. The studies do not adequately assess adjacent segment and facet joint degeneration, which are the problems Total Disc Replacements are designed to improve. This is partly because these conditions will take time to develop and the majority of follow up is only at two or five years (Guyer et al., 2012; Zigler et al., 2012; 2013; Janssen et al., 2015). Therefore, although Total Disc Replacements show promise, until longer term trials are completed, it is difficult to conclude if they have significant advantages over fusion.

Total Disc Replacements are a form of joint replacement and they have some similarities with Total Hip and Knee Replacements. Therefore, much of the research into these implants is also relevant to Total Disc Replacement. However, one key difference is the age and activity levels of the patients. The median patient age in the UK is 69 and 68 years for Total Hip and Knee Replacement procedures, respectively (National Joint Registry, 2016). In contrast patients who have undergone Total Disc Replacement procedures in the US and in Europe are typically middle aged, working and more active (van Ooij et al., 2003; German and Foley, 2005; Siepe et al., 2007; Guyer et al., 2009). This places extra demands on the design of Total Disc Replacements, particularly with respect to the device's life expectancy (van den Eerenbeemt, 2010).

2.3.1 Total Disc Replacement Designs

Typically Total Disc Replacement designs have either an articulating ball and socket joint or a flexible elastomer insert. The Charité (DePuy Synthes Spine, Raynham, MA, USA), ProDisc-L (DePuy Synthes Spine, Raynham, MA, USA) and Maverick (Medtronic, Minneapolis, MN, USA), Total Disc Replacement designs are all lumbar implants with a ball and socket joint (Figure 2.8). Both

the Charité and the ProDisc-L are manufactured from Cobalt Chrome Molybdenum (CoCr) alloy and ultra-high molecular weight polyethylene (UHMWPE), whereas, the Maverick has two CoCr parts. These materials are both commonly and successfully used in Total Hip and Knee Replacements. The Cadisc-L (Ranier Technology Ltd., Cambridge, UK) has an elastomeric polymer body with no articulating parts (Figure 2.8).

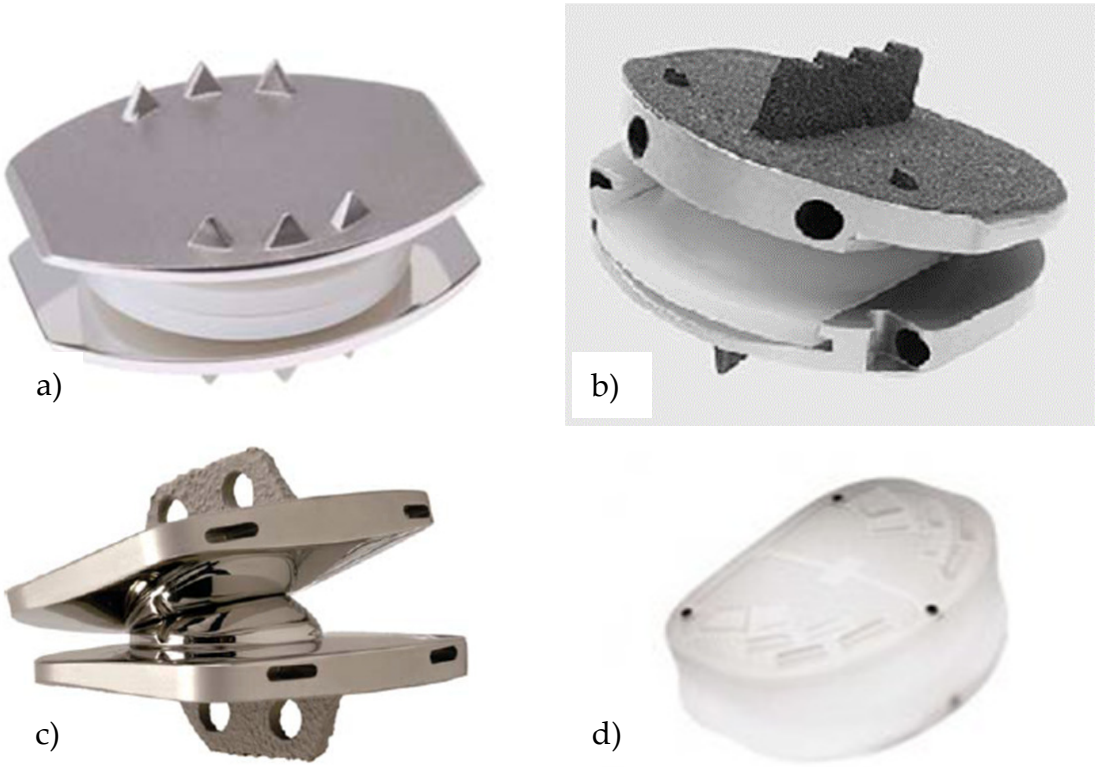

Figure 2.8: Examples of lumbar Total Disc Replacements; a) Charité (Spine Universe, 2016); b) ProDisc-L (Spine Universe, 2016); c) Maverick (Neurosurgery Blog, 2016); d) Cadisc-L (Which Medical Device, 2016)

Cervical Total Disc Replacements do not have to support as much weight as lumbar devices, which opens up more design and material options. For example, the Bryan disc replacement (Medtronic, Minneapolis, MN, USA) has a more biomimetic design, with a flexible polyurethane core contained by a titanium alloy shell (Figure 2.9). The Prestige device (Medtronic, Minneapolis,

MN, USA) is an articulating ball and socket design manufactured from stainless steel (Figure 2.9).

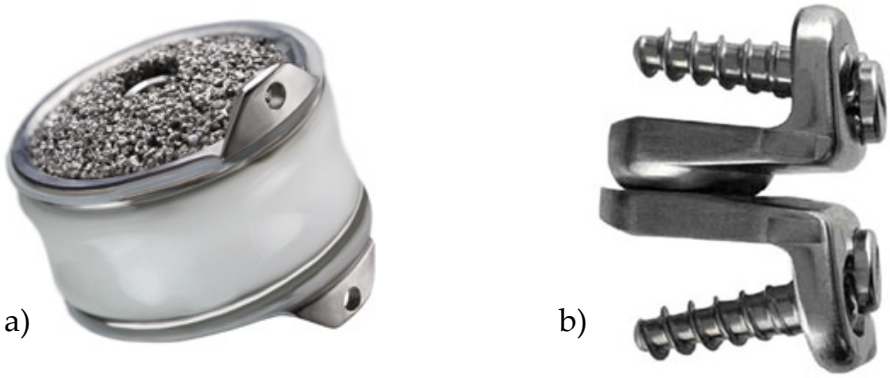

Figure 2.9: Examples of cervical Total Disc Replacements; a) Bryan (Medtronic, 2016); b) Prestige (The Burton Report, 2016)

Ceramics have been successfully used in Total Hip and Knee Replacements and they are now starting to be used in cervical Total Disc Replacements. ALTIA is an articulating silicon nitride design (Amedica Corporation, Salt Lake City, UT, USA), which has undergone initial *in vitro* testing (Finn et al., 2009). The Discocerv device has an alumina-on-zirconia bearing pair (Alphatec Spine Inc., Carlsbad, CA, USA). Enan et al. (2011) have conducted a preliminary clinical trial with the device, finding promising results with 81% of patients having good or excellent outcomes. Also, Nuvasive Inc. (San Diego, Ca, USA) began conducting a clinical trial in the United States of their CerPass, ceramic-on-ceramic implant in 2001 (Clinicaltrials.gov, 2016)

2.3.2 Failure of Total Disc Replacements

There are several reasons why Total Disc Replacements fail, and revision or fusion surgery is needed. One reason is aseptic loosening, where the fixation of the implant to the bone becomes loose (van Ooij et al., 2007; Punt et al., 2008; 2009). Aseptic loosening can be caused by osteolysis, which is an inflammatory

response to the wear debris produced by the articulating surfaces of the implant (Ingham and Fisher, 2000; 2005). This wear debris will enter the soft tissues surrounding the implant. White blood cells, called macrophages, recognise the wear debris as a foreign body and phagocytose it. Phagocytosis is the mechanism by which pathogens are removed from the body. The macrophage will engulf the particle, but this will have no effect because it is a relatively bioinert material. The macrophages then release mediators of inflammation, which summon other cells to the site to help remove the particle. These mediators cause osteoclastic bone resorption, which leads to osteolysis and the eventual loosening of the implant. This also occurs in both Total Hip and Knee Replacements and has been identified as a major factor which limits the longevity of these implants (Schmalzried et al., 1992; Gallo et al., 2013).

The number, size, shape and volume of wear particles all affect the process described above (Green et al., 1998). Green et al. (1998) investigated the bioreactivity of different sized UHMWPE particles *in vitro*. They concluded that the most biologically active particles are those which macrophages are physically able to phagocytise, i.e. 0.3 – 10 μm. In a later study they found that the volumetric concentration of particles is also a critical factor (Green et al., 2000). When the volumetric concentration was raised, particle sizes which were previously inactive became active, and vice versa. Total Disc, Knee and Hip Replacement designs are frequently tested *in vitro* to determine their wear rate, with low rates being desirable (Nevelos et al., 2000; McEwen et al., 2005; Williams et al., 2011; Moghadas et al., 2013; 2015; Xin et al., 2013). However, a low wear rate does not necessarily mean low numbers of biologically reactive sized particles.

Analysis of retrieved lumbar Total Disc Replacements has shown other modes of failure, apart from osteolysis. The Charité implant has been found to fail due to prostheses migration, subsidence of the implant into the vertebrae (Figure 2.10a), fracture of the rim and metal marker wire (Figure 2.10b), and adjacent segment degeneration (van Ooij et al., 2003; 2007; Punt et al., 2008). Impingement is the unintended contact of peripheral surfaces of the implant at the limit of its range of motion (Figure 2.10c) (Siskey et al., 2016). This can be due to poor positioning, subsidence, migration or an incorrectly sized device. The Charité and ProDisc implants have all been found to suffer from impingement, which causes high levels of wear on the rim of the implant (Kurtz et al., 2012a).

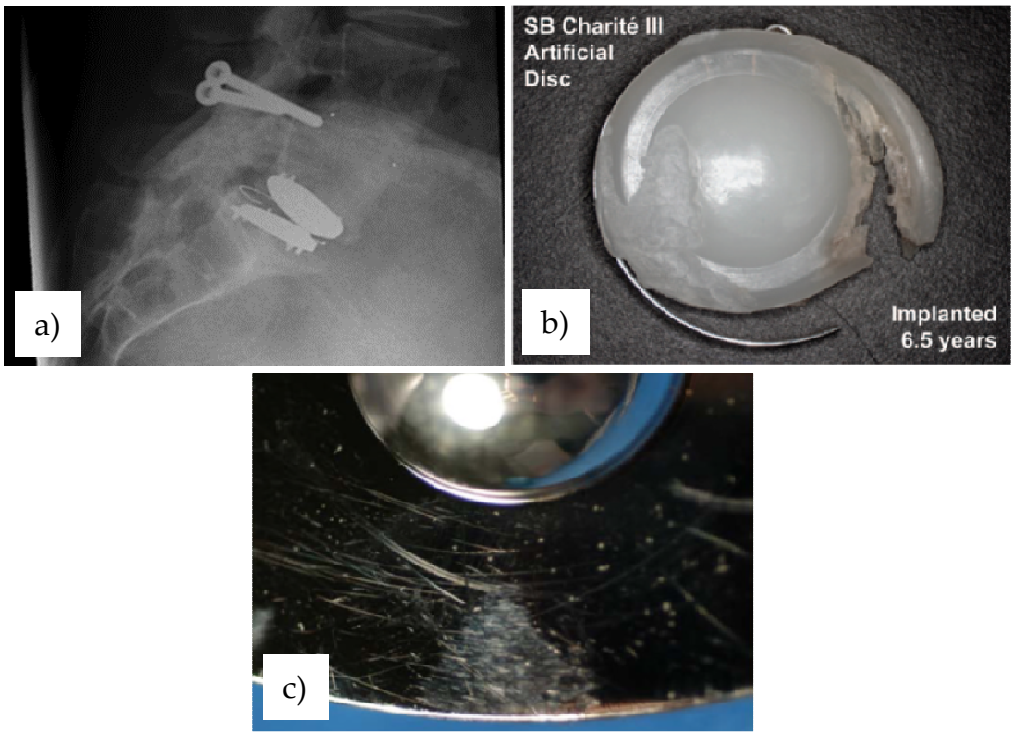

Figure 2.10: Explanted lumbar Total Disc Replacement failure modes; a) Subsidence of a Charité (van Ooij et al., 2007); b) Rim and metal wire fracture of the same Charité (van Ooij et al., 2007); c) Scratches on end plates of a Maverick showing impingement (Kurtz et al., 2012a)

Cervical Total Disc Replacements have also been shown to suffer from impingement due to migration, subsidence, poor positioning etc. (Bertagnoli et al., 2005; Kurtz et al., 2012a; 2012b). For example an analysis of explanted implants conducted by Kurtz et al. (2012a) showed that 67% of Prestige implants and 30% of Bryan implants showed evidence of endplate impingement (Figure 2.11a). In one explanted Prestige implant impingement led to the fracture of the head of the locking screw and moderate wear (Kurtz et al., 2012b). A study of 10 explanted Prestige implants also found evidence of localised screw hole fretting and fretting of the heads of the bone screws in all cases (Figure 2.11b) (Kurtz et al., 2012b). In the case of the Bryan implant wear debris from the titanium endplate due to impingement caused third body wear of the polyurethane core. The Bryan implant's polyurethane sheath has also been shown to experience degradation, leading to folding, permanent deformation and cracking (Figure 2.11c). Another issue which affects cervical total disc replacements is heterotopic ossification (HO), abnormal bone growth in the soft tissues surrounding the implant, which restricts the range of motion of the joint (Figure 2.11d). A study by Leung et al. (2005) of 90 patients with Bryan implants found 17.8% had some HO and in 11% it had severely restricted the range of motion of the joint to less than 2 degrees in flexion/extension. Another study of 48 patients with Bryan and Prestige implants by Lee et al., (2010) found 27% had HO but it only affected the range of motion in 4% of the patients.

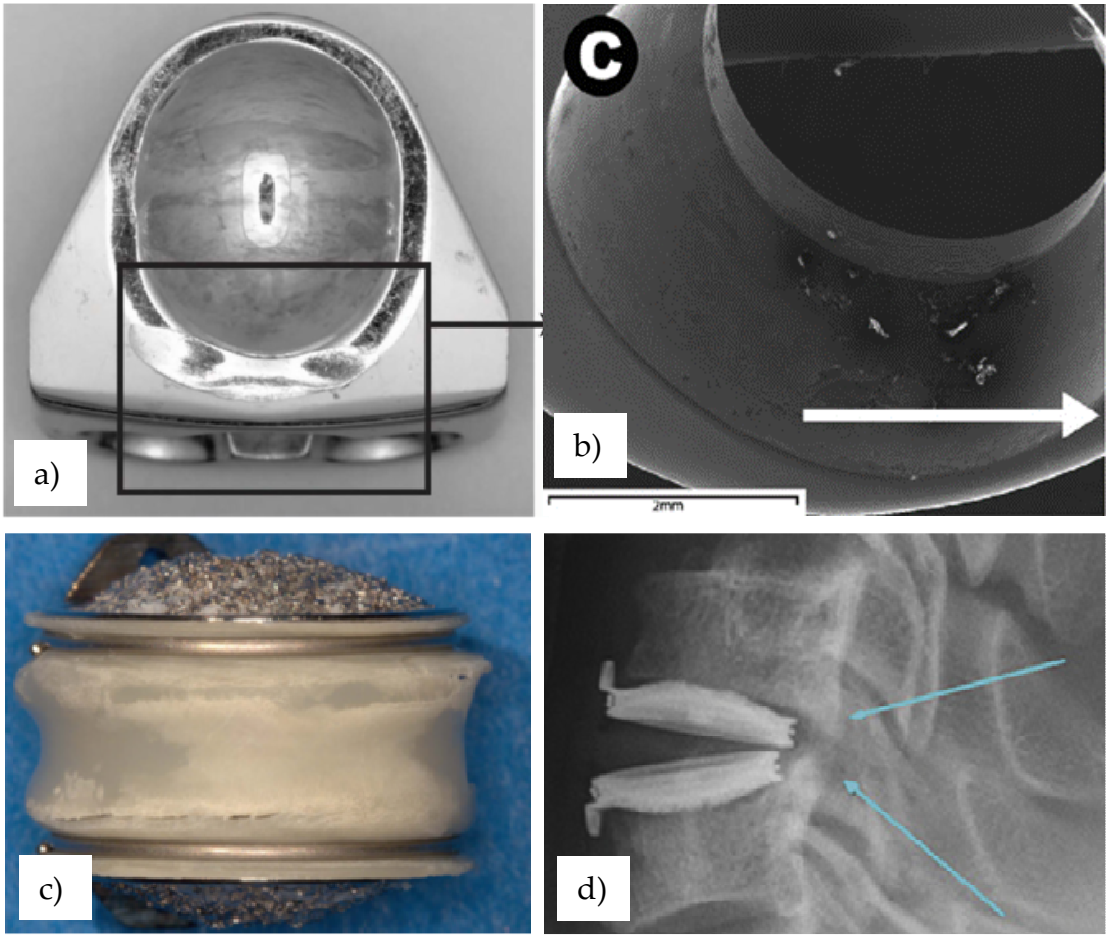

Figure 2.11: Explanted cervical Total Disc Replacement failure modes; a) Impingement on the endplate of a Prestige implant (Kurtz et al., 2012a); b) Screw hole fretting on a Prestige implant (Kurtz et al., 2012b), c) Biodegradation and cracking of the sheath in a Bryan implant (Kurtz et al., 2012a); d) Heterotopic ossification affecting the range of motion of a Bryan implant (Lee et al., 2010)

2.4 The Tribology of Total Disc Replacement

2.4.1 Tribology

Tribology is the study of the lubrication, friction and wear of interacting surfaces, in relative motion to each other (Stachowiak and Batchelor, 2013). The tribological behaviour of two surfaces is highly complex and is determined by

their material properties, microstructures, surface textures, and the lubricant surrounding them. The choice of bulk materials for the two articulating surfaces will determine the properties and microstructure and is key in achieving the desired tribological performance. Hence, the focus on material choice when discussing the wear of Total Disc Replacements. The apparent contact area between two surfaces is much larger than the real contact area between the surface asperities on microscopic scale (Bhushan, 2013). As the two surfaces slide over one another the surface asperities will interact and it is at these junctions that wear and friction originate. Therefore, the surface texture of the articulating surfaces, and the manufacturing techniques used to produce them, play an important role in the tribology of Total Disc Replacements.

2.4.2 Friction

Friction is a force which resists movement between two objects or surfaces. It is tangential to the interface between the surfaces and acts in the opposite direction to the motion. The magnitude of the frictional force can be described by the coefficient of friction, μ, which is defined as the frictional force, F, divided by the normal force, N. The frictional force is independent of the apparent contact area and the sliding velocity between the two surfaces. Friction is a non-conservative force because the work done against friction is dependent on the path taken. Friction is a source of inefficiency, and energy is dissipated in the form of heat, plastic deformation, sound or vibration. The majority of the energy is dissipated in the form of heat (Bayer, 2004). The energy dissipated through friction degrades the surfaces and can cause wear to occur.

It is a commonly held misconception that if friction between two surfaces is reduced the wear will also be reduced. Whilst this is frequently true there are many exceptions. For example, Teflon sliding against steel has a coefficient of

friction of less than 0.1. However, the wear of this system will be significantly higher than that of steel against steel, which has a coefficient of friction of 0.2 (Bayer, 2004). It is clear from this that friction and wear are tribological system responses and not bulk material properties (Bhushan, 2013).

High frictional torques have been shown to cause mechanical loosening and failure of Total Hip Replacements (Simon et al., 1975; Brockett et al., 2007). Therefore, it is possible that high frictional torques also affect the fixation between Total Disc Replacements and the vertebrae. Measuring the frictional torques produced by the articulating surfaces of Total Disc Replacements can provide useful information on how they are interacting with and wearing against each other (Moghadas et al., 2012a; 2012b; Xin et al., 2013; Eckold, 2016). Knowing the frictional torques at different frequencies also enables Stribeck curves to be plotted, which determine the lubrication regime within which the Total Disc Replacements are operating, see Section 2.4.3.1.

2.4.3 Lubrication Regime

When a lubricant is introduced between two articulating surfaces it will normally reduce the friction between them and/or the wear of the surfaces. Lubrication can be described by three regimes: boundary lubrication, fluid film lubrication and mixed lubrication. Each of these regimes is described below and depicted in Figure 2.12.

Boundary Lubrication—There is extensive contact between the asperities of the articulating surfaces. The hydrodynamic pressure in the lubricant is not high enough to support the load and separate the surfaces. Total Disc Replacements and Total Hip Replacements typically operate in this lubrication regime (Scholes and Unsworth, 2000; Moghadas et al., 2013; Xin et al., 2013).

Fluid Film Lubrication—The articulating surfaces are fully separated by a thick film of lubricant, also known as hydrodynamic lubrication.

Mixed Lubrication—The articulating surfaces are partially separated by the lubricant, but some asperities remain in contact with each other. It is an intermediary state between boundary and fluid film lubrication.

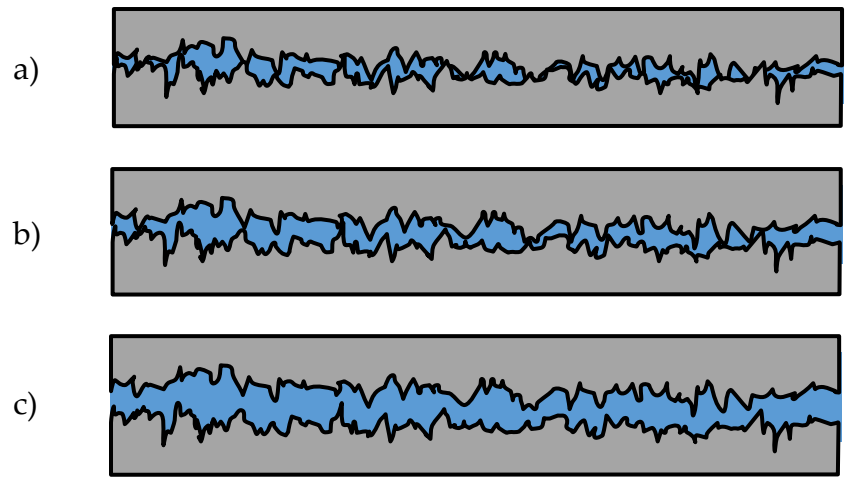

Figure 2.12: Lubrication regimes at the asperity level of articulating surfaces; a) Boundary; b) Mixed; c) Fluid film

2.4.3.1 Stribeck Analysis

Stribeck analysis (Stribeck, 1902) is a method for assessing which lubrication regime bearings are acting under, but has more recently been applied to joint replacements. It has been used in both Total Disc Replacement (Moghadas, 2012) and Total Hip Replacement (Scholes and Unsworth, 2000; 2006; Smith et al., 2001). A Stribeck plot shows the relationship between the friction factor, given by Equation 2.1, and the Sommerfeld number, given by Equation 2.2 (Unsworth, 1978; Scholes and Unsworth, 2000). These equations normalise the friction and velocity and enable comparison between other joint replacements with different loads, geometries and testing conditions.

$$ƒ = \frac{T}{rL} \quad \textbf{Equation 2.1}$$

$$Z = \frac{\eta u r}{L} \quad \textbf{Equation 2.2}$$

where ƒ is the friction factor, T is the frictional torque, r is the radius of the Total Disc Replacement ball, L is the applied load, Z is the Sommerfeld number, η is the viscosity of the lubricant and u is the entraining velocity. The entraining velocity is calculated using Equations 2.3 and 2.4 (Shaheen and Shepherd, 2007).

$$\mathrm{u} = \frac{\omega \mathrm{r}}{2} \quad \textbf{Equation 2.3}$$

$$\omega = \frac{2\pi\theta}{180} f \quad \textbf{Equation 2.4}$$

where ω is angular velocity, θ is the angular displacement and f is the frequency.

The shape of the Stribeck curve indicates the lubrication regime the joint replacement is operating in. Figure 2.13 shows an idealised Stribeck plot. At lower Sommerfeld numbers a constant friction factor is typically observed, which indicates boundary lubrication. As the Sommerfeld number increases the friction factor decreases, which indicates mixed lubrication. As the Sommerfeld number increases further, the friction factor will increase again indicating fluid film lubrication.

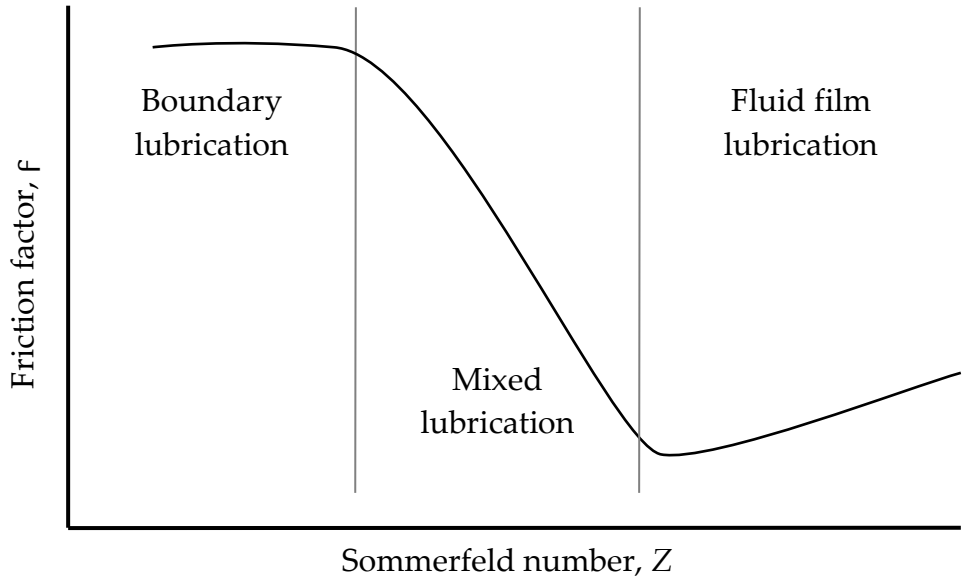

Figure 2.13: Idealised Stribeck plot showing the different lubrication regimes

2.4.4 Lubricant Choice

2.4.4.1 Synovial Fluid

In the case of the human body most joints are synovial, which means they are surrounded by a cavity filled with synovial fluid. Synovial fluid is a viscous, non-Newtonian fluid which consists of the proteins albumin and globulin, the proteoglycan lubricin, phospholipids and hyaluronic acid suspended in interstitial fluid (Smith et al., 2014; Ghosh et al., 2015). In patients with diseased joints, such as osteoarthritis, the composition of the synovial fluid changes. The total protein concentration increases, whilst the amount of lubricin and hyaluronic acid decreases (Smith et al., 2014; Ghosh et al., 2015), see Table 2.1.

It is widely recognised that the proteins, phospholipids and lubricin found in synovial fluid play a significant role in the boundary lubrication of natural and replacement joints (Liao et al., 1999; Mazzucco et al., 2004). These molecules bind to the articulating surfaces of the joint and help the surface asperities slide

over one another in boundary lubrication. Hyaluronic acid increases the viscosity of the synovial fluid and plays an important role in fluid film lubrication (Mazzucco et al., 2004; Ghosh et al., 2015).

The intervertebral disc does not have a synovial cavity and is instead surrounded by a fluid of unknown composition, which is probably similar to interstitial fluid (Shaheen and Shepherd, 2007; Hyde et al., 2016). The protein concentration of interstitial fluid is similar to that of synovial fluid, see Table 2.1.

2.4.4.2 Bovine Serum

Diluted bovine serum is typically specified by standards as the lubricant for *in vitro* testing of joint replacements, including Total Disc Replacements, because the wear rates produced are clinically relevant (Wang et al., 2004; Scholes and Joyce, 2013; British Standards Institution, 2009; 2011a; 2014). Bovine serum is used as a substitution for synovial fluid because it contains albumin and globulin and can be diluted to produce a lubricant with the required total protein content. However, it is not a perfect match in terms of its protein and phospholipid content (Scholes and Joyce, 2013) and does not contain hyaluronic acid (Smith et al., 2014).

Current standards for *in vitro* wear testing of joint replacements specify the total protein content required in the lubricant, see Table 2.1. Several studies on UHMWPE Total Hip Replacements have shown that increasing the total protein content in the lubricant reduces wear rate of the joint (Wang et al., 2004; Brandt et al., 2010). However, a recent study of UHMWPE/CoCr cervical Total Disc Replacements, where the protein content was varied from 30 to 1.875 g/l, has found that the wear rate increases with increasing protein content (Hyde et al.,

2016). Scholes and Unsworth (2000) conducted experiments on alumina Total Hip Replacements and found that there was a statistically significant increase in friction between 0% bovine serum and all other bovine serum concentrations. It has been shown that ceramic-on-ceramic implants operate in a fluid film lubrication regime when they are lubricated by fluids with no protein content (Scholes et al., 2000). Therefore, the increase in wear and friction with protein content is probably due to the proteins in the serum adhering to the surface of the implant and disrupting the fluid film lubrication.

There is also the issue of biodegradation of the bovine serum during the wear tests. Albumin degrades within three days and globulin starts to degrade immediately (Scholes and Joyce, 2013). This leads to a solid boundary layer being formed on the articulating surfaces which reduces wear (Scholes and Joyce, 2013). To limit biodegradation the lubricant used for *in vitro* wear testing is changed regularly which results in the removal of wear particles, which may affect the results.

The viscosity of the lubricant plays a key role in the fluid film lubrication of joint replacements. The viscosity of bovine serum diluted to 20 g/l, as specified by the International Standard for wear testing Total Disc Replacements (British Standards Institution, 2011a), is 1.03 mPa s (Xin, 2013). As discussed in Section 2.4.4.1 the intervertebral disc is probably surrounded by a fluid which is more like interstitial fluid than synovial. Interstitial fluid has a viscosity of 1.24 mPa s (Shaheen and Shepherd, 2007). Moghadas (2012) suggests that the composition of interstitial fluid is between diluted bovine serum and Ringer's solution. However, Ringer's solution has a much lower viscosity of 0.72 mPa s (Moghadas, 2012) and does not contain any proteins to aid boundary

lubrication. Therefore, diluted bovine serum appears to be a more suitable model for the fluid surrounding the intervertebral disc.

Table 2.1: Protein concentrations in different lubricants

Lubricant	Total Protein Concentration (g/l)	Author
Bovine Calf Serum	72	Wang et al. (2004)
Healthy Synovial Fluid	18	Scholes et al. (2013)
Osteoarthritic Synovial Fluid	27	Mazzucco et al. (2004)
Interstitial Fluid	20.6	Fogh-Andersen et al. (1995)
ISO Standard for TDR	20	BSI (2011a)

2.4.5 Wear

Wear is the progressive damage caused to a surface due to relative motion with another surface. The energy dissipated due to friction will degrade the surfaces causing wear. Wear is not only characterised by material loss, but also deformation, changes to the microstructure due to heat damage, and the formation of micro-cracks on the surface (Bayer, 2004). Wear can also be considered as the progressive change to a surface which affects the performance and function of that surface. There are five categories of wear, defined by the mechanism of damage, which are relevant to Total Disc Replacements: adhesion, abrasion, fatigue, fretting, and corrosion (Bhushan, 2013).

Adhesive wear is attributed to high wear rates and high, unstable coefficients of friction (Stachowiak and Batchelor, 2013). Where asperities from opposing

surfaces make contact, they can form a bond, or adhesive junction, due to electron transfer. As the two surfaces move against each other this bond will either be broken or an asperity from one of the surfaces will shear off. The asperity will either stay attached to the other surface or break away to form a wear particle (Bhushan, 2013). Metals are more prone to adhesive wear than ceramics because they are more reactive (Stachowiak and Batchelor, 2013). Burnishing, caused by adhesive wear, has been found in explanted Total Disc Replacements with UHMWPE-on-metal articulating surfaces (Anderson et al., 2006; Kurtz et al., 2007).

Abrasive wear occurs when the asperities of a harder surface slide against a softer surface and damage the surface through plastic deformation or fracture (Bhushan, 2013). The wear can be caused by micro-cutting, micro-fracture, grain pull out or fatigue (Stachowiak and Batchelor, 2013). Abrasive wear in metals and plastics is more likely to be characterised by plastic deformation and micro-cutting, due to their ductility. In brittle ceramics abrasive wear tends to be characterised by micro-fracture and cracking, although plastic flow is also seen (Bhushan, 2013). Abrasive wear has been found on retrieved Charité implants, as well as alumina-on-alumina Total Hip Replacements (Rieker et al., 2001; Anderson et al., 2006; Kurtz et al., 2007; Prokopovich et al., 2011). This type of wear can also be caused by third body particles, such as wear debris, and has been shown to occur in Total Disc Replacements (Kurtz et al., 2007; Lebl et al., 2012).

Repeated loading and unloading of two surfaces in contact can lead to fatigue wear. This can cause micro-cracks to propagate on the surface or subsurface of the material. Eventually these cracks will cause asperities to break away from the surface and form wear debris (Bhushan, 2013). The UHMWPE cores of the

Charité devices have been found with rim fracture and delamination caused by fatigue (Anderson et al., 2006; Kurtz et al., 2007; Hyde et al., 2015).

If the movement between the two surfaces is less than a few millimetres, such as vibrations, fretting can occur (Bayer, 2004). The wear debris produced by fretting tends to be finer than that caused by other mechanisms and is often trapped between the surfaces (Stachowiak and Batchelor, 2013). Fretting is associated with corrosion because the fine wear debris oxidises and causes abrasive wear, which causes more oxidisation, and so on (Bhushan, 2013). Fretting has been observed around the screw heads of the cervical Prestige device (Anderson et al., 2006; Kurtz et al., 2012a; 2012b). It is also a significant failure mode at the stem-cement interface of Total Hip Replacements (Blunt et al., 2009; Cook et al., 2015).

Corrosive wear occurs in and is made worse by a corrosive environment, such as oxygen. The thin oxidised layer on the surface of the object is worn away by the sliding motion, allowing further oxidisation to take place (Bhushan, 2013). Cobalt chrome alloys are frequently used for Total Disc Replacement designs because of their resistance to corrosion (Pham et al., 2015).

2.5 Summary

Back pain is major public health issue for developed societies, which has a significant social and economic impact. One cause of back pain is degenerative disc disease, which can cause painful disc bulges and herniations, arthritis in the facet joints and spinal stenosis. If conservative treatment for these conditions fails then patients may need surgical intervention. Spinal fusion is the gold standard operation, but it alters the biomechanics of the spine and can lead to adjacent segment degeneration.

An alternative intervention is Total Disc Replacement, which aims to maintain the natural movement of the spine. The implants usually have an articulating ball and socket joint or a flexible elastomer insert. Clinical trials have shown that Total Disc Replacement is equivalent to, and in some areas superior to fusion. However, longer term studies are needed to assess adjacent segment and facet joint degeneration, and determine if Total Disc Replacements have significant advantages over fusion.

Retrieval analyses of explanted Total Disc Replacements have found several failure modes. One of which is aseptic loosening of the implant/bone interface caused by osteolysis, which is an inflammatory response to the wear debris produced by the articulating surfaces of the implant. Other failure modes have also been found in explanted implants, such as migration, poor positioning, subsidence, rim fracture, and impingement.

It is clear that there is still room for improvement in the design of Total Disc Replacements. It is particularly important to increase the longevity of the implants because they are typically used in active, middle aged patients rather than retired, elderly patients, like Total Hip and Knee Replacements. Studying the tribology of the articulating surfaces of Total Disc Replacements can give insights into why implants fail and help to improve designs. For example, *in vitro* wear testing of Total Disc Replacements can provide valuable information on the wear rate and wear debris produced by different designs and materials.

Ceramics are emerging materials in Total Disc Replacement designs and their tribological performance needs to be better understood in this context. It is expected that the use of ceramics in Total Disc Replacement would produce very low wear rates. This is because their use in Total Hip Replacement, which is a similar application, produced wear rates as low as 0.017 mg/million cycles

(Clarke et al., 2000). These wear rates are several orders of magnitude lower than those reported for cervical Total Disc Replacements made from plastic-on-metal, metal-on-metal and plastic-on-plastic bearing materials. The loads placed on cervical Total Disc Replacements are an order of magnitude smaller than those placed on Total Hip Replacements. Therefore, one could expect the wear rates in ceramic cervical Total Disc Replacements to be similar or even lower than those recorded in ceramic Total Hip Replacements. Therefore, the overall aim of this study was to investigate the use of ceramics in cervical Total Disc Replacements to evaluate their tribological performance.

In the following chapter a series of alumina cervical Total Disc Replacements were manufactured, which were later used for *in vitro* friction and wear testing. The study aimed to determine if the surface finish and dimensional tolerance specification for the implants could be achieved using grinding methods alone, and no polishing operations.

Chapter 3

Production of the Articulating Surfaces of Ceramic Total Disc Replacements Using Grinding Methods

Overview

This chapter explores the use of grinding techniques in producing the high quality surface finish required on the articulating surfaces of ceramic Total Disc Replacements. Section 3.1 introduces the chapter, whilst Section 3.2 explains the theory of how the grinding conditions and parameters are related to surface roughness. Section 3.3 details the materials and methods for this study. The results of the grinding tests are presented in Section 3.4. Section 3.5 compares the results of these tests against the specification and discusses areas for improvement. The chapter is concluded in Section 3.6.

3.1 Introduction

Over the lifetime of a Total Disc Replacement the articulating surfaces of the implant articulate against each other and wear debris can be produced. Wear debris, predominantly that in the size range 0.3 – 10 μm (Green et al., 1998), can cause an adverse reaction in the periprosthetic tissues called osteolysis. Osteolysis can cause aseptic loosening of the implant and lead to failure and the need for revision surgery (Ingham and Fisher, 2000; 2005). Therefore, it is important to minimise the volume of wear debris produced of this size, through the design and material choice for the articulating surfaces of the Total Disc Replacement.

Ceramics are starting to be used in Total Disc Replacement design; however, there is currently no published data on their wear performance. Ceramics, such as alumina and zircona toughened alumina, are successfully used in Total Hip Replacements because they have low wear rates when compared to other materials (Clarke et al., 2000). It is expected that the use of ceramics in Total Disc Replacement would produce similar results to Total Hip Replacements. The overall aim of this thesis was to investigate the use of ceramics in Total Disc Replacements to explore if they can provide lower wear rates than conventional material combinations. The aim of this chapter was to manufacture alumina cervical Total Disc Replacements to be used for i*n vitro* wear testing, which would enable comparison with other materials.

An important factor in the wear performance of any articulating surfaces is their surface finish. There is no international standard which specifies the surface finish for the articulating surfaces of Total Disc Replacements. However, there is an ISO standard for the similar articulating surfaces of Total Hip Replacements, BS ISO 7206-2:2011 (British Standards Institution, 2011b), which

will be used as a guide for this work. It states that for metallic components the surface roughness, *Ra,* must not be greater than 0.05 μm and for ceramic components the *Ra* must not be greater than 0.02 μm. Also, the maximum profile height, the distance between the top and bottom of the surface peaks and troughs, *Rt*, must not be greater than 1.0 μm.

As well as the surface finish requirements there are also specifications for the dimensional tolerances of the components. The diameter of the femoral head and acetabular cup shall have tolerances of 0 to - 0.2 mm and + 0.1 to + 0.3 mm, respectively. There are also tolerances for the sphericity of the articulating surfaces. The femoral head and acetabular cup must have radial separation values of less than 10 μm and 100 μm, respectively.

The high quality surface finish required by the standards is usually achieved using polishing and lapping processes. The ceramic components are first sintered at a low temperature to produce a small grain size and then undergo hot isostatic pressing to increase the density (Macdonald and Bankes, 2014). They are then ground to the required shape, removing any geometrical deviations, using diamond abrasive tools (Turger et al., 2013). The implants are then polished or lapped to remove any grinding marks and produce the surface finish required. The challenge with polishing operations is to improve the surface finish whilst maintaining the tight dimensional tolerances achieved at the grinding stage (Denkena et al., 2008). These polishing processes can cost up to 10 - 15% of the total manufacturing cost (Jain, 2008). Therefore, the aim of this study was to explore if the surface finish and dimensional tolerance specification for the ceramic articulating surfaces can be met using grinding tools alone with no polishing process.

The grinding processes which will be used in this chapter to produce parts with low surface roughness and high form accuracy, are defined in the literature as ultra-precision grinding processes (Brinksmeier et al., 2010). Ultra-precision grinding sits between conventional grinding and polishing, and aims to improve the surface finish produced by grinding techniques so as to reduce the cost of polishing.

The manufacture and grinding of the implants was conducted by the author at the Advanced Manufacturing Science Research Centre at University College Dublin under the supervision of Dr Eamonn Aherne and funded by a Universitas 21 PhD Scholarship. The work was presented at the 30th International Manufacturing Conference, Dublin, 2013 and published in the proceedings (Green et al., 2013).

3.2 Theory

Grinding removes material through chip formation, in a similar way to machining techniques such as milling and turning, but on a much smaller scale. The process is much less predictable than machining due to the variation in the size, shape and direction of the diamond grit which produces the multiple cutting points on each tool. However, mathematical models have been developed which predict the size of the chips produced and the surface roughness produced by different grinding conditions. Figure 3.1 defines the key parameters used in the mathematical model described below.

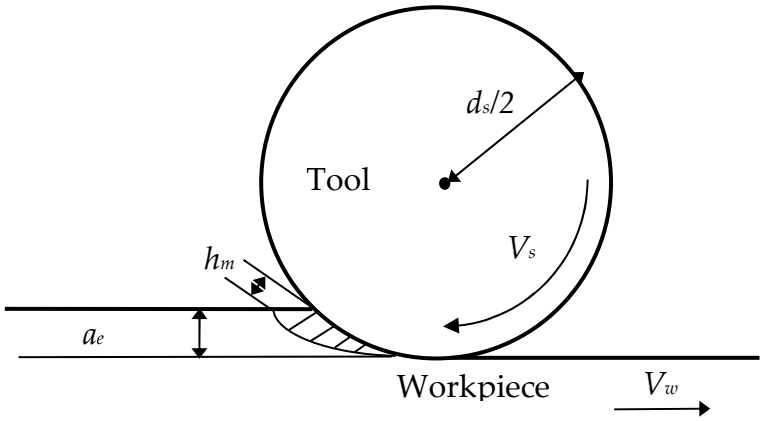

Figure 3.1: Schematic of the process kinematics in peripheral grinding (adapted from Malkin, 1989), where a_e is the depth of cut, h_m is the undeformed chip thickness, V_w is the workpiece feed rate, V_s is the tool speed and d_s is the tool diameter

The theoretical surface roughness, *Ra* in metres, of a surface produced by peripheral grinding is given by Equation 3.1 (Malkin, 1989):

$$Ra = \frac{1}{9\sqrt{3}}\left(\frac{V_w L}{V_s d_s^{1/2}}\right)^2 \qquad \textbf{Equation 3.1}$$

where V_w is the workpiece feed rate in metres/second, V_s is the tool speed in metres/second, d_s is the tool diameter in metres and L is the spacing between cutting points in metres, given by Equation 3.2:

$$L = \frac{2}{Crh_m} \qquad \textbf{Equation 3.2}$$

where C is the density of the active cutting points in grits/metre^2, r is the ratio of the width of the average chip to its height and h_m is the undeformed chip thickness in metres. Huang and Liu (2003) state that the maximum undeformed chip thickness, h_{max}, is given by Equation 3.3:

$$h_{\max} = \left(\frac{3}{C\tan\alpha}\right)^{1/2}\left(\frac{V_w}{V_s}\right)^{1/2}\left(\frac{a_e}{d_s}\right)^{1/4} \qquad \textbf{Equation 3.3}$$

where α is the semi-included angle of the undeformed chip cross section in degrees and a_e is the wheel depth of cut in metres.

On a larger scale the size of the tool and the design of the tool path also affects the quality of the surface finish for freeform grinding. Each toolpath is offset from the previous one by an amount called the stepover or path interval. When using a ball nose grinding tool this leads to scalloping, see Figure 3.2 (Feng and Li, 2002). For a given tool radius the larger the stepover, the larger the scallop height and the higher the surface roughness will be, as explained by Equation 3.4 (Kim and Kim, 1995):

$$h = r - \sqrt{r^2 - \frac{L}{4}^2} \qquad \textbf{Equation 3.4}$$

where h is the scallop height, r is the tool radius and L is the stepover.

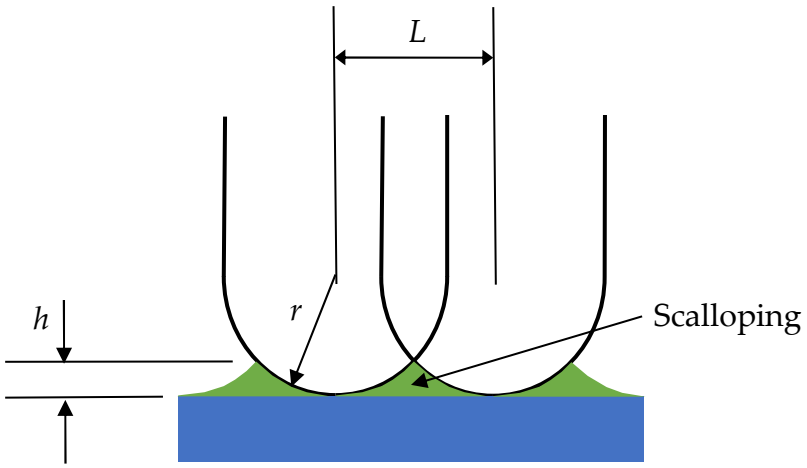

Figure 3.2: Diagram of scalloping, where *L* is the stepover, *h* is the scallop height and *r* is the tool radius

3.3 Materials and Methods

3.3.1 Ceramic Implant Design

The design of the ceramic Total Disc Replacements produced in these tests was focused on the articulating surfaces for wear testing and the fixation to the vertebrae was not considered. The implants were designed to be generic cervical implants with a ball and socket joint based on a sphere with a radius of 7 mm (Figure 3.3 and 3.4). The implants were designed on the CAD software Inventor2014, Build 170 (Autodesk Ltd, Farnborough, UK).

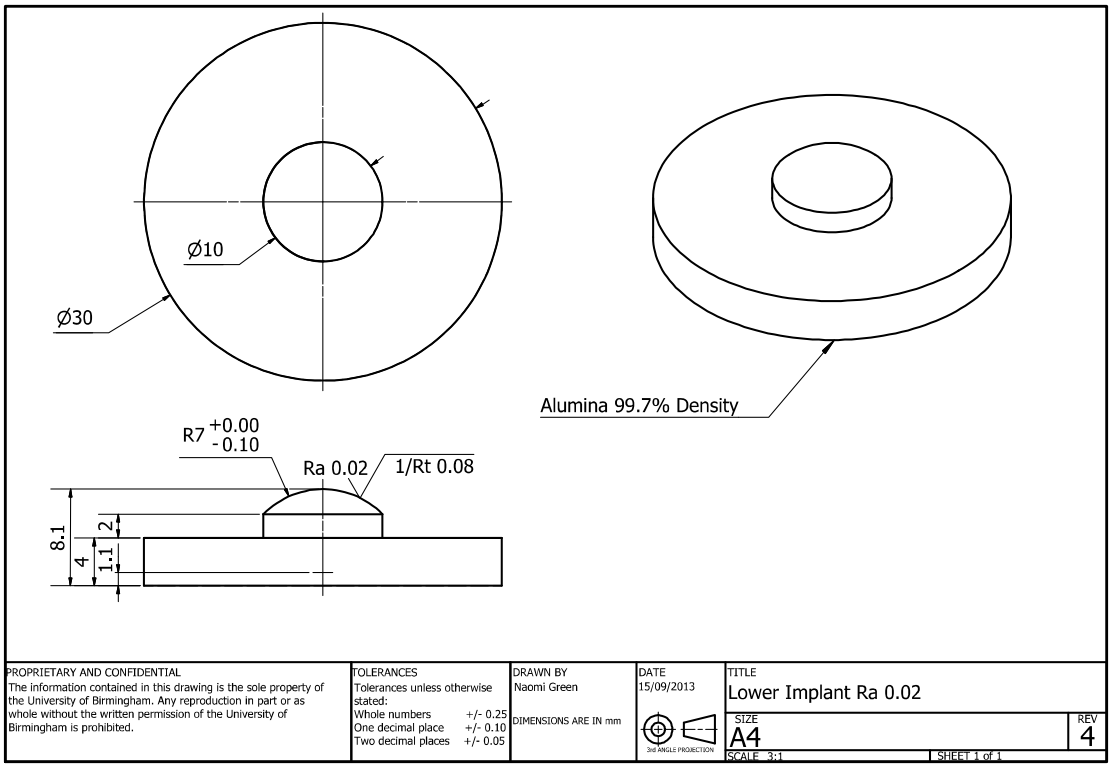

Figure 3.3: Engineering drawing for lower implant

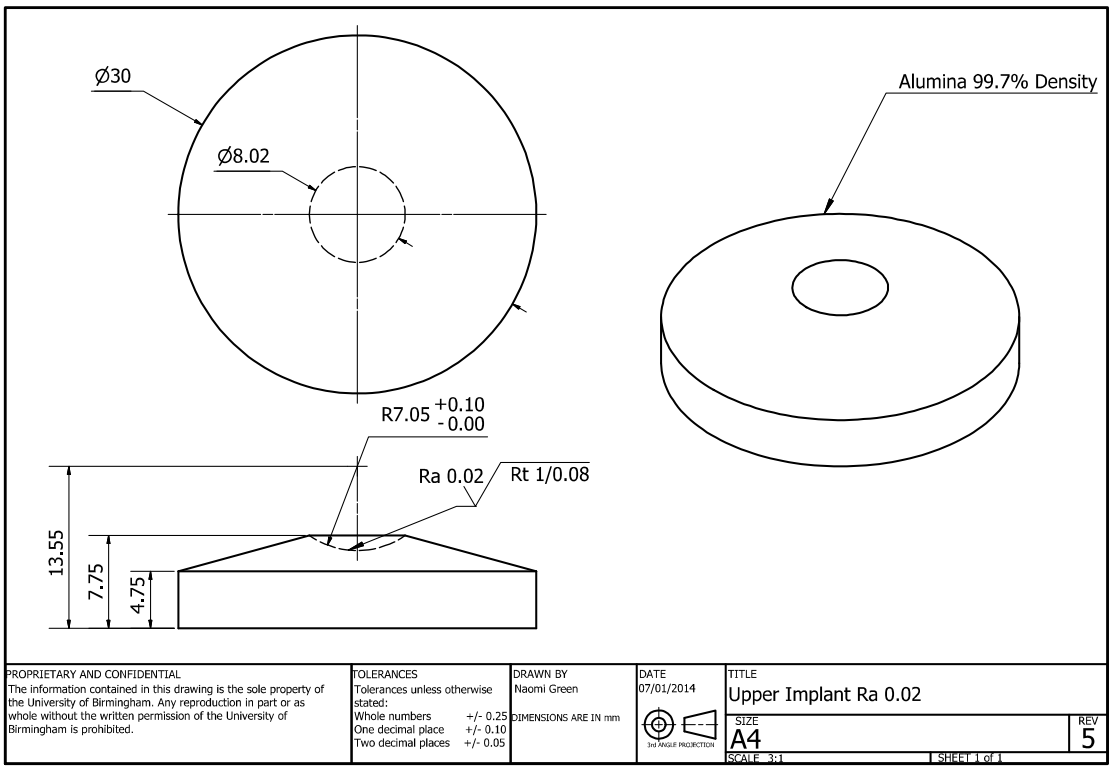

Figure 3.4: Engineering drawing for upper implant

The implants were ground to shape from blanks of alumina 30 mm in diameter and 10 mm in length (Technical Glass Company, Huntingdon, UK). The alumina had a purity of 99.7%, a bulk density of 3.75 g/cm^3, a Young's modulus of 300 – 380 GPa and a flexural strength in 3 point bending of 300 MPa (Robinson, 2012, pers. comm.).

3.3.2 Fixture Design

Fixtures were designed which would enable the implant to be attached to both the grinding machine and the spine simulators used for wear testing in Chapter 4 (Figures 3.5 and 3.6). The fixtures were manufactured from a stainless steel 316L round bar (Alstain Metal Services, Birmingham, UK). The implants were fixed into the recess in the fixture using a high shear strength Epoxy resin (Hysol 9466A, Loctite, Hemel Hempstead, UK). The fixtures were designed on the CAD software Inventor2014, Build 170 (Autodesk Ltd, Farnborough, UK).

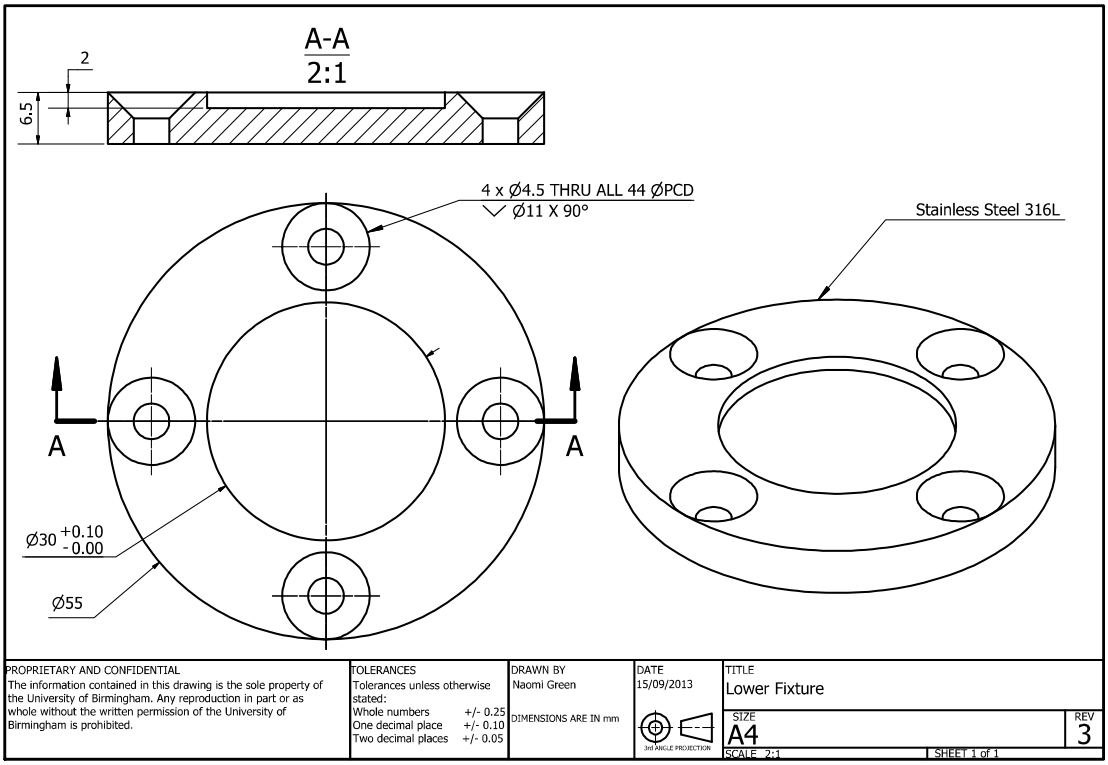

Figure 3.5: Engineering drawing for lower implant fixture

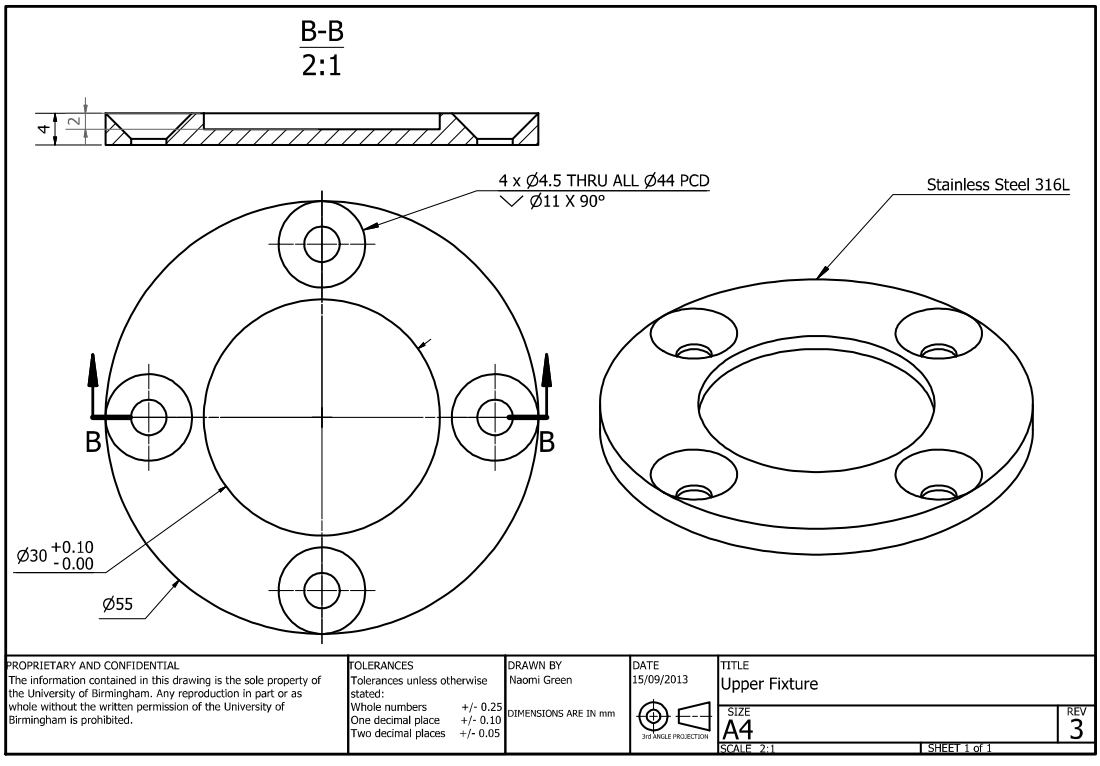

Figure 3.6: Engineering drawing for upper implant fixture

3.3.3 Grinding Tools

The grinding tools were electroplated with two sizes of diamond grit, D64 and D8-12, with an average grain size of 64 μm and 8 μm, respectively (Figure 3.7). The D8-12 grit used diamond particles called Hyperion (Diamond Innovations, Ohio, US) for the first time on a fixed tool. The diamond particles have more surface cutting points than a typical monocrystalline diamond, and when used as slurry they produce higher material removal rates and a better surface finish. The tools were produced (Finzler, Schrock & Kimmel, Bad Ems, Germany) in two different shapes to enable both roughing of the parts and freeform grinding of the articulating surfaces (Figure 3.8).

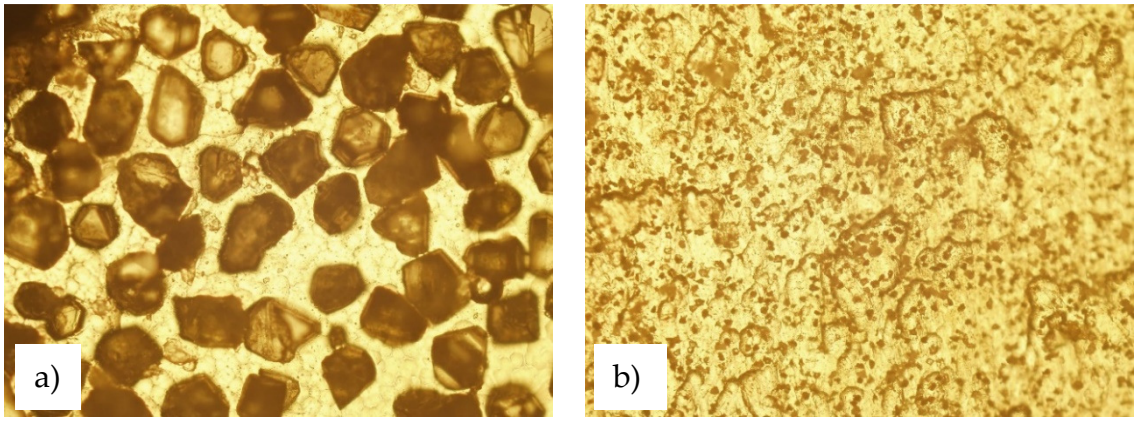

Figure 3.7: Microscope image of the grinding tools taken at 20× magnifiction; a) D64 grit; b) D8-12 Hyperion grit

Table 3.1: Grinding tool parameters

Grinding Parameter	Test A	Test B
Nominal Diamond Size (μm)	D64	D8-12
C, Concentration (grits/cm^2)	~15,000	<300,000
D_s, Tool Diameter (mm)	8	8
α, Semi-included Angle of Undeformed Chip Cross-Section	60	60
r, Ratio of the Width of the Average Chip to its Height	10	10

Table 3.1 shows the dimensions and assumptions made for the tool parameters needed for Equations 3.1 – 3.3 to calculate the predicted undeformed chip thickness and surface roughness.

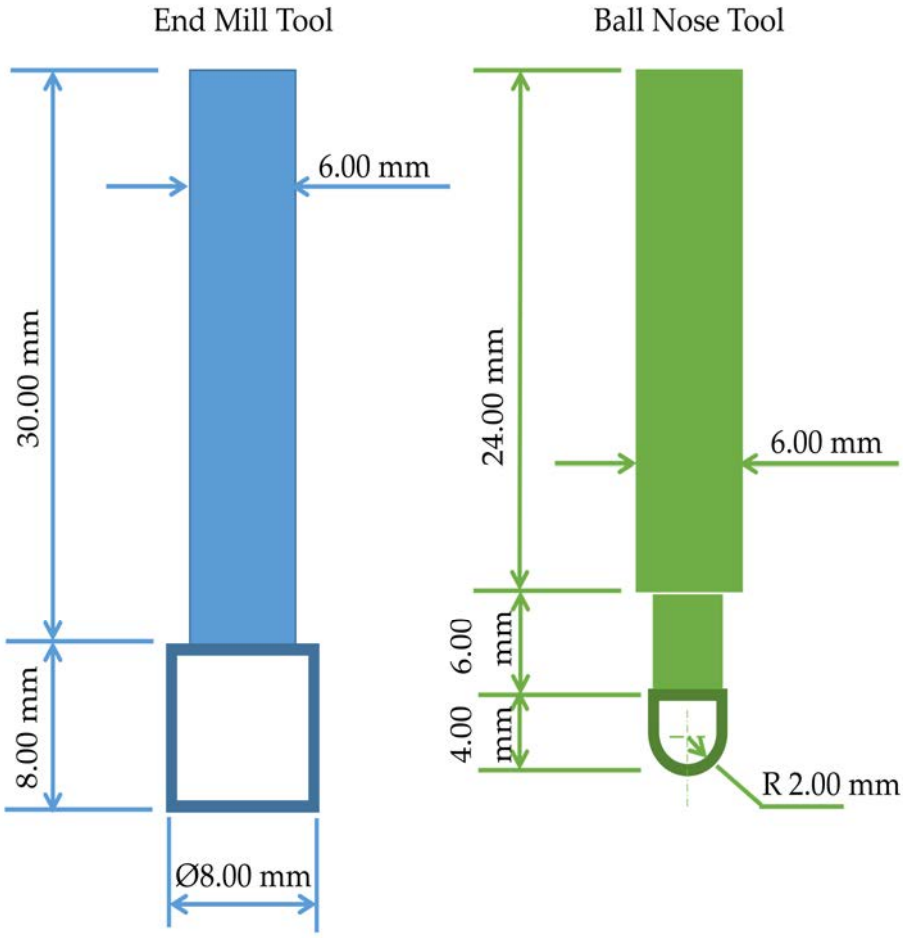

Figure 3.8: Grinding tool dimensions

3.3.4 Grinding Machine

The tests were carried out using a Mori Seiki NMV1500 DCG 5-axis, high precision, computer controlled machining centre (Mori Seiki, Nagoya, Japan) (Figure 3.9). The machine has been designed for use in the medical device industry and can be used for micro-milling, grinding and polishing processes. The spindle has a maximum speed of 60,000 rpm. Vibration is virtually eliminated by driving structural parts at their centre of gravity which improves

precision, surface finish quality and tool life. The grinding tools were held in an HSK E32 6mm diameter heat shrink tool holder (Fenn Tool Ltd, Braintree, UK).

Figure 3.9: Mori Seiki NMV1500 DCG 5-axis vertical machining centre

3.3.5 Coolant System Design

The Mori Seiki was not designed to grind hard ceramic materials. The grinding debris would have entered the coolant and the moving parts of the machine and caused damage. Therefore, a separate self-contained cooling system was designed and fabricated (Figure 3.10). A system drawing for the cooling system can be seen in Figure 3.11.

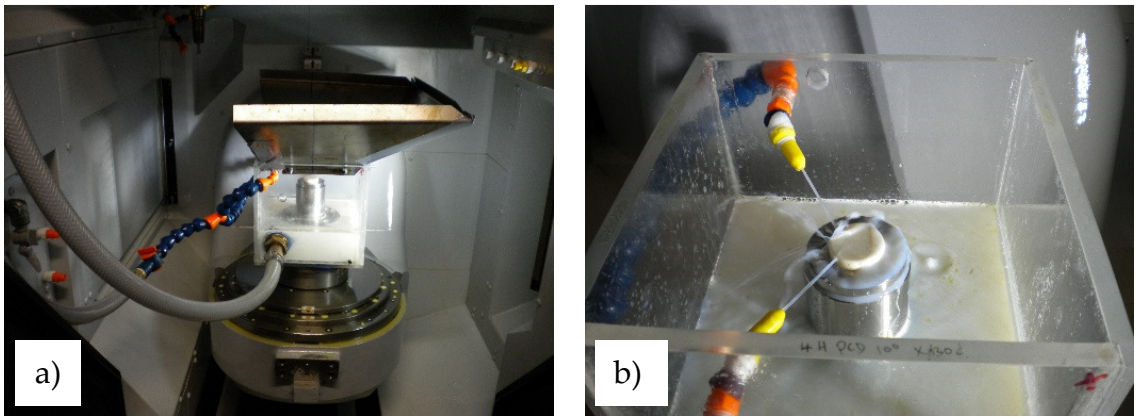

Figure 3.10 a) Self-contained cooling system installed in machine; b) Close up of coolant acting on the workpiece

A perspex container was used as a sump for the coolant. The container was bolted to the machine's pallet via a stainless steel fixture, with a rubber gasket between the two to prevent leakage. This meant only 3 axes could be used for machining. A flexible outlet hose was fitted to the container which fed into a filter for removing the grinding debris. This hose then fed into a valve which controlled the flow through a Lowara CEAM 120/5/A pump (Xylem Inc, Montecchio Maggiore, Italy). A flexible hose from the pump then fed into a Loc-Line modular hose system (Lockwood Products, OR, USA). The Loc-Line system split into two and delivered the coolant to opposite sides of the workpiece via nozzles. The coolant flow rate was controlled by a valve at the start of the Loc-Line system. The sump was fitted with a drain to remove the coolant easily on disassembly. The alumina blanks and fixtures, described in Sections 3.3.1 and 3.3.2, were screwed onto another fixture. This raised the blank up to enable the grinding tool access to it without clashing into the container. Finally a series of sheet steel splash collectors were attached to the container. The parts for the coolant system were designed on the CAD software Inventor2014, Build 170 (Autodesk Ltd, Farnborough, UK) and the engineering drawings can be found in Appendix A.

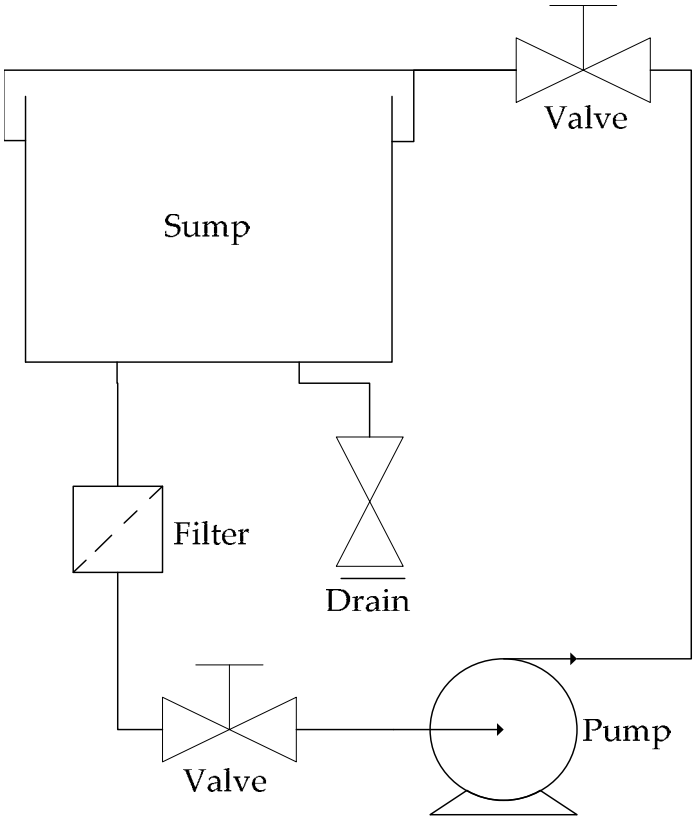

Figure 3.11: System drawing of self-contained coolant system for grinding in Mori Seiki machine

An important variable in grinding experiments is the coolant used and its speed and flow rate. Similar high speed grinding tests by Hwang et al. (2000), on silicon nitride with electroplated diamond wheels, used water soluble oil at a 5% concentration. Therefore, in these tests a similar water soluble oil coolant, Fuchs Ecocool (Fuchs Lubricants, Stoke-on-Trent, UK), was used at a concentration of 5%. The flow rate and speed of the coolant jet are important in keeping the grinding tool clean from debris and removing heat energy from the workpiece and tool. Grinding tests carried out by Webster et al. (2002) determined that the coolant flow rate should be a minimum of 4 l/min per millimetre of grinding width. The tests were conducted on a steel workpiece with an alumina grit tool and a water soluble oil coolant at a concentration of

4%. The tool sped varied between 20 and 35 m/s and the workpiece speed was 0.2 m/min. In the majority of the grinding tests conducted in this chapter, the grinding width was below 1 mm. Therefore, the flow rate was set at 4 l/min to exceed this minimum requirement. It has been shown by Cui (1995) that the speed of the coolant jet should be equal to the speed of the grinding wheel. The maximum tool speed in these grinding tests was 25 m/s. However, the coolant jet speed was set to 34 m/s because this is the closest speed which could be achieved with the 4 l/min flow rate and the smallest available nozzle size, 1/16" diameter.

3.3.6 Initial Peripheral Grinding Tests

An initial set of peripheral grinding tests were undertaken using the end mill tools to investigate the appropriate parameters to use for the freeform grinding of the Total Disc Replacements. Test A was conducted using the D64 tool alone and test B used the D64 tool followed by the D8-12 tool. Equations 3.1 – 3.3 and the tooling parameters in Table 3.1 were used to determine initial test parameters for tests A and B, which would produce a target *Ra* of 0.1 μm and 0.02 μm, respectively (Table 3.2). All tool paths were programmed using CAM software ESPRIT 2012 (DP Technology Corp, Camarillo, CA, USA).

Table 3.2: Initial peripheral grinding tests: grinding parameters and tooling

Test	Tool	Tool Velocity, V_s		Workpiece Velocity, V_w	Grinding Width, B_s	Depth of Cut, a_e
		rpm	m/s	mm/min	mm	μm
A	D64 End Mill	30,000	12.5	2,250	8	10
B	D8-12 End Mill	60,000	25	1,000	8	5

3.3.7 Initial Freeform Grinding Tests

The next phase of the study was to conduct initial freeform grinding tests to produce the articulating surfaces of the implants. During the initial peripheral grinding tests the D8-12 tool failed, see Section 3.4.1. Therefore, it was redesigned and manufactured with multiple layers of diamond grit to improve its longevity and performance.

The first freeform test, Lower Implant C, focused on roughing out the shape of the lower implant from the alumina blank using the D64 End Mill. The operations, tools and parameters are summarised in Table 3.3 and depicted in Figure 3.12. Not all the parameters detailed in Table 3.3 to 3.8 are applicable to every grinding operation. The depth of cut and grinding width parameters apply to the more simple peripheral grinding operations and step over applies only to freeform grinding operations. Operations 1 and 2 were cylindrical grinding processes designed to swiftly remove the top and sides of the blank, respectively, leaving behind a central cylinder from which the spherical articulating surface would be ground. The workpiece velocity and depth of cut were increased from test A to reduce the production time. The third operation followed a freeform toolpath which produced the spherical shape of the articulating surface. The sphere was oversized to allow for a future finishing operation with the D8-12 tool which would remove the deeper grinding marks from the D64. There was a concern over crashing the tool into the workpiece so this operation was purposely positioned 100 μm higher in the z-direction than needed to produce the desired dimensions. This created a 100 μm high cylinder at the pole of the sphere which meant the implant could not be used for some measurements and the wear tests.

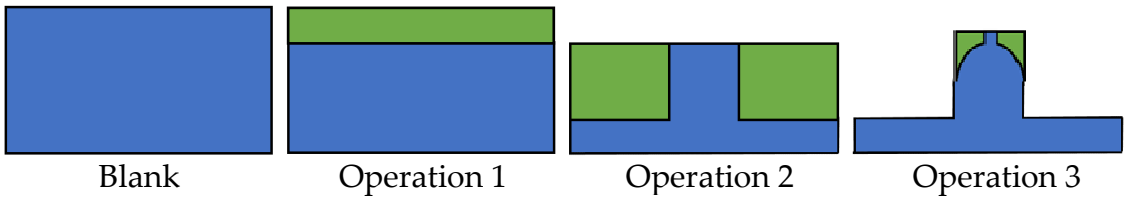

Figure 3.12: Lower Implant C: schematic of grinding operations. (Green areas denote material removed by each operation)

Table 3.3: Lower Implant C: grinding parameters and tooling

Operation		Tool	Tool Velocity, V_s		Workpiece Velocity, V_w	Grinding Width, B_s	Depth of Cut, a_e	Step Over
			rpm	m/s	mm/min	μm	μm	μm
1	Rough	D64 End Mill	30,000	12.5	4,000	1,500	20	N/A
2	Rough	D64 End Mill	30,000	12.5	4,000	2,100	20	N/A
3	Rough	D64 End Mill	30,000	12.5	2,500	N/A	N/A	5

The second freeform test, Lower Implant D, refined the processes in test C and added a pre-finishing process with the D64 ball nose tool and a finishing process with the D8-12 tool to improve the surface finish, see Table 3.4 and Figure 3.13. Operation 1 combined the tool paths of operations 1 and 2 from the previous test to rough out the central cylinder. Operation 2 roughed out the spherical shape of the articulating surface. The aim of operation 3 was to improve the surface finish and remove the deeper pits left by the previous faster operations, by applying a slower pre-finishing process with the D64 ball mill. The final finishing process, operation 4, improved the surface finish by using the D8-12 ball mill at a much higher tool speed, and lower workpiece velocity and step over than test C, see Table 3.3. In order to eliminate machine generated vibrations as the tool moved towards the pole of the sphere, the workpiece velocity was decreased (< 1 mm radius, 300 mm/min; <0.3 mm radius, 100 mm/min).

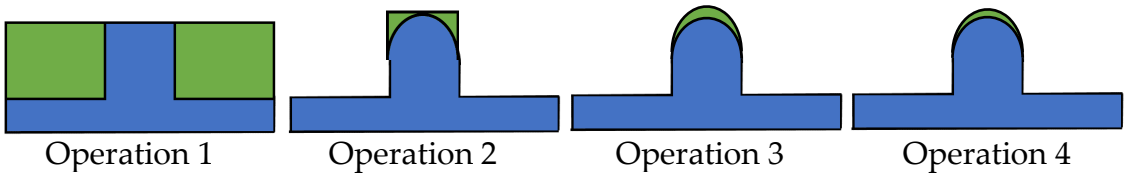

Figure 3.13: Lower Implant D: schematic of grinding operations. (Green areas denote material removed by each operation)

Table 3.4: Lower Implant D: grinding parameters and tooling

Operation		Tool	Tool Velocity, V_s		Workpiece Velocity, V_w	Depth of Cut, a_e	Step Over
			rpm	m/s	mm/min		µm
1	Rough	D64 End Mill	30,000	12.5	2,000	20	N/A
2	Rough	D64 End Mill	30,000	12.5	2,000	N/A	20
3	Pre Finish	D64 Ball Nose	30,000	Max 6.28	1,500	N/A	10
4	Finish	D8-12 Ball Nose	55,000	Max 11.52	1,000	N/A	5

The third freeform test, Upper Implant E, concentrated on roughing out the first upper implant. The operations, tools, and parameters are summarised in Table 3.5 and depicted in Figure 3.14. Operation 1 roughed out the external shape of the implant using the same parameters as operation 1 in test D. Operation 2 used the D64 ball nose tool to grind out the concave spherical pocket in the implant. The workpiece velocity was significantly reduced, when compared to the other roughing operations, because in this process the tool was grinding on both sides and there was a risk of overheating and tool failure.

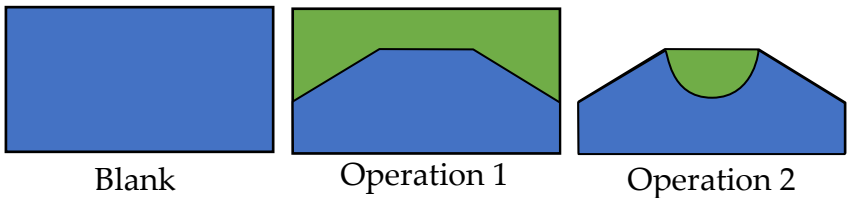

Figure 3.14: Upper Implant E: schematic of grinding operations. (Green areas denote material removed by each operation)

Table 3.5: Upper Implant E: grinding parameters and tooling

Operation		Tool	Tool Velocity, V_s		Workpiece Velocity, V_w	Step Over
			rpm	m/s	mm/min	μm
1	Rough	D64 End Mill	30,000	12.5	2,000	20
2	Rough	D64 Ball Nose	30,000	Max 6.28	140	1 μm incremental depth max z

The fourth freeform test, Upper Implant F, was identical to test E, but added a finishing process to the articulating surface with the D8-12 ball mill, see Table 3.6 and Figure 3.15. The workpiece velocity was increased slightly from the roughing operation because the pocket had already been ground down, therefore, the tool would not be grinding on both sides. Once again, the workpiece velocity was reduced as the tool moved towards the pole of the sphere. However, unfortunately the multilayer D8-12 tool failed again during this process; see Section 3.4.1 for further details.

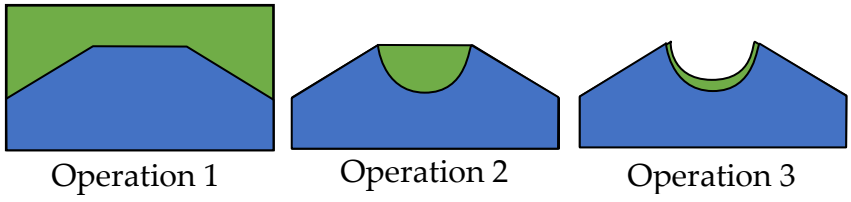

Figure 3.15: Upper Implant F: schematic of grinding operations. (Green areas denote material removed by each operation)

Table 3.6: Upper Implant F: grinding parameters and tooling

Operation		Tool	Tool Velocity, V_s		Workpiece Velocity, V_w	Depth of Cut, a_e	Step Over
			rpm	m/s	mm/min	μm	μm
1	Rough	D64 End Mill	30,000	12.5	2,000	N/A	20
2	Rough	D64 Ball Nose	30,000	Max 6.28	140	N/A	1 μm incremental depth max z
3	Finish	D8-12 Ball Nose	55,000	Max 11.52	500	3	N/A

3.3.8 Implant Manufacture

After the initial tests it became clear that the D8-12 tool was prone to failure and not reliable. Therefore, the two final implant pairs were manufactured using only the D64 tools. The same grinding operations were used for the lower implants as in tests D and F, but for the finishing operations the D8-12 tool was replaced with the D64 (Table 3.7 and Table 3.8). The parameters for the finishing operations were made the same for both the upper and lower implants in the expectation that they would produce similar surface finishes for each pair.

Table 3.7: Lower Implants G and H: grinding parameters and tooling

Operation		Tool	Tool Velocity, V_s		Workpiece Velocity, V_w	Depth of Cut, a_e	Step Over
			rpm	m/s	mm/min	μm	μm
1	Rough	D64 End Mill	30,000	12.5	2,000	20	N/A
2	Rough	D64 End Mill	30,000	12.5	2,000	N/A	20
3	Pre Finish	D64 Ball Nose	30,000	Max 6.28	1,500	70	N/A
4	Finish	D64 Ball Nose	45,000	Max 9.42	300	20	N/A

Table 3.8: Upper Implants I and J: grinding parameters and tooling

Operation		Tool	Tool Velocity, V_s		Workpiece Velocity, V_w	Depth of Cut, a_e	Step Over
			rpm	m/s	mm/min	μm	μm
1	Rough	D64 End Mill	30,000	12.5	2,000	N/A	20
2	Rough	D64 Ball Nose	30,000	Max 6.28	140	N/A	1 μm incremental depth max z
3	Finish	D64 Ball Nose	45,000	Max 9.42	300	20	N/A

3.3.9 Surface Characterisation

The articulating surfaces were characterised using a non-contacting optical 3D micro coordinate system, InfiniteFocus (Alicona Imaging GmbH, Raab/Graz, Austria) which can measure both form, surface roughness and true colour in one scan. The InfiniteFocus has an electronic stage which provides precise movement in the *x*-*y* plane and an objective turret with the following lenses: 5×, 10×, 20×, 50× and 100×. The InfiniteFocus is based on focus variation technology, which uses the limited depth of field of the optic to determine the 3D topography of the sample. For each position on the sample the optic is moved in the vertical or *z*-direction and a series of images are taken. An algorithm then calculates in which image that position is most in focus and therefore, its *z*-depth.

The surface roughness measurements were taken in accordance with the ISO standard for the similar articulating surfaces of hip implants, BS ISO 7206-2:2011, which references BS EN ISO 4287:1998 and BS EN ISO 4288:1998 (British Standards Institution, 2011b; 1998a; 1998b). The measurements were taken using the InfiniteFocus software MeasureSuite v5.1. Five measurements were taken on the articulating surface; one at the pole and one in each quadrant roughly 30° from the pole. BS ISO 7206-2:2011 specifies values for *Ramax* and

Rtmax, which are simply the largest of the 5 measurements taken for each parameter, and also specifies that the average values are reported. Therefore, both the maximum and average of each parameter were calculated for each test.

The appropriate cut off length, λc, and profile evaluation length, l, depend upon the roughness of the item being sampled (British Standards Institution, 1998b). The surface roughness, *Ra*, of these implants is in the range $0.1 < Ra \geq 2$ μm for which λc and l should be 0.8 mm and 4 mm, respectively. However, BS ISO 7206-2:2011 specifies that λc and l should be 0.08 mm and 0.4 mm respectively, so these values were used for the measurements instead.

The form removal function of the InfiniteFocus MeasureSuite software was used to produce detailed images of articulating surfaces of the implants. Each scan was cropped to the diameter of the articulating surface so that only the spherical segment was included. The form removal function was then used to subtract a spherical form from the data and therefore, produce an image which shows where the data deviates from a perfect sphere. This technique enables grinding marks and dimensional errors to be clearly seen (Figure 3.16).

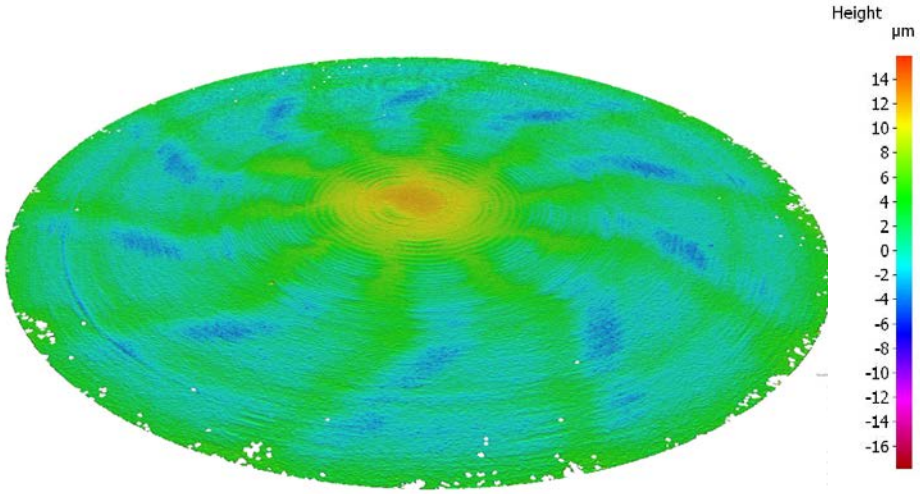

Figure 3.16: Grinding marks on upper implant

The surface of Lower Implant C was sputter coated with gold and then imaged using an Environmental Scanning Electron Microscope (SEM), XL30 ESEM FEG (Philips, The Netherlands) operated at 10.0 kV.

3.3.10 Sphericity and Dimensional Tolerances

The sphericity of the implants was also measured using the InfiniteFocus. The method used was similar to that outlined in BS ISO 7206-2:2011. Each scan by the InfiniteFocus produced a set of *x*, *y*, *z* coordinates which described the topology of the articulating surface. The average radius and the coordinates of the centre were calculated from these points using the least squares method. The radial separation, r_s, is defined in the ISO standard as:

$$r_s = \vec{OP} - r_a \qquad \textbf{Equation 3.5}$$

where OP is the distance from the centre of the sphere to the measured point which is the furthest away from the average radius, r_a. The average radius measurements were also compared against the nominal radius, *r*, to determine the dimensional error, r_{err}, and therefore, whether the implant dimensions were within the specified tolerances:

$$r_{err} = r - r_a \qquad \textbf{Equation 3.6}$$

These calculations were undertaken using a custom MATLAB function called '*dimensional_analysis.m*', MATLAB version r2015a (Mathworks, Massachusetts, USA), see Appendix B.1. This function crops the InfiniteFocus scan to the size of the articulating surfaces. It then calls the MATLAB function '*spherefit.m*', which was downloaded from the MATLAB File Exchange (Jennings, 2013), to calculate the average radius and centre of the sphere. This function was adapted to also calculate the radial separation, see Appendix B.2.

3.4 Results

3.4.1 Tool Performance

During the initial peripheral tests the D64 grinding tool performed well in terms of a repeatable material removal rate at a level that would enable the rough shaping of the Total Disc Replacements in a practical cycle time. Test B was stopped after only the third grinding cycle, because the D8-12 tool reached total wear, and the abrasive and bond had been removed to expose the bare metal (Figure 3.17). This led to discoloration of the surface of the sample and a notable increase in frictional torque. Therefore, a new D8-12 tool was designed with multiple layers of grit in an attempt to extend its life.

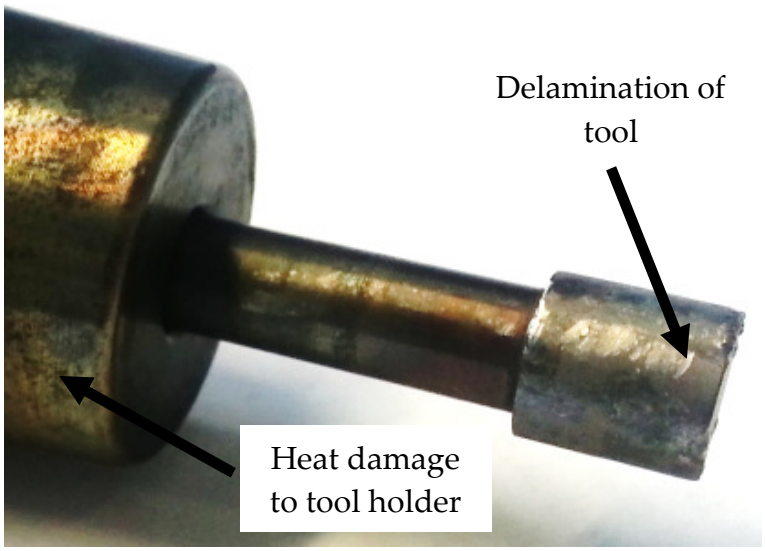

Figure 3.17: Damage to D8-12 tool

A completed lower and upper implant can be seen in Figure 3.18. As with the peripheral tests the D64 tool performed well in terms of removal rate and both the lower and upper implants were successfully roughed out. The new multilayer D8-12 tool performed well on the finishing process of Lower Implant D. However, it failed again during the finishing process on Upper Implant F, embedding metal fragments in the articulating surface and making the implant

unusable for wear testing. It was decided, due to its unreliability, not to use the D8-12 tool for the manufacture of any further implants.

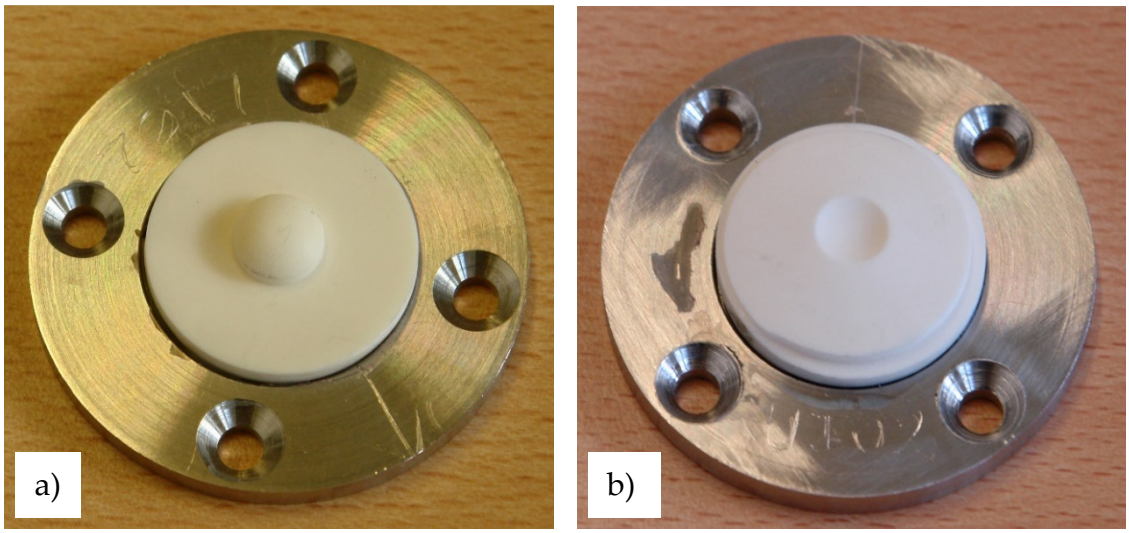

Figure 3.18: Manufactured implants; a) Lower implant D; b) Upper implant E

3.4.2 Surface Characterisation

Table 3.9 shows the surface characterisation results of the initial peripheral grinding tests and compares them against the theoretical predictions made using Equations 3.1 – 3.3.

Table 3.9: Initial peripheral grinding tests: predicted and measured surface parameters

	Predicted *Hm*	Predicted *Ra*	Measured *Ra*	Measured *Rt*
	µm	µm	µm	µm
Test A	1.096	0.103	0.448	2.888
Test B	0.098	0.002	0.200	0.985

Figure 3.19a shows a SEM image of the surface topography of Lower Implant C, with the centre of the implant on the left and the edge of the implant on the right of the image. The tooling marks from the grinding process can be clearly seen, with some significant gouging towards the centre. Figure 3.19b shows a

higher magnification image of the surface topography towards the edge of the implant and Figure 3.19c shows the gouging in the centre of the implant in more detail.

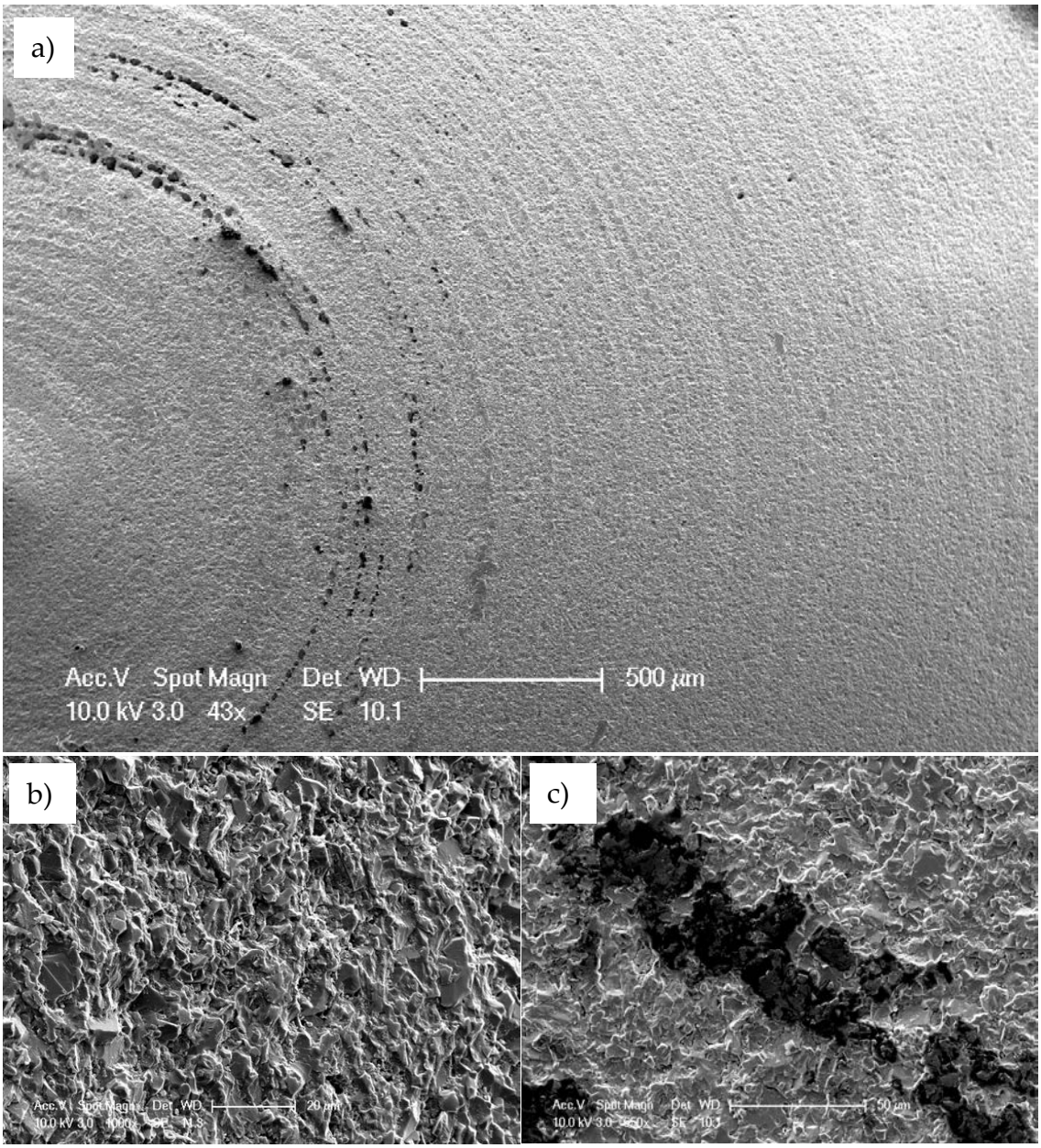

Figure 3.19: SEM images of Lower Implant C; a) 43× magnification of the centre to the edge of the implant; b) 1000× magnification of the edge of the implant; c) 650× magnification of the gouging at the centre of the implant

The results of the surface characterisation for all the freeform grinding tests can be seen in Table 3.10. Only four measurements were taken for Lower Implant C and Upper Implant F, due to the extra 100 microns at the pole, see Section 3.3.7, and the failure of the D8-12 tool before reaching the pole, respectively.

Table 3.10: Freeform grinding tests: maximum and average measured surface parameters

	Ra max	*Ra ave*	*Rt max*	*Rt ave*
	μm	**μm**	**μm**	**μm**
Lower Implant C	0.386	0.326	1.943	0.946
Lower Implant D	0.268	0.209	2.011	1.274
Lower Implant G	0.389	0.323	2.675	1.904
Lower Implant H	0.363	0.328	2.053	1.958
Upper Implant E	0.534	0.366	3.439	2.401
Upper Implant F	0.370	0.357	2.064	1.915
Upper Implant I	0.545	0.438	2.750	2.512
Upper Implant J	0.480	0.391	3.298	2.478

Due to the geometry of the lower implant there was a flat surface on each part which was produced using face grinding with the D64 end mill. Surface characterisation was undertaken on these surfaces in order to compare them with the results of the freeform grinding and better understand the effect of the freeform tool path on the *Ra* and *Rt* values, see Table 3.11.

Table 3.11: Face grinding: measured surface parameters

	Ra	*Rt*
	μm	**μm**
Lower Implant C	0.337	2.681
Lower Implant D	0.115	0.621
Lower Implant G	0.196	1.008
Lower Implant H	0.185	1.442

Surface roughness measurements were taken in four locations from the centre to the edge of a lower and upper implant to analyse if the position on the radius of the sphere affected the surface finish, see Table 3.12.

Table 3.12: Surface parameters measured from centre to edge of implant; a) Lower Implant D; b) Upper Implant E

a)

	Ra	*Rt*
	μm	**μm**
Centre	0.582	3.449
	0.549	3.470
	0.942	5.855
Edge	1.326	9.942

b)

	Ra	*Rt*
	μm	**μm**
Centre	0.481	4.270
	0.749	4.495
	0.869	5.757
Edge	1.004	6.256

3.4.3 Sphericity and Dimensional Tolerances

The results of the dimensional analysis and sphericity tests can be found in Table 3.13. Lower Implant C could not be analysed because it was purposefully manufactured with an extra 100 microns at the pole, see Section 3.3.7. Upper Implant F could also not be analysed because of the failure of the D8-12 tool during the finishing process.

Table 3.13: Sphericity and dimensional errors

	Average Radius, r_a	Dimensional Error, r_{err}	Radial Separation, r_s
	mm	mm	μm
Lower Implant D	6.93	- 0.07	17.11
Lower Implant G	6.99	- 0.00	9.67
Lower Implant H	6.98	- 0.02	17.88
Upper Implant E	7.10	+ 0.05	16.15
Upper Implant I	7.16	+ 0.11	12.73
Upper Implant J	7.15	+ 0.10	25.16

3.5 Discussion

The initial peripheral grinding tests produced higher surface roughnesses, *Ra*, than those predicted by the equations given in Section 3.2 (Table 3.9). The *Ra* for the D64 tool was a factor of 4 higher and the *Ra* for the D8-12 was 100 higher. Equations 3.1 to 3.3 were designed for use with ductile metals and may, therefore, not have been suitable for use with brittle ceramics. It has been shown, however, that at small depths of cut, ductile material removal can occur in brittle materials because plastic flow becomes more energetically favourable than fracture (Bifano et al., 1991). The equations have also been previously used in other similar studies on the grinding of ceramics (Li and Liao, 1997; Yin and Huang, 2004).

The difference between the predicted and measured *Ra* value for the D64 tool, however, was much smaller than that for the D8-12 which suggests the prediction problem has more to do with this tool than the theory. This could be because the tool failed during use and did not reach its full potential or it could be due to the assumptions made regarding the density of the active cutting points, *C*. It is well documented that measuring and estimating the number of

active cutting points is problematic and there are a variety of methods and formulas for doing so (Li and Liao, 1997). The D8-12 tool was using a new type of grit, Hyperion, and the assumption for *C* was based on the maximum number of particles which can theoretically fit within a square unit. However, not all of the particles will be in contact with the workpiece at once, due to the irregular shape of the grit and the three dimensional nature of the tool surface. Early on in the life of the tool the percentage of particles in contact and, therefore, active cutting points may be as low as 10%. As these particles grind down, more particles will come into contact with the workpiece and the number of active particles will increase. Therefore, the density of the active cutting points may have been overestimated, or due to the early tool failure the percentage of particles in contact with the workpiece may not have increased to its maximum value.

The surface roughness, *Ra*, achieved on the freeform grinding test ranged from 0.268 to 0.545 μm (Table 3.10). None of the grinding tests met the ISO standard surface roughness specification ($Ra < 0.02$ μm, $Rt < 1$ μm). Use of the D8-12 tool did lower the *Ra* when compared to similar D64 tests, but these values were still at least a factor of 10 higher than specified. The *Rt* values were also lowered by the D8-12 tool but were only a factor of 2 higher than specified.

When compared with similar studies on the grinding of ceramics, the surface roughness values produced by the tests in this chapter are of a similar order of magnitude. A study of freeform grinding of alumina Total Knee Replacements using toric diamond tools with D46 and D15 grit sizes produced *Ra* values of roughly 0.9 and 0.7 μm, respectively (Denkena et al., 2008). A later study by the same group produced a *Ra* of 0.1 μm using only grinding processes, but then they polished the implant with a flexible silicone bond diamond tool to produce

a *Ra* of 0.008 μm (Turger et al., 2013). Yin and Huang (2004) conducted grinding tests on alumina using a D160 grit tool at a range of speeds from 40 to 160 m/s. They found that at 160 m/s there was a transition between brittle and ductile behaviour, which only resulted in an associated reduction in *Ra* from roughly 0.8 to 0.7 μm.

This suggests that even with development and further parameter testing the D8-12 tool is unlikely to be able to produce a surface quality which meets the ISO standard specification for the articulating surfaces of the implant. However, the tool did improve the *Ra* and *Rt* values so it is still worth developing the tool to use in pre-finishing processes because it will reduce the time and cost involved in the polishing process.

The size of the diamond grit on the grinding tool is not the only factor affecting the surface quality of the articulating surfaces. The grinding mechanism used to produce the surface has a significant impact on its roughness. For example, the flat surfaces, produced by the D64 end mill, on the lower implants have lower *Ra* and *Rt* values (Table 3.11) than those produced by both peripheral and freeform grinding with the D8-12 tool (Tables 3.9 and 3.10), despite the larger diamond grain size of the tool. This result is supported by a study of face and peripheral grinding of silicon by Denkena and Friemuth (2003) which showed that under the same conditions, face grinding produced an *Ra* seven times lower than that produced by peripheral grinding. The reason for this difference is that during face grinding the same area of the workpiece has repeated contacts with the grinding tool, due to the overlapping of the toolpath, and forms a low surface roughness. Due to its shape, the ball nose tool used in the freeform tests makes contact with the workpiece more like a peripheral grinding tool than a face grinding tool, which will lead to higher *Ra* values.

The other factor which affects the surface quality of ground freeform surfaces is the toolpath used to generate the part. On the whole the flat surfaces produced by both the peripheral and face grinding tests had lower *Ra* and *Rt* values than the freeform articulating implant surfaces. In fact the peripheral grinding test B, with the D8-12 end mill tool, was the only test to come in under specification for the *Rt* value. This shows that the scalloping produced by the ball nose tool and the stepover between the three-dimensional toolpaths are responsible for the reduced surface quality.

When using the ball nose tool the scallop height and, therefore, the surface finish and *Rt* values, can be reduced by reducing the stepover between the toolpaths or increasing the diameter of the tool, see Equation 3.4. However, in three-dimensions and with a radius of curvature on the surface this equation becomes more complex and the scallop height varies depending on the tool's position on the sphere (Warkentin et al., 1996). At the edge of the sphere the scallop height is at its largest whilst at the centre of the sphere it tends to zero. This was clearly seen in the freeform grinding tests for both the upper and lower implants, with the surface finish at its best in the centre of the spheres (Table 3.12). This variance in scallop height can be minimised by using a constant scallop height toolpath generation method which varies the stepover between adjacent toolpaths to maintain a constant scallop height (Lartigue et al, 1999; Feng and Li, 2002; Tournier and Duc, 2002).

The freeform grinding tests were much more successful in meeting the specification regarding sphericity and dimensional tolerances. All of the upper implants were within the radial separation, r_s, specification of less than 100 μm. For the lower implants test G was just within the r_s specification of less than 10 μm and the other were all within 18 μm. The definition of radial separation is

the distance from the furthest point away from the average radius. Since the peak to valley heights or *Rt* values are larger than specified it could lead to an increase in radial separation. Therefore, by resolving the issues with surface finish, the sphericity would also be improved. All of the lower implants were measured with a radius within the tolerance of 0 to - 0.2 mm. The radius of Upper Implant 1 was within the + 0.1 to + 0.3 mm tolerance, but the other two tests were below this value. However, this is not an issue with the quality of manufacture and can be rectified in future by changing the part design and increasing the radius slightly.

3.6 Summary

This chapter studied the use of ultra-precision grinding techniques to produce the articulating surfaces of alumina Total Disc Replacements. Particularly, whether the surface finish and dimensional tolerance specification could be met using grinding methods alone, and no polishing.

Unfortunately, the surface finishes of the articulating surfaces produced in this chapter did not meet the requirements of the ISO standard BS ISO 7206-2:2011. However, they were of a similar order of magnitude to other studies on the freeform grinding of ceramics. The use of the new Hyperion D8-12 tool did improve the surface finish slightly, but even with further testing, to better understand its use, it is likely that a polishing process will still be needed to meet the specification. It is clear from these preliminary tests that the D8-12 tool needs further development and testing to improve the life of the tool. The main area of focus for design improvement would be on the electroplated bond between the grit and tool. Developing the tool further would be worthwhile as it could be used in pre-finishing processes to reduce the time and cost involved in the polishing process.

Further testing needs to be done to understand how the toolpath and stepover can be adapted to improve the surface finish of the freeform spherical articulating surfaces. In particular the use of constant scallop height tool path generation methods need to be explored.

Most of the implants produced in this chapter were within the dimensional tolerances specified by ISO standard BS ISO 7206-2:2011. The upper implants met the 100 μm radial separation requirement but the lower implants narrowly missed the smaller 10 μm requirement. However, by improving the surface finish, in particular the *Rt* values, the radial separation should also improve.

In the next chapter a tribological assessment was carried out on the alumina Total Disc Replacements produced in this chapter. *In vitro* wear and friction tests were conducted and the results were compared with those from similar tests on other implant designs.

Chapter 4

Tribology of Ceramic Total Disc Replacements

Overview

In this chapter *in vitro* wear and friction tests were conducted on alumina-on-alumina cervical Total Disc Replacements and compared with the results of tests on other implants. The chapter begins with an introduction to why friction and wear are important in understanding implant performance, Section 4.1. Section 4.2 details the materials and methods for the wear tests. In Section 4.3 the results of the tests are presented and in Section 4.4 they are compared with those from similar tests on other Total Disc and Total Hip Replacements. The chapter is concluded in Section 4.5.

4.1 Introduction

Tribological analysis is an important tool in understanding the wear performance of different Total Disc Replacements design and materials. Wear debris from the articulating surfaces of the implants can cause osteolysis which in turn can cause aseptic loosening of orthopaedic implants (Ingham and Fisher, 2000; 2005). Retrieval analyses of metal-on-metal and metal-on-plastic Total Disc Replacements have shown osteolysis and aseptic loosening to be one of the possible causes of implant failure (Van Ooij et al., 2003; Van Ooij et al., 2007; Punt et al., 2008; Kurtz et al., 2012). *In vitro* wear testing enables the volume, shape and size of wear debris produced by different Total Disc Replacement bearing materials to be measured and compared.

Measuring the frictional torques produced by the bearing surfaces can also provide useful information on the performance of Total Disc Replacements. High frictional torques have been shown to cause mechanical loosening and failure of Total Hip Replacements (Simon et al., 1975; Brockett et al., 2007). Therefore, it is probable that high frictional torques also affect the fixation between the Total Disc Replacement and the vertebrae. Knowing the frictional torques at different frequencies also enables Stribeck curves to be plotted, which determine the lubrication regime within which the Total Disc Replacements are operating. This gives a valuable insight into how the articulating surfaces are interacting with and wearing against each other.

The use of ceramic-on-ceramic bearing materials is well established in Total Hip Replacement and alumina implants have been found to have wear volumes as low as 0.017 mg/million cycles (Clarke et al., 2000). This is several orders of magnitude lower than the gravimetric wear rates reported for the metal-on-plastic, metal-on-metal and plastic-on-plastic cervical Total Disc Replacements,

shown in Table 4.1. This suggests that using ceramics in Total Disc Replacements has the potential to reduce the volume of wear debris and the failure rate of the implants.

Table 4.1: Gravimetric wear rates of cervical Total Disc Replacements. Ultra-high molecular weight polyethylene (UHMWPE), cobalt-chrome (CoCr), polyetheretherketone (PEEK), polyurethane (PU)

Implant	Bearing Pair	Gravimetric Wear Rate (mg/million cycles)	Author
Braun 'active C'	UHMWPE-CoCr	2.3	Hyde et al. (2016)
Braun 'active C'	UHMWPE-CoCr	1.0	Grupp et al. (2010)
Prodisc-C	UHMWPE-CoCr	1.99	Nechtow et al. (2008)
Prodisc-C	UHMWPE-CoCr	1.82	Bushelow et al. (2008)
NuNec	PEEK-PEEK	1.0	Xin et al. (2013)
Bryan	Titatinium-PU	1.2	Anderson et al. (2003)

The aim of this chapter was to carry out a tribological assessment of the alumina-on-alumina cervical Total Disc Replacements manufactured in Chapter 3. *In vitro* testing was conducted to determine the frictional torques produced, the lubrication regime and the wear performance of the Total Disc Replacements. These tests were carried out on spine simulators which replicated the movement of the cervical spine. The results of the tests were compared against similar tests carried out on Total Disc Replacements and Total Hip Replacements manufactured from a variety of materials in order to

draw conclusions about the performance of the alumina-on-alumina Total Disc Replacements.

4.2 Materials and Method

4.2.1 Bose Spine Simulator

The tests were conducted on one of three Bose SDWS-1 Spine Simulators (Bose Corporation, Eden Prairie, Minnesota, USA) (Figure 4.1). The simulators can apply a 3 kN axial load, and have 6 degrees of freedom with the following ranges: ± 12° in flexion/extension, ± 10° in lateral bending and ± 8° in axial rotation. The spine simulator used for the friction tests was equipped with a 6 axis AMTI MC3A-1000 load cell (Advanced Mechanical Technology Inc, Massachusetts, USA), which can measure the frictional torques transmitted through the implant. The other two spine simulators were fitted with uni-axial Bose 1010CCH-1K-B load cells, which cannot measure frictional torque and were, therefore, used for the wear tests only. Both load cells were calibrated by the manufacturer each year.

Figure 4.1: Bose SDWS-1 spine simulator

The spine simulators were controlled by WinTest 4.1 software (Bose Corporation, Eden Prairie, Minnesota, USA). WinTest was used to create input waveforms, control the machine actuators and fluid temperature, and acquire data. The simulators were fitted with four actuators; two moved the base plate in axial rotation and axial compression, and two moved the top plate in flexion/extension and lateral bending (Figure 4.2).

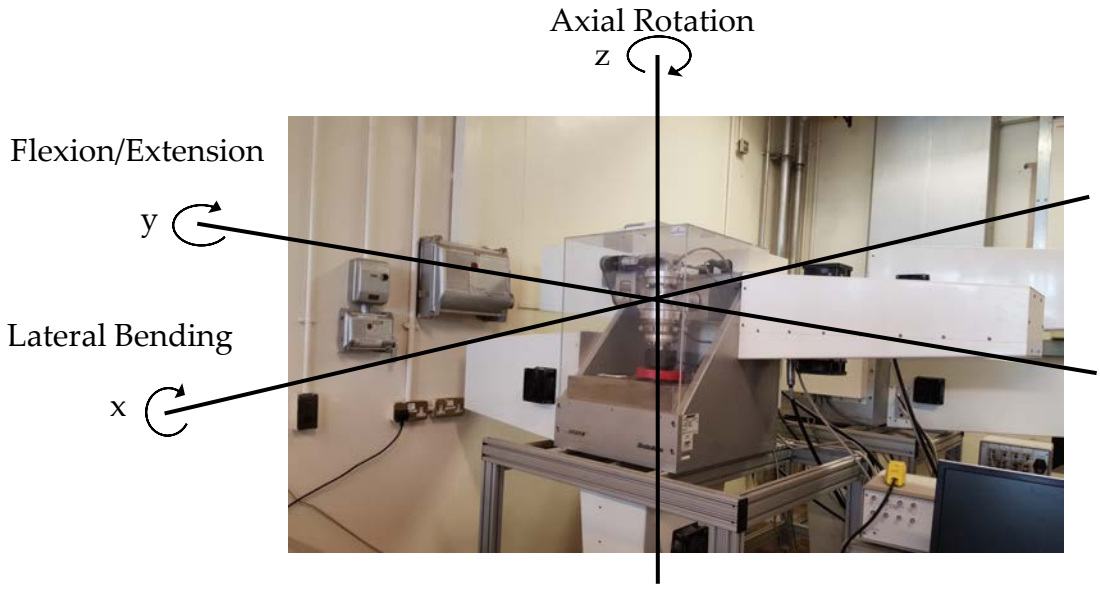

Figure 4.2: Directions of motion on Bose spine simulator

The key features of the spine simulator are shown in Figure 4.3. The top plate could only be moved by the actuators, unlike the base plate which was attached to an x-y stage. This allows the user to align the upper and lower halves of the implant to be tested. The x-y stage could be moved ± 5 mm in the x and y directions by manually adjusting four screws, which were then used to lock the stage in position. The removable lubricant bath fits over the heating element, which was fixed to the base plate, and was locked into position using split clamps. Temperature feedback was provided to the WinTest software via a temperature probe in the lubricant bath.

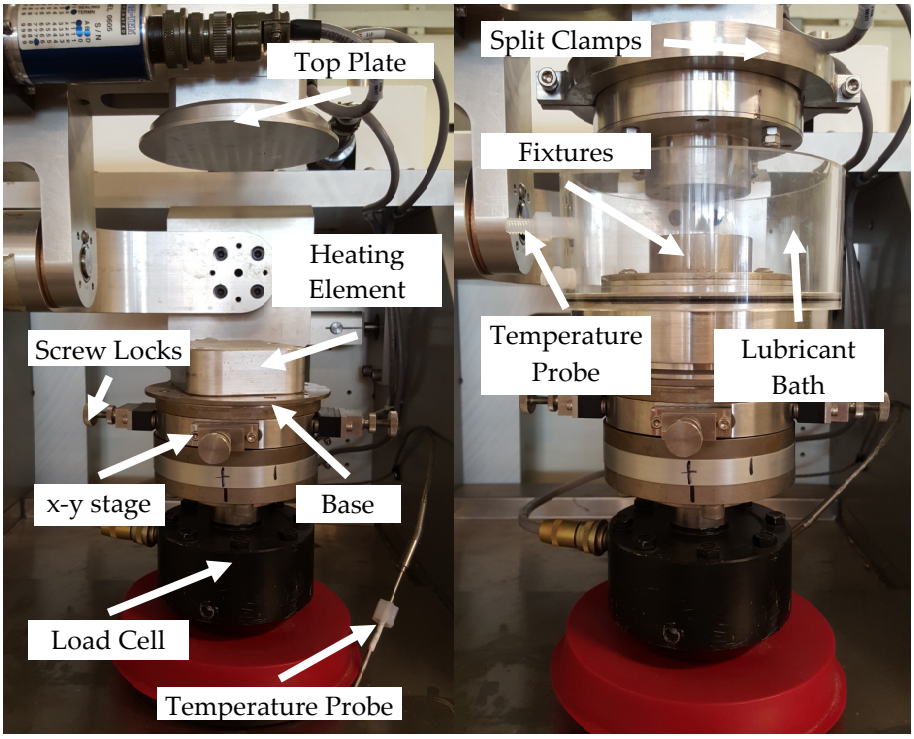

Figure 4.3: Key features of Bose spine simulator

4.2.2 Implants

The tests were conducted on three pairs of alumina-on-alumina cervical Total Disc Replacements. The implants were designed to be generic cervical implants with a ball and socket joint based on a sphere with a radius of 7 mm. The manufacture of the implants was described in Chapter 3. Implant 1 was formed from Lower Implant G and Upper Implant H, Implant 2 from Lower Implant H and Upper Implant J, and Implant 3 from Lower Implant D and Upper Implant E.

4.2.3 Fixtures

User designed fixtures which hold the implant in place were attached to the machine by screwing into the base of the water bath and using a split clamp to fix to the top plate. In designing these fixtures, some key dimensions had to be taken into consideration (Figure 4.4). The centre of rotation of the implant has to

be aligned with the centre of rotation for the Flexion/Extension, 42.5 mm below the machine fixture, to prevent undesirable bending moments. The available space for fixtures between the top plate and the base of the lubricant bath was 110 mm. The base plate can be moved ± 12 mm vertically, but as it was moved away from the zero position the machine's ability to reach the required force was reduced. A series of fixtures were used to meet these two constraints as can be seen in Figure 4.5. Some of the fixtures were already available from previous studies (Moghadas; 2012), but the upper and lower fixtures were custom designed on the CAD software Inventor2014, Build 170 (Autodesk Ltd, Farnborough, UK) and the engineering drawings are shown in Appendix A.

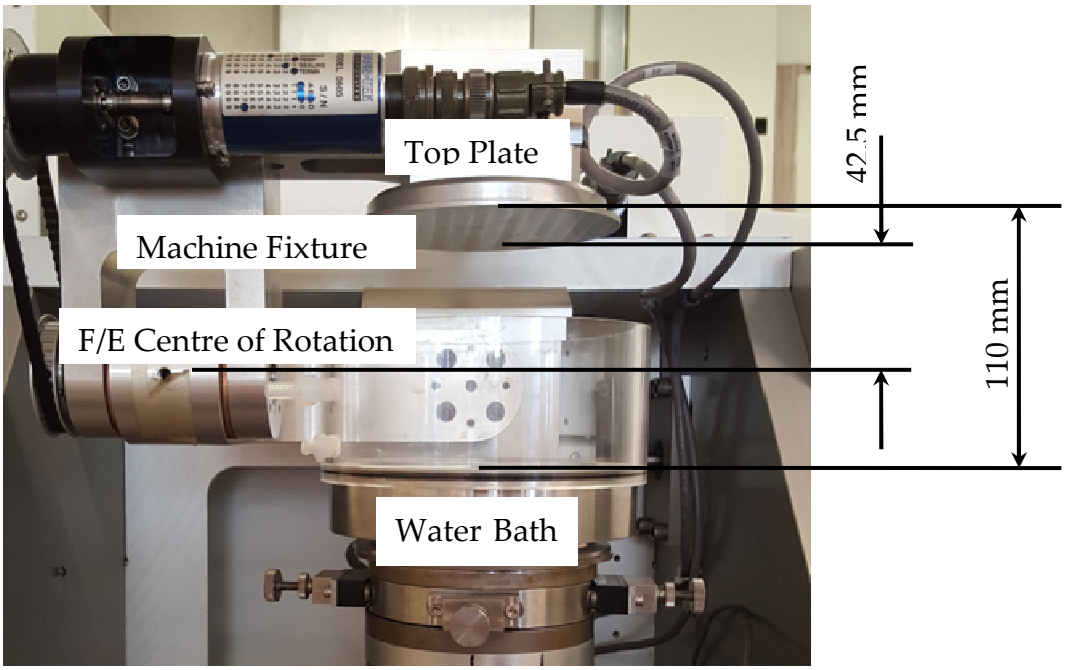

Figure 4.4: Key dimensions on the Bose spine simulator

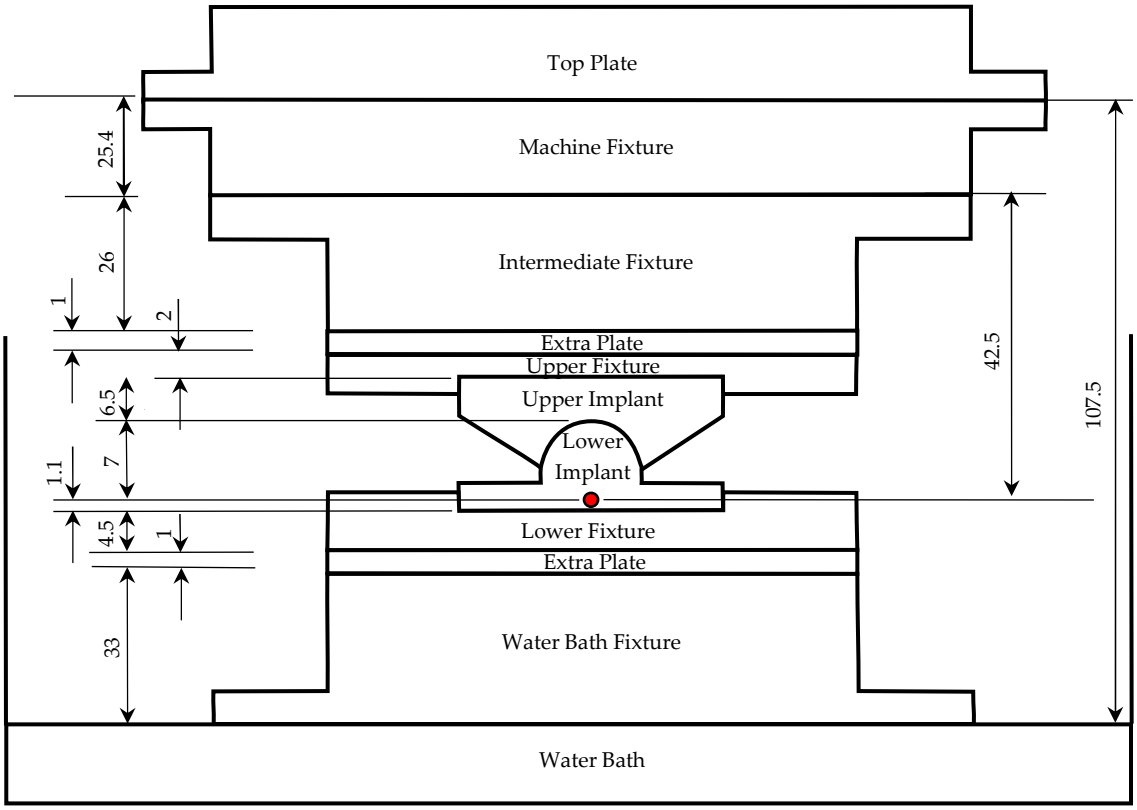

Figure 4.5: Assembly drawing of the fixtures used to place the centre of rotation of the implant (red dot) at the centre of rotation of the flexion/extension motion

4.2.4 Lubricant

All tests were conducted in a lubricant which consisted of bovine calf serum (Sera Laboratories International Ltd, West Sussex, UK) diluted to a protein concentration of 1.2 g/L with de-ionised water. Each litre of the diluted calf serum had 0.3 g of the antimicrobial reagent sodium azide (Sigma-Aldrich, Gillingham, Dorset, UK) mixed into it to reduce biodegredation. Once made up, the lubricant was labelled, dated and stored in the fridge for no more than a week before being disposed of. All friction and wear tests were carried out at 37 °C to replicate the temperature of the human body.

The lubricant viscosity was measured using an AR-G2 cone-on-plate rheometer (TA Instruments Ltd., New Castle, Delaware, USA) at 0.5% constant strain and

a temperature of 37 °C. The instrument was controlled and the test data was recorded using the AR Instrument Control software (TA Instruments Ltd., New Castle, Delaware, USA). The average viscosity of the lubricant was calculated to be 0.71 ± 0.02 mPa s.

4.2.5 Sample Preparation and Cleaning

The implant samples were cleaned prior to any testing using the protocol below:

1) Clean with 70% methanol/water solution (Sigma-Aldrich, Gillingham, Dorset, UK).
2) Soak in disinfectant to kill bacteria, made from 10 mg Virkon powder for each litre of water (Antec International, Sudbury, UK), for between 2 and 24 hrs.
3) Rinse once with tap water and twice with distilled water.
4) Dry on low lint clean room wipes (Cleanroom Shop, Halton, Lancashire, UK).
5) Clean in an ultrasonic bath with propan-2-ol (Scientific Laboratory Supplies, Nottingham, UK) for 5 minutes.
6) Wash with acetone (Sigma-Aldrich, Gillingham, Dorset, UK)
7) Dry and wipe with low lint clean room wipes.
8) Store in a container for 48 hours at room temperature to stabilise.
9) Before testing use air duster (Office Depot Europe BV, Venlo, The Netherlands) to remove any rogue dust particles.

The protocol is a combination of the guidelines in the standard BS ISO 14242-2 (British Standards Institution, 2000) and the Standard Operating Protocol for

Spine Wear Simulator Studies (SOP01.6) of the Institute of Medical and Biological Engineering, University of Leeds.

4.2.6 Friction Tests

The frictional torques transmitted through the implant were measured using the spine simulator fitted with the 6 axis AMTI MC3A-1000 load cell (Advanced Mechanical Technology Inc, Massachusetts, USA). There is no international standard which specifies the testing parameters for friction testing of Total Disc Replacements. Therefore the testing parameters were chosen with respect to the British Standard ISO 18192-1:2011, Implants for surgery — Wear of total intervertebral spinal disc prostheses Part 1 (British Standards Institution, 2011b). This standard specifies angular displacement, loads, frequencies and testing conditions that are similar to those experienced by Total Disc Replacements *in vivo.* For cervical Total Disc Replacements the standard specifies a sinusoidal axial load of between 50 and 150 N. Since the aim of this experiment was to identify the maximum frictional torques, a static axial load of 150 N was applied. The specified limits for the sinusoidal angular displacements for the three rotations are shown in Table 4.2. The standard specifies that the wear tests should be conducted at a frequency of 1 Hz and/or up to 2 Hz. Therefore, to test the influence of frequency on the frictional torques the friction tests were carried out at 0.25, 0.5, 0.75, 1, 1.25, 1.5, 1.75 and 2 Hz. Each combination of frequency and angular displacement was repeated four times and the tests were undertaken in a random order. The data acquisition rate was 1000 points/second. Each test was conducted for 100 cycles to allow the system to reach a steady state. Where steady state was defined as the difference between each peak frictional torque and the mean peak fictional torque being less than 1% of the mean peak frictional torque.

Table 4.2: Load and angular displacement limits for cervical total disc replacements

	Minimum Limit	Maximum Limit
Flexion/Extension	-7.5 °	7.5 °
Axial Rotation	-4 °	4 °
Lateral Bending	-6 °	6 °

4.2.7 Stribeck Analysis

A Stribeck analysis was carried out for each of the three implants tested to determine which lubrication regime they were operating under, with friction factor, f, plotted against Sommerfeld Number, Z. The theory behind Stribeck analysis can be found in Section 2.4.3.1. The final 10 cycles of each test were analysed to determine the minimum and maximum frictional torque for each cycle. The arithmetic mean of the extrema were then calculated and used in determining the friction factor. The Stribeck analyses were carried out using custom MATLAB programs, version r2015a (Mathworks, Massachusetts, USA). Figure 4.6 shows a high level flowchart of the main processes carried out by the *FormatData.m, CalculateStribeck.m, PlotStribeck.m* and *PlotAllStribeck.m* scripts; see Appendices B.3 – 6 for the full codes.

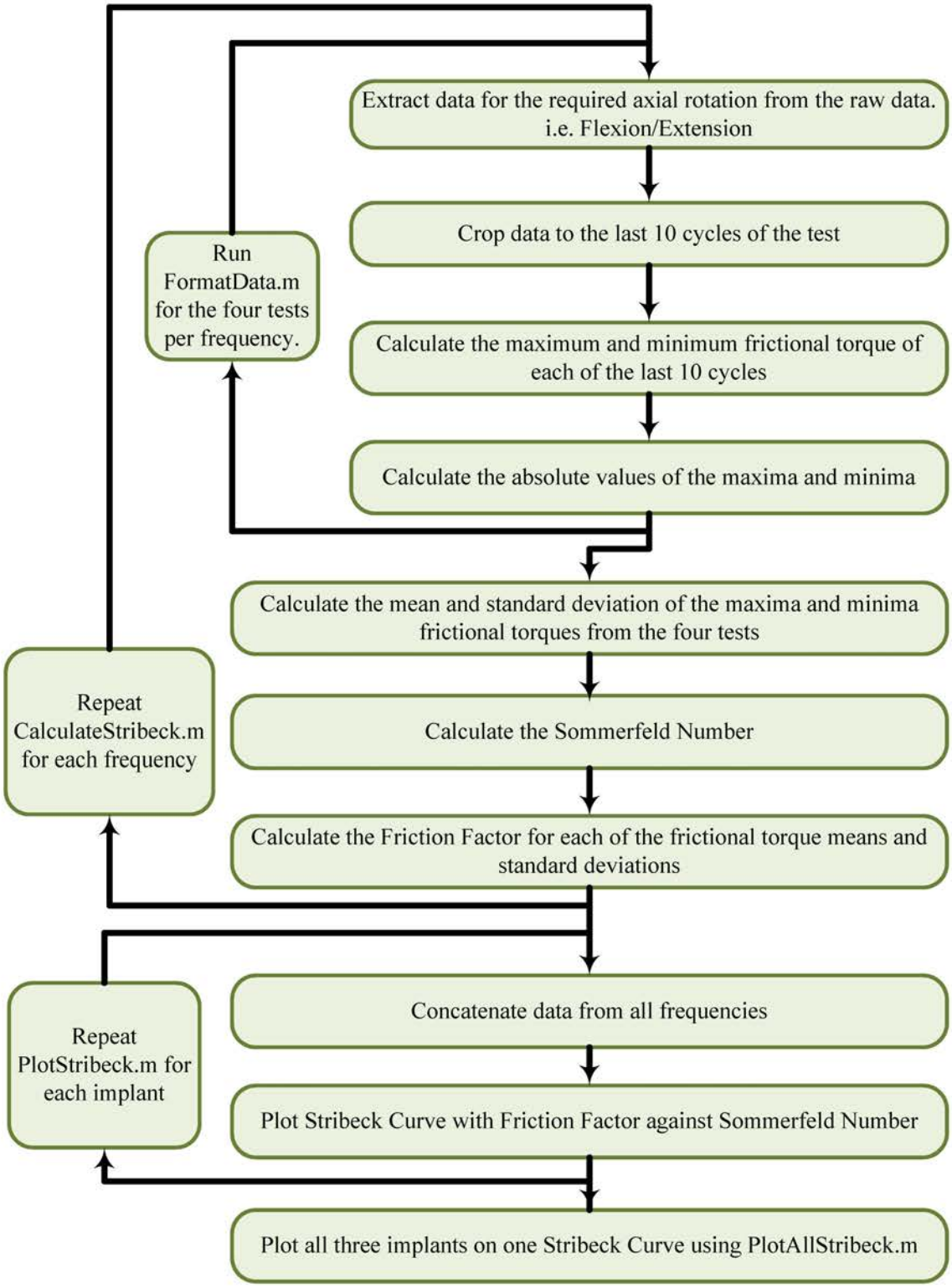

Figure 4.6: Flow chart showing the main processes in the MATLAB programs *FormatData.m, CalculateStribeck.m, PlotStribeck.m* and *PlotAllStribeck.m*

4.2.8 Wear Tests

Wear tests were carried out in accordance with the parameters set down for cervical Total Disc Replacements in the British Standard ISO 18192-1:2011 (British Standards Institution, 2011b). A sinusoidal axial load was applied between 50 and 150 N. The test was conducted at a frequency of 1 Hz. Each cycle of movement was a combination of all three angular displacements varying sinusoidally between the limits in Table 4.2. The lateral bending sine wave was out of phase with the flexion/extension sine wave by 90°, and the lateral bending and axial rotation sine waves by 180°.

The ISO standard states that Total Disc Replacements should undergo 10 million cycles of testing, which would take roughly 6 months to complete. However, previous wear testing of Total Disc Replacements has shown, that after a few million cycles the wear rate reaches a steady state (Nechtow et al., 2008; Vicars et al., 2010; Moghadas et al., 2013). Therefore, the alumina-on-alumina implants were tested to 2 million cycles, which was adequate to compare them with other material combinations.

The mass loss due to wear was measured gravimetrically at 0.25, 0.5, 1, 1.5 and 2 million cycles. Prior to being weighed the samples were cleaned and dried following the protocol in Section 4.2.5. For each implant six measurements were taken using an Ohaus GA200D analytical balance with a precision of ± 0.1 mg (Ohaus Corporation, Parsippany, New Jersey, USA). The arithmetic mean of the six measurements was calculated. The mass loss was converted to volume loss using a density for alumina of 3.9 g/cm^3. Unfortunately due to equipment failure Implant 3 was damaged early on in a wear test so only the results for Implants 1 and 2 are reported.

Due to evaporation the lubricant was topped up each day using deionised water. In order to reduce biodegradation of the lubricant, see Section 2.4.4.2, it was replaced after every 0.25 million cycles, roughly 3 days, and the lubricant bath and sample were cleaned following the procedure below:

1) Drain the lubricant bath and wash with household detergent
2) Soak in disinfectant to kill bacteria, made from 10 mg Virkon powder for each litre of water (Antec International, Sudbury, UK), for between 2 and 24 hrs
3) Rinse once with tap water and twice with distilled water

Following completion of the wear tests the surface of the implants were sputter-coated with gold and then imaged using an Environmental Scanning Electron Microscope (SEM), XL30 ESEM FEG (Philips, The Netherlands) operated at 10.0 kV.

The statistical analysis was conducted using Minitab version 17.2.1 (Minitab Ltd. Coventry, UK). The gravimetric results of the wear tests, total mass and volume loss, were plotted against the number of wear cycles. A linear regression analysis with the intercept through the origin was carried out on the wear test results to model the relationship between mass and volume loss and the number of wear cycles.

4.3 Results

4.3.1 Friction Tests

The maximum mean frictional torque was 7.48 ± 0.35 N m. The torques do not follow a clear pattern of increase or decrease and remain fairly constant as the frequency increases (Figure 4.7) In lateral bending the maximum mean frictional torque was 6.92 ± 0.84 N m. The torques show a slight decrease as the

frequency increases, but again remain fairly constant (Figure 4.8). The results for axial rotation are not presented here because the frictional torques were negligible.

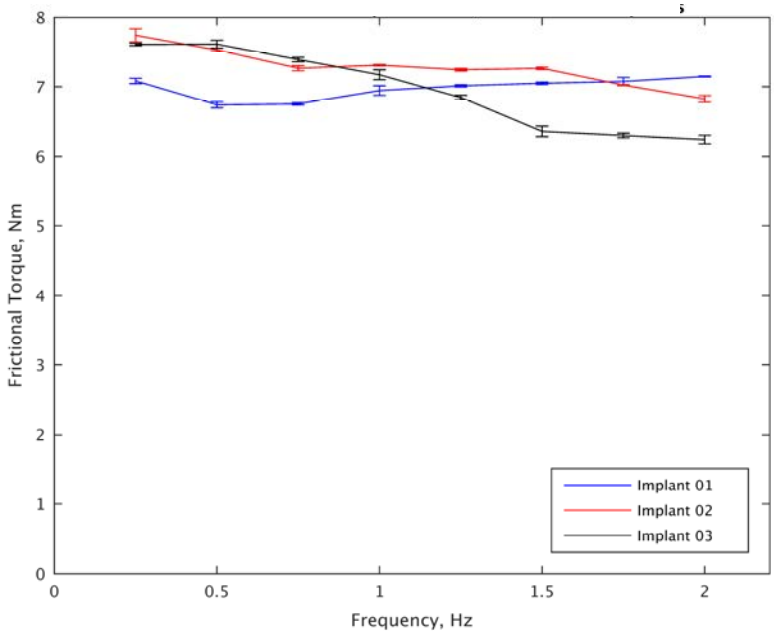

Figure 4.7: Frictional torques for all implant samples in flexion/extension. Error bars represent standard deviations

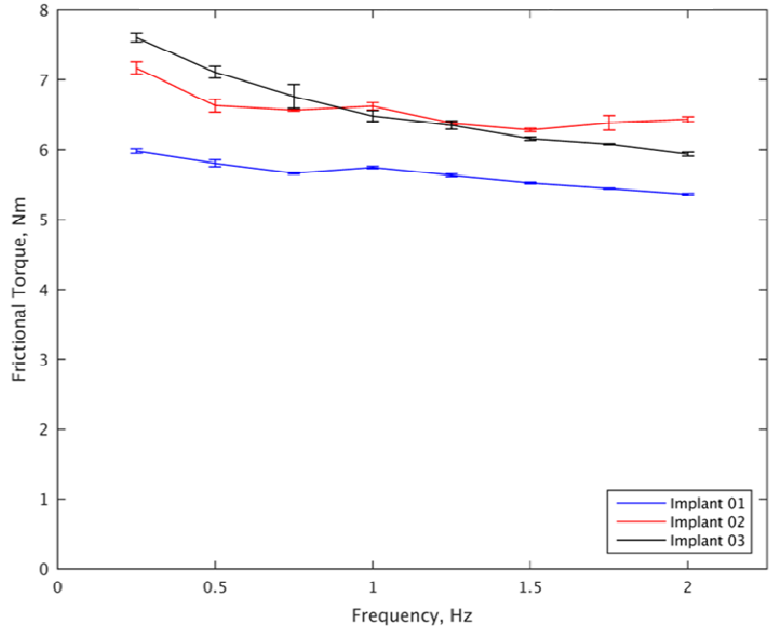

Figure 4.8: Frictional torques for all implant samples in lateral bending. Error bars represent standard deviations

The Stribeck plot for flexion/extension (**Figure 4.9**) shows that the friction factor remains relatively constant as the Sommerfeld number increases. The plot for lateral bending (Figure 4.10) was similar although there was a slight decrease in friction factor at higher Sommerfeld numbers.

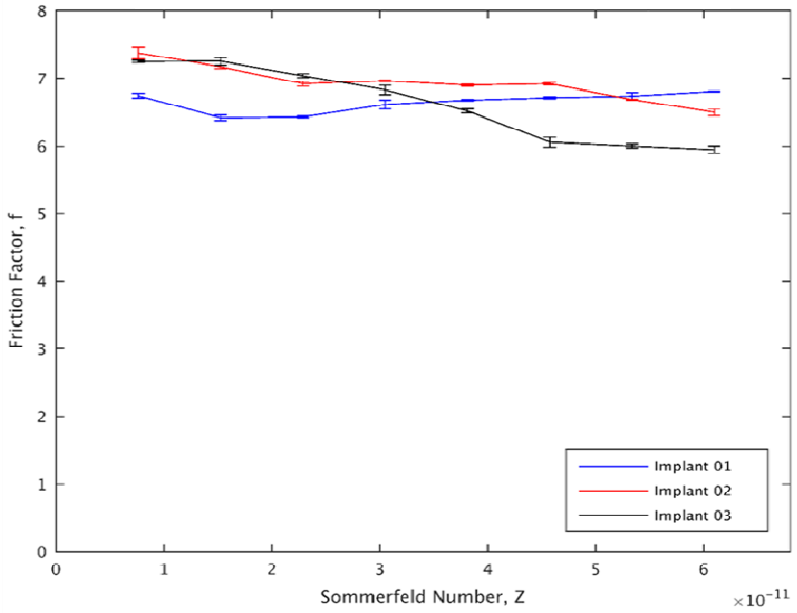

Figure 4.9: Stribeck curve for all implant samples in flexion/extension. Error bars represent standard deviations

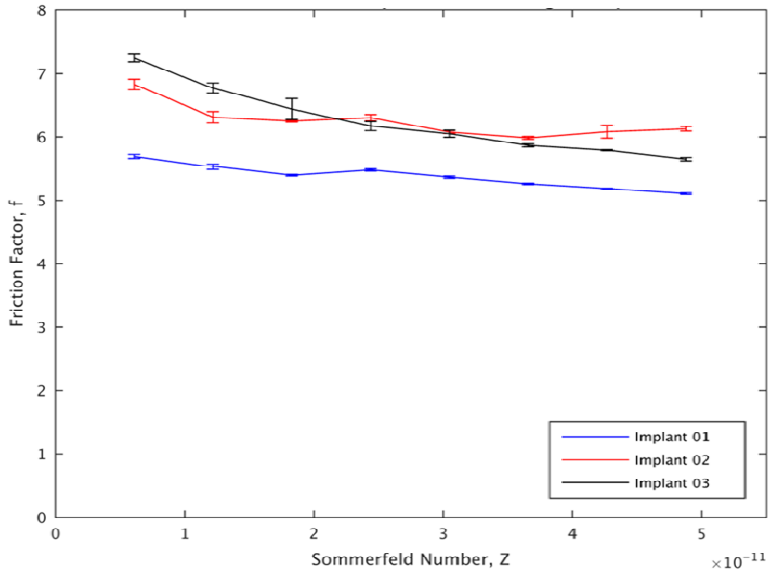

Figure 4.10: Stribeck curve for all implant samples in lateral bending. Error bars represent standard deviations

4.3.2 Wear Tests

The gravimetric wear rates for Implants 1 and 2 were 97.2 and 25.9 mg/million cycles (24.9 and 6.6 mm^3/million cycles), respectively, based on the linear regression analysis (Figure 4.11). The mass loss for Upper Implant 2 at 2 million cycles is not reported because the part came loose from its fixture and had to be reglued. This led to a change in mass and therefore, an inaccurate result.

a)

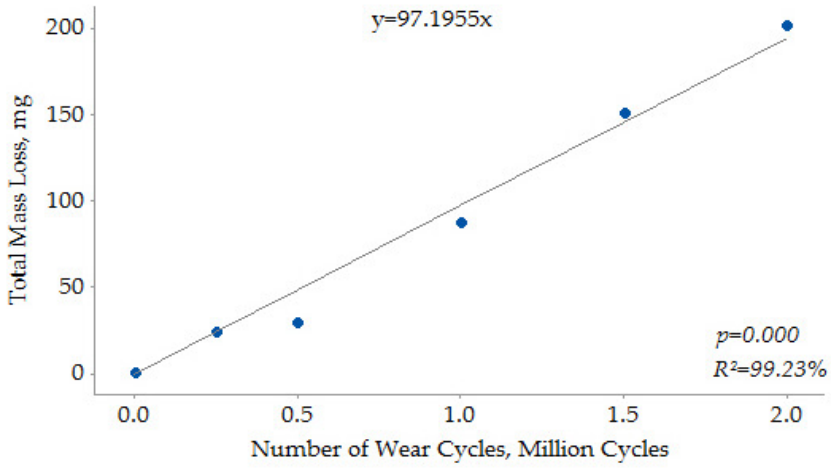

b)

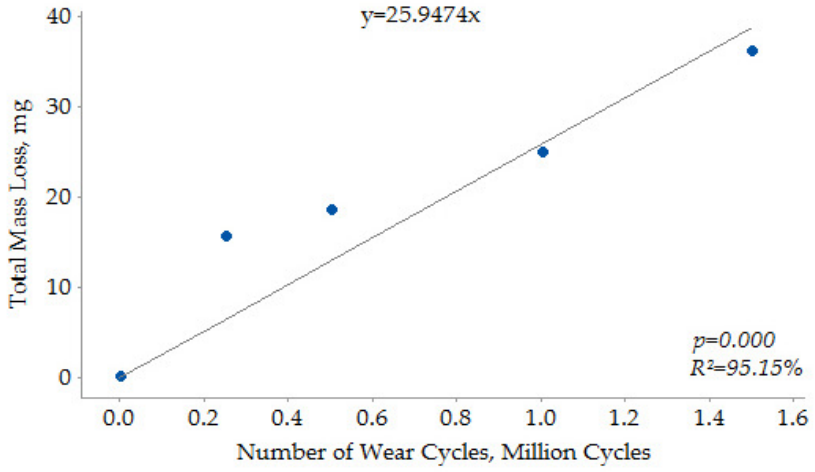

Figure 4.11: Wear of implants determined using the gravimetric method; a) Implant 1; b) Implant 2

The apparent difference between the two wear rates was due to chipping around the edge of Lower Implant 1, which began to occur at 0.5 million cycles, see the SEM images in Figure 4.14 for more details. The wear rate was higher in

this implant than Implant 2 due to the mass loss of the chips but also because the debris created by these chips became trapped within the bearing surfaces and caused third body wear in the centre of the implant. The increased mass loss for this part can be clearly seen in Figure 4.12.

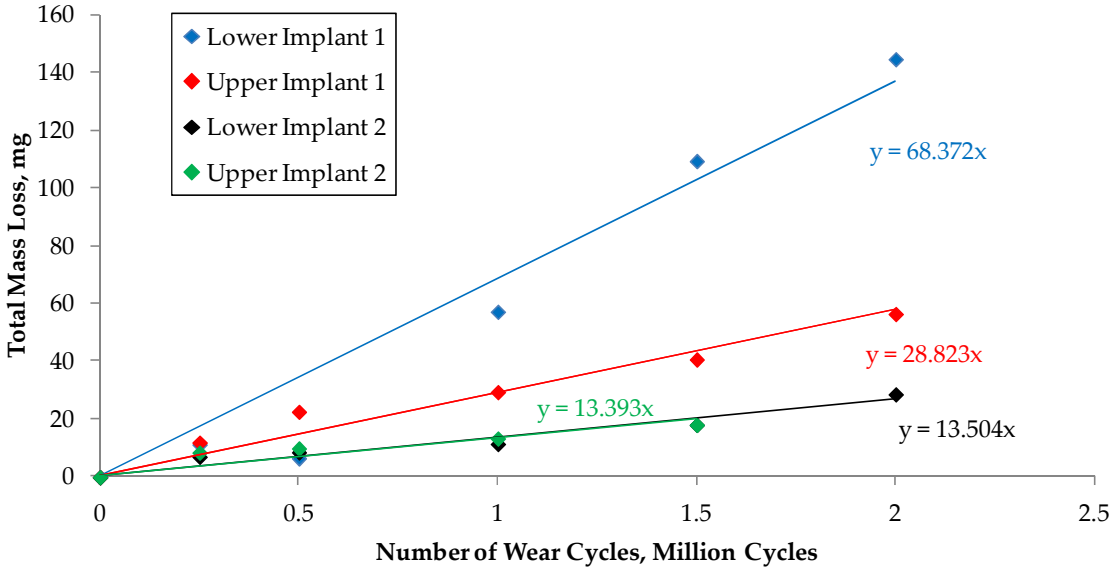

Figure 4.12: Wear of upper and lower implants determined using the gravimetric method mass loss. (The trend lines for lower and upper implant 2 are similar and overlap)

Table 4.3 summarises the wear rates for each implant and part calculated using linear regression analysis. Based on the *p*-values being less than 0.05 and the high coefficient of determinations, R^2, it was reasonable to model the relationships between mass loss and the number of cycles as linear.

Table 4.3: Wear rates for each implant and the upper and lower implants, including linear regression statistics

Part	Gravimetric Wear Rate mg/M cycles	Volumetric Wear Rate mm^3/M cycles	*p*-value	Coefficient of Determination, R^2 %
Implant 1	97.2	24.9	0.000	99.23
Implant 2	25.9	6.6	0.000	95.15
Lower Implant 1	68.4	17.5	0.000	97.17
Upper Implant 1	28.8	7.4	0.000	97.97
Lower Implant 2	13.5	3.5	0.000	98.45
Upper Implant 2	13.4	3.4	0.001	93.94

Figure 4.13 shows SEM images of the surface morphology of the unworn surface of Lower Implant C, from Chapter 3, and the worn surfaces of the Lower Implant 1 and 2 after 2 million cycles. A comparison of the surface morphologies of the worn implants and the unworn implant clearly shows that the peaks of the worn surfaces have been removed due to wear, creating a flatter surface. This appeared more pronounced in the image of Lower Implant 1 because the wear rate was higher than that of Lower Implant 2 (Figure 4.13b).

The SEM images in Figure 4.14 show raised lips around the edges of both Lower Implants 1 and 2. The upper implants have a smaller diameter than the lower implant. Therefore, as the wear tests progressed the centre of the lower implants wore away, leaving behind these raised lips. Due to the design of the spine simulator it was difficult to precisely realign the upper and lower implants after each lubricant change and wear measurement. On loading, this misalignment would have produced high stress concentrations in the lip and caused the chipping seen in Lower Implant 1 (Figure 4.14a).

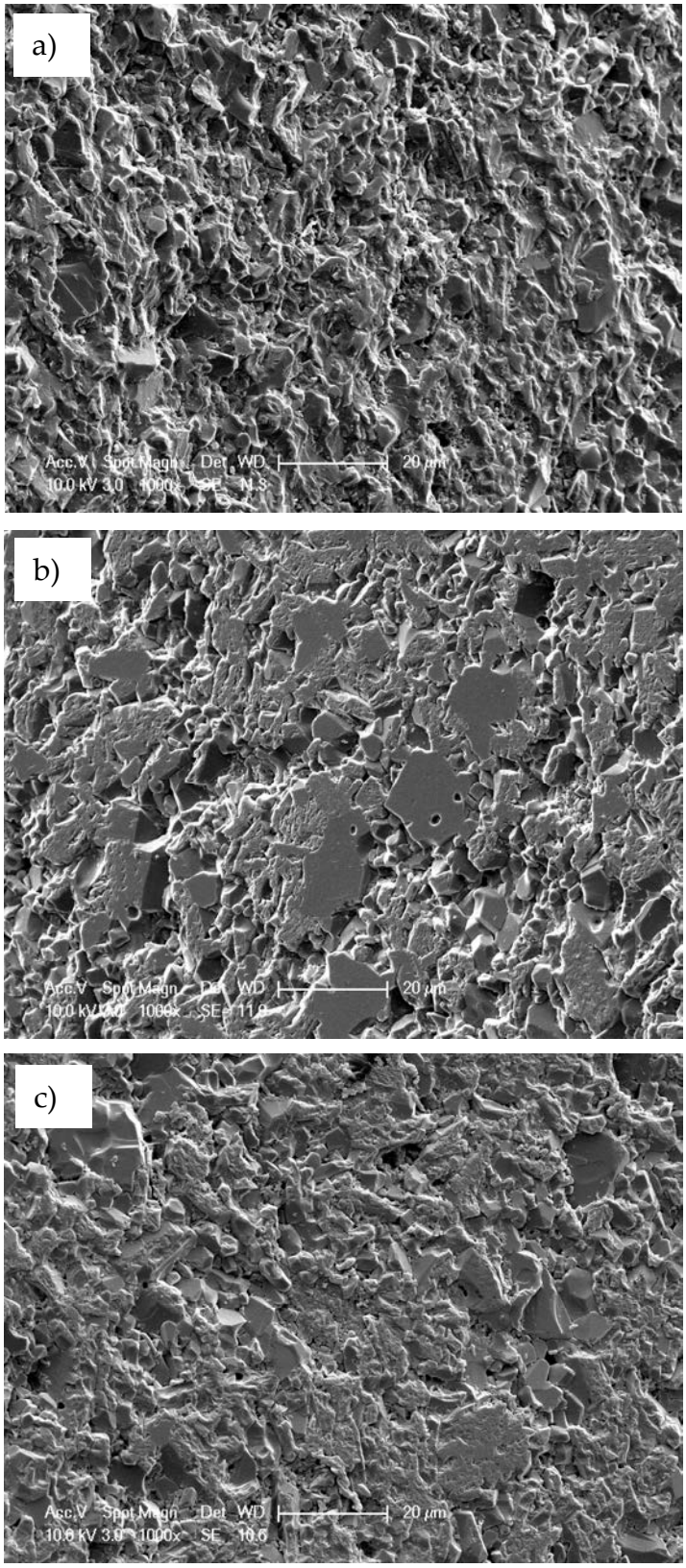

Figure 4.13: SEM images of surface morphology; a) Unworn surface of Lower Implant C; b) Lower Implant 1 after 2 million cycles; c) Lower Implant 2 after 2 million cycles

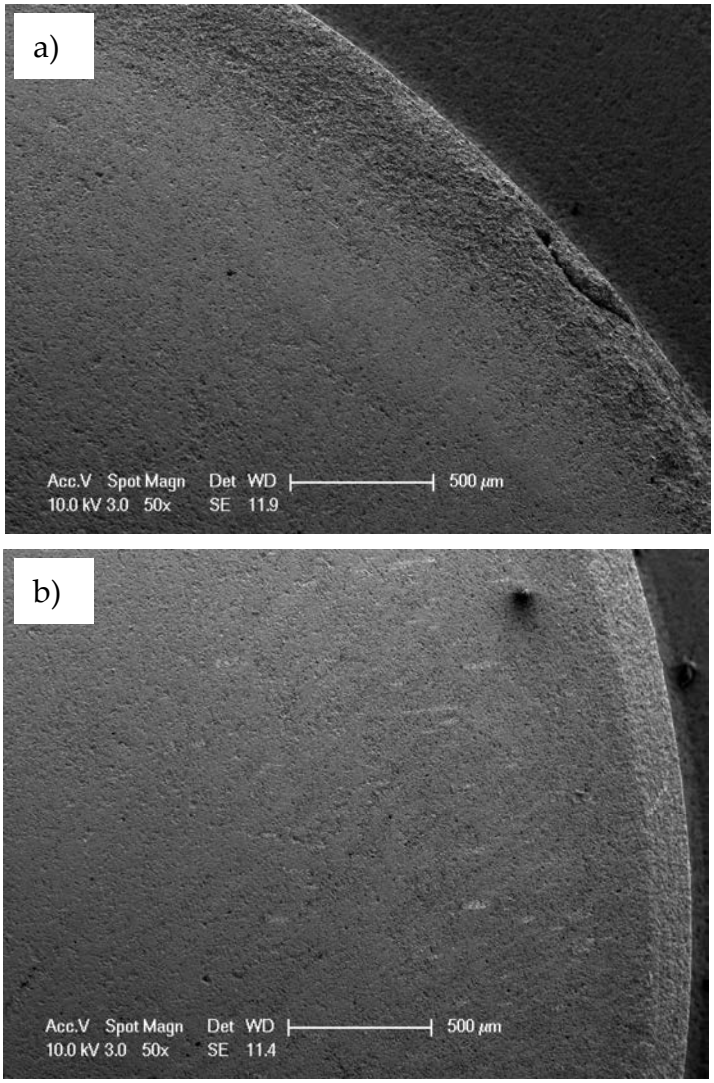

Figure 4.14: SEM images showing raised lip around edge of the worn implants; a) Lower Implant 1 with chip; b) Lower Implant 2

4.4 Discussion

The maximum mean frictional torques of the ceramic implants were 7.48 N m in flexion/extension and 6.92 N m in lateral bending. These results were just below the bending strength of the natural cervical disc, which Przybyla et al. (2007) found to be 8.4 N m in extension and 6.7 N m in flexion. If the ceramic Total Disc Replacements have frictional torques which are similar to the bending strength of the natural disc this should help to maintain the natural

biomechanics of the spine and therefore, the health of the surrounding tissues and segments.

The maximum mean frictional torque of 7.48 N m in flexion/extension is a similar magnitude to other tests on Total Disc Replacements. Comparable tests on the Poly-ether-ether-ketone (PEEK) NuNec cervical Total Disc Replacement produced a lower maximum mean frictional torque of 3.71 N m (Xin, 2013). For lumbar Total Disc Replacements a maximum mean frictional torque of 9.5 N m and 3.21 N m was produced for a cobalt-chromium-molybdenum (CoCrMo) bearing and a CoCrMo-UHMWPE bearing, respectively (Moghadas et al., 2012a; 2012b). However, these results were conducted under higher loads and with larger radius ball and socket joints than the cervical tests presented in this thesis. Moghadas et al. (2012a) showed that frictional torque increased with both load and radius. Therefore, these results are not directly comparable, but do give an indication of where the ceramic-on-ceramic implants sit within the range of frictional torques found in Total Disc Replacements.

A study of lumbar Total Disc Replacements predicted that unlike metal-on-metal and metal-on-plastic, ceramic-on-ceramic bearings could theoretically operate under a fluid film lubrication regime (Shaheen and Shepherd, 2007). Studies have also shown that ceramic-on-ceramic Total Hip Replacements are theoretically capable of fluid film lubrication (Scholes and Unsworth, 2000; Brockett et al, 2007). However, all of these studies showed that at lower velocities and bearing radii, ceramic-on-ceramic bearings will operate with boundary and mixed lubrication. These predictions are based on the Hamrock-Dowson equation (Hamrock and Dowson, 1978) which calculates the minimum film thickness from the radius, load, lubricant viscosity, entraining velocity and Young's modulus. Cervical Total Disc Replacements have smaller radii and are

tested under lower loads than lumbar Total Disc Replacements and Total Hip Replacements which will reduce the predicted film thickness and reduce the likelihood of them operating in a fluid film regime. Shaheen and Shepherd (2007) predicted that a ceramic-on-ceramic Total Disc Replacement with a bearing diameter of 21 mm would move from mixed to fluid film lubrication with increased angular velocity. Reducing the diameter to 14 mm led to the Total Disc Replacement operating in boundary to mixed lubrication. Therefore, a reduction in bearing diameter to 7 mm and the load to 150 N would make it likely these cervical ceramic-on-ceramic Total Disc Replacements are operating in boundary lubrication.

There are limitations to using the Hamrock-Dawson equation to predict the lubrication regime an implant will operate within. For example the equation does not take into account how the chemical composition of the lubricant can affect the lubrication regime. It has been shown that the proteins in bovine serum can attach to the bearing surfaces and form a solid layer up to 20 nm thick (Spikes, 1996). This layer can reduce the amount of asperity contact between the two bearing surfaces when the implant is operating in boundary lubrication and therefore, reduce the amount of wear (Scholes and Unsworth, 2000). In the case of ceramic-on-ceramic implants the presence of this solid layer of proteins can affect the lubrication regime the implant operates in. It has been shown that ceramic-on-ceramic Total Hip Replacements operate in a fluid film lubrication regime when they are lubricated by fluids with no protein content (Scholes et al., 2000). Ceramic-on-ceramic Total Hip Replacements show a statistically significant increase in friction between 0% bovine serum and all other concentrations of bovine serum (Scholes et al., 2000; Brockett et al, 2007). It is believed that the layer of proteins on the bearing surface increases the

surface roughness, thus reducing the film thickness of the lubricant and disrupting the fluid film lubrication regime. This is another reason why even though theoretically some Total Disc Replacements can operate under fluid film lubrication it is unlikely that ceramic-on-ceramic cervical Total Disc Replacements would do so.

The experimental results in this chapter are consistent with the prediction that ceramic-on-ceramic Total Disc Replacements would operate in boundary to mixed lubrication. The Stribeck curve for flexion/extension was flat which, as explained in Section 2.4.3.1, which indicates that the Total Disc Replacements were operating in a boundary lubrication regime. The Stribeck curve for lateral bending was also largely flat but decreased slightly at higher Sommerfeld numbers. This indicates the lubrication regime was boundary, but moving towards mixed lubrication. The results also agree with similar tests on a variety of cervical and lumbar Total Disc Replacements which showed the implants operate in a boundary or mixed lubrication regime (Moghadas et al., 2012; Xin et al., 2013; Eckold, 2016).

The gravimetric wear rates for the alumina-on-alumina Total Disc Replacements of 97.2 and 25.9 mg/million cycles do not compare favourably with other cervical Total Disc Replacements and are an order of magnitude larger (Table 4.1). The wear rates are the same order of magnitude as lumbar Total Disc Replacements, but still considerably higher. For example, the lumbar Charite Total Disc Replacement has a UHMWPE-CoCr bearing and has been shown by Moghadas et al. (2015) to have a wear rate of 12.0 ±1.4 mg/million cycles which was supported by other similar studies (Vicars et al., 2009; Prokopovich et al., 2011).

The high wear rates presented in this thesis are in part due to the chipping which occurred on Lower Implant 1 at 0.5 million cycles. This highlights a major issue with the use of brittle ceramics in Total Disc Replacements, and the need to be mindful of this when designing them.

The other factor in the high wear rates seen in these experiments is the high surface roughness of the implants prior to testing. The grinding techniques used in Chapter 3 produced surface roughnesses in the range 0.268 to 0.545 μm. The international standard specifies a surface roughness of 0.02 μm which is well below that of the implants tested in this chapter. Surface roughness plays an important role in the wear and lubrication of articulating surfaces. Analysis of different bearing materials in Total Hip Replacements has demonstrated that although friction factors are of the same order of magnitude, only ceramic-on-ceramic bearings are capable of operating in fluid film lubrication regimes due to their lower surface roughness (Scholes et al., 2000; Brockett et al., 2007). It is clear that high surface roughness reduces the effectiveness of the lubricant, which will in turn increase the wear rate, because the loads are being supported by the surface asperities rather than the fluid. Indeed it has been demonstrated in Total Hip Replacements that there is an exponential relationship between the wear rate and surface roughness (Lancaster et al., 1997). As the surface roughness of the articulating surfaces increases so does the wear rate.

It should also be noted that at 0.5 million cycles Lower Implant 1 showed a net gain in mass. Previous studies have shown that this is due to the protein film formed on the bearing surfaces of the implant, as discussed above (Clarke et al., 2000; Scholes and Unsworth, 2000). In wear tests of Total Hip Replacements the wear rates of the alumina femoral heads were so low that these fluctuations in mass made the wear rate virtually immeasurable using the gravimetric method

(Williams et al., 2011). Had the ceramic-on-ceramic implants used in these tests had lower surface roughness and produced the expected low wear rates this problem may have been more pronounced and there would have been issues measuring the wear rates gravimetrically.

4.5 Summary

A tribological assessment of alumina-on-alumina cervical Total Disc Replacements was carried out to determine the wear performance of the implants and to compare them with other Total Disc Replacements. The frictional torques transmitted by the implants were the same order of magnitude as other Total Disc Replacements but at the higher end of the range. The implants were also shown to operate under boundary lubrication which was again similar to other Total Disc Replacements. However, the wear tests produced wear rates which were very high compared to other cervical Total Disc Replacements and ceramic Total Hip Replacements. This was due to the high surface roughness produced by the manufacturing process described in Chapter 3 and also chipping of the brittle alumina.

Despite these high wear rates there were some issues with measuring the mass loss using the gravimetric method. Therefore, the aim of the following chapter was to develop a new method for measuring volumetric wear, which would improve on the gravimetric method. It contains a preliminary study which explores the use of non-contacting optical microscopy to measure the low volumetric wear rates usually associated with ceramic bearings.

Chapter 5

Assessment of Non-Contacting Optical Microscopy to Measure Wear and Surface Roughness in Ceramic Ball-on-Disc Tests

Overview

This chapter presents a preliminary study of a non-contacting optical method for measuring the low volumetric wear expected in ceramic Total Disc Replacements. The results of the optical method are then compared against the standard gravimetric method. Section 5.1 explains the limitations of the gravimetric method and the need for a more precise method. The materials and methods used in the study are detailed in Section 5.2. The results of the study can be found in Section 5.3 and discussed in Section 5.4. Finally the chapter is summarised in Section 5.5.

5.1 Introduction

It is important to measure the volume of wear debris produced by different Total Disc Replacement bearing materials in order to compare their wear performance and their potential to cause osteolysis. Implant retrieval analyses have shown that aseptic loosening can occur in Total Disc Replacements with metal-on-metal and metal-on-plastic bearings (Van Ooij et al., 2003; Van Ooij et al., 2007; Punt et al., 2008; Kurtz et al., 2012). Whilst there are no published retrieval analyses for ceramic-on-ceramic Total Disc Replacements, studies have shown that osteolysis can occur in ceramic Total Hip Replacement (Yoon et al., 1998).

In vitro wear tests, using spinal simulators, can be used to find volumetric wear rates for Total Disc Replacement devices (Xin et al., 2013; Moghadas et al., 2013; 2015). Although there is no published data for ceramic-on-ceramic Total Disc Replacements, retrieval analyses and similar tests on Total Hip Replacements have demonstrated that ceramic-on-ceramic bearings have volumetric wear rates as low as 0.004 $mm^3/10^6$ cycles (Clarke et al., 2000). The standard method for determining the volumetric wear rate of an implant is the gravimetric method, where the change in mass during the test is measured and converted into volume loss. The gravimetric method gives the overall wear volume, but not specific data on local wear patterns or the wear mechanism (Carmignato et al., 2011; Sagbas and Durakbasa, 2012). It is also not suitable for assessing wear of explanted implants as the initial mass is unknown (Blunt et al., 2009; Carmignato et al., 2011; Sagbas and Durakbasa, 2012). As the design of orthopaedic implants and biomaterials has improved the gravimetric method has reached the limit of its resolution (Bills et al., 2005; Blunt et al., 2009, Williams et al., 2011). Indeed some studies of ceramic femoral heads from Total

Hip Replacements have concluded that it is practically impossible to measure the volumetric wear rate using the gravimetric method, even with severe wear rates (Clarke et al., 2000; Sagbas and Durakbasa, 2012). Given the small size of Total Disc Replacements and the low wear rate for ceramic-on-ceramic bearings it will be difficult to accurately measure the mass change due to wear using the gravimetric method.

Volumetric wear measurement is now prevalent in the assessment of wear in retrieved Total Hip Replacements and coordinate measurement machines (CMM) are the most commonly used method (Langton et al., 2014). Langton et al. (2014) argue that for metal-on-metal and metal-on-plastic bearing surfaces an accuracy of 1 mm^3 would be clinically relevant, but for low wearing ceramic-on-ceramic bearings this would be too high and errors of 0.5 mm^3 would be more appropriate. Langton et al. (2011) have developed the Lord Joyce Langton (LJL) method for calculating the change in volume between a worn and unworn Total Hip Replacement. The LJL method used MATLAB to analyse coordinate data taken using a CMM. The unworn surface data was used to calculate the radius of the original surface of the implant. The worn surface data was then subtracted from the original radius to find the depth of the wear at each data point. A grid was interpolated between adjacent points across the surface and the wear volume was calculated for each grid square by multiplying the area by the average wear depth for the adjacent points. All of the grid square volumes were then summed together to find the total wear volume. When the LJL method was combined with a coordinate measurement machine with a measurement accuracy of 0.8 μm it was found to measure the volumetric wear of metal-on-metal Total Hip Replacement bearings and tapers with an accuracy of 0.5 mm^3 and 0.2 mm^3, respectively (Lord et al., 2011; Bone et al., 2015). Other

studies have evaluated the uncertainty in the volumetric measurement of Total Hip Replacements using CMMs, as defined in ISO/IEC Guide 98-3 (International Standards Organisation, 2008). They found uncertainties of ± 3.4 mm^3 and ± 1.859 mm^3, for ceramic-on-ceramic and retrieved metal-on-metal implants, respectively (Carmignato et al., 2011; Bills et al., 2012). This shows that the accuracy of volumetric measurements depends upon both the equipment used to measure the bearing surface and the method used to calculate the change in volume.

Non-contacting optical measurement methods offer a promising route for determining low wear volumes. They can measure both form and surface roughness in one scan with a vertical resolution of approximately 1 nm and a resolution across the contacting surfaces of approximately 1 μm. Non-contacting optical methods such as white light interferometry (Clarke et al., 2000; Serra et al., 2002) and laser confocal profilometry (Stoner et al., 2013; Turger et al., 2013) have been successfully used to measure the volumetric wear of ceramic hip and knee implants. They also have the advantage over the gravimetric method that the pattern of wear across the implant surface can be seen, and areas of severe wear identified.

The primary objective of this study was to develop a method for measuring the low volumetric wear expected in ceramic Total Disc Replacements using non-contacting optical methods. A series of alumina-on-alumina, ball-on-disc tests were conducted with test conditions approximating those of cervical Total Disc Replacement wear tests. The test samples were scanned to determine form and surface roughness using a white light interferometer. The data from these scans were then used to develop a method for determining the volume lost during the test due to wear. The study also investigated the effect of changing the

magnification of the lens of the interferometer on the surface roughness parameters and volumetric wear calculations.

This chapter is based on the publication by Green et al. (2015).

5.2 Material and Methods

5.2.1 Ball-on-Disc Tests

A custom built tribometer (Longshore Systems Engineering, Delabole, UK) was used to carry out ball-on-disc tests (Figure 5.1). The ball-on-disc test conditions were based on the International Standards Organisation (ISO) standard, BS ISO 18192-1:2011, for the wear testing of cervical Total Disc Replacements (British Standards Institution, 2011a). The balls were 99.9% purity alumina precision spheres, Grade 50, with a grain size of between 1 and 12 μm (Goodfellow Ceramic and Glass Division, Huntingdon, UK) with the material properties shown in Table 5.1. The balls had a diameter of 14 mm, chosen to represent the size of a typical cervical Total Disc Replacement (Figure 5.2a). The discs were 99.7% purity alumina (Dynamic Ceramic, Crewe, UK) with the material properties shown in Table 5.1. The discs were 20 mm in diameter and 1 mm in thickness (Figure 5.2b).

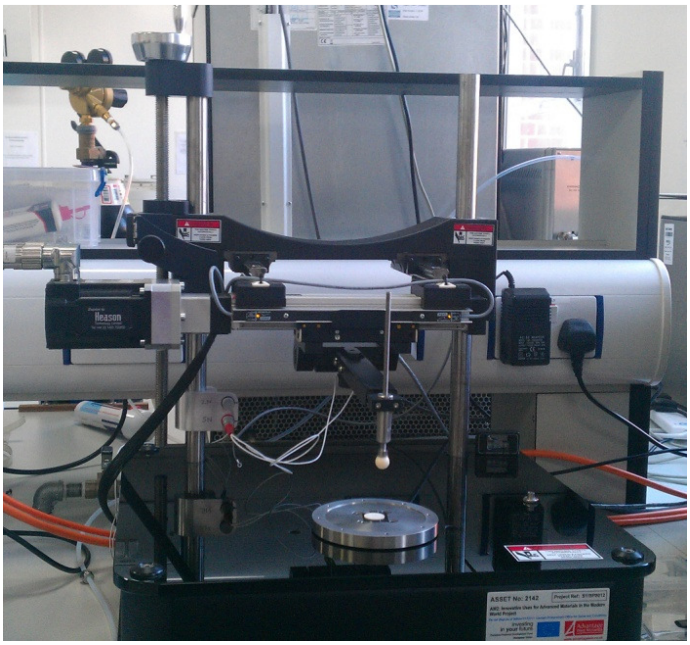

Figure 5.1: Tribometer—Custom built

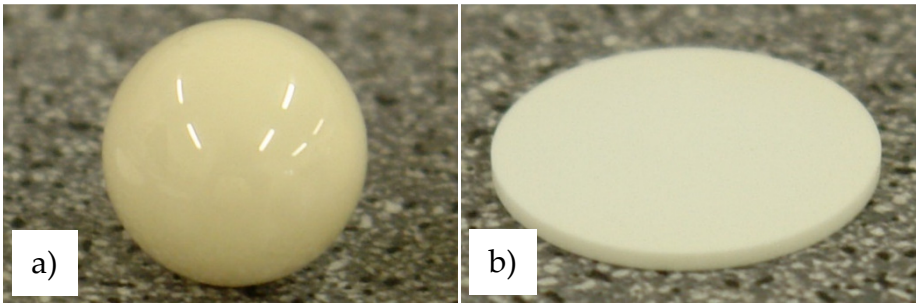

Figure 5.2: Alumina samples a) Ball; b) Disc

Table 5.1: Material properties of alumina
(Taylor, 2012, pers. comm.; Dynamic Ceramic, 2014)

	Ball	Disc
Alumina Content	99.9%	99.7%
Density (g/cm³)	3.90	3.89
Young's Modulus (GPa)	365	330
Poisson's Ratio	0.25	0.22
Hardness (GPa)	15.7	15.7

Before testing, the balls and discs were ultrasonically cleaned in ethanol, wiped with a lint free cloth and left to dry in air at room temperature. The disc was

glued (Super Glue Universal, Loctite, Hemel Hempstead, UK) to a glass microscope slide which was then fixed to the rotating base of the tribometer using double sided tape (Nisshin EM Co. Ltd., Tokyo, Japan) (Figure 5.3). The ball was glued (Evo-Stik, Epoxy Rapid, Bostik, Leicester, UK) to a hexagonal M5 cap screw, which was then screwed into the lever arm of the tribometer (Figure 5.3). A normal load of 5 N was applied to the ball, giving a mean Hertzian contact stress of 580 MPa. The disc was rotated against the ball for a distance of 3,665 m, which is an approximation of the sliding distance of the ISO wear tests. The tests were carried out at sliding velocities of 0.022 m/s and 0.044 m/s, which represent the testing frequencies for the ISO Total Disc Replacement wear tests (British Standards Institution, 2011a) of 1 Hz and 2 Hz, respectively. To achieve the required velocities, the following combinations of disc rotational velocity and radial position of the ball on the disc were used: 3.35 rad/s and 6.5 mm (0.022 m/s); 5.86 rad/s and 7.5 mm (0.044 m/s). The tests were unlubricated, carried out at a controlled room temperature of 18 ± 1 °C, and a relative humidity of 30-40 %. Each test was repeated four times.

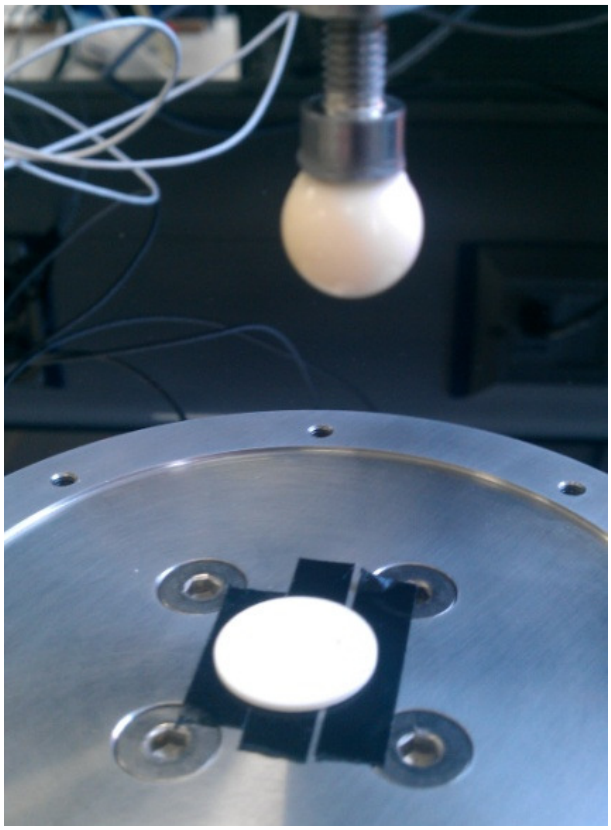

Figure 5.3: Ball and disc mounted on the tribometer

5.2.2 Profilometer

An attempt was made to obtain the surface topography of a disc surface using a contacting profilometer, Form Talysurf 120L (Taylor Hobson Ltd., Leicester, UK), with a 2 μm radius diamond stylus (Figure 5.4). The resolution in the z-direction (normal to the x-y plane of the surface of the disc) is 12.8 nm and a spatial sampling rate of 0.25 μm (Ku Leuven, 2016). The surface topography and cross-sectional profile were obtained using the software TalyMap Universal V 3.1.8 (Taylor Hobson Ltd., Leicester, UK), as shown in Figure 5.5.

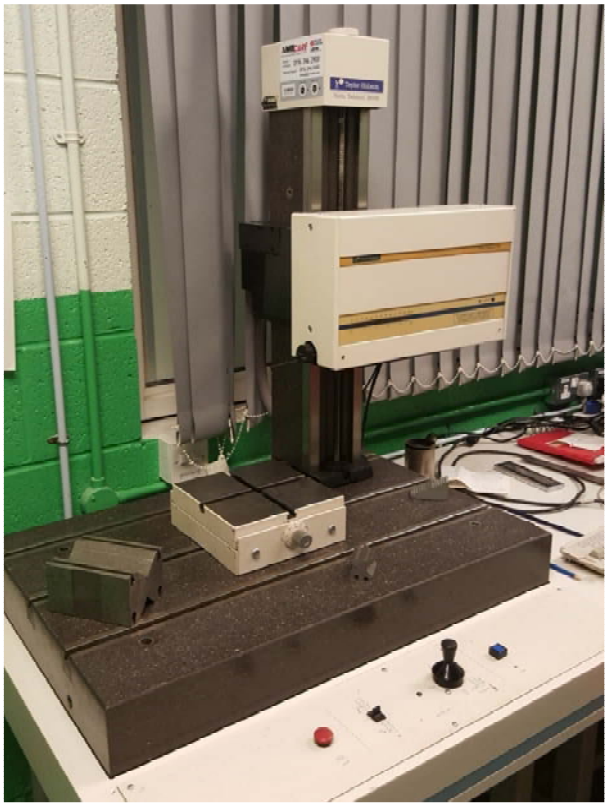

Figure 5.4: Profilometer—Form Talysurf 120L

It can be seen from Figure 5.5 that the profilometer did detect a change in the surface topography of the disc in the region of the wear track. However, the difference between the worn and unworn surface was minimal and it was difficult to define exactly where the wear track starts and ends which will affect the accuracy of the wear volume calculations.

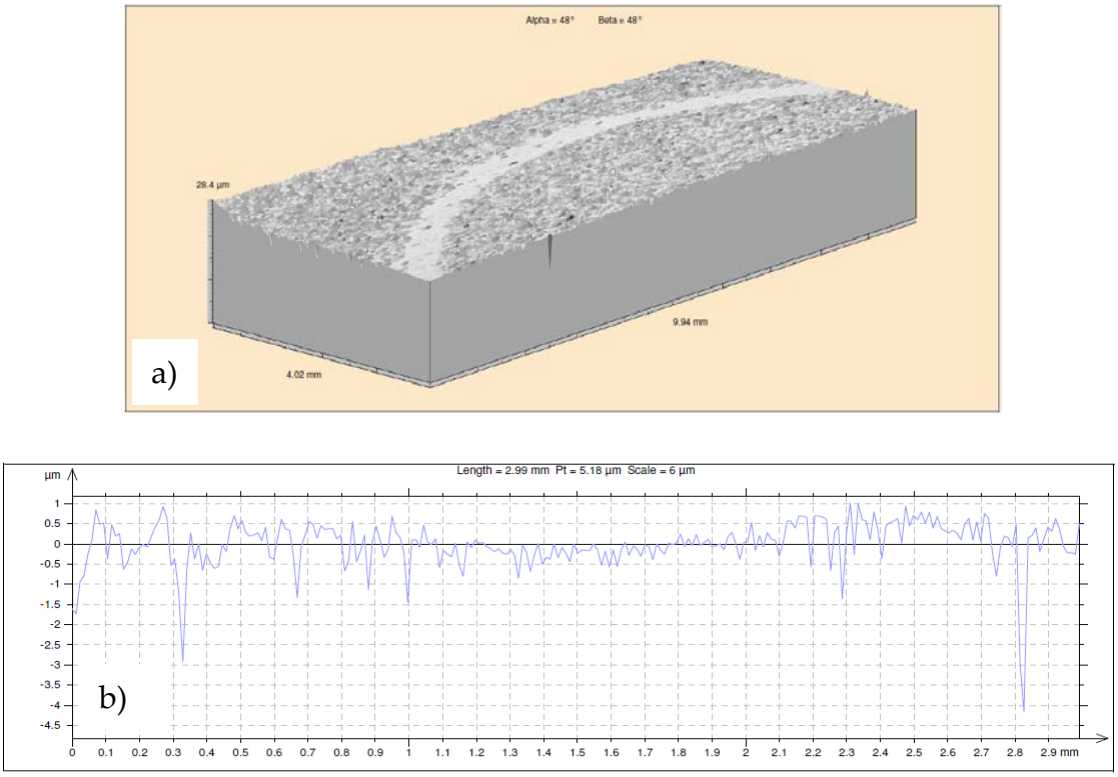

Figure 5.5: Wear track on an alumina disc after ball-on-disc test conducted at a sliding velocity of 0.044 m/s; a) Profilometer image of *z*-depth; b) Cross-sectional profile of the wear track

5.2.3 Interferometer

5.2.3.1 Disc

Instead of using the profilometer, the surface topography of both the ball and the disc were obtained using a more accurate three-dimensional non-contacting optical profilometer, which uses a white light interferometric microscope, MicroXAM2, (KLA Tencor, Wokingham, UK) (Figure 5.6). The data produced by the interferometer was processed and analysed using MapVUE AE version 2.27.1 (KLA Tencor, Wokingham, UK) and Scanning Probe, Image Processor, SPIP version 4.4.3.0 (Image Metrology, Hørsholm, Denmark). The in-plane measurement area, optical resolution, and spatial sampling rate vary depending on the magnification of the microscope, as shown in Table 5.2. The resolution in the z-direction (normal to the x- y plane of the surface of the disc) was

approximately 1 nm which was greater than the 12.8 nm resolution of the profilometer.

Figure 5.6: Interferometer— MicroXAM2

Table 5.2: Interferometer magnification properties (Phase Shift Technology Inc., 2014)

Objective Magnification	**10×**	**20×**	**50×**
Measurement Area (μm)	827 × 626	413 × 313	165 × 125
Spatial Sampling (μm)	1.1 × 1.3	0.55 × 0.65	0.22 × 0.26
Optical Resolution (μm)	0.92	0.69	0.5

For each disc, a section across the wear track was scanned in two different locations with a *z*-depth of 200 μm. In order to scan the full width of the wear track a number of images were stitched together using the stitch function in MapVUE AE. These images were then transferred to SPIP for processing and analysis. The interpolate function was used to fill in void pixels before using the plane correction facility to automatically correct plane distortions in the data using polynomial functions. In this case a first order polynomial was used as the slope on the data appeared linear. The mean *z*-value was then adjusted to

zero. To determine the surface roughness before and after the ball-on-disc test, a 492 μm × 433 μm area of the main image was sampled in two locations, inside the wear track and on the unworn surface. The surface roughness, *Sa*, for each location was then calculated using the SPIP software.

5.2.3.2 Balls

For the balls the wear flat was scanned with a *z*-depth of 400 μm, and a magnification of 10×. The interpolate function was used to fill in void pixels. A region of interest was defined around the observed wear flat on the ball and the rest of the image was excluded from processing. The data inside the region of interest was then corrected for any curvature using the plane correction facility and a second order polynomial. The mean *z*-value was also adjusted to zero. The surface roughness, *Sa*, and dimensions for the wear flat were calculated using the SPIP software. To determine the surface roughness before the ball-on-disc test, a single scan was taken with a *z*-depth of 400 μm, and a magnification of 50×. The image was corrected as above for the wear flat.

5.2.4 Wear Calculations

5.2.4.1 Disc

The data from the interferometer was used to calculate the volume loss for the disc. For each of the two interferometer images taken for each disc, an average cross-sectional profile of the wear track was calculated using SPIP. The edges of the wear track were found visually and the average profile cut to these edges. The mean surface calculated by the software takes into account the depth of the wear track and is, therefore, not a true representation of the *z*-depth of the unworn surface. To adjust for this, a new mean surface was calculated from the average of the *z*-depths of the two outer edge data points and subtracted from

the z-depth values of all the data points. The area above this curve is, therefore, the cross-sectional area of the wear track and was used to calculate the volume loss. Using freeware Octave software, version 3.6.2 (John W. Eaton, University Wisconsin Madison, Wisconsin, USA) the approximate cumulative integral of z with respect to x was calculated using trapezoidal integration (Figure 5.7). The width of the trapezoids is defined by the spatial sampling rate of the interferometer in the x-direction. It was assumed that the calculated cross-sectional area was constant throughout the wear track and therefore, the volume loss could be calculated by revolving the area around the circumference of the track.

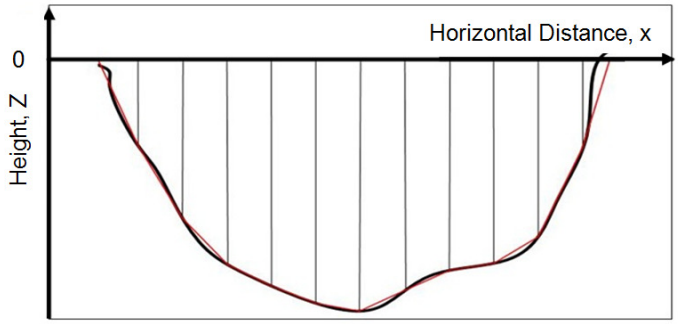

Figure 5.7: Schematic showing approximate cumulative integral calculated using trapezoidal integration

5.2.4.2 Balls

For the balls it was assumed that the volume loss, V_b, takes the form of a spherical cap as shown in Figure 5.8, whose volume was calculated from:

$$V_b = \frac{1}{6}\pi h(3a^2 + h^2) \qquad \textbf{Equation 5.1}$$

where a is the radius of the wear flat and h the height of the spherical cap calculated from:

$$h = r - \sqrt{r^2 - a^2} \qquad \textbf{Equation 5.2}$$

where r is the radius of the ball itself.

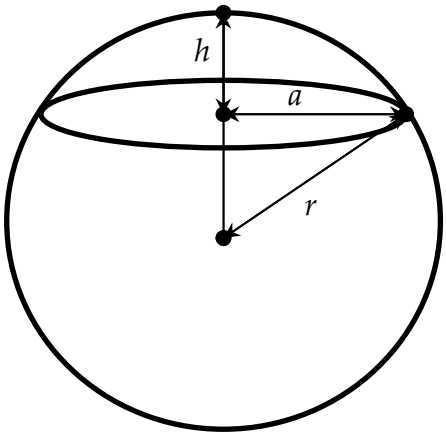

Figure 5.8: Schematic showing a spherical cap, where *a* is the radius of the wear cap, *r* is the radius of the ball and *h* is the height of the spherical cap

5.2.5 Scanning Electron Microscopy

The worn and unworn disc surface topography were sputter-coated with gold and then imaged using a Scanning Electron Microscope (SEM), JEOL 7000 (JEOL, Japan) operated at 10.0 kV.

5.2.6 Statistical Analysis

The statistical analysis was conducted using Minitab version 16.2.3 (Minitab Ltd. Coventry, UK). Anderson-Darling tests were used to check that the data followed a normal distribution, based on a probability (*p*-value) of less than 0.05. Two sample t-tests were then used to determine if there were significant differences between surface roughness measurements on the worn and unworn surfaces, based on a probability (*p*-value) of less than 0.05.

5.3 Results

5.3.1 Surface Study

5.3.1.1 Disc

The interferometer image of the disc surface, taken with a 10× lens (Figure 5.9a), clearly shows the loss of material in the wear track and also a small build-up of

material on the inner edge. The cross-sectional profile showing the *z*-depths across the wear track (Figure 5.9b) clearly supports these observations. Figure 5.10a shows an image of the same disc, taken with a 20× lens and the wear track was not so easily identifiable. The cross-sectional profile in Figure 5.10b shows the wear track was positioned higher than the unworn surface which is an incorrect result. This type of image and data were typical of that produced by the 20× lens and suggests a method problem caused by the change in magnification.

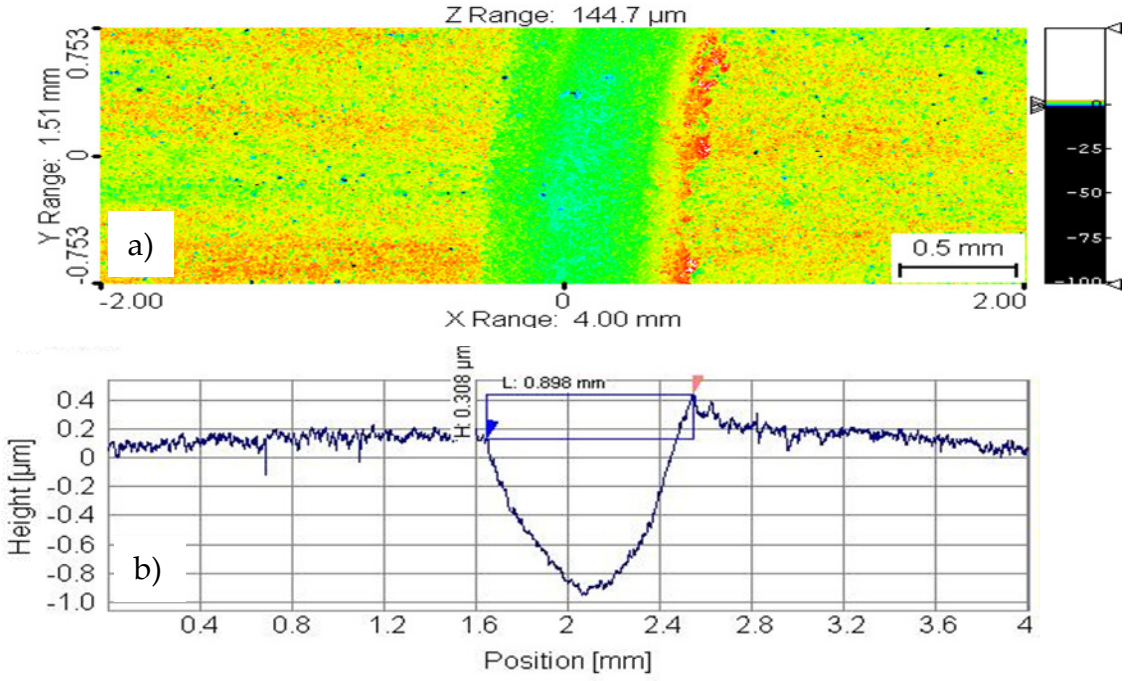

Figure 5.9: Wear track on an alumina disc after ball-on-disc test conducted at a sliding velocity of 0.022 m/s; a) Interferometer image of z-depth taken at 10× magnification; b) Cross-sectional profile of the wear track

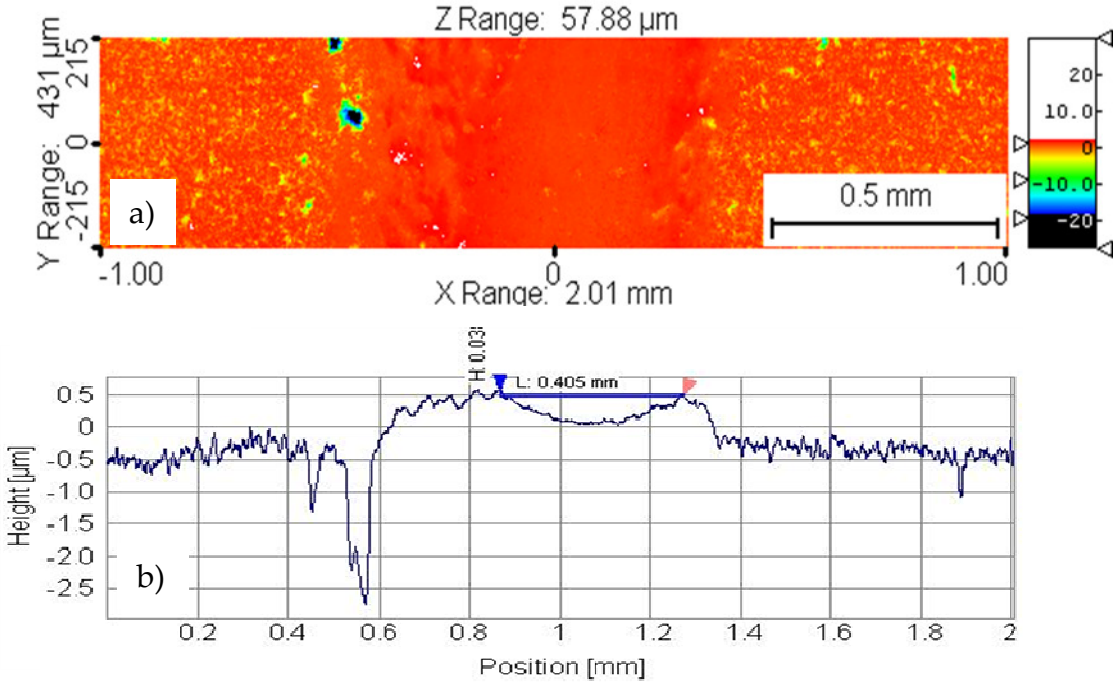

Figure 5.10: Wear track on an alumina disc after ball on disc test conducted at a sliding velocity of 0.022 m/s; a) Interferometer image of z-depth taken at 20× magnification; b) Cross-sectional profile of the wear track

On visual inspection the worn surface was noticeably more polished than the unworn surface suggesting that the surface roughness was lower on the worn surface. Marks which were left on the discs from the manufacturing process were removed during the test and cannot be seen on the worn surface. There were marks in the direction of travel of the ball in the worn surface suggesting third body wear from wear debris trapped between the ball and the disc.

The surface roughness, *Sa*, as measured using both a 20× and 10× lens on the interferometer, of the unworn and the worn surfaces is shown in Table 5.3, with the two measurements for each test denoted by a and b. A two sample t-test showed that the *Sa* values measured by the 10× and the 20× lens for the unworn surface were significantly different (p=0.000), but there was no significant difference for the worn surface (p=0.313). It was evident from the data that the 20× lens consistently measures a decrease in surface roughness, as seen visually

on the surface of the discs. However, seven of the 10× lens measurements showed an increase in surface roughness and this was not in agreement with the visual evidence. Therefore, it was assumed that the 20× lens measurements were the more reliable. A two sample t-test on the 20× lens surface roughness measurements confirmed that there was a significant difference between the unworn and worn surfaces (p=0.000).

Table 5.3: Surface roughness, *Sa*, interferometer measurements of the unworn and worn disc surface with 10× and 20× lenses

	10× magnification Surface Roughness, *Sa* (μm)			20× Magnification Surface Roughness, *Sa* (μm)		
Test No	**Unworn Surface**	**Worn Surface**	**Change**	**Unworn Surface**	**Worn Surface**	**Change**
1a	0.2	0.2	0.0	0.7	0.3	-0.4
1b	0.3	0.2	-0.1	0.8	0.2	-0.5
2a	0.2	0.2	0.0	0.5	0.4	-0.1
2b	0.2	0.2	0.0	0.5	0.4	-0.0
3a	0.2	0.1	-0.1	0.5	0.2	-04
3b	0.2	0.1	-0.1	0.6	0.3	-0.4
4a	0.3	0.2	-0.1	0.7	0.1	-0.5
4b	0.2	0.2	0.0	0.7	0.1	-0.6
5a	0.2	0.3	0.1	0.6	0.3	-0.4
5b	0.2	0.3	0.1	0.6	0.2	-0.4
6a	0.2	0.2	0.0	0.6	0.2	-0.4
6b	0.2	0.2	0.0	0.6	0.2	-0.4
7a	0.8	0.4	-0.4	1.0	0.5	-0.5
7b	0.8	0.4	-0.4	0.8	0.7	-0.1
8a	0.1	0.2	0.0	0.4	0.1	-0.3
8b	0.1	0.2	0.0	0.4	0.1	-0.3
Mean	0.3	0.2	0.0	0.6	0.3	-0.3
Standard Deviation	0.2	0.1	0.2	0.2	0.2	0.2

Visual analysis of the images of all the discs suggested that the 20× lens measured a number of 'pits' in the unworn surface which the 10× lens did not measure. This was confirmed by Figure 5.11, where one of these pits was imaged with both the 10× and 20× lenses. In Figure 5.11a the *Sa* value was 0.683 µm and the maximum depth of the pit was 28 nm and in Figure 5.11b the *Sa* value was 0.25 µm and the maximum depth of the pit was 17 nm. These pits were not measured on the worn surface by either the 20× or 10× lenses.

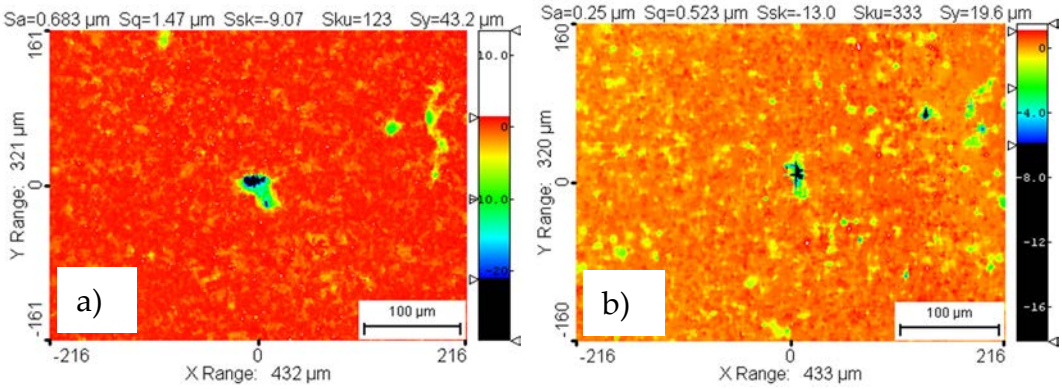

Figure 5.11: Interferometer image of a pit in the unworn surface of the disc; a) Taken with 20× lens; b) Taken with 10× lens

Figure 5.12a shows a SEM image of the surface of the disc shown in Figure 5.9 and Figure 5.10. The wear track was clearly identifiable on the image as a dark stripe. The wear track width was measured using the SEM software to be 0.805 mm and compares reasonably well with the interferometer measurement of 0.898 mm from the 10× lens image in Figure 5.8b. The SEM image agrees with the interferometer images in that there was a series of deep pits on the unworn surface, but they cannot be identified on the worn surface. The detailed SEM image of the worn surface (Figure 5.12b) showed what appears to be a tribofilm (Olofsson et al., 2012) of compacted wear debris and a series of micro-cracks. The wear debris produced by the tests can be clearly seen as a powder around the edges of the wear track in Figure 5.13.

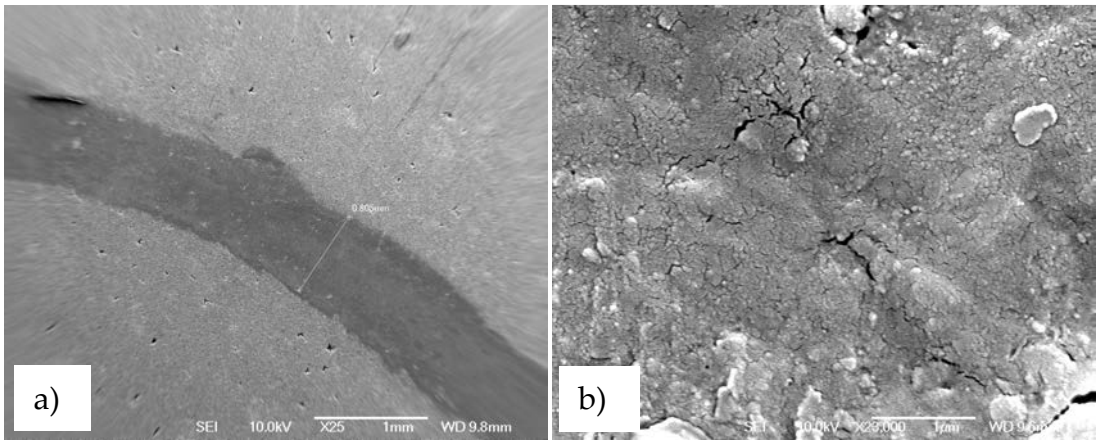

Figure 5.12: SEM image of an alumina disc after ball-on-disc test conducted at a sliding velocity of 0.022 m/s; a) Overview of wear track and unworn surface; b) Detailed view of worn surface

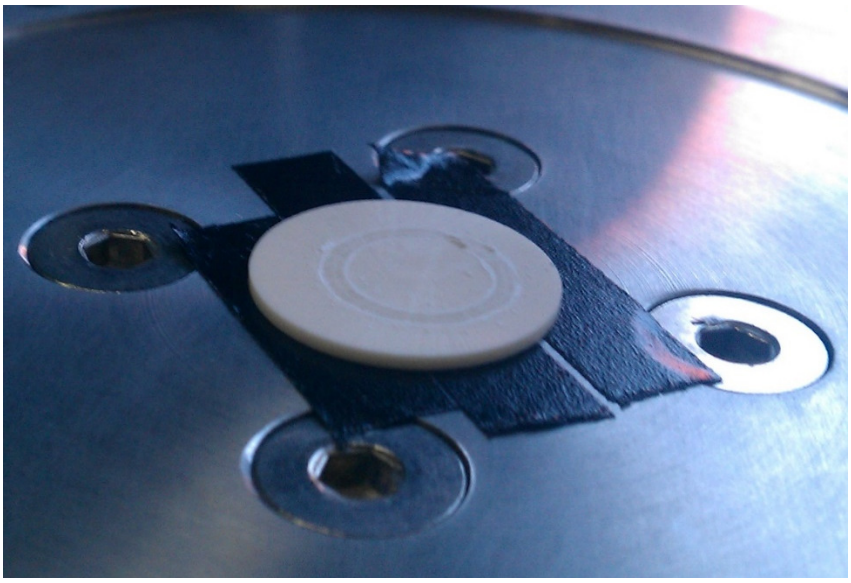

Figure 5.13: Wear debris produced by the tests

5.3.1.2 Balls

The three-dimensional interferometer image of a ball, shown in Figure 5.14a, taken after a ball on disc test, clearly shows the wear flat which formed on the surface during the tests. Images of the wear flat taken with both the SEM and interferometer show some directional marks and an uneven edge on the top right quarter of the flat, see Figures 5.14 b and c. This suggests third body wear

due to trapped wear debris, or possibly a transfer of the tribofilm described above. The surface roughness, *Sa*, of the unworn and the worn surface of the balls can be seen in Table 5.4. A two sample t-test showed there was a significant difference between the *Sa* of the ball before and after the tests (p=0.003). This is supported by the visual appearance of the wear flat being duller than the unworn surface. The mean *Sa* of the ball after a 0.044 m/s test was 0.2 ± 0.1 μm and after a 0.022 m/s test was 0.6 ± 0.2 μm.

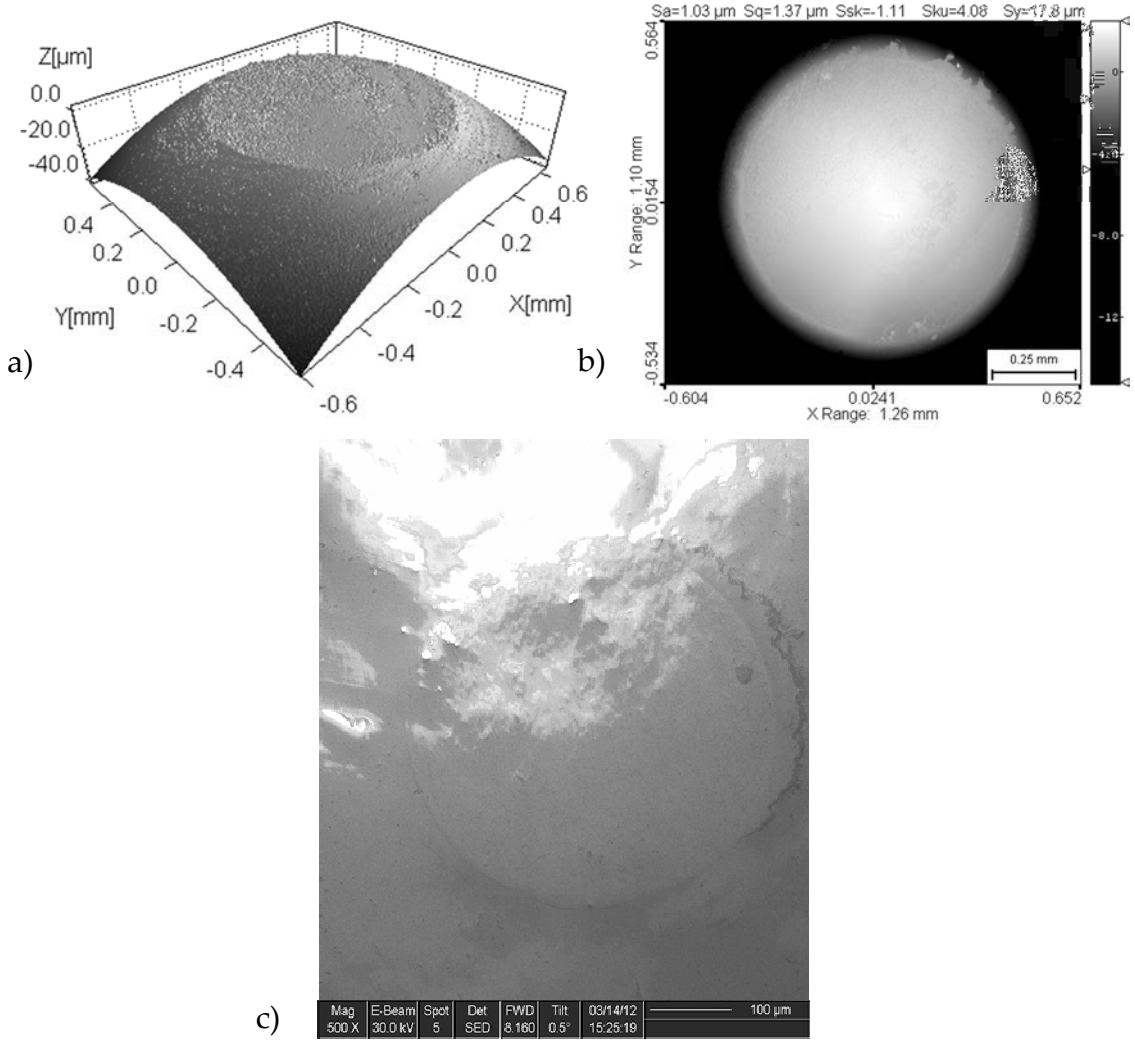

Figure 5.14: Images of the wear flat on an alumina ball after ball-on-disc test conducted at a sliding speed of 0.022 m/s; a) Interferometer three-dimensional image; b) Inteferometer processed two-dimensional image c) SEM image

Table 5.4: Surface roughness, *Sa*, interferometer measurements of the unworn and worn ball surfaces. (Reported to different precisions due to different measurement techniques)

Test Number	Unworn Surface *Sa* (μm)	Worn Surface *Sa* (μm)
1	0.008	0.2
2	0.007	0.1
3	0.014	0.3
4	0.007	0.2
5	0.012	0.6
6	0.008	0.8
7	0.007	0.4
8	0.009	0.7
Mean	0.009	0.4
Standard Deviation	0.003	0.3

5.3.2 Wear

5.3.2.1 Discs

The wear volumes for the discs were 0.019 ± 0.009 mm^3 (mean ± standard deviation) and 0.02 ± 0.01 mm^3 for speeds of 0.044 and 0.022 m/s, respectively. The wear volumes calculated for each disc can be seen in Table 5.5, with the two measurements for each test denoted by a and b. These wear volumes correspond to a mass loss of 0.08 ± 0.04 mg and 0.10 ± 0.05 mg, assuming a density value of 3.89 g/cm^3.

Table 5.5: Disc wear volumes; a) Velocity 0.044m/s; b) Velocity 0.022m/s

a)

Test Number	Wear Volume (mm^3)
1a	0.029
1b	0.032
2a	0.022
2b	0.019
3a	0.006
3b	0.007
4a	0.018
4b	0.022
Mean	**0.019**
Standard Deviation	**0.009**

b)

Test Number	Wear Volume (mm^3)
5a	0.03
5b	0.04
6a	0.03
6b	0.02
7a	0.04
7b	0.03
8a	0.00
8b	0.01
Mean	**0.02**
Standard Deviation	**0.01**

5.3.2.2 Balls

The wear volumes for the balls were 0.0015 ± 0.0009 mm^3 (mean ± standard deviation) and 0.004 ± 0.003 mm^3 for speeds of 0.044 and 0.022 m/s, respectively (Table 5.6). These wear volumes correspond to a mass loss of 0.006 ± 0.004 mg and 0.01 ± 0.01 mg, assuming a density value of 3.90 g/cm^3.

Table 5.6: Ball wear volumes; a) Velocity 0.044 m/s; b) Velocity 0.022 m/s

a)

Test Number	Wear Volume (mm^3)
1	0.0028
2	0.0012
3	0.0008
4	0.0012
Mean	**0.0015**
Standard Deviation	**0.0009**

b)

Test Number	Wear Volume (mm^3)
5	0.004
6	0.003
7	0.007
8	0.001
Mean	**0.004**
Standard Deviation	**0.003**

5.4 Discussion

The main aim of this study was to develop and assess a novel method for measuring low wear volumes expected in alumina-on-alumina Total Disc Replacements, using non-contacting optical methods. The volume loss due to wear on the discs in these experiments was low and the mass loss would have been in the order of 0.01 mg. The ISO standard for the wear testing of Total Disc Replacements (British Standards Institute, 2011a), cites the standard for Total Hip Replacements (British Standards Institute, 2000), which specifies the use of a mass balance with an accuracy of ± 0.1 mg. Such a balance would have been unable to detect the mass loss in these experiments. There are mass balances on the market which can detect mass changes in the order of 0.0001, 0.001 and 0.01 mg for masses below 2.1, 31 and 60 g, respectively (Sartorius UK Ltd, 2014a and b). Total Disc Replacement components weigh between 15 and 20 g, but once fixtures are added, which maintain the position of the implant in the wear testing machine, the combined weight is over 60 g. Analytical balances which can weigh masses above 60 g have a readability of 0.1 mg (Sartorius UK Ltd,

2014b) which would be unable to detect the mass loss in these experiments. Blunt et al. (2008) described similar issues with measuring small mass changes in large components, such as Total Knee Replacements, using even the best high-resolution balances. Grupp et al. (2009) used an analytical balance with a readability of ± 0.1 mg to measure the wear on a metal-on-plastic Total Disc Replacement which had undergone a wear simulation based on ASTM F2423-05 (ASTM International, 2005). The mean wear rate was 0.14 ± 0.06 mg which was close to the readability of the mass balance and demonstrates the need for a measurement method with a higher precision. Blunt et al. (2009) have had problems with measuring mass changes in the order of 0.005 mg on larger implants, such as Total Hip Replacements and Total Knee Replacements. The method developed in this study can measure volume changes equivalent to a mass loss of 0.0001 mg which is several orders of magnitude lower than suitable mass balances.

Aside from measuring low wear volumes, this non-contacting optical method has the advantage over the gravimetric method that both the form and the surface roughness of the implant can be measured from just one scan. The data can be used to identify changes to the surface topography at the micro-scale and the wear mechanism, and also the location and pattern of the wear at a macro-scale. This method could be further developed to measure the wear in explanted implants, where the initial mass is unknown and the gravimetric method cannot be used (Blunt et al., 2009; Carmignato et al., 2011; Sagbas and Durakbasa, 2012).

The study also aimed to measure the surface roughness of the worn and unworn surfaces of the test samples and investigate the effect of changing the magnification of the optical lens on the measurements. The worn surfaces of the

discs had a mean *Sa* of 0.3 μm which is significantly lower than the unworn surfaces, which had a mean *Sa* of 0.6 μm. This can be explained by the presence of a tribofilm covering the wear track and filling in the deep pits in the unworn surface and reducing the surface roughness (Lee et al., 1990; Blomberg et al., 1994; Adachi et al., 1997; Adachi and Kato, 2000; Kato and Adachi 2002; Roy et al., 2007a; Olofsson et al., 2012). As the alumina disc wears, grains break away from the surface and are then trapped between the contacting surfaces and ground down into smaller wear particles. The directional marks seen in the disc wear track are indicative of this type of third body wear. Over time these small particles combine together to form agglomerates, which are then plastically deformed into compacted layers covering the surface of the wear track. Additional sliding leads to the development of interconnected micro-cracks as seen in the SEM image (Figure 5.12b).

The presence of this tribofilm has highlighted a potential pitfall with the use of using non-contacting optical methods to measure form. The results show that when using the 20× lens the stitching function gives a spurious result, with the worn surface being higher than the unworn surface. When scanning larger surface areas the interferometer takes a series of smaller scans and then MapVue AE stitches them together to produce one larger scan. The stitching algorithms are designed for surfaces with a reasonably consistent surface roughness. In these tests the 20× lens measured an appreciable difference between the surface roughness of the worn and unworn surfaces. Therefore, there would have been a discontinuity in the surface roughness at the boundary between the worn and unworn surfaces causing the stitching algorithms to misalign the heights of the individual scans. Since the 10× lens does not measure this difference in surface roughness and there is no discontinuity in the

scanned surface, the stitching algorithms give more reliable results in terms of form measurement. However, the results also show that the higher resolution of the 20× lens provides more reliable results in terms of surface roughness measurements.

5.5 Summary

A technique for measuring low wear volumes (<0.0001 mm^3/ 0.0001 mg) in ceramic bearings using non-contacting optical methods was successfully developed. The results showed that this method was able to measure small changes in volume due to wear which would not have been identifiable by using the gravimetric method. The results also showed that, when using non-contacting optical methods, the user needs to be aware of the effect of the magnification of the lens on the reliability of the measurements. This method is not just limited to ceramic Total Disc Replacements and low levels of wear, but could be applied to more severe wear, and other orthopaedic implants made from any material. A further advantage of this method is that with one scan the user can measure changes in surface topography, volumetric wear and the location of the wear on the implant surface. The method could be further developed for use in measuring wear in explanted implants.

In the next chapter the success of this preliminary study was built upon, and the optical method was developed further. Focus variation microscopy was used to calculate the volumetric wear of the alumina cervical Total Disc Replacements wear tested in Chapter 4. The results from the optical method were compared with those calculated using the standard gravimetric method.

Chapter 6

Use of Non-Contacting Optical Microscopy to Measure Wear and Surface Roughness of Ceramic Total Disc Replacements

Overview

In this chapter a novel non-contacting optical method for measuring the volumetric wear of ceramic Total Disc Replacements is described and compared against the traditional gravimetric method. Section 6.1 introduces the current methods for measuring wear volumetrically in joint replacements and their potential advantages over the gravimetric method. Section 6.2 details the development of the new optical method and uses it to measure the volumetric wear of the ceramic Total Disc Replacements wear tested in Chapter 4. The results from the two measurement methods are compared in Section 6.3 and the advantages and disadvantages of the optical method are discussed in Section 6.4. The chapter is concluded in Section 6.5.

6.1 Introduction

As already described in Chapter 4, it is necessary to accurately measure the volumetric wear loss of Total Disc Replacements to understand the behaviour of the bearing materials. Wear debris can lead to an adverse reaction in the periprosthetic tissues called osteolysis which can cause aseptic loosening of orthopaedic implants (Ingham and Fisher, 2000; 2005) and the need for revision. The gold standard for establishing the wear rate of an implant is the gravimetric method (Langton et al., 2014), where the change in mass of the implant is measured and converted into a loss of volume. However, the design of orthopaedic implants and their bearing materials has improved to the extent that in some cases the gravimetric method has reached the limit of its resolution (Bills et al., 2005; Blunt et al., 2009). The gravimetric method also has disadvantages; it cannot be used for implant retrieval analyses because the original weight is unknown, and it only gives the total wear volume with no information about the location of the wear.

The alternative to gravimetric wear measurement is some form of volumetric wear measurement, which can be achieved using several techniques such as micro computed tomography (micro-CT), coordinate measurement machines (CMMs) and optical measurement. Volumetric wear measurement is more commonly used in the assessment of retrieved joint replacements, but has also been used for *in vitro* studies.

CMMs have been widely used in the volumetric wear assessment of retrieved Total Hip Replacements, as discussed in Section 5.1, but have been rarely used in Total Disc Replacements. They have been used to find the change in the vertical height of the ultra-high molecular weight polyethylene (UHMWPE) cores of lumbar and cervical Total Disc Replacement after *in vitro* wear

simulations (Grupp et al., 2009; 2010). These measurements were not used to calculate the overall volume loss due to wear, but to map the location of high levels of wear on the implant surface.

Micro-CT is more commonly used than CMMs in the wear assessment of Total Disc Replacements, for both retrieval analyses and *in vitro* testing. Several studies have used both micro-CT and the gravimetric method to assess the wear of the Charité UHMWPE core after *in vitro* testing. Vicars et al. (2009) found the micro-CT method had a repeatability of 3 mm^3, which was significantly larger than that of the gravimetric measurements at 0.007 mm^3. However, Moghadas et al. (2015) compared the results of micro-CT and the gravimetric method using a Bland-Altman plot and found no significant difference between the results of the two measurement techniques. Micro-CT has also been used in retrieval analyses of Charité cores to identify internal cracks, penetration and changes in central thickness (Kurtz et al., 2007). Although micro-CT has the advantage of being able to see internal defects, it is time consuming and costly (Stoner et al., 2013) and the studies above suggest the technique would be unlikely to be able to detect the low wear volumes expected in ceramic Total Disc Replacements.

Volumetric wear can also be measured using a form of non-contacting optical microscopy, such as a laser or focus variation. Stoner et al. (2013) used a desktop laser scanner to obtain the topography of retrieved Total Knee Replacement tibial inserts. The point cloud of the implant surface produced by the laser scanner was aligned with a CAD model of the unworn surface using an Iterative Closest Point algorithm. The calculated change in vertical height was mapped across the implant surface, but again not used to calculate the overall volume loss. Retrieved Total Hip Replacement tapered stems have also

been assessed for volumetric wear using an Alicona InfiniteFocus which uses focus variation to obtain the surface topography of the implant (Cook et al., 2015). An isosurface was generated to approximate the unworn surface and the worn surface was compared against it. As such, the volume loss calculations were considered a robust estimate rather than a definite value.

Although some volumetric wear assessment methods are not yet fully mature it can be seen from the above and Chapter 5 that they are showing promise and have several advantages over the gravimetric method. Therefore, this chapter built on the work in Chapter 5 and developed a novel method for measuring low wear volumes using non-contacting optical microscopy. The new optical method was used to calculate the volumetric wear loss of the alumina Total Disc Replacements wear tested in Chapter 4. The worn surface of the implant was scanned after each set of wear cycles and compared to the unworn surface using a custom MATLAB program. The volumetric wear loss was then compared against the gravimetric wear loss found in Chapter 4 to compare the two methods. In addition the optical method was used to obtain images of the surface damage and identify changes in surface roughness.

6.2 Materials and Method

6.2.1 Non-Contacting Optical Microscopy

The interferometer used in Chapter 5 did not have the computational power to scan the implant surfaces, which were considerably larger than the ball and discs. Therefore, the implants were scanned using a non-contacting optical 3D micro coordinate system, InfiniteFocus, (Alicona Imaging GmbH, Raab/Graz, Austria) which uses focus variation microscopy to measure both form, surface roughness and true colour in one scan, see Section 3.3.9 for more details.

The optical method used InfiniteFocus scans of each implant to obtain a set of x, y, z, coordinates which describe their surface topography. Before the wear tests began, a baseline scan was taken of the unworn surface of each implant. After each set of wear cycles on the spine simulators, the scan was repeated to obtain the worn surface of the implants. A MATLAB function, MATLAB version r2015a (Mathworks, Massachusetts, USA), was written which compares the coordinates of the worn surface with the baseline coordinates of the unworn surface to determine the change in volume of the implant, see Section 6.2.4 for more details.

The implants were scanned using the 10× magnification lens. The lateral resolution of the scan was set to 7 μm and the vertical resolution to 60 nm for each scan. The x, y, z coordinates were exported as a plain text .txt file, using the InfiniteFocus software MeasureSuite v5.1. As this was an optical method, ideally the light intensity would remain the same for each scan. However, as the implant surface wore, parts of it became more reflective, resulting in void pixels and a lack of data in these areas of the surface. Therefore, when needed, the light intensity was lowered to reduce the number of void pixels and increase the amount of data recorded. The light setting values ranged from 140 to 200 μs.

When comparing the difference in volume between a worn and unworn implant it is important that both scans have the same coordinate system and global origin, otherwise there will be errors in the volume calculations. One major issue with the InfiniteFocus is that the global origin is not permanent, because it can be redefined by the user at any time, and there is no default position. Therefore, when scanning the surface of the implants after each set of wear cycles the origin may have been changed causing the x, y, z coordinate data to be misaligned.

Practical steps were taken to set a consistent global origin for each scan. To ensure the implants were positioned in the same place and orientation for each scan, a fixture was designed which attached the implant to the *x*-*y* stage of the InfiniteFocus, see Appendix A for the engineering drawing. The fixture was produced using an Objet Eden 250 stereolithography printer (HK Rapid Prototype Ltd., Rugby, UK) and Fullcure 720 resin (HK Rapid Prototype Ltd., Rugby, UK). For each implant the *x*-*y* area remains constant so the only variable in the volume calculation was the *z*-height. Therefore, the origin of the *z*-axis was particularly critical to the accuracy of the volume calculation. To set the origin of the *z*-axis before each scan the 50× lens of the microscope was focused on a reference sample with a surface roughness, *Ra*, of 0.02 μm (Rubert 501X, Rubert and Co. Ltd., Cheadle, UK). The origin of the less critical *x* and *y* axes was set by focusing the microscope on the centre of the spherical region of the implant and selecting the pole by eye.

6.2.2 Surface Characterisation

Surface roughness measurements were taken using the MeasureSuite software for each implant before and after each set of wear cycles on the spine simulators. There is no international standard which defines the surface roughness requirements for the articulating surfaces of a Total Disc Replacement. Therefore, the measurements were taken in accordance with the ISO standard for the similar articulating surfaces of hip implants, BS ISO 7206-2:2011, which references BS EN ISO 4287:1998 and BS EN ISO 4288:1998 (British Standards Institution, 2011b; 1998a; 1998b). Full details of this method can be found in Section 3.3.9.

6.2.3 Wear Images

As in Section 3.3.9, the form removal function of the MeasureSuite software was used to produce images of the wear on the articulating surfaces of the implants. The function subtracted a spherical form from the raw data to produce an image showing where the data deviates from a perfect sphere, see Figure 6.1. A negative height indicates an area of wear and a positive height indicates the unworn surface. However, it was unclear how the form removal function was calculated by the software and the reliability of the results is questionable. For example, in Figure 6.1 the unworn surface around the edge of the implant, which should have a height of roughly 0 microns is calculated to be 50 μm above the surface. Therefore, the images provide an indication of the wear patterns but the results cannot be used to calculate the volume loss due to wear.

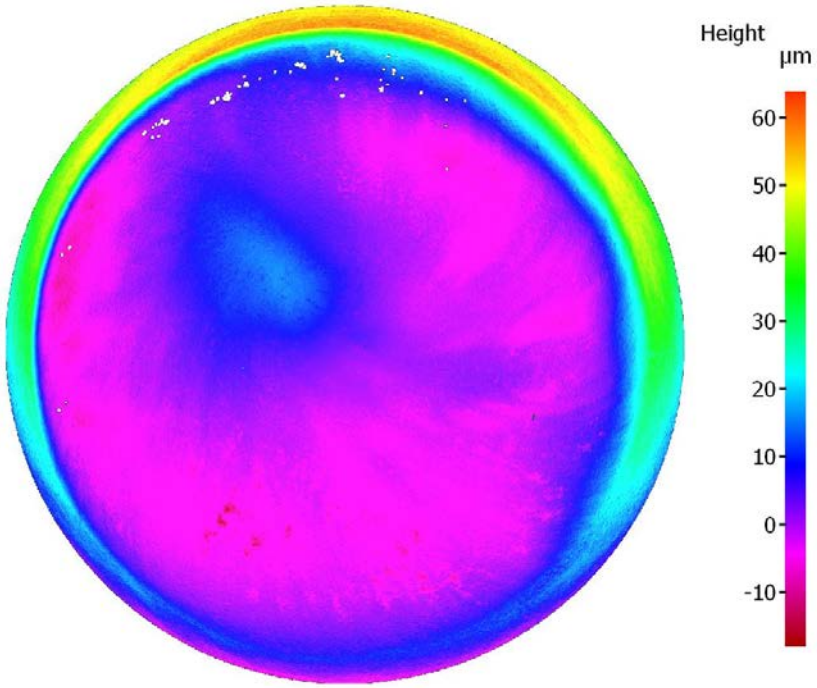

Figure 6.1: Example of a form-removed image showing areas of wear on the implant's articulating surface

6.2.4 Optical Method for Calculating Volume

A MATLAB function called '*GenAliconaImport.m*', (Eckold, 2016) was used to calculate the volume of the implant from the *x*, *y*, *z* coordinates exported from the InfiniteFocus, see Appendix B.7 for the full code. Figure 6.2 shows a high level flowchart of the main processes carried out by the code.

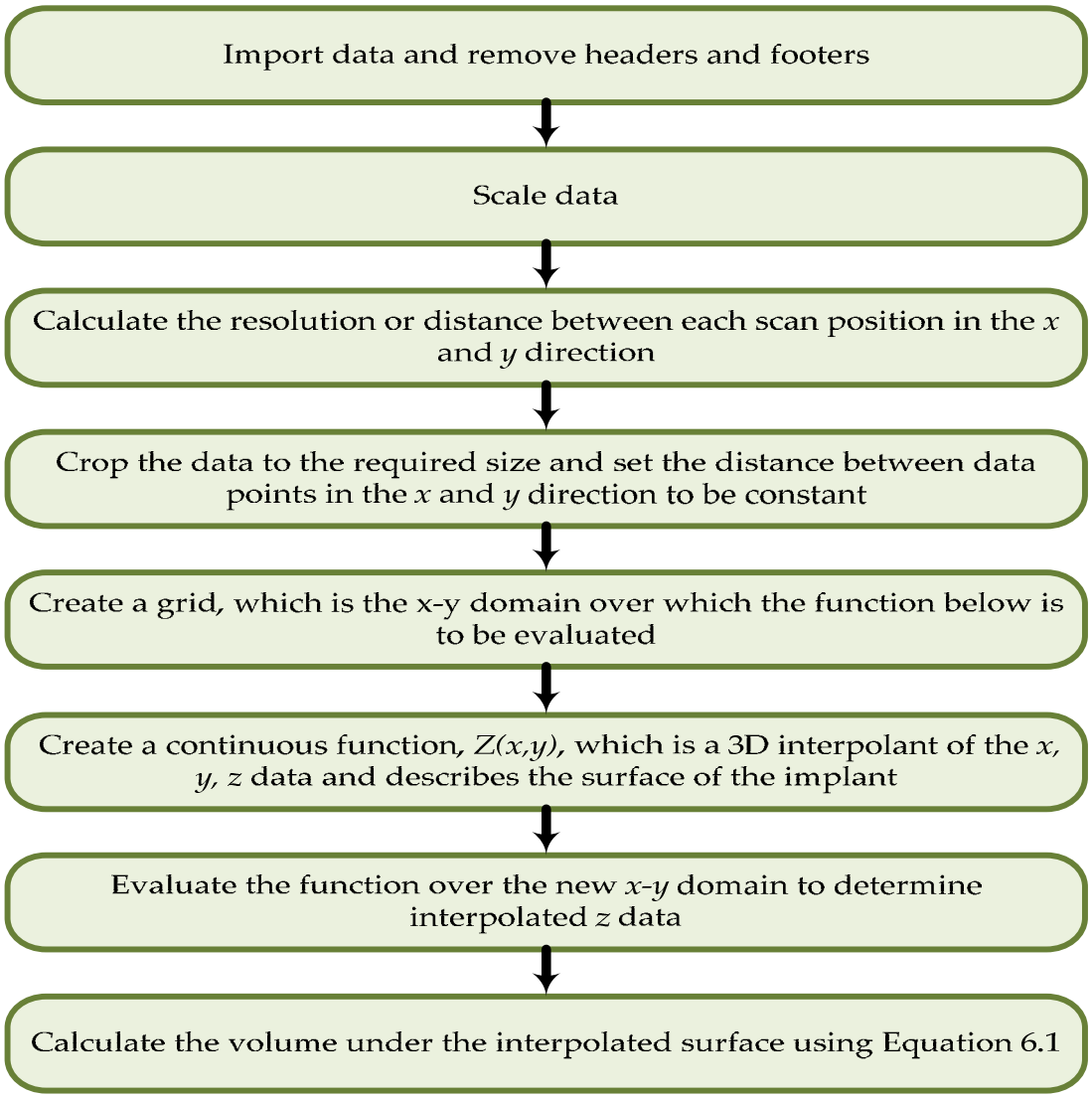

Figure 6.2: Flow chart showing the main processes in the MATLAB function *GenAliconaImport.m*

Firstly the text file from the InfiniteFocus was imported, the text headers and footers were removed and three separate matrices for the *x*, *y*, and *z* coordinates

were output, (this code was autogenerated by MATLAB). If required the function can then scale the matrices to a different unit system, although it was not required in this case. The resolution of the scan or the distance between each position in the x or y directions, dx and dy, varied within each scan. Therefore, the program calculated dx and dy for the first step in the data and then used this to set a constant step size for a new x-y domain, which was then defined. The limits of the new x-y domain were set so as to crop the data and provide a consistent x-y area for each volume calculation. The scan images of the implants often had void pixels where the InfiniteFocus had not recorded data for that position. Figure 6.3 shows a particularly bad example of this, with missing data shown as white pixels around the edge of the implant. In a calculation to determine volume, this missing data would cause the volume to be underestimated. To prevent this from occurring the standard MATLAB function '*scatteredInterpolant*' was used to calculate a continuous function, $Z(x, y)$, which described the surface of the implant. The *scatteredInterpolant* function uses 3D interpolation to calculate $Z(x, y)$ from the x, y, z coordinates. The function used interpolation and extrapolation methods, which could be chosen from several options. In this case the default natural neighbour interpolation was selected and there was no extrapolation to avoid the function creating data outside the scanned region and giving bogus results. The function, Z, is evaluated to determine the interpolated z-data for each position in the previously defined x-y domain. The volume, V, under the interpolated surface of the implant was then calculated using Equation 6.1.

$$V = \sum_{x_1}^{x_2} \sum_{y_1}^{y_2} Z(x, y) \Delta x \Delta y \qquad \textbf{Equation 6.1}$$

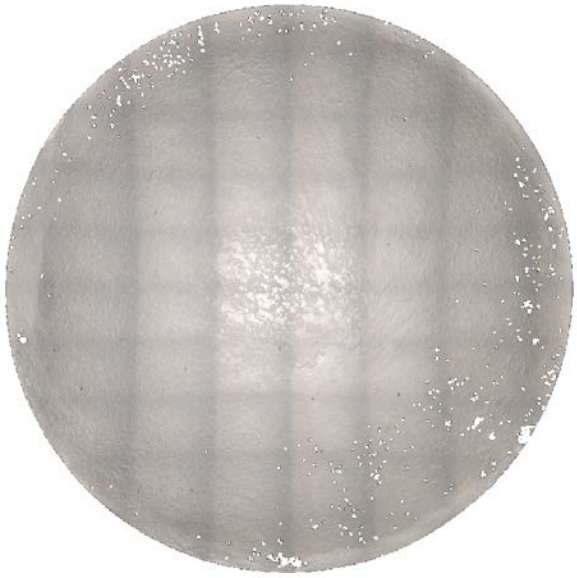

Figure 6.3: Example of void pixels on InfinteFocus scan image

6.2.5 Assessment of the Accuracy of the Optical Method

To assess the accuracy of the optical method a specimen sample, with a simple geometrical shape, was measured using both the InfiniteFocus and a micrometer. The specimen sample was an aluminium cylinder, nominally 5.5 mm in diameter and 1 mm in height, which was turned down from a cylinder with a larger diameter, see Figure 6.4. The height and diameter of the top of the cylinder were measured using a micrometer and the volume calculated, as shown in Table 6.1.

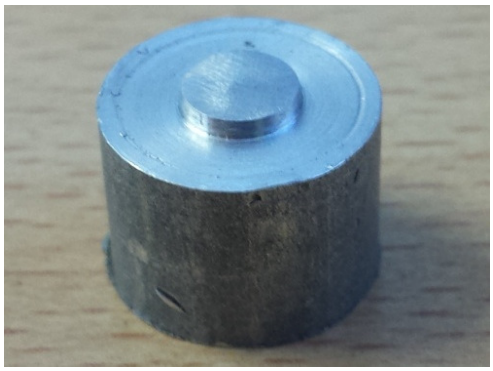

Figure 6.4: Aluminium sample specimen

Table 6.1: Specimen sample micrometer measurements

	Measurement				
Dimension	**1**	**2**	**3**	**Mean**	**Standard Deviation**
Diameter of cylinder (mm)	5.466	5.456	5.460	5.461	0.005
Height of cylinder (mm)	1.038	1.052	1.052	1.047	0.008
Volume (mm^3)	**24.357**	**24.595**	**24.6315**	**24.528**	**0.149**

The specimen sample was scanned three times using the InfiniteFocus at a magnification of 10×. A MATLAB program was written called *'FindVolume.m'*, which uses the *GenAliconaImport* function to calculate the volume of the cylinder. To calculate the volume of the specimen cylinder correctly the *z*-plane, or origin of the *z*-axis, must be located on the surface at the base of the cylinder, which will be referred to as the reference plane from now on. This was achieved by cropping the *x, y, z* data to remove the cylinder and obtain only the reference plane, finding the mean of the reference plane and then subtracting this mean from the *z*-coordinates of the specimen cylinder. Figure 6.5 shows a high level flowchart of the main processes carried out by the *FindVolume.m* script, see Appendix B.8 for the full code. The results are shown in Table 6.2.

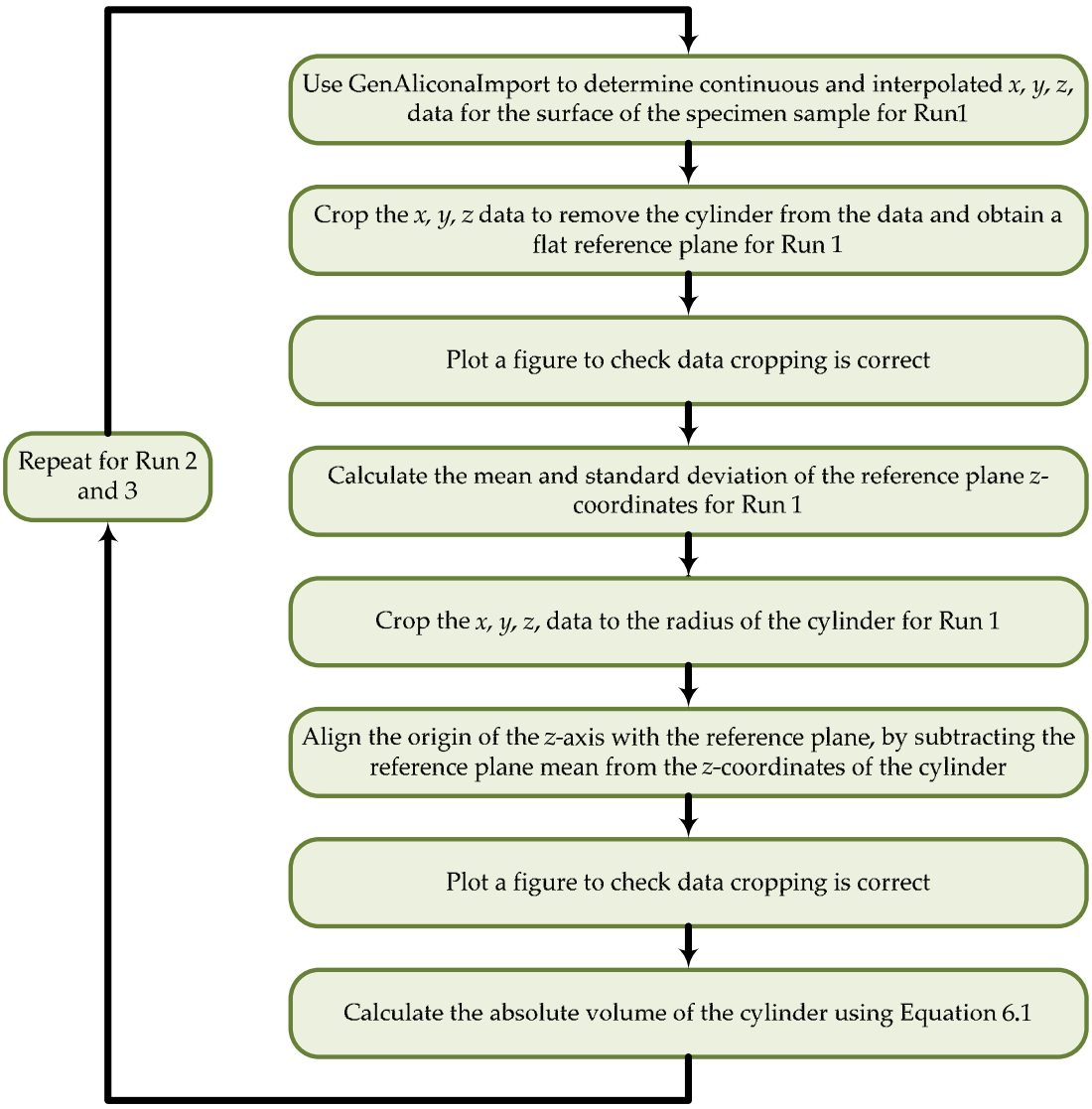

Figure 6.5: Flow chart showing the main processes in the MATLAB program *FindVolume.m*

Table 6.2: Specimen sample InfiniteFocus measurements

	Scan				
	Run 1	**Run 2**	**Run 3**	**Mean**	**Standard Deviation**
Volume (mm³)	23.875	24.294	24.335	24.209	0.254

The volume of the specimen was calculated to be 24.528 mm³ using the measurements taken with the micrometer in Table 6.1 and 24.209 mm³ when

measured using the optical method. The InfiniteFocus scans showed that the diameter of the cylinder was not constant due to manufacturing errors and the base of the cylinder had a smaller diameter than the top. This resulted in the micrometer measurements overestimating the volume of the specimen and it was presumed that the optical method was more accurate in calculating the volume. However, the standard deviation of the optical method was larger than the micrometer measurement which indicates the optical method was not as precise. The main source of error in the optical method was likely to be how the origin of the z-axis was determined and aligned with the reference plane. As explained in Section 6.2.1 the origin of the z-axis was particularly critical to the accuracy of volume calculation.

6.2.6 Trials to Improve the Precision of the Optical Method

A series of trials were carried out to assess how changes in the method for aligning the *z*-coordinates affected the precision of the optical method's volume calculation. For each trial an aspect of the code was altered and the effect on the precision of the volume calculation determined. As discussed in Chapter 5 mass balances capable of measuring the mass of an implant and its fixtures have a precision of 0.1 mg (Green et al., 2015). The density of the alumina used in these implants was 3.9 g/cm^3 so the precision of the gravimetric method equates to 0.0256 mm^3. Therefore, the goal of these trials is to see if it is possible to achieve a precision of 0.0256 mm^3 or less using the optical method.

The same three InfiniteFocus scans were used as in Section 6.2.5. Figure 6.6 shows a high level flowchart of the main processes carried out in the trial MATLAB scripts. The processes highlighted in blue are the part of the code on which the trials were carried out. The process in green remained the same throughout the trials.

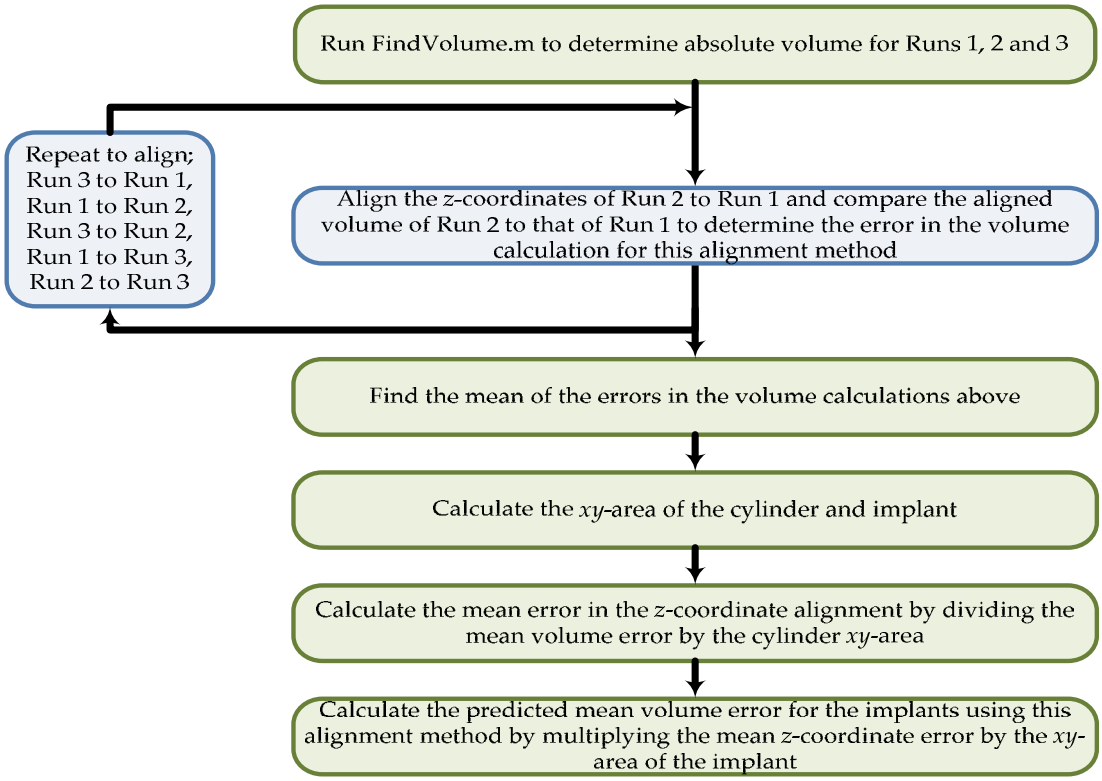

Figure 6.6: Flow chart showing the main processes of the MATLAB scripts used in the trials.

For all the trials the script *FindVolume.m* was used to determine the volumes of the cylinder from all three scans. For each trial a different method was used to align each scan to the other two scans, e.g. Runs 2 and 3 were aligned with Run 1, etc. The volumes of the newly aligned runs were then calculated and compared with that of the other run, e.g. aligned Runs 2 and 3 were compared with the volume of Run 1. If the alignment method had worked perfectly there would be no difference between the compared volumes. Therefore, the difference in volume between the aligned scan and the original scan gives an indication of the error in the alignment method. The mean difference in volume was divided by the xy area of the cylinder to find the mean error in the alignment method, Δz. This result was then used to predict the precision of the volume calculation for one of the implants by multiplying the xy area of the implant by Δz.

6.2.6.1 Trial 1

Trial 1 used the difference between the means of the reference planes to align the scans. Figure 6.7 shows the main processes and calculations for this alignment method. The full MATLAB script *Trial1.m* can be found in Appendix B.9. The result of this trial was a precision of 1.0276 mm^3, which is a long way from the target of 0.0256 mm^3.

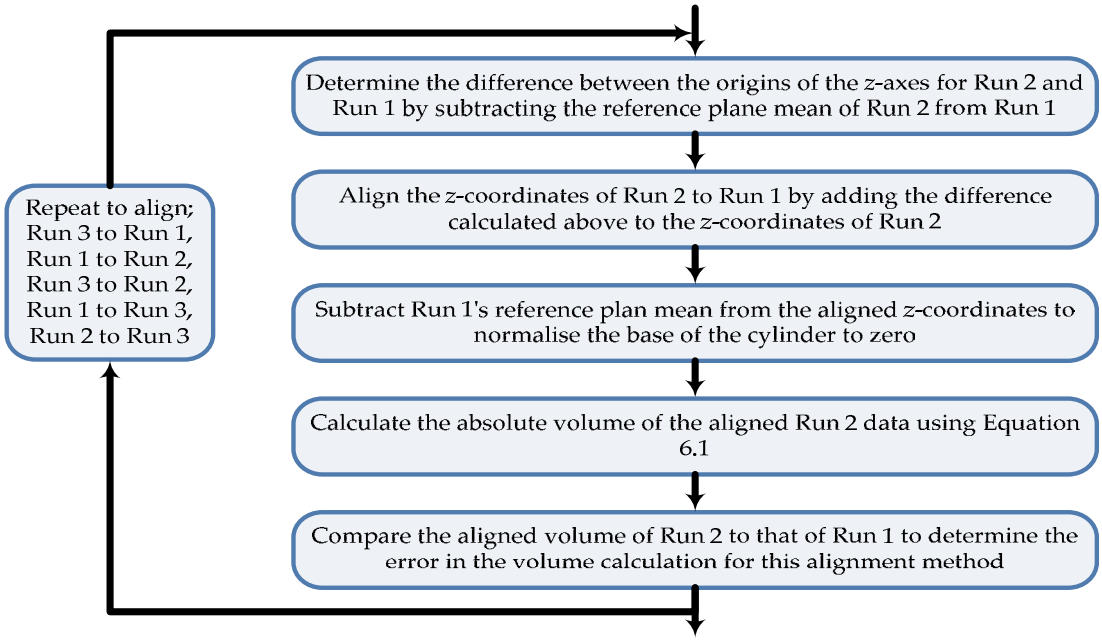

Figure 6.7: Flow chart showing the main processes in the MATLAB program *Trial1.m*

6.2.6.2 Trial 2

To significantly improve the precision of the volume calculation a different approach to the alignment method was required. Trial 2 investigated the use of the Iterative Closest Point (ICP) algorithm, which iteratively searches for the best alignment of two point clouds by minimising the mean squared error between the closest points in the two clouds. The MATLAB script *icp.m* was downloaded from the MATLAB File Exchange (Wilm and Kjer, 2013). The script returns the following: a translation and rotation matrix which minimises

the distance between the two point clouds, the root mean square of the errors for each iteration, and the calculation time for each iteration. The results of the ICP algorithm need to be sanity checked because it can become trapped in a local minimum and produce a nonsense answer. Figure 6.8 shows the main processes and calculations for this alignment method. The sections in red show the areas of the code which have been altered between trials. The full MATLAB script *Trial2.m* can be found in Appendix B.10. To try and keep calculation times reasonable a patch of data on the top of the cylinder was cropped to 2000 × 2000 μm, to produce the two point clouds to be aligned. To align the two scans together, the translation matrix calculated by the *icp.m* script was applied to the *z*-coordinates of the cylinder. The result of this trial was a precision of 0.0420 mm^3 which was considerably closer to the target of 0.0256 mm^3, but it still needed improvement.

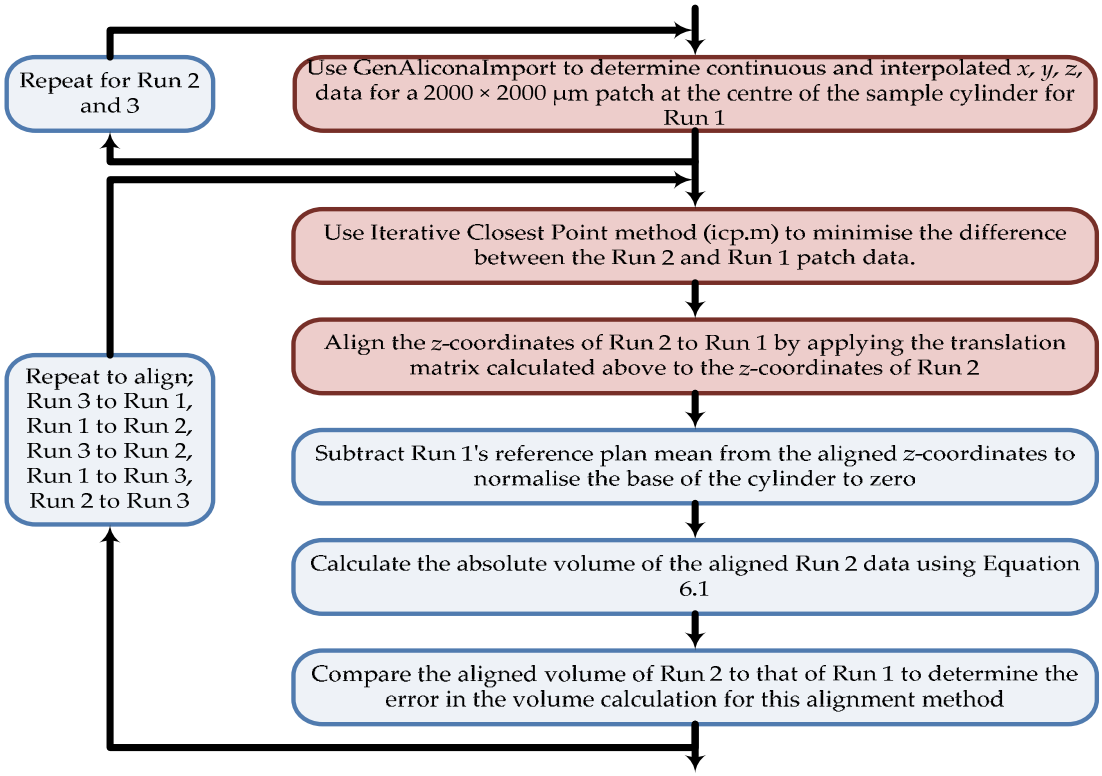

Figure 6.8: Flow chart showing the main processes in the MATLAB program *Trial2.m*

6.2.6.3 Trial 3

Trial 3 kept the changes made in Trial 2 because they had decreased the error in the volume calculations. During Trial 2 it was noted that *dx* and *dy* were not the same for each scan; they varied between 4.6681 μm and 7.0429 μm. This trial investigated if setting *dx* and *dy* to 4.6681 for all scans improved the precision of the volume calculations. The hypothesis behind this investigation was that if the distance between points in *x* and *y* was the same for both scans it might improve the speed and accuracy of the ICP calculation by reducing the distance between the closest points in the two point clouds. The variables *dx* and *dy* were set by altering lines 85 and 86 in *GenAliconaImport.m to:*

```
85.  dx= 4.6681;
86.  dy=4.6681;
```

Figure 6.9 shows the main processes and calculations for this alignment method. The result of this trial was a precision of 0.0420 mm^3 which was the same as Trial 2. The change had no significant effect and the method still required further refinement to reach the target of 0.0256 mm^3.

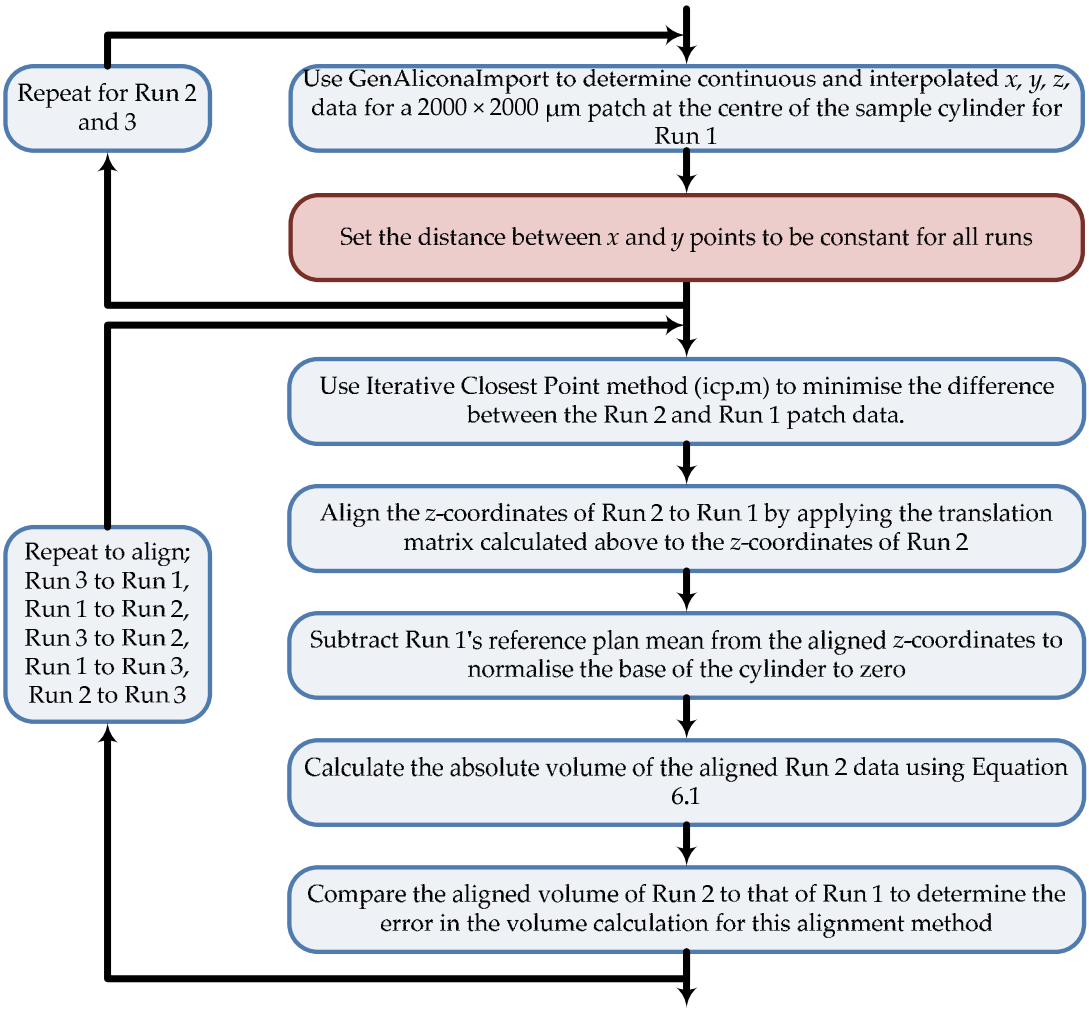

Figure 6.9: Flow chart showing the main processes in the MATLAB program *Trial3.m*

6.2.6.4 Trial 4

Trial 4 investigated if increasing the amount of data used to calculate the translation matrix improved the precision of the volume calculation. Instead of using a patch of data from the top of the cylinder, all the data from each scan was input into the ICP algorithm. In Trial 2 the patch contained 184,000 data points and on average the script took 2.5 minutes to execute. In this trial the number of data points was increased to 2,250,000 and the script took on average 177 minutes to execute. Figure 6.10 shows the main processes and calculations for this alignment method. The result of this trial was a precision of 0.0300 mm^3

which was an improvement on Trial 3 but the method still required further refinement to reach the target of 0.0256 mm^3.

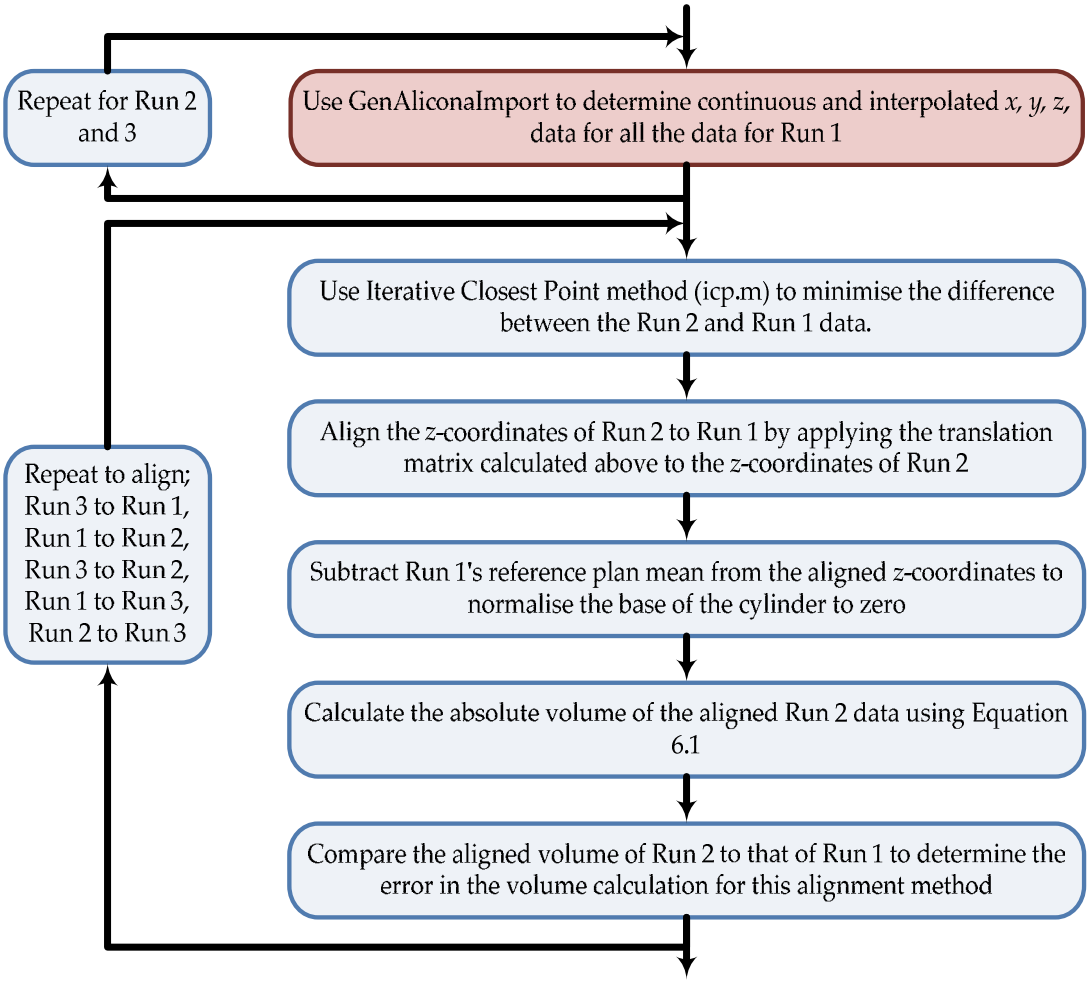

Figure 6.10: Flow chart showing the main processes in the MATLAB program *Trial4.m*

6.2.6.5 Trial 5

Trial 5 investigated if applying both the translation and rotation matrix to all of the *x*, *y*, *z* coordinates would increase the precision instead of applying just the translation matrix to the *z*-coordinates. Figure 6.11 shows the main processes and calculations for this alignment method. The full MATLAB script *Trial5.m* can be found in Appendix B.11. The result of this trial was a precision of 0.0170 mm^3 which was below the target of 0.0256 mm^3. Therefore, the use of this

alignment method for the optical method resulted in greater precision than the gravimetric method.

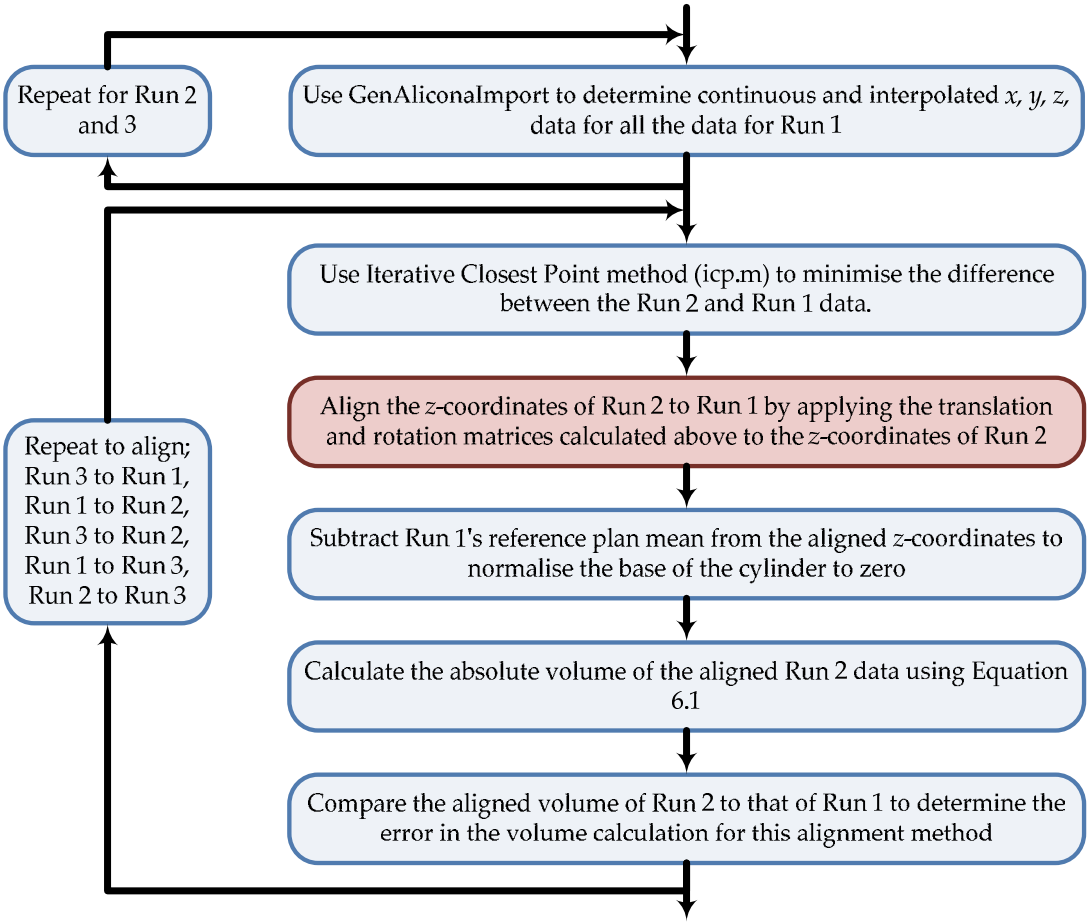

Figure 6.11: Flow chart showing the main processes in the MATLAB program *Trial5.m*

6.2.7 Implant Volume Calculations

The optical method was only carried out on Implant 2, because the chipping that occurred to Implant 1 during the wear tests, see Section 4.4, would have affected the accuracy of the calculations. A final code was developed to calculate the change in volume between the scan of the worn surface of the implant and the baseline scan for the unworn surface of the implant. The MATLAB script *UpperImplantVolCalc.m* was largely based on *Trial5.m* because the volume calculations had the highest precision. The following decisions on

the calculation method were made having learned from the trials carried out in Section 6.2.6.

A slightly different methodology was employed for the implant volume calculations. For the implant wear measurements it was important to know the change in volume between two sets of wear cycles rather than the absolute volume of the implant as calculated in the trials. Given the geometry of the upper implant in particular it would have been difficult to set the origin of the z-axis to the correct position to enable the absolute volume to be calculated with accuracy. Therefore, instead it was decided to focus on calculating the change in volume rather than the absolute volume. The new method aimed to align the coordinate system of the worn scan with the unworn scan and calculate the change in volume between the two.

Although Trial 3 showed no change to the precision of the volume calculation when setting *dx* and *dy* to be constant for all scans in *GenAliconaImport.m*, it was decided to keep this feature as it reduced calculation times.

Trial 4 showed that increasing the amount of data in the two point clouds compared by the Iterative Closest Point method improved the precision of the calculation. However, it was not possible to include all the data for two reasons. Firstly, to compare all the data in both scans would mean comparing the worn surface with the unworn surface which would lead to misalignment of the coordinate systems. Secondly, the time it took to calculate the translation and rotation matrices using *icp.m* was prohibitive. Therefore, the unworn surface of the implants from each scan was used as the reference surface and input into *icp.m*. The implant geometry meant that on the upper implant the edge between the articulating surface and the reference surface wore during the test. This area

therefore, had to be excluded from the reference surface for every scan to prevent misalignment.

There was considerable improvement in the volume calculation precision in Trial 5, therefore, both the translation and rotation matrices calculated by *icp.m* were used to align the worn and unworn implant scans.

The full MATLAB script which analyses the upper implant *UpperImplantVolCalc.m* can be found in Appendix B.12. The script which analyses the lower implant has only minor changes due to geometry and therefore, it is not reproduced in this thesis. Figure 6.12 shows the main processes and calculations for the final code.

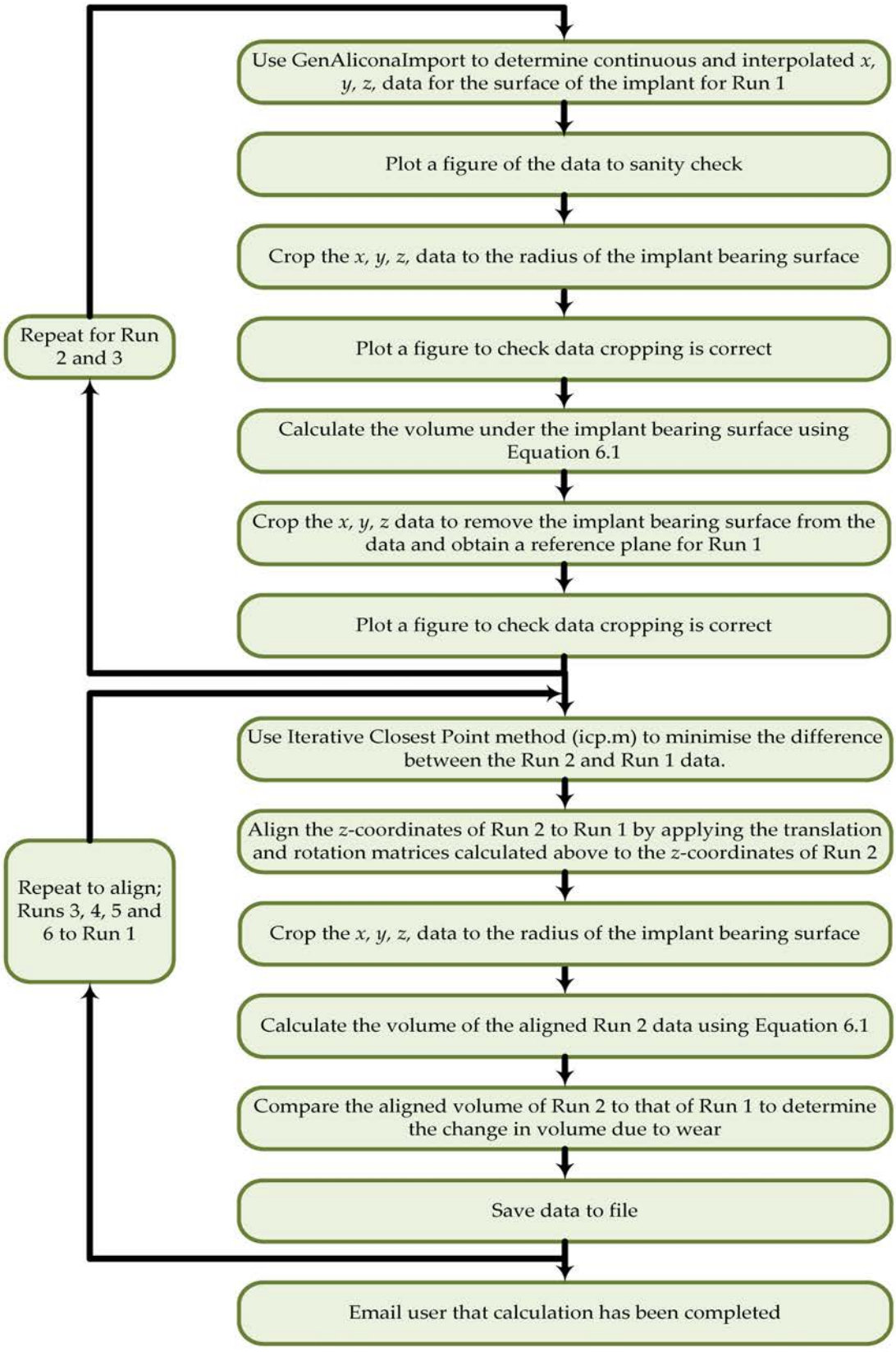

Figure 6.12: Flow chart showing the main processes in the MATLAB program *UpperImplantVolCalc.m*

6.2.8 Statistical Analysis

The statistical analysis of the results was conducted using Minitab version 17.2.1 (Minitab Ltd. Coventry, UK). The Bland-Altman method (Bland and Altman 1986; Bland and Altman 1999) was used to compare how well the gravimetric and optical measurement methods agree. Firstly, the results of one measurement method were plotted against the other, along with a line of equivalence. If the data points all lie on the line of equivalence there is perfect agreement between the methods. However, data points are frequently clustered around the line of equivalence and it can be hard to interpret the differences between methods using this plot. Therefore, the next step in the Bland-Altman method was to plot the difference between the measurement methods against the mean of each measurement. The mean, $\bar{x}$, and standard deviation, σ, of the difference were also calculated. If the differences were normally distributed then 95% of the differences will fall within the limits, $\bar{x} \mp 1.96\sigma$. Normal distribution was confirmed using an Anderson-Darling test. The limits are referred to as the upper limit of agreement (ULA) and the lower limit of agreement (LLA). The mean, standard deviation, ULA and LLA were then interpreted to compare the gravimetric and optical measurement methods.

6.3 Results

6.3.1 Surface Characterisation

Figure 6.13 shows the surface characterisation results for both Implant 1 and 2. The overall trend in both *Ra max* and *Rt max* was an initial decrease before rising again around 1.5 million cycles.

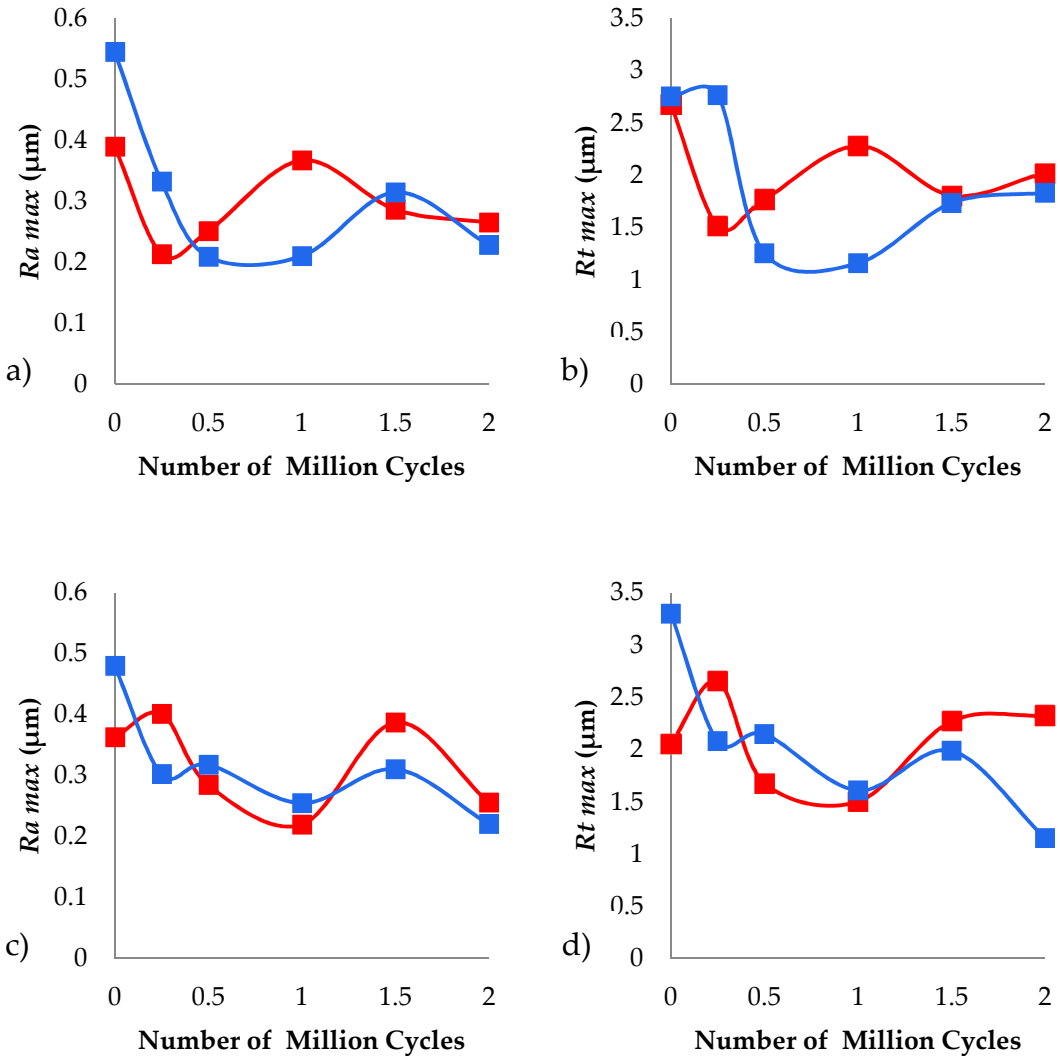

Figure 6.13: Change in surface roughness against the number of wear cycles; a) Implant 1, *Ra max*; b) Implant 1, *Rt max*; c) Implant 2, *Ra max*; d) Implant 2, *Rt max*. Lower Implant (—■—), Upper Implant (—■—)

6.3.2 Wear Images

The InfinteFocus scans produced clear images of the articulating surfaces of the implants. For example, Figure 6.14 shows the chipping which occurred on the edge of Lower Implant 1, as described in Section 4.4. The grid which can be seen across the articulating surface, was an artefact produced by stitching together multiple images into one scan. The grid only affected the colour of the scan and not the *x*, *y* and *z* data, which describes the surface topology.

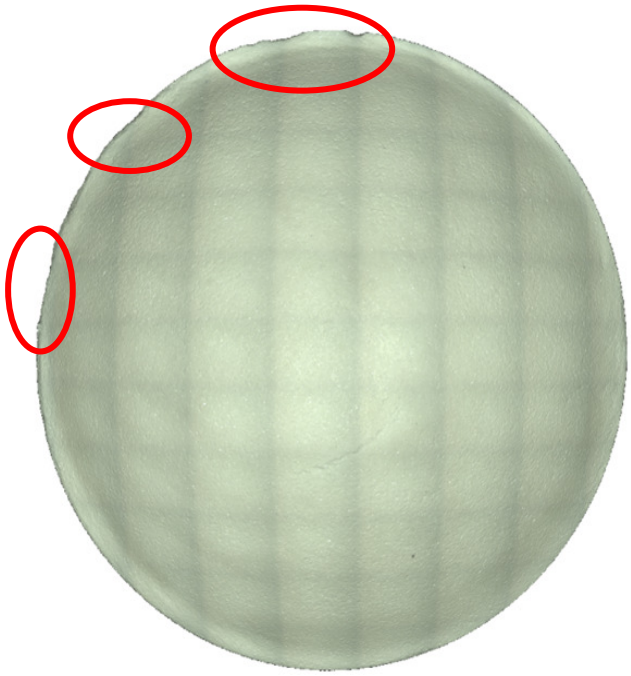

Figure 6.14: InfiniteFocus image of Lower implant 1, with red ellipses highlighting the chips on the implant edge

The form-removed images, where a perfect sphere has been subtracted from the surface to show areas of wear, also provided useful information about where the wear damage had occurred on the articulating surface of the implants. Figures 6.15 and 6.16 show that as the wear test progressed a raised lip formed around the edge of both Lower Implant 1 and 2. The images of the upper implants show that the wear was at its highest at the edge of the articulating surface; this was the opposite of the lower implants (Figures 6.17 and 6.18).

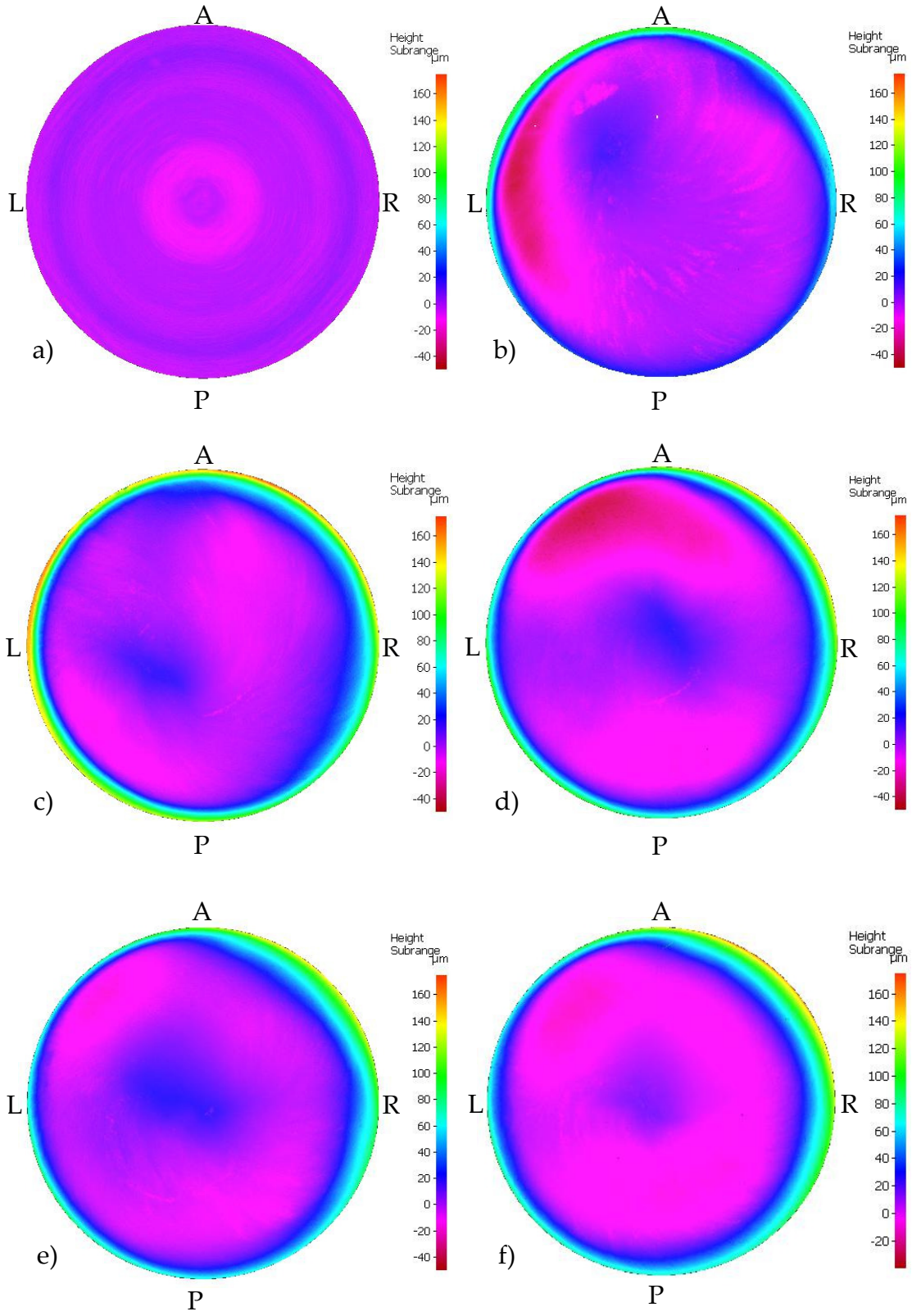

Figure 6.15: Lower Implant 1; a) Unworn surface; b) 0.25 million cycles; c) 0.5 million cycles; d) 1 million cycles; e) 1.5 million cycles; f) 2 million cycles. P=Posterior, A= Anterior, L= Left, R= Right

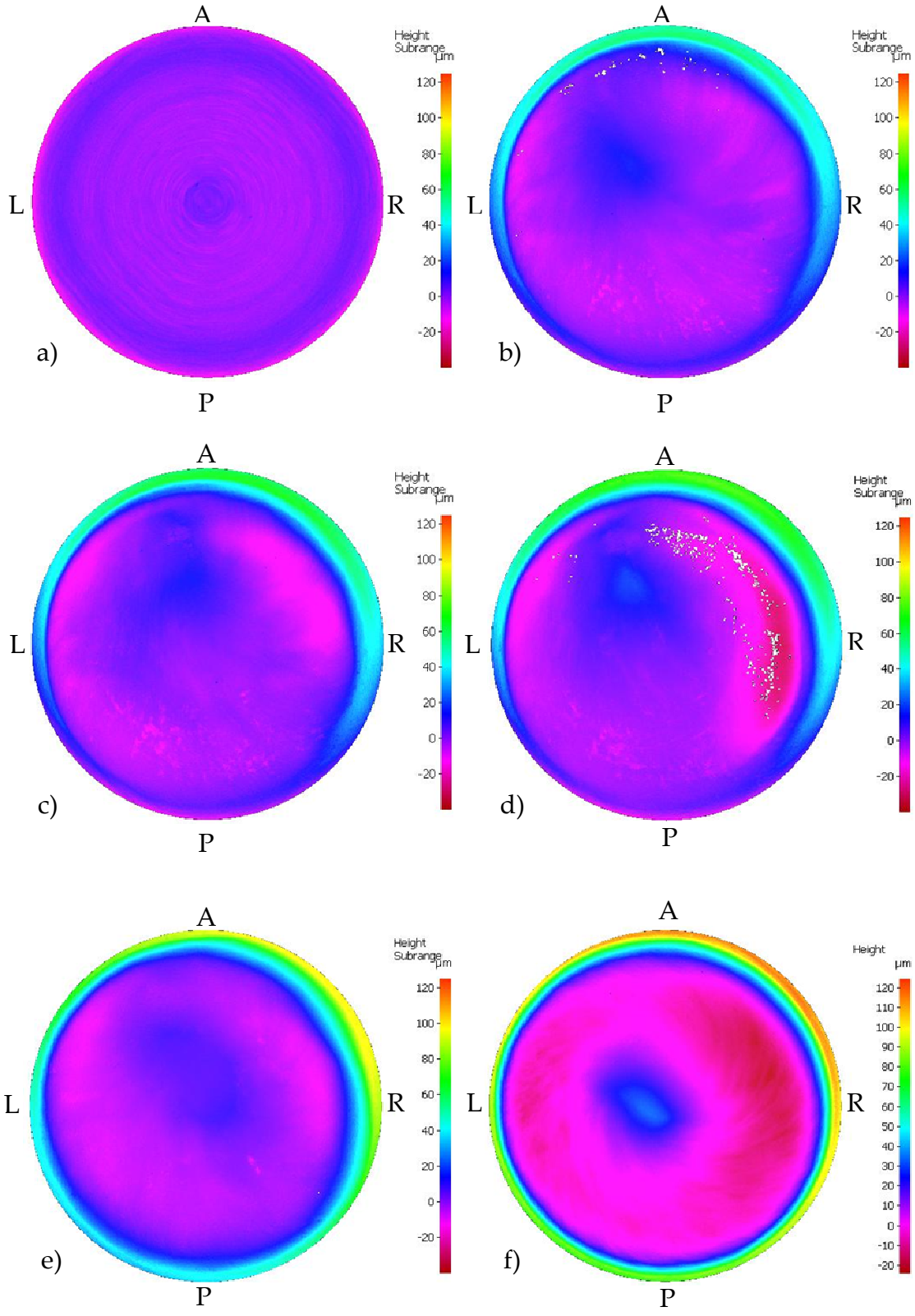

Figure 6.16: Lower Implant 2; a) Unworn surface; b) 0.25 million cycles; c) 0.5 million cycles; d) 1 million cycles; e) 1.5 million cycles; f) 2 million cycles. P=Posterior, A= Anterior, L= Left, R= Right

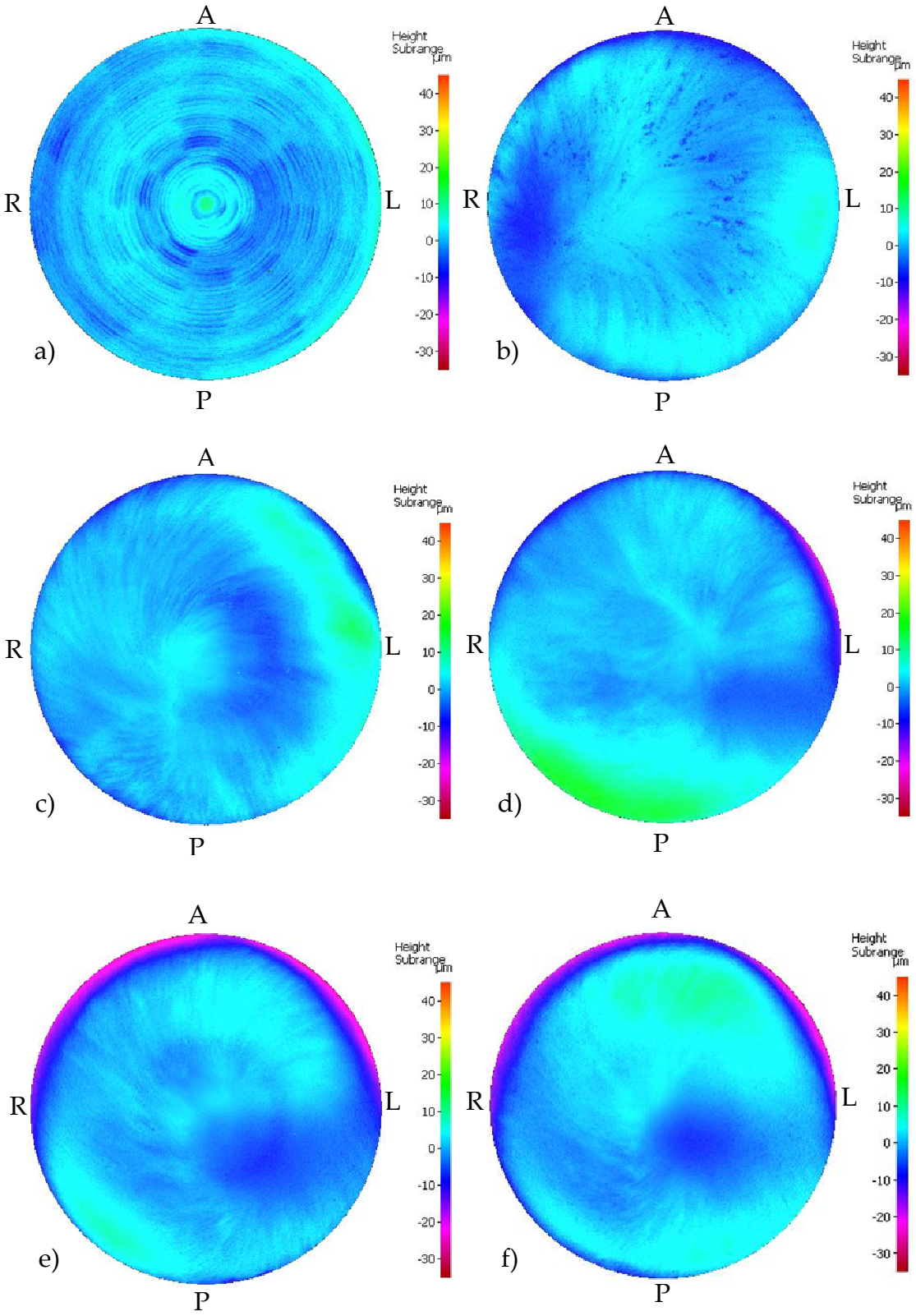

Figure 6.17: Upper Implant 1; a) Unworn surface; b) 0.25 million cycles; c) 0.5 million cycles; d) 1 million cycles; e) 1.5 million cycles; f) 2 million cycles. P=Posterior, A= Anterior, L= Left, R= Right

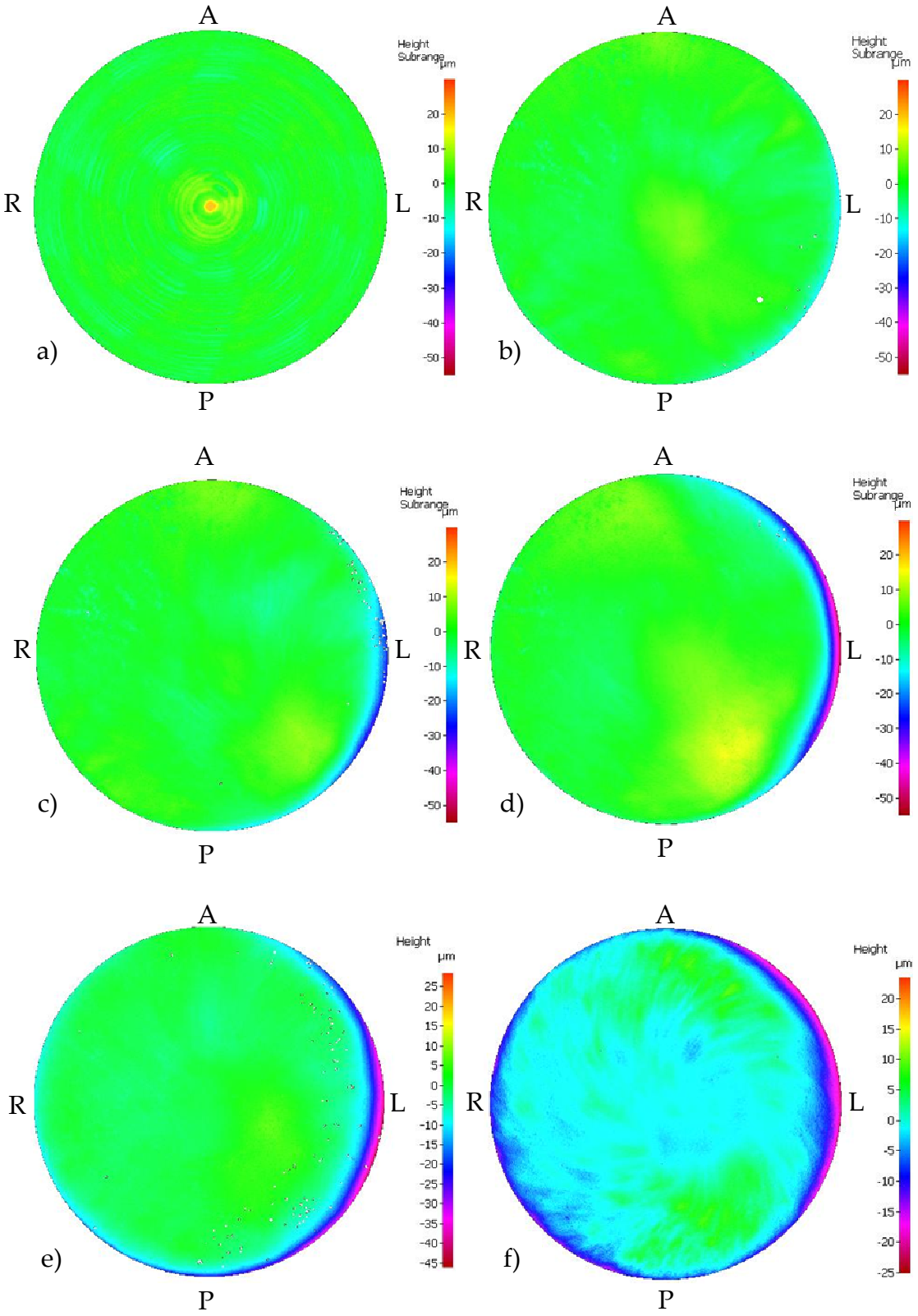

Figure 6.18: Upper Implant 2; a) Unworn surface; b) 0.25 million cycles; c) 0.5 million cycles; d) 1 million cycles; e) 1.5 million cycles; f) 2 million cycles. P=Posterior, A= Anterior, L= Left, R= Right

6.3.3 Optical Method Wear Volume Calculations

Table 6.3 shows the cumulative and delta change in volume of Lower and Upper Implant 2 as calculated by both the optical and gravimetric methods. The gravimetric result for Upper Implant 2 at 2 million cycles is not reported because the part came loose from its fixture and had to be reglued. This led to a change in mass and therefore, an inaccurate result.

Table 6.3: Comparison between gravimetric method and optical method for wear volume measurements; a) Lower Implant 2; b) Upper Implant 2

a)

Number of Wear Cycles (M Cycles)	Cumulative Volume Change (mm^3)		Delta Volume Change (mm^3)	
	Optical	Gravimetric	Optical	Gravimetric
0	0.0000	0.0000	N/A	N/A
0.25	2.2609	1.8120	2.2609	1.8120
0.5	2.6869	2.2094	0.426	0.3974
1	2.9328	2.9487	0.2459	0.7393
1.5	4.2891	4.6410	1.3563	1.6923
2	7.7817	7.3590	3.4926	2.7179

b)

Number of Wear Cycles (M Cycles)	Cumulative Volume Change (mm^3)		Delta Volume Change (mm^3)	
	Optical	Gravimetric	Optical	Gravimetric
0	0	0	N/A	N/A
0.25	1.5877	2.1838	1.5877	2.1838
0.5	1.7822	2.5513	0.1945	0.3675
1	2.2368	3.4444	0.4546	0.8932
1.5	3.2521	4.641	1.0153	1.1966
2	4.7513	N/A	1.4992	N/A

Table 6.4 shows the volumetric and gravimetric wear rates as measured by the optical and gravimetric methods, for Implant 2 and its lower and upper parts. The wear rates were calculated by linear regression analysis (Figures 4.11, 4.12, 6.19).

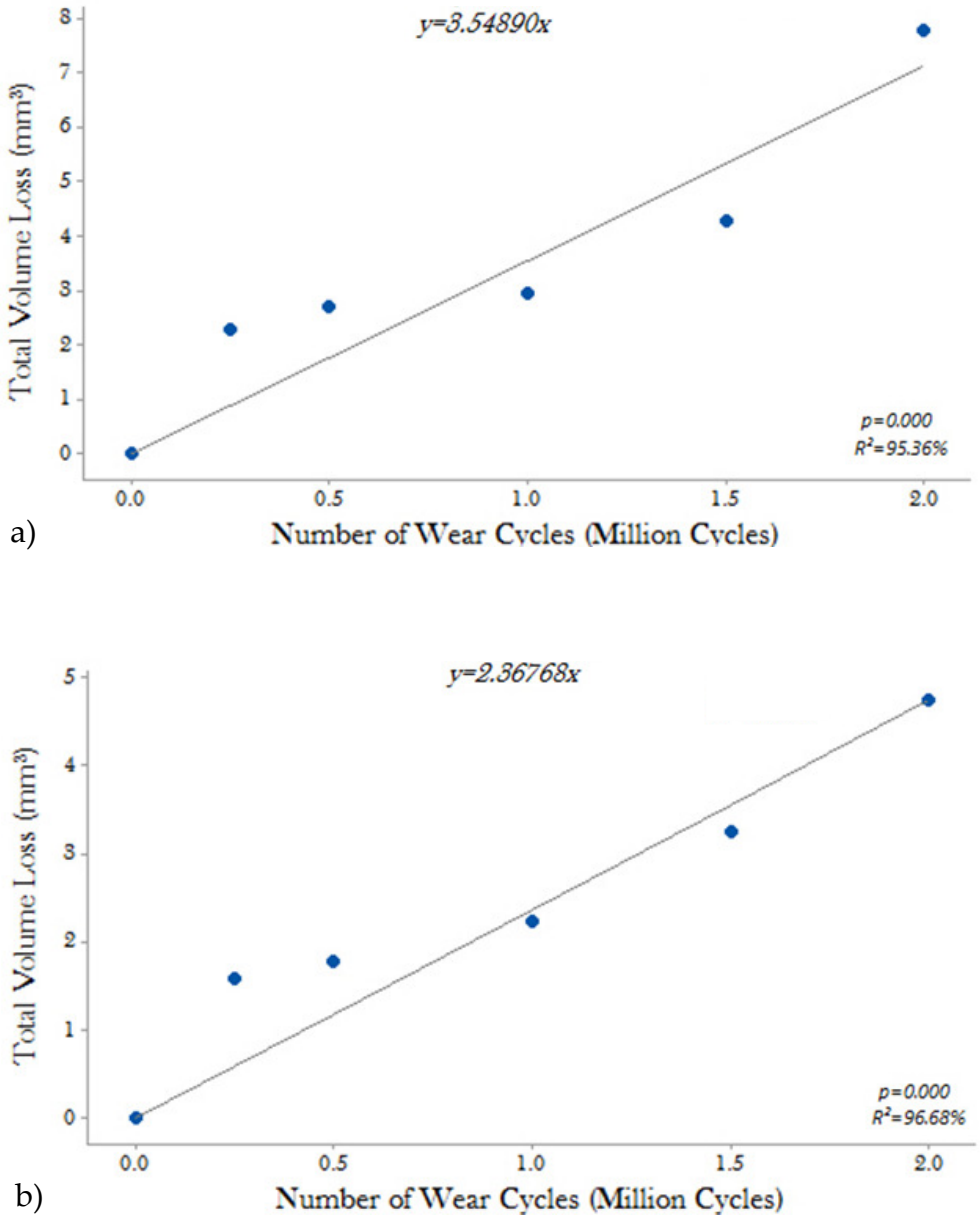

Figure 6.19: Wear of implants determined using the optical method; a) Lower Implant 2; b) Upper Implant 2

Table 6.4: Comparison of wear rates calculated using the optical and gravimetric method

	Optical Method		Gravimetric Method	
Part	**Volumetric Wear Rate (mm^3/M cycles)**	**Gravimetric Wear Rate (mg/M cycles)**	**Volumetric Wear Rate (mm^3/M cycles)**	**Gravimetric Wear Rate (mg/M cycles)**
Implant 2	6.7	26.0	6.6	25.9
Lower Implant 2	3.5	13.8	3.5	13.5
Upper Implant 2	2.4	9.2	3.4	13.4

6.3.4 Statistical Comparison of the Optical and Gravimetric Methods

The Anderson-Darling tests showed the differences were normally distributed for both Lower and Upper Implant 2, so the Bland-Altman method could be applied to assess the agreement between the optical and gravimetric methods. If the two methods are in agreement then 95% of the differences between measurements will lie within the upper and lower limits of agreement. As Figure 6.20 shows, all of the differences lie within the limits of agreement for both Lower and Upper Implant 2, so the two methods were in agreement. The mean difference between methods was - 0.1963 mm^3 and 0.9904 mm^3 for Lower Implant 2 and Upper Implant 2, respectively.

a)

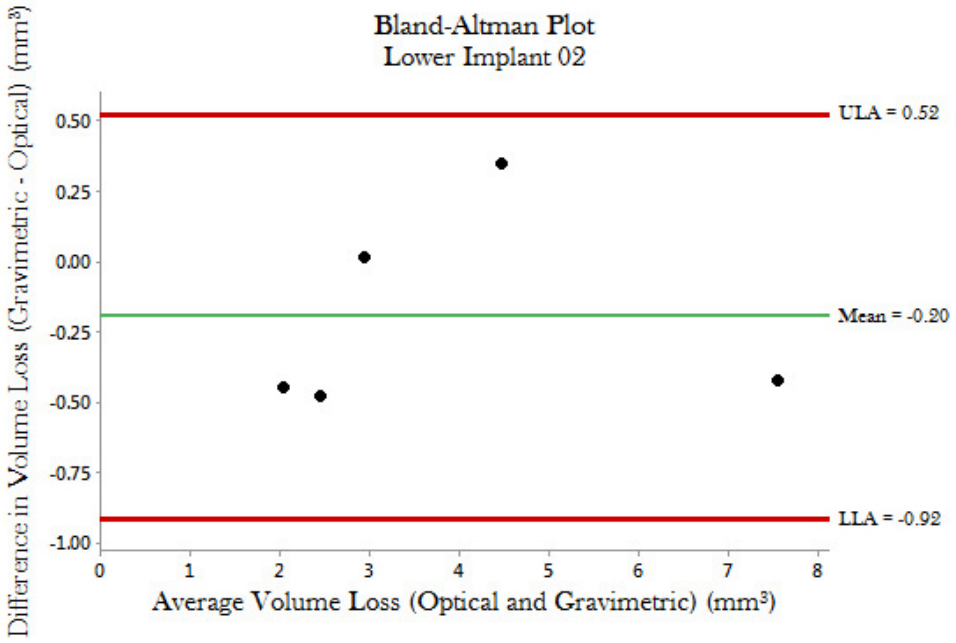

b)

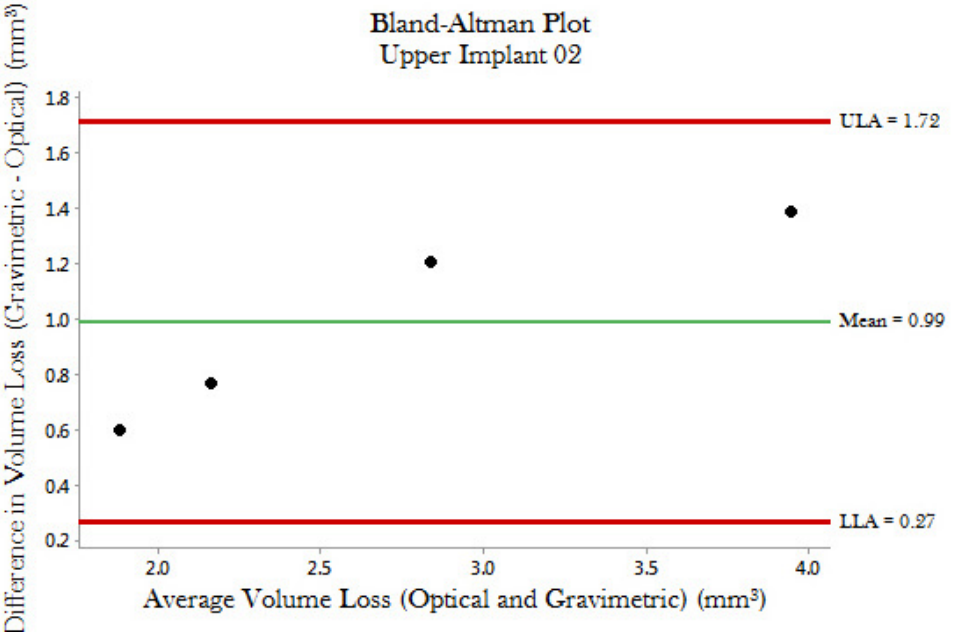

Figure 6.20: Bland-Altman Plot a) Lower Implant 2; Upper Implant 2

6.4 Discussion

The optical method has the advantage over the gravimetric method that in addition to calculating the wear volume, the location of the wear damage and the surface roughness can be determined. The other advantage is that all this

data is acquired through scanning with only one piece of equipment, the InfiniteFocus. Previous studies of orthopaedic implants have used multiple pieces of equipment, such as CMMs, Micro-CT, profilometers, and the gravimetric method to obtain this data (Blunt et al., 2008; Grupp et al., 2010; Maru et al., 2015, Moghadas et al., 2015).

The additional information provided by the optical method can provide a better understanding of the underlying wear mechanisms. For example, the surface characterisation of Implant 2 showed that despite an initial decrease, both the *Ra* and *Rt* values increased between 1 to 1.5 million wear cycles. The results in Table 6.3 indicated that at the same time the delta change in wear volume roughly doubled for both the lower and upper implants. At 1.5 million cycles the form-removed images also showed an increase in the depth and width of the raised lip around the edge of Lower Implant 2 (Figure 6.16). When all this evidence was combined it suggested that the alumina bearing underwent a wear transition at 1.5 million cycles.

Wear transitions describe when the wear mechanisms change and the wear rate increases from mild to severe wear (Hsu et al., 1989). When in the mild wear regime, micro-cracks propagate along grain boundaries. During the wear transition these grains begin to break away, creating wear debris and increasing the wear rate (Roy et al., 2007b). This grain pull-out leads to an increase in surface roughness. Therefore, measuring the surface roughness of the articulating surfaces can provide further understanding of the wear performance of the bearing materials.

The form removed images also provided useful information about the design of the implants. Lower Implant 1 experienced chipping around the edges of the implant, but the cause was unclear. Figures 6.15 and 6.16 showed that as the

wear tests progressed the centre of the lower articulating surfaces wore away, leaving behind raised lips. This is because the upper implants have a smaller diameter than the lower implant. Due to the design of the spine simulator it was difficult to precisely realign the upper and lower implants after each lubricant change and wear measurement. This was demonstrated in Figures 6.15 and 6.16 by the changing shape of the raised lip after each wear measurement. If the implant was perfectly aligned then the raised lip would be a constant thickness throughout the wear tests. The uneven wear on the edges of the upper implant was also evidence of this misalignment (Figures 6.17 and 6.18). On loading, this misalignment will have produced high stress concentrations in the lip and caused chipping. This demonstrates that when using brittle materials, it is important to consider during the design process how the surface topography will change due to wear, and if this will lead to stress concentrations.

It was explained in Chapter 5, that mass balances capable of measuring the mass of implants have a precision of 0.1 mg (Green et al., 2015), which is equivalent to a volume of 0.0256 mm^3 of alumina. It was shown in Section 6.2.6.5 that the precision of the volume calculations was 0.0170 mm^3. Therefore, the InfiniteFocus and optical method have a greater precision than the gravimetric method.

The Bland-Altman method showed that the optical and gravimetric methods were in agreement. However, the mean of the differences between the methods suggests the optical method underestimated the volume of the upper implant by 1 mm^3, and overestimated the lower implant volume by 0.2 mm^3. Both the optical and gravimetric methods calculated the wear rate of Lower Implant 2 to

be 3.5 mm^3/million cycles. However, as with the volume calculations, there was a 1 mm^3/million cycle difference between the two methods for Upper Implant 2.

Several studies of volumetric wear measurement of Total Hip Replacements have concluded that the misalignment of the coordinate systems for the worn and unworn surfaces plays a significant role in the accuracy of the results (Carmignato et al., 2011; Bills et al., 2012; Langton et al., 2014). Therefore, this difference in accuracy between the lower and upper implant volume calculations was likely due to the scan realignment method and the differing geometry of the parts. The lower implant had a flat surface, which was used as the reference plane to align the *z*-coordinates of the unworn and worn scans. Whereas, the upper implant reference surface had a diagonal slope around the articulating surface. The Iterative Closest Point algorithm, used in the MATLAB script *UpperImplantVolCalc.m,* aligned the flat surface more accurately because it was a less complex geometry than the three-dimensional slope of the upper implant. This could be easily improved on in future tests by designing the upper implant to have a similar flat surface to use as a reference surface.

A study which measured the volumetric wear of the Charité Total Disc Replacement using micro-CT, determined that the method had an accuracy of 3 mm^3 (Vicars et al., 2009). The accuracy of both the lower and upper implant volume calculations were a significant improvement on this. Studies measuring the volumetric wear of the articulating surfaces and taper junctions of Total Hip Replacements, using CMMs, had an accuracy of 0.5 mm^3 and 0.2 mm^3 respectively (Lord et al., 2011; Langton et al., 2012). The optical method presented in this chapter had a similar level of accuracy. Langton et al. (2014) have argued that volumetric wear measurement methods with an accuracy of 1 mm^3 are clinically relevant for metal-on-metal and metal-on-plastic implants,

and an accuracy of 0.5 mm^3 is suitable for ceramic-on-ceramic implants. The more accurate volume calculation for the lower implant, to within an average of 0.2 mm^3, was well within this guideline.

6.5 Summary

The aim of this chapter was to develop a novel method for measuring the volumetric wear of ceramic Total Disc Replacements using non-contacting optical microscopy. This new optical method has the advantage of being able to measure wear volume, surface roughness and the location of the wear damage, all in one scan. This additional data provided insights into the wear performance of the articulating surfaces, such as the wear mechanisms and transitions. The ability to visualise the location of the wear damage also provided information about how the design of the implant could be improved in the future.

It was demonstrated that the non-contacting optical microscopy can measure the wear volume of Total Disc Replacements to a higher precision than the gravimetric method. The accuracy of the method, although comparable to other studies and within clinically relevant guidelines, could be improved. This would be achieved by further developing the method of aligning the scans of the worn and unworn surface, as this is the biggest source of error in the calculation.

The next chapter contains the overall conclusions to this thesis and provides recommendations for further research.

Chapter 7

Overall Conclusions and Future Work

7.1 Overall Conclusions

The overall aim of this thesis was to investigate the use of ceramics in Total Disc Replacements and evaluate their tribological performance. This was achieved through the manufacture of alumina cervical Total Disc Replacements, which were then used for *in vitro* wear and friction tests. The results of these tests were used to conduct a tribological assessment of the articulating surfaces of the implants, including the frictional torques produced, the wear performance and the lubrication regime. Despite high wear rates, caused by chipping and a high surface roughness on the articulating surfaces, there were some issues with measuring the wear using the gravimetric method. Other studies have also had problems using the gravimetric method and they concluded that it has reached the limit of its resolution (Bills et al., 2005; Blunt et al., 2009, Williams et al., 2011). Therefore, the rest of the thesis was focused on developing and validating new methods for measuring volumetric wear using non-contacting optical microscopy.

Polishing operations can cost up to 10 - 15% of the total manufacturing cost (Jain, 2008). Therefore, the aim of the manufacturing study, in Chapter 3, was to explore whether the surface finish and dimensional tolerance specification, for the articulating surfaces of the ceramic implants, could be achieved using only grinding methods. Ultra-precision grinding techniques were used with a novel grinding tool, which had a D8-12 sized Hyperion grit. Unfortunately, the surface finishes of the articulating surfaces produced by the grinding tests did not meet the specification in ISO Standard BS ISO 7206-2:2011 (British Standards Institution, 2011b). However, the quality of the surface finish was similar to other freeform ceramic grinding studies (Yin and Huang, 2004; Denkena et al., 2008; Turger et al., 2013). The tests were much more successful

in meeting the specification for sphericity and dimensional tolerances. It was concluded, that even with further research into the grinding methods and tools, it is likely that a polishing process would still be necessary to meet the surface finish specification.

In Chapter 4 a tribological assessment of the alumina cervical Total Disc Replacements, produced in Chapter 3, was carried out. The results were compared with other Total Disc Replacements designs and materials. The frictional torques produced by the implants were of a similar magnitude to other Total Disc Replacements, but at the higher end of the scale (Moghadas et al., 2012a; 2012b; Xin, 2013). The Stribeck analysis showed that, like other Total Disc Replacements, the ceramic implants operated under a boundary lubrication regime (Moghadas et al., 2012a; Xin et al., 2013; Eckold, 2016).

However, the alumina implants produced wear rates which were an order of magnitude higher than other cervical Total Disc Replacements (Anderson et al., 2003; Nechtow et al, 2008; Xin et al., 2013; Hyde et al., 2016). This unexpected result was due to both the high surface roughness of the articulating surfaces produced in Chapter 3, and also chipping around the implant edge, due to the brittle nature of alumina. This highlights a major issue with the use of brittle ceramics in Total Disc Replacements, and the need to be mindful of this in their design.

A preliminary study into the use of non-contacting optical microscopy to measure low wear rates was carried out in Chapter 5. White light interferometry was used to scan the worn surface of alumina samples after ball-on-disc wear tests. The optical technique could measure low wear volumes (<0.0001 mm^3/ 0.0001 mg), which would not have been identifiable using the gravimetric method specified by the ISO standard for the wear testing of Total

Disc Replacements (British Standards Institute, 2011a). The optical method also identified the formation of a tribofilm over the bearing surface (Adachi and Kato, 2000), which would not have been found using the gravimetric method. However, users need to be aware of the effect the magnification of the lens can have on the reliability of the measurements.

In Chapter 6 the optical method was developed further and used to calculate the volumetric wear loss of the alumina Total Disc Replacements wear tested in Chapter 4. The method used a focus variation microscope to scan the worn articulating surfaces of the implants. A custom MATLAB code was written which compared the volume under the worn surface with that of the unworn surface to find the change in volume and, therefore, the volumetric wear rate. The results from the optical method were compared with those from the gravimetric method. It was found that the optical method can measure the wear volume of Total Disc Replacements to a higher precision than the gravimetric method (Green et al., 2015). The accuracy of the method is comparable to other studies and within clinically relevant guidelines, but could be improved (Lord et al., 2011; Langton et al., 2012; 2014).

The new optical method has the advantage that with one scan the user can measure changes in surface topography, volumetric wear and the location of the wear on the implant surface. This additional data gave insights into the tribological performance of the ceramic articulating surfaces, such as the wear mechanisms and transitions. The ability to visualise the location of the wear damage also provided information about how the design of the implant could be improved in the future.

7.2 Future Work

The main issue with the ceramic Total Disc Replacements manufactured using grinding processes in Chapter 3 was that the surface roughness specification was not achieved. Further testing needs to be done to better understand how the toolpath and stepover parameters can be varied to improve the surface finish of the articulating surfaces. The use of a ball nose grinding tool on a three-dimensional part causes a variation in scallop height across the surface and therefore, a variation in the surface roughness. This can be minimised using constant scallop height tool path generation methods which vary the stepover between adjacent toolpaths to maintain a constant scallop height. This appears to be a promising route for any future tests in this area. Another factor in the poor surface finish of the Total Disc Replacements was the reliability of the novel D8-12 tool. Further development needs to be done to improve the bond of the Hyperion grit to the tool, which will improve its longevity and reliability. Future work should look at how best to use the improved D8-12, in terms of grinding parameters, in order to produce a lower surface roughness than the tests in this thesis. However, given the results so far it is unlikely the use of the D8-12 tool alone will be able to produce the specified surface roughness and a polishing process will be required. The D8-12 is still worth developing in the future because it can be used in pre-finishing processes, which would reduce the time and cost involved in polishing.

Further studies into the tribological performance of alumina Total Disc Replacements need to be conducted, similar to those conducted in Chapter 4. These tests were not a fair representation of how ceramic implants could perform in terms of wear rate, because the surface finish of the articulating surfaces was well above the specification. Once the manufacturing process has

been refined, as described above, to produce ceramic Total Disc Replacements with the required surface roughness specification the tests should be repeated. It would also be beneficial if more samples were tested as well as increasing the number of wear cycles, which would improve our understanding of their wear performance. It would also be interesting to test samples manufactured from zirconia toughened alumina, in particular the market leader BIOLOX delta (CeramTec, Germany) if permission could be obtained. This material has been very successfully used in Total Hip Replacements and it would be useful to understand its wear performance in Total Disc Replacement and compare it with alumina.

Chapters 5 and 6 demonstrated that non-contacting optical microscopy can measure the wear volume of Total Disc Replacements to a higher precision than the gravimetric method. However, the precision of the method could be increased by improving the method for aligning the scans of the unworn and worn implants, because this is the largest source of error in the calculation (Carmignato et al., 2011; Bills et al., 2012; Langton et al., 2014). The method also needs to be used more extensively to validate its accuracy and precision. Any further wear tests on ceramic Total Disc Replacements, as described above, should use the optical method, alongside the gravimetric method, to provide more data. Also in terms of future work the optical method is not just limited to ceramic Total Disc Replacements and low levels of wear, but could be applied to more severe wear, and other orthopaedic implants made from any material. The method could also be further developed for use in measuring wear in explanted implants, which cannot be measured gravimetrically (Blunt et al., 2009; Carmignato et al., 2011; Sagbas and Durakbasa, 2012).

7.3 Summary

The overall conclusions of this thesis are:

- Ultra-precision grinding methods for manufacturing ceramic implants could not produce the specified surface finish for the articulating surface, and a polishing process was still needed. However, they would be helpful in reducing the time and cost associated with polishing.
- The alumina-on-alumina Total Disc Replacements produced high wear rates, due to chipping and the poor surface finish of the articulating surfaces.
- Non-contacting optical microscopy had several advantages over the traditional gravimetric method, including better measurement precision and the ability to visualise the location of the wear damage.

Appendix A

Engineering Drawings

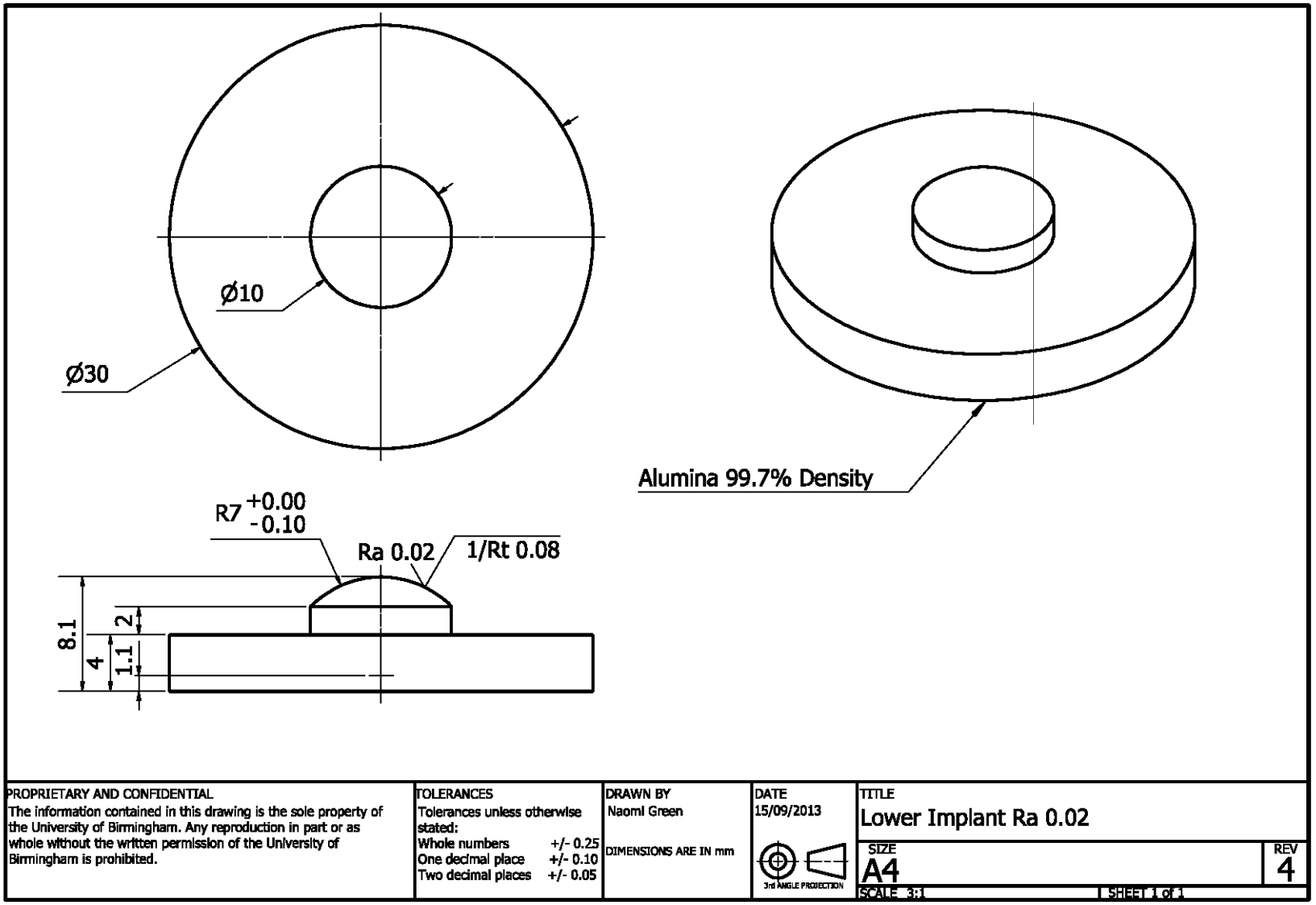

PROPRIETARY AND CONFIDENTIAL The information contained in this drawing is the sole property of the University of Birmingham. Any reproduction in part or as whole without the written permission of the University of Birmingham is prohibited.	TOLERANCES Tolerances unless otherwise stated: Whole numbers +/- 0.25 One decimal place +/- 0.10 Two decimal places +/- 0.05	DRAWN BY Naomi Green DIMENSIONS ARE IN mm	DATE 15/09/2013 3rd ANGLE PROJECTION	TITLE Lower Implant Ra 0.02 SIZE A4 REV 4 SCALE 3:1 SHEET 1 of 1

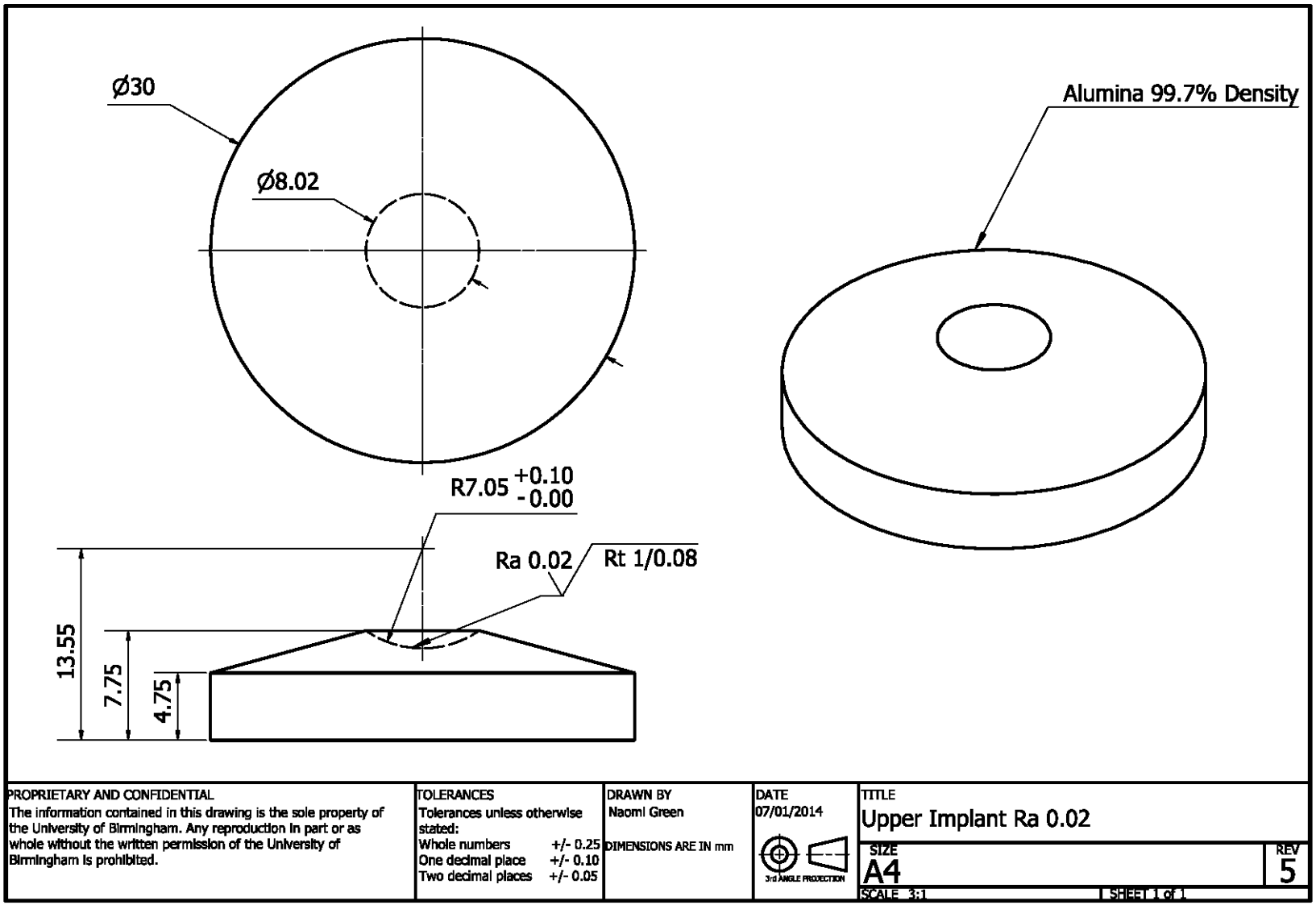

PROPRIETARY AND CONFIDENTIAL The information contained in this drawing is the sole property of the University of Birmingham. Any reproduction in part or as whole without the written permission of the University of Birmingham is prohibited.	TOLERANCES Tolerances unless otherwise stated: Whole numbers +/- 0.25 One decimal place +/- 0.10 Two decimal places +/- 0.05	DRAWN BY Naomi Green DIMENSIONS ARE IN mm	DATE 07/01/2014 3rd ANGLE PROJECTION	TITLE Upper Implant Ra 0.02 SIZE A4 REV 5 SCALE 3:1 SHEET 1 of 1

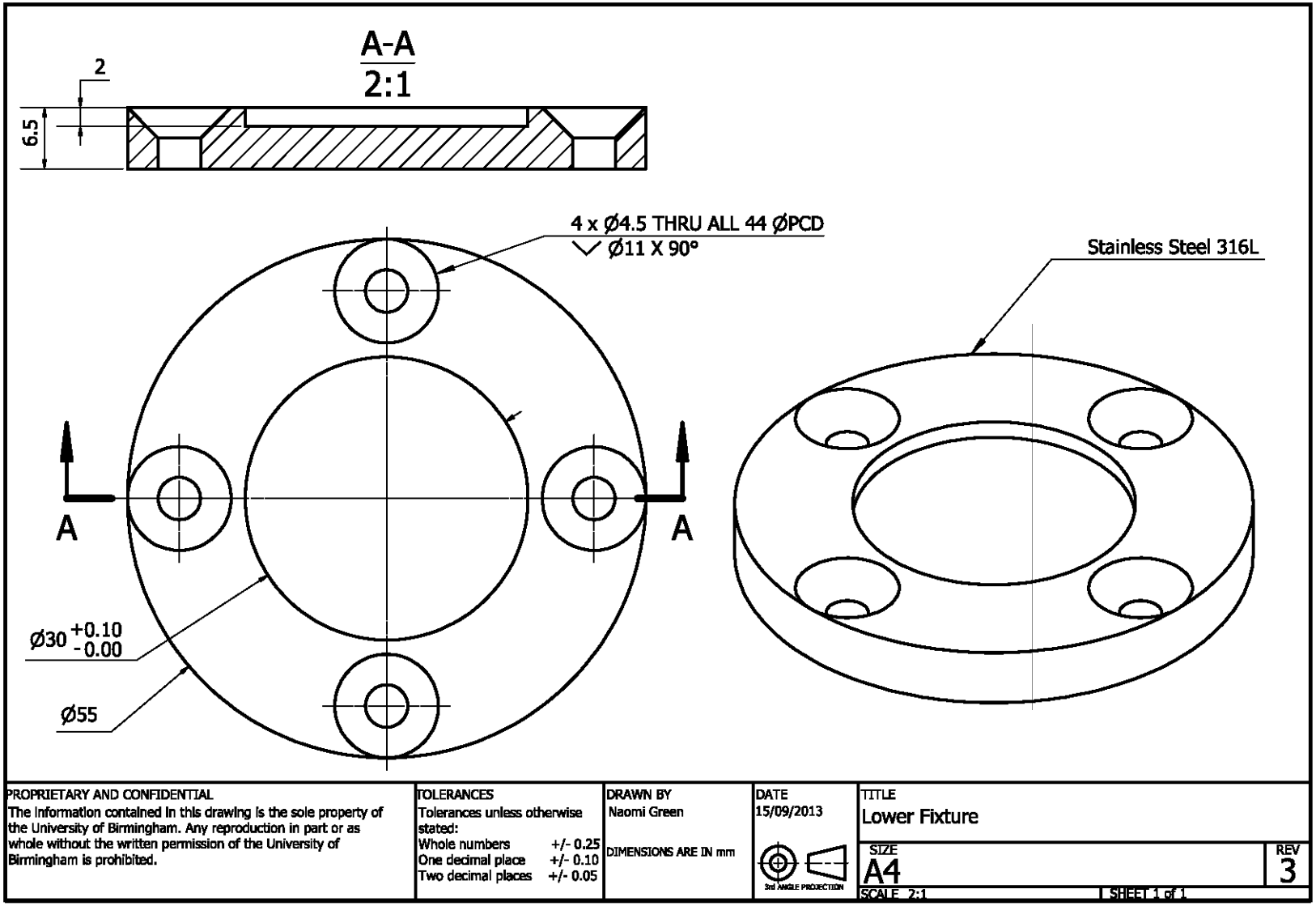
A-A
2:1
2
6.5
4 x Ø4.5 THRU ALL 44 ØPCD
Ø11 X 90°
Stainless Steel 316L
A
A
Ø30 +0.10 -0.00
Ø55
PROPRIETARY AND CONFIDENTIAL
The information contained in this drawing is the sole property of the University of Birmingham. Any reproduction in part or as whole without the written permission of the University of Birmingham is prohibited.
TOLERANCES
Tolerances unless otherwise stated:
Whole numbers +/- 0.25
One decimal place +/- 0.10
Two decimal places +/- 0.05
DRAWN BY
Naomi Green
DIMENSIONS ARE IN mm
DATE
15/09/2013
3rd ANGLE PROJECTION
TITLE
Lower Fixture
SIZE
A4
REV
3
SCALE 2:1
SHEET 1 of 1

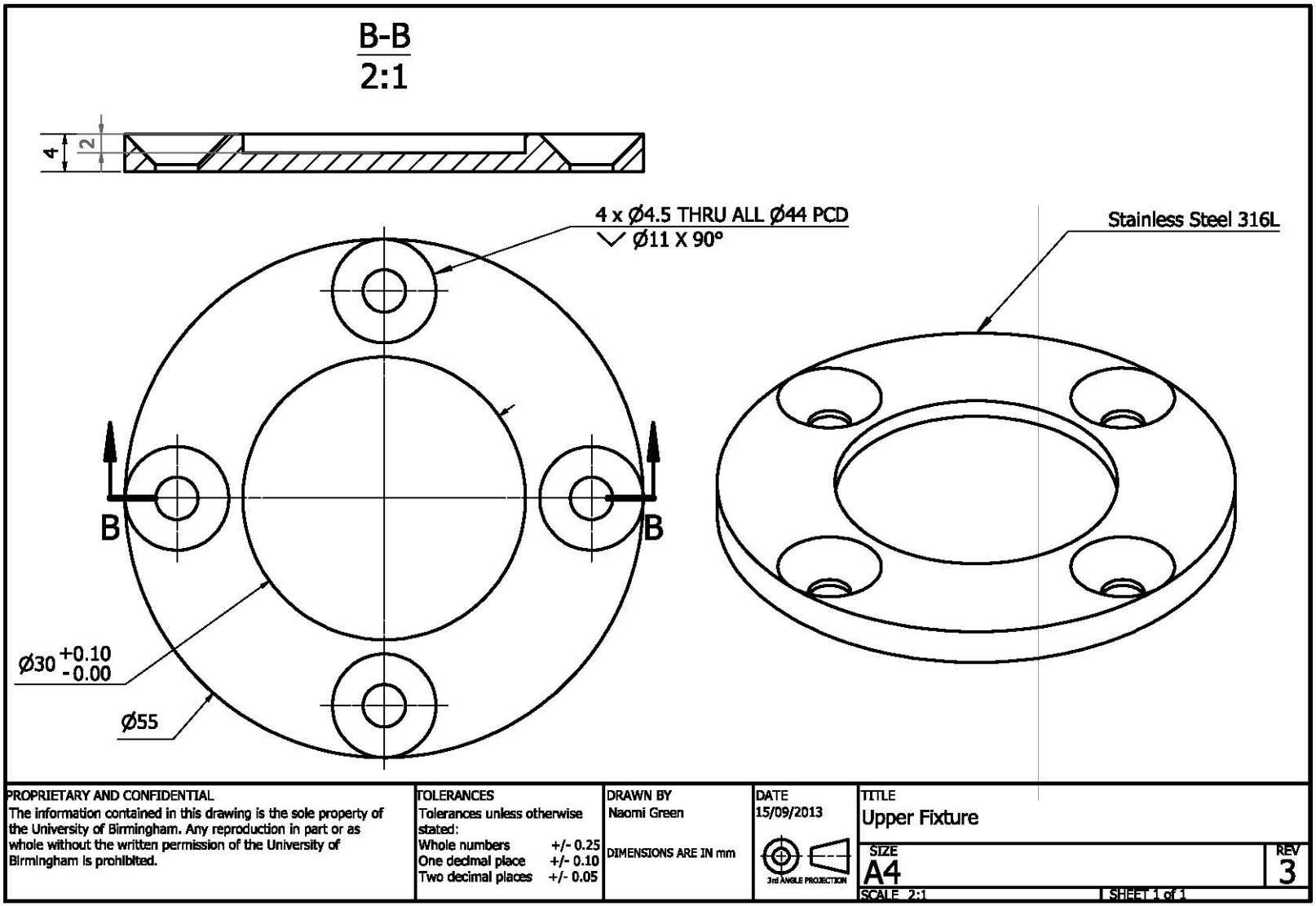
B-B
2:1
4
2
4 x Ø4.5 THRU ALL Ø44 PCD
Ø11 X 90°
Stainless Steel 316L
B
B
Ø30 +0.10 -0.00
Ø55
PROPRIETARY AND CONFIDENTIAL
The information contained in this drawing is the sole property of the University of Birmingham. Any reproduction in part or as whole without the written permission of the University of Birmingham is prohibited.
TOLERANCES
Tolerances unless otherwise stated:
Whole numbers +/- 0.25
One decimal place +/- 0.10
Two decimal places +/- 0.05
DRAWN BY
Naomi Green
DIMENSIONS ARE IN mm
DATE
15/09/2013
3rd ANGLE PROJECTION
TITLE
Upper Fixture
SIZE
A4
REV
3
SCALE 2:1
SHEET 1 of 1

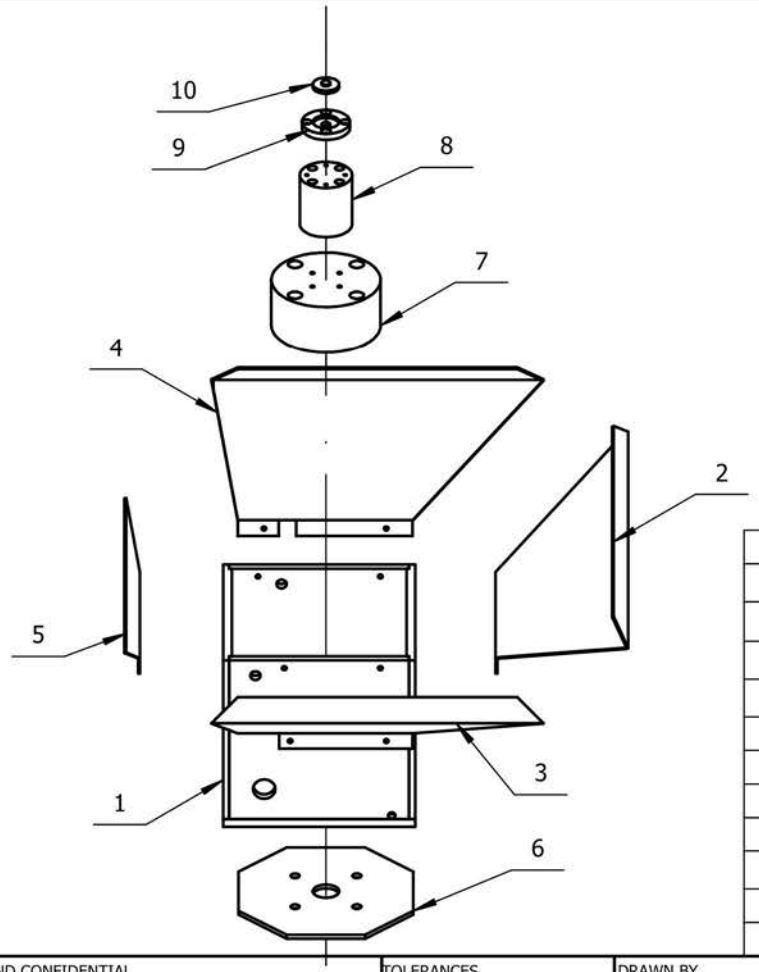

ITEM	Name	QTY	MATERIAL
10	Lower Implant	1	Ceramic
9	Lower Fixture	1	Stainless Steel
8	Elevation Fixture	1	Stainless Steel
7	Pallet Fixture	1	Stainless Steel
6	Gasket	1	Sheet Rubber
5	Splash Collector D	1	Sheet Steel
4	Splash Collector C	1	Sheet Steel
3	Splash Collector B	1	Sheet Steel
2	Splash Collector A	1	Sheet Steel
1	Container Assembly	1	Perspex

PARTS LIST

TOLERANCES
Tolerances unless otherwise stated:
Whole numbers +/- 0.25
One decimal place +/- 0.10
Two decimal places +/- 0.05

DRAWN BY
Naomi Green

DIMENSIONS ARE IN MM

DATE
02/10/2013

TITLE
Coolant System Assembly

SIZE
A4

REV
2

SCALE 0.15:1

SHEET 1 of 1

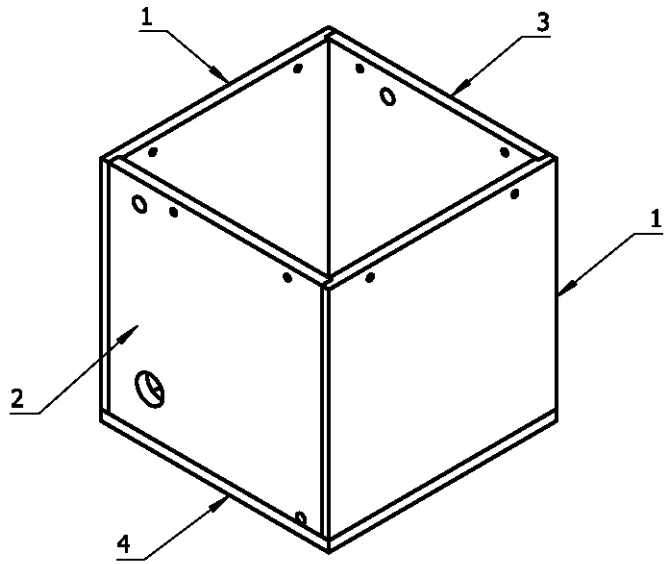

ITEM	Name	QTY	Material
1	Container Part A	2	Perspex
2	Container Part B	1	Perspex
3	Container Part C	1	Perspex
4	Container Part D	1	Perspex

PARTS LIST

TOLERANCES
Tolerances unless otherwise stated:
Whole numbers +/- 0.25
One decimal place +/- 0.10
Two decimal places +/- 0.05

DRAWN BY
Naomi Green

DIMENSIONS ARE IN MM

DATE
19/09/2013

TITLE
Container Assembly

SIZE
A4

REV
1

SCALE 1:4

SHEET 1 of 1

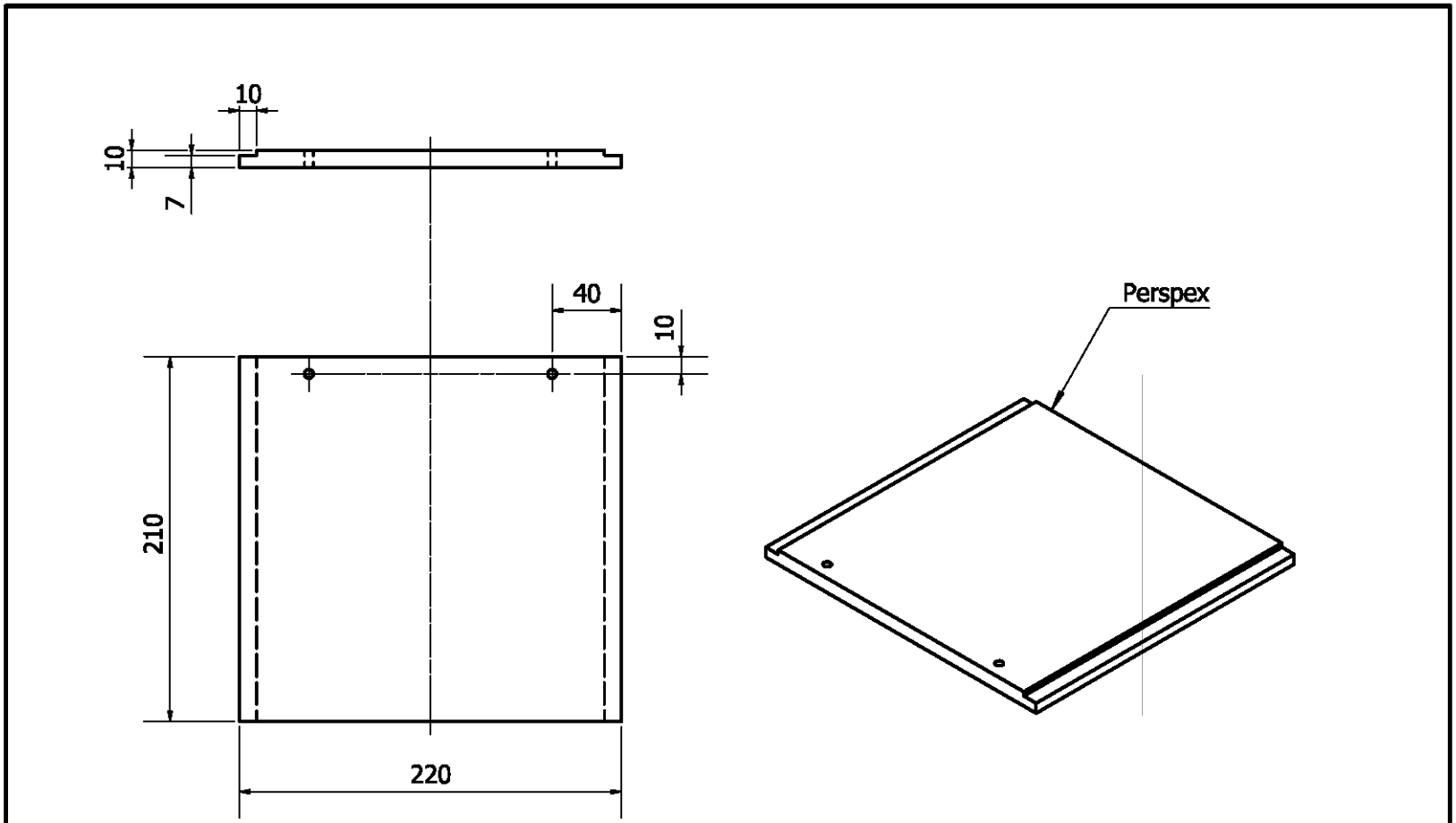

PROPRIETARY AND CONFIDENTIAL The information contained in this drawing is the sole property of the University of Birmingham. Any reproduction in part or as whole without the written permission of the University of Birmingham is prohibited.	TOLERANCES Tolerances unless otherwise stated: Whole numbers +/- 0.25 One decimal place +/- 0.10 Two decimal places +/- 0.05	DRAWN BY Naomi Green DIMENSIONS ARE IN mm	DATE 15/09/2013 3rd ANGLE PROJECTION	TITLE Container Part A SIZE A4 REV 1 SCALE 1:3 SHEET 1 of 1

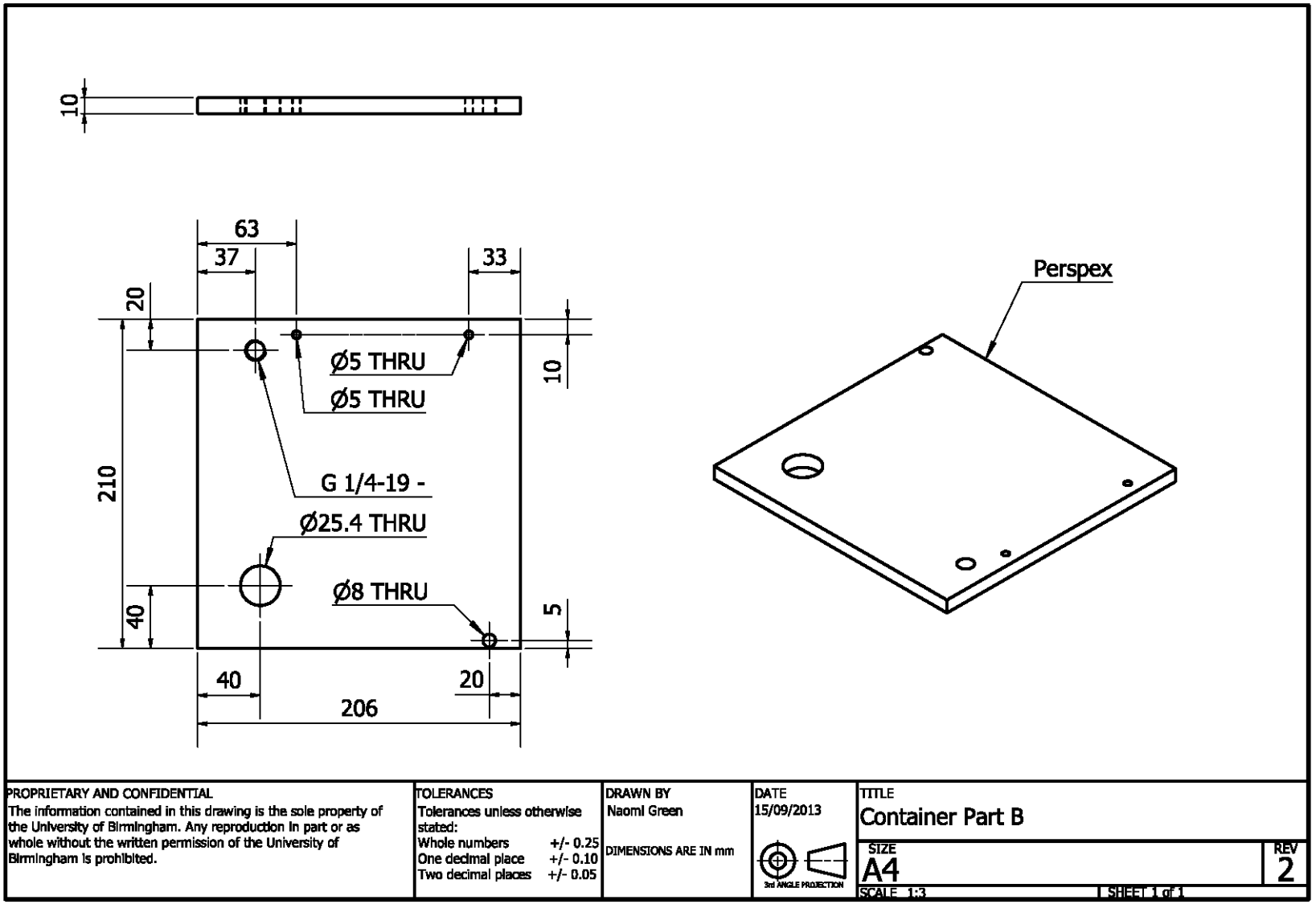

PROPRIETARY AND CONFIDENTIAL The information contained in this drawing is the sole property of the University of Birmingham. Any reproduction in part or as whole without the written permission of the University of Birmingham is prohibited.	TOLERANCES Tolerances unless otherwise stated: Whole numbers +/- 0.25 One decimal place +/- 0.10 Two decimal places +/- 0.05	DRAWN BY Naomi Green DIMENSIONS ARE IN mm	DATE 15/09/2013 3rd ANGLE PROJECTION	TITLE Container Part B SIZE A4 REV 2 SCALE 1:3 SHEET 1 of 1

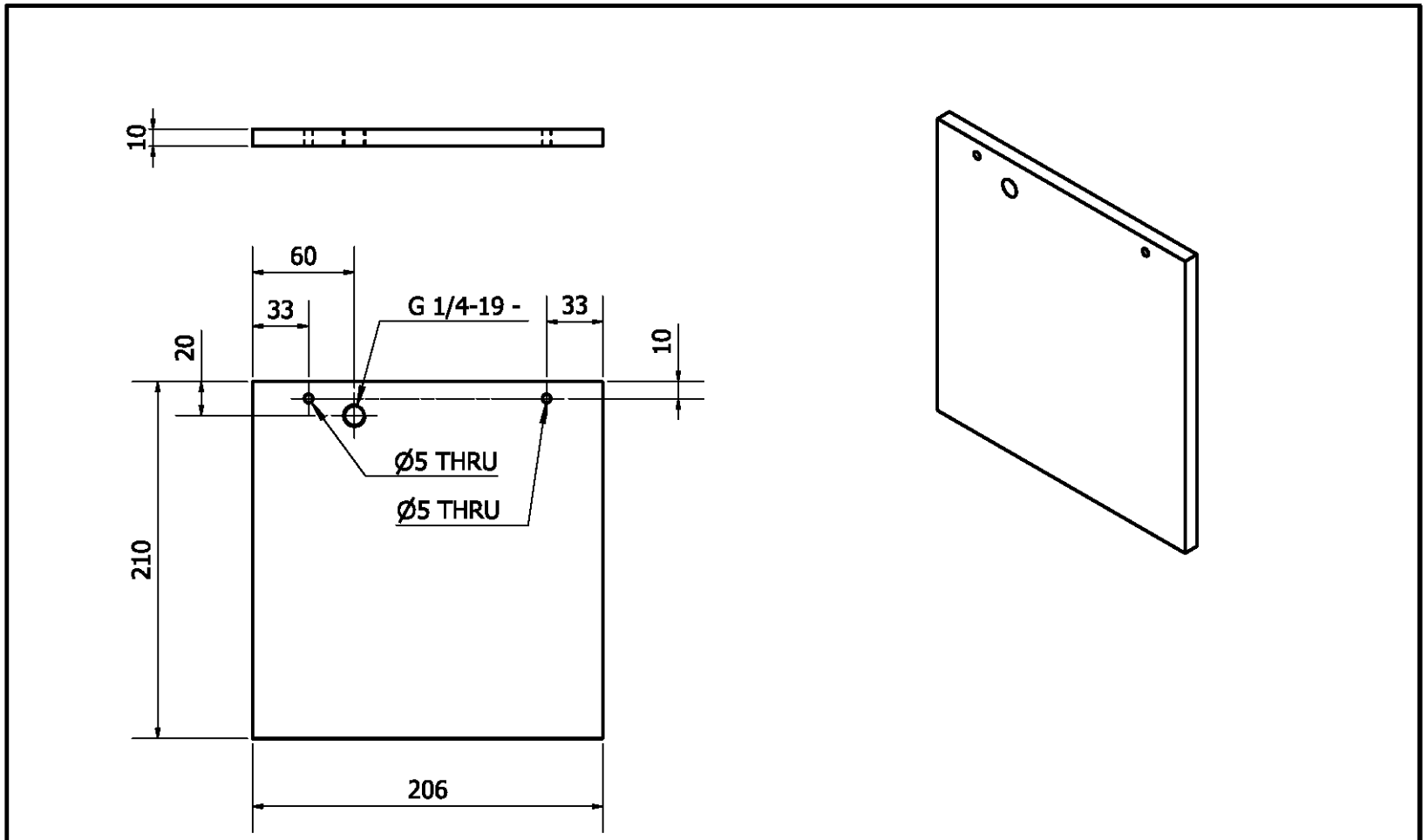

TOLERANCES
Tolerances unless otherwise stated:
Whole numbers +/- 0.25
One decimal place +/- 0.10
Two decimal places +/- 0.05

DRAWN BY
Naomi Green

DIMENSIONS ARE IN mm

DATE
15/09/2013

3rd ANGLE PROJECTION

TITLE
Container Part C

SIZE
A4

REV
2

SCALE 1:3

SHEET 1 of 1

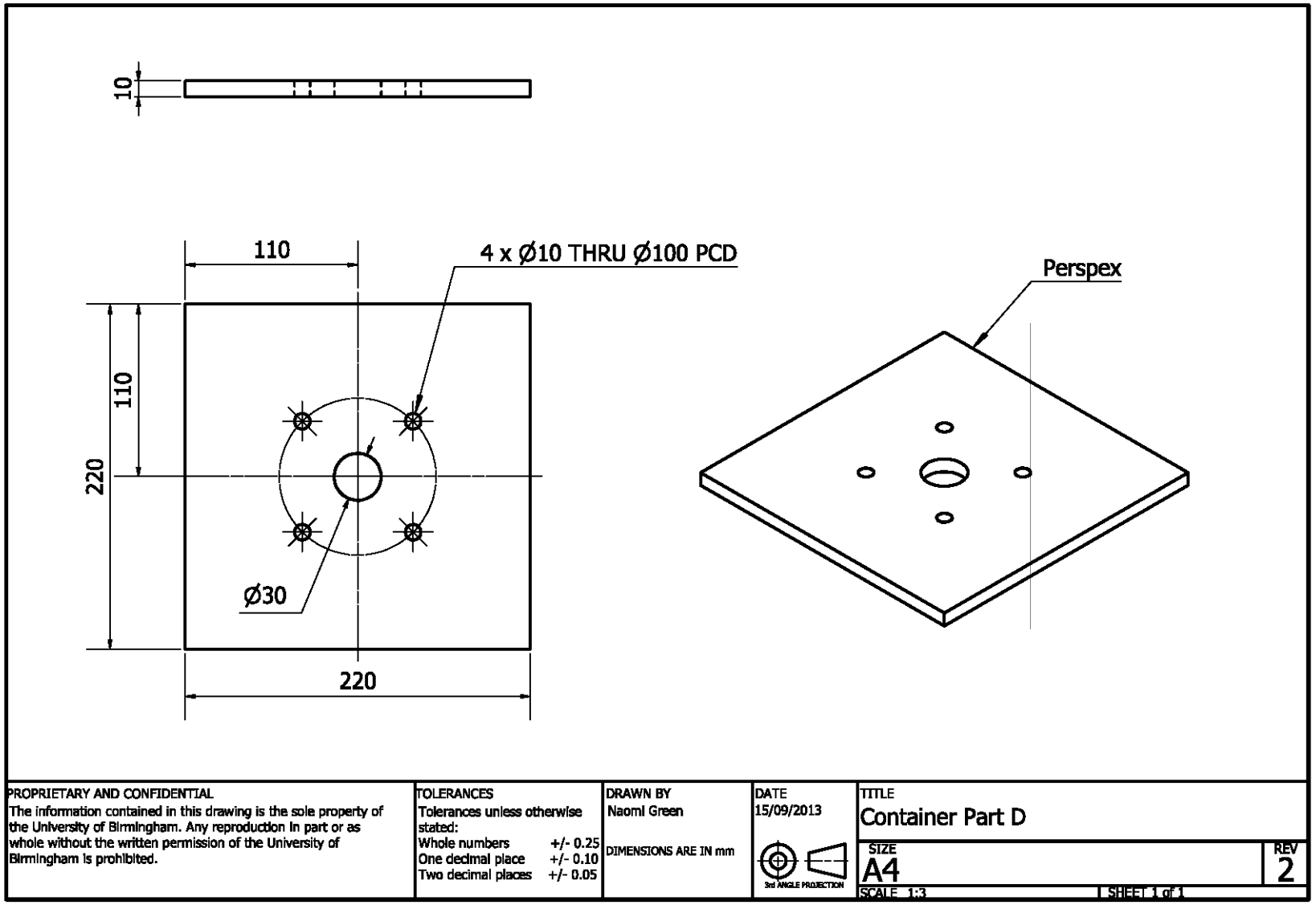
10
110
4 x Ø10 THRU Ø100 PCD
110
220
Ø30
220
Perspex
PROPRIETARY AND CONFIDENTIAL
The information contained in this drawing is the sole property of the University of Birmingham. Any reproduction in part or as whole without the written permission of the University of Birmingham is prohibited.
TOLERANCES
Tolerances unless otherwise stated:
Whole numbers +/- 0.25
One decimal place +/- 0.10
Two decimal places +/- 0.05
DRAWN BY
Naomi Green
DIMENSIONS ARE IN mm
DATE
15/09/2013
3rd ANGLE PROJECTION
TITLE
Container Part D
SIZE
A4
REV
2
SCALE 1:3
SHEET 1 of 1

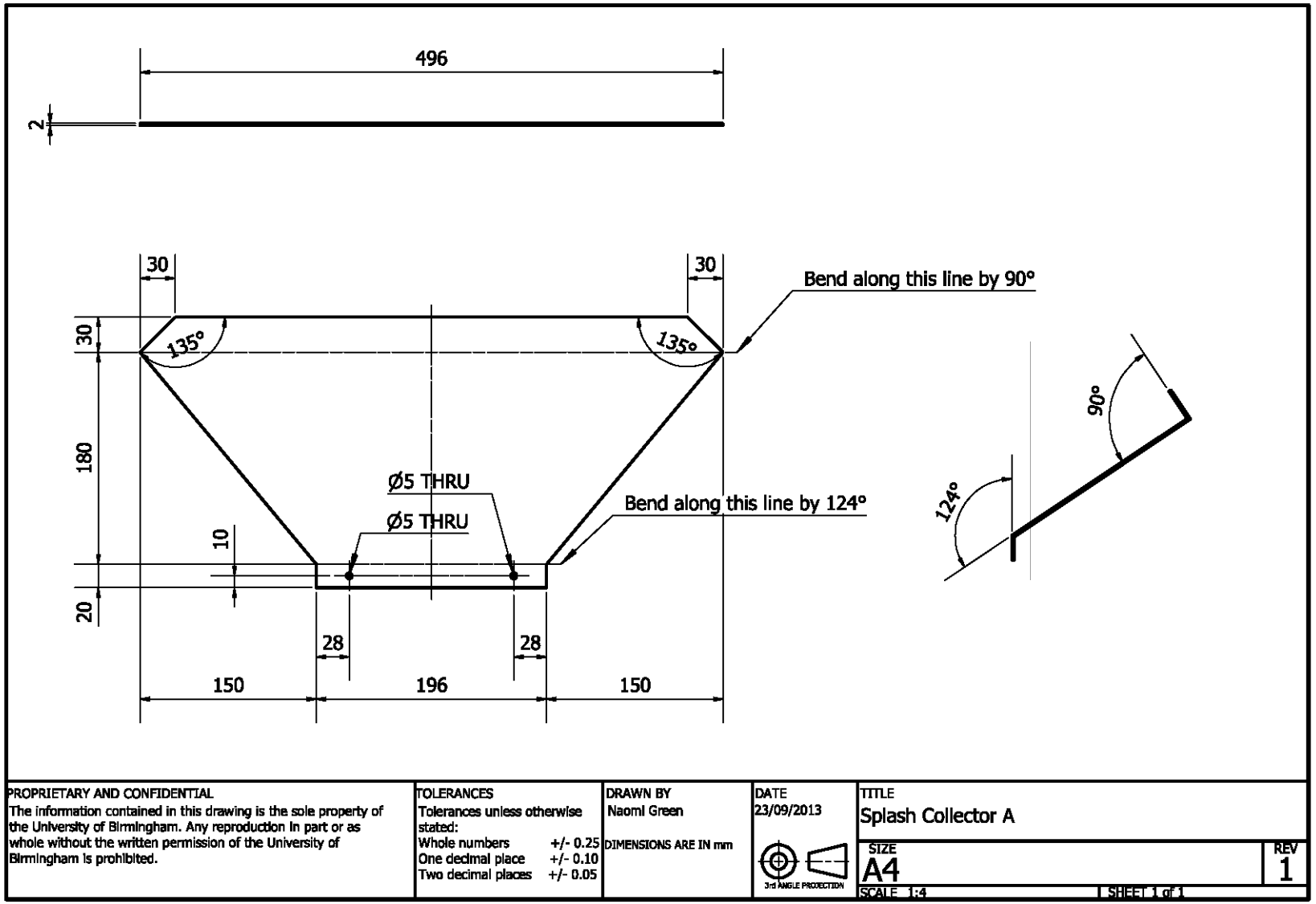
496
2
30
30
135°
135°
Bend along this line by 90°
30
180
20
10
Ø5 THRU
Ø5 THRU
Bend along this line by 124°
28
28
150
196
150
90°
124°
PROPRIETARY AND CONFIDENTIAL
The information contained in this drawing is the sole property of the University of Birmingham. Any reproduction in part or as whole without the written permission of the University of Birmingham is prohibited.
TOLERANCES
Tolerances unless otherwise stated:
Whole numbers +/- 0.25
One decimal place +/- 0.10
Two decimal places +/- 0.05
DRAWN BY
Naomi Green
DIMENSIONS ARE IN mm
DATE
23/09/2013
3rd ANGLE PROJECTION
TITLE
Splash Collector A
SIZE
A4
REV
1
SCALE 1:4
SHEET 1 of 1

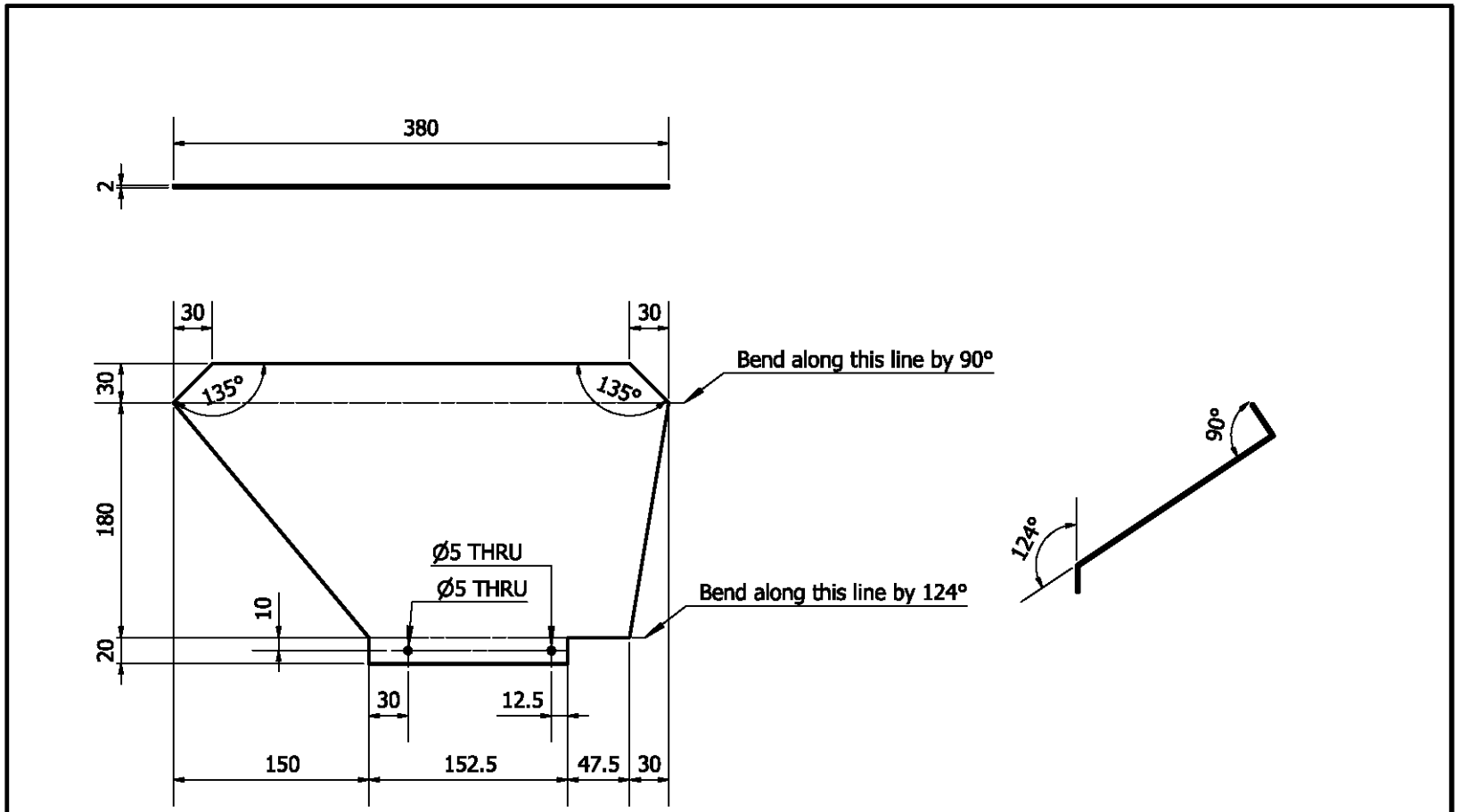

TOLERANCES
Tolerances unless otherwise stated:
Whole numbers +/- 0.25
One decimal place +/- 0.10
Two decimal places +/- 0.05

DRAWN BY
Naomi Green

DIMENSIONS ARE IN mm

DATE
23/09/2013

3rd ANGLE PROJECTION

TITLE
Splash Collector B

SIZE
A4

REV
2

SCALE 1:4

SHEET 1 of 1

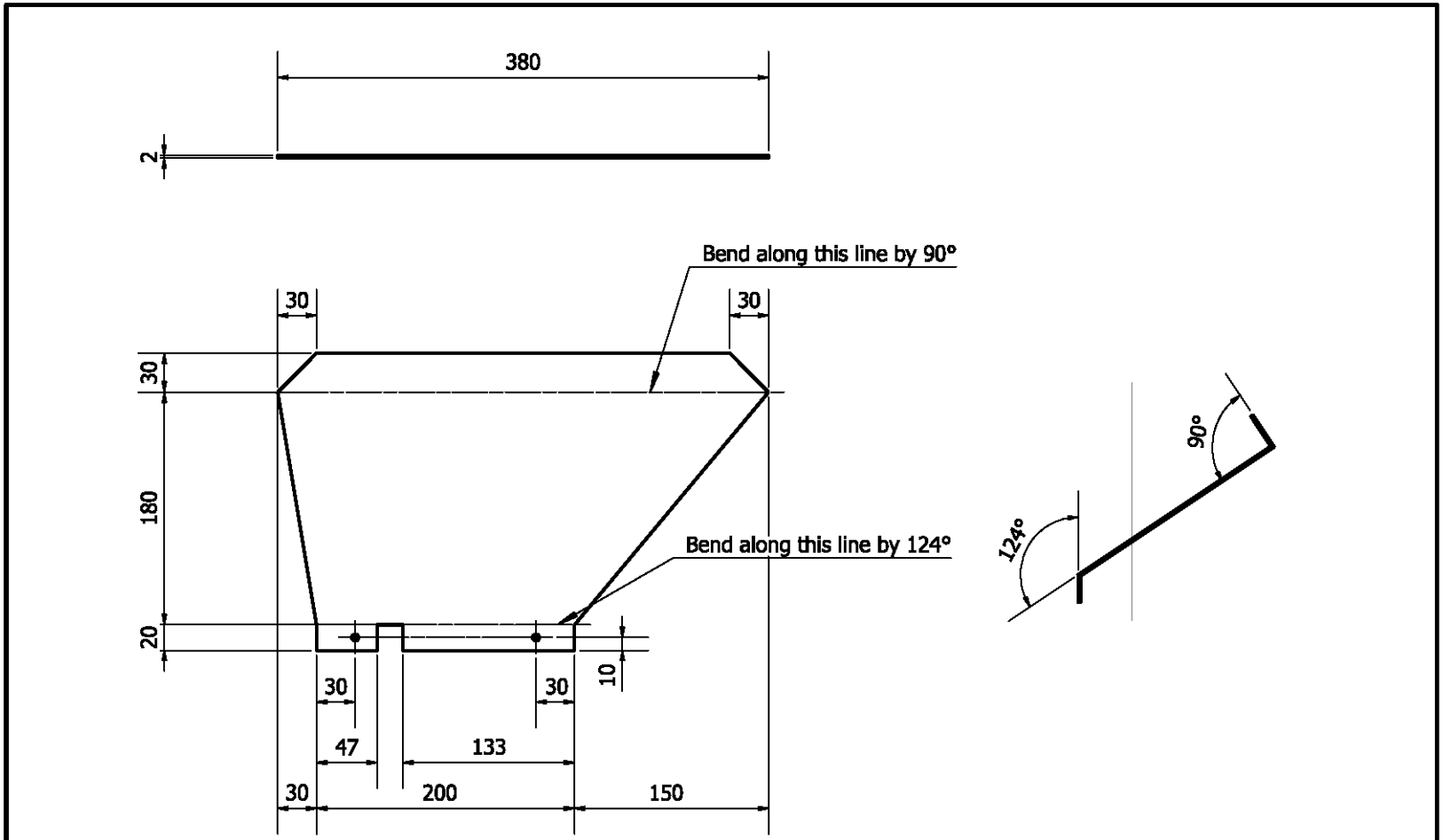

PROPRIETARY AND CONFIDENTIAL The information contained in this drawing is the sole property of the University of Birmingham. Any reproduction in part or as whole without the written permission of the University of Birmingham is prohibited.	TOLERANCES Tolerances unless otherwise stated: Whole numbers +/- 0.25 One decimal place +/- 0.10 Two decimal places +/- 0.05	DRAWN BY Naomi Green DIMENSIONS ARE IN mm	DATE 23/09/2013 3rd ANGLE PROJECTION	TITLE Splash Collector C SIZE A4 REV 1 SCALE 1:4 SHEET 1 of 1

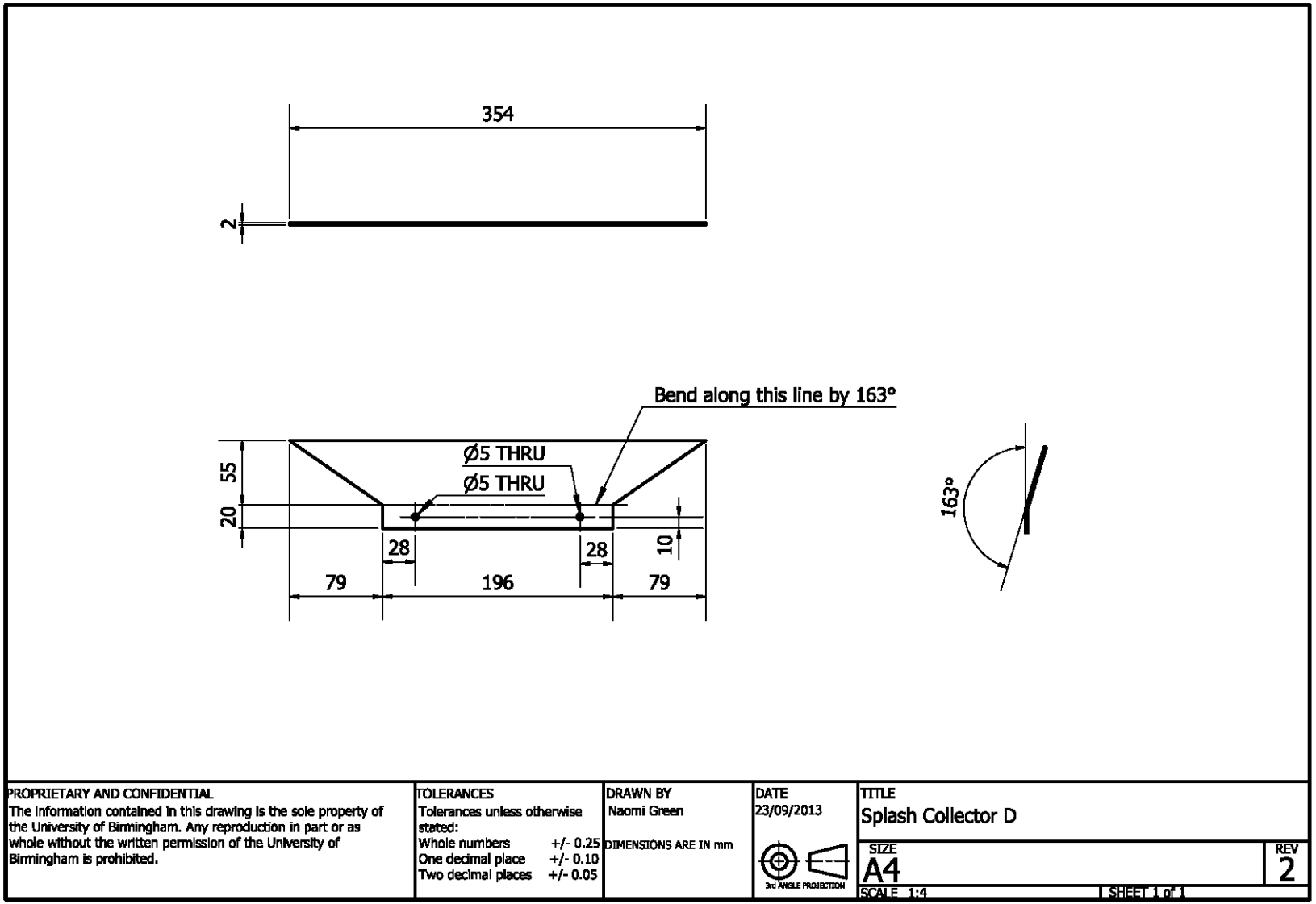
354
2
Bend along this line by 163°
Ø5 THRU
Ø5 THRU
55
20
28
28
10
79
196
79
163°
PROPRIETARY AND CONFIDENTIAL
The information contained in this drawing is the sole property of the University of Birmingham. Any reproduction in part or as whole without the written permission of the University of Birmingham is prohibited.
TOLERANCES
Tolerances unless otherwise stated:
Whole numbers +/- 0.25
One decimal place +/- 0.10
Two decimal places +/- 0.05
DRAWN BY
Naomi Green
DIMENSIONS ARE IN mm
DATE
23/09/2013
3rd ANGLE PROJECTION
TITLE
Splash Collector D
SIZE
A4
REV
2
SCALE 1:4
SHEET 1 of 1

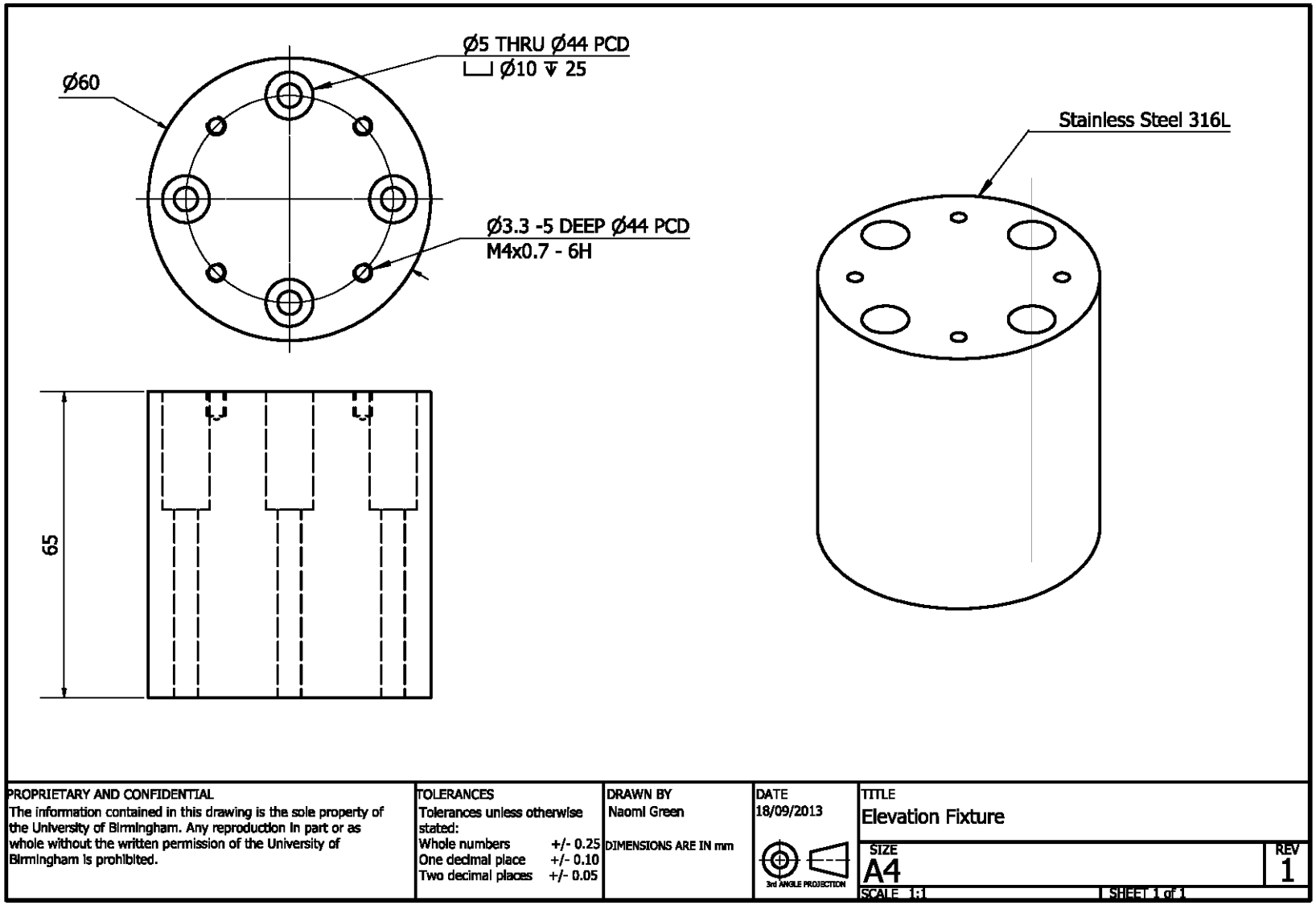
Ø5 THRU Ø44 PCD
⌴ Ø10 ↧ 25
Ø60
Ø3.3 -5 DEEP Ø44 PCD
M4x0.7 - 6H
Stainless Steel 316L
65
PROPRIETARY AND CONFIDENTIAL
The information contained in this drawing is the sole property of the University of Birmingham. Any reproduction in part or as whole without the written permission of the University of Birmingham is prohibited.
TOLERANCES
Tolerances unless otherwise stated:
Whole numbers +/- 0.25
One decimal place +/- 0.10
Two decimal places +/- 0.05
DRAWN BY
Naomi Green
DIMENSIONS ARE IN mm
DATE
18/09/2013
3rd ANGLE PROJECTION
TITLE
Elevation Fixture
SIZE
A4
REV
1
SCALE 1:1
SHEET 1 of 1

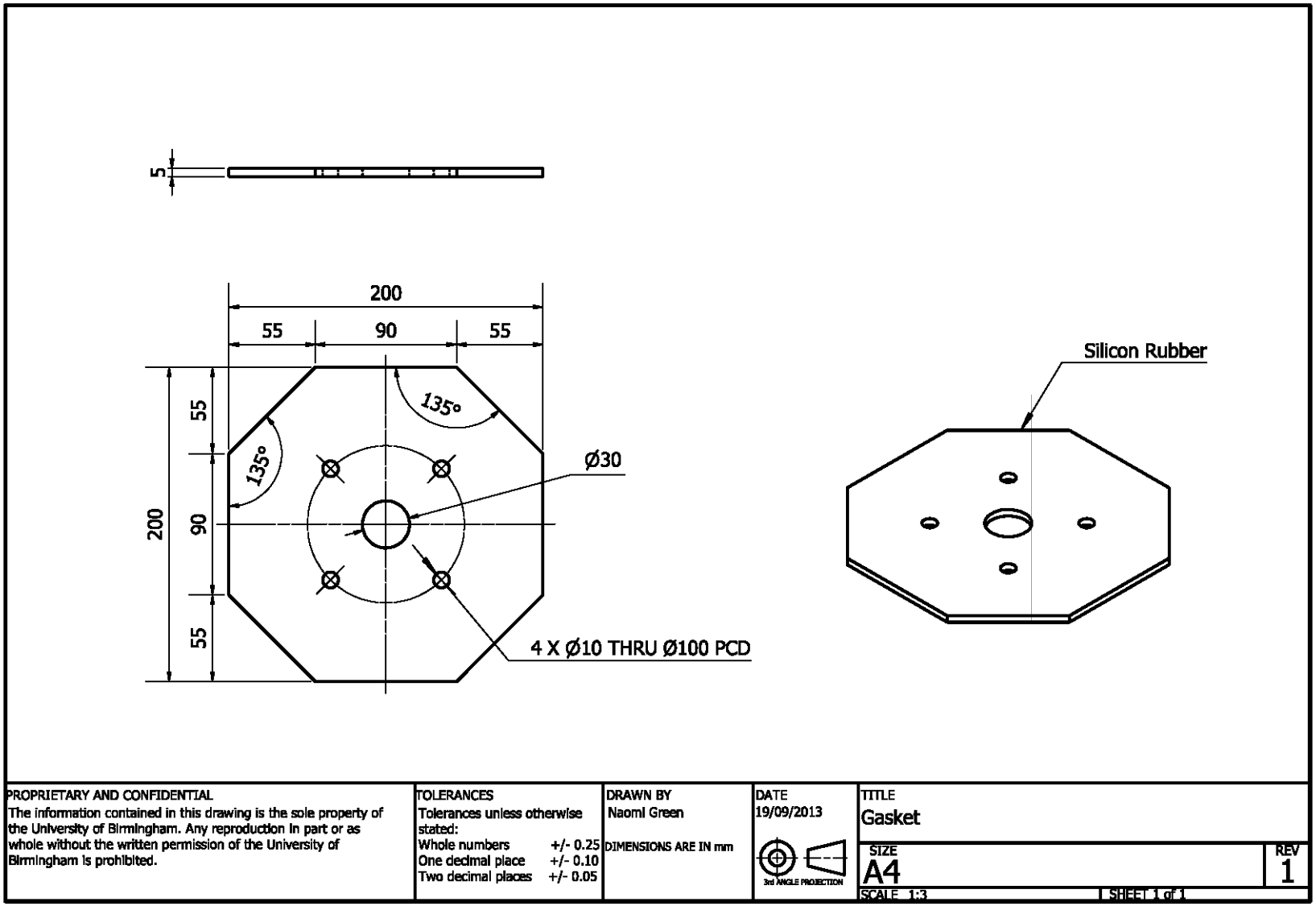

PROPRIETARY AND CONFIDENTIAL The information contained in this drawing is the sole property of the University of Birmingham. Any reproduction in part or as whole without the written permission of the University of Birmingham is prohibited.	TOLERANCES Tolerances unless otherwise stated: Whole numbers +/- 0.25 One decimal place +/- 0.10 Two decimal places +/- 0.05	DRAWN BY Naomi Green DIMENSIONS ARE IN mm	DATE 19/09/2013 3rd ANGLE PROJECTION	TITLE Gasket SIZE A4 REV 1 SCALE 1:3 SHEET 1 of 1

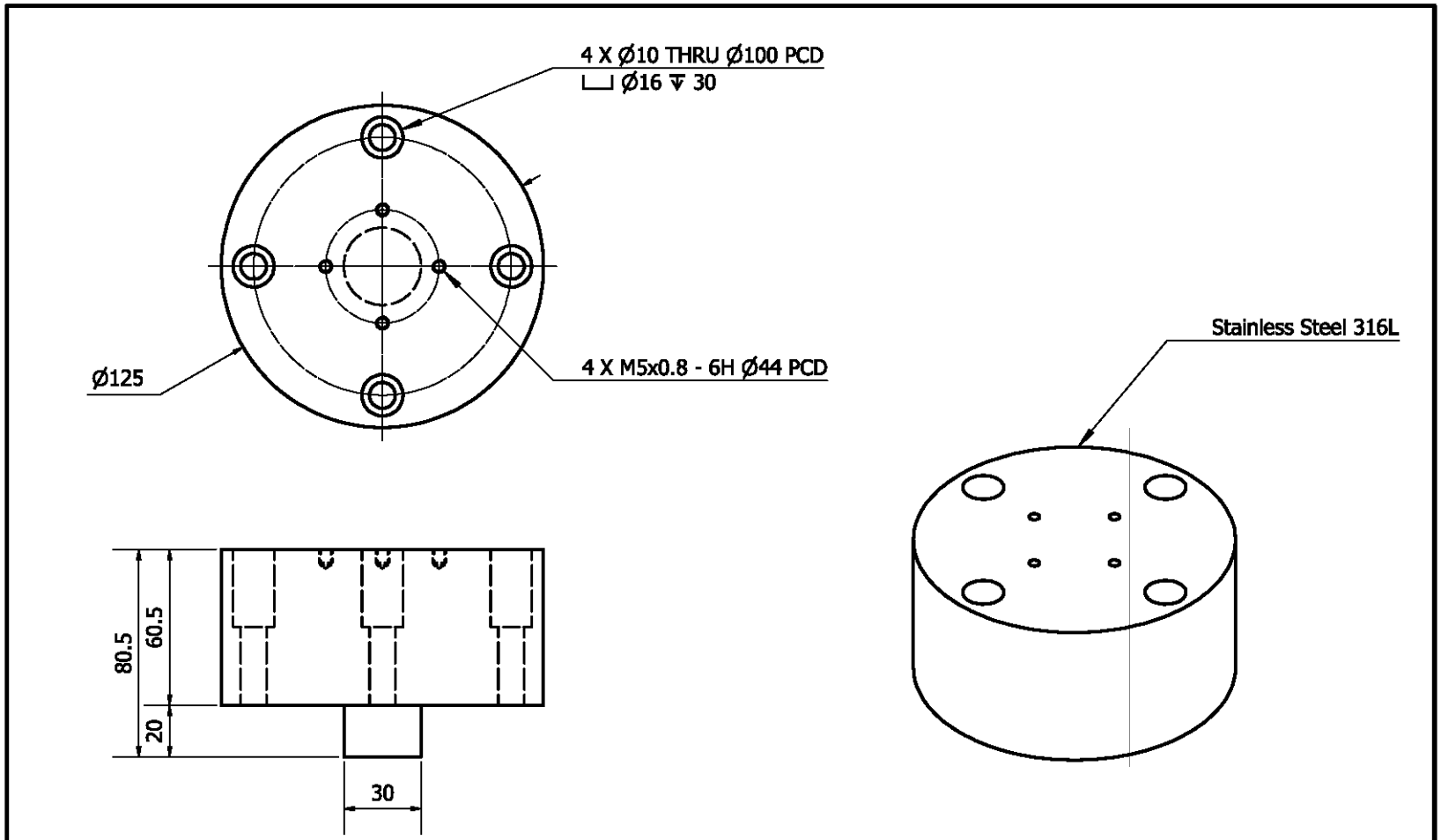

TOLERANCES
Tolerances unless otherwise stated:
Whole numbers +/- 0.25
One decimal place +/- 0.10
Two decimal places +/- 0.05

DRAWN BY
Naomi Green

DIMENSIONS ARE IN mm

DATE
19/09/2013

3rd ANGLE PROJECTION

TITLE
Pallet Fixture

SIZE
A4

REV
1

SCALE 1:2

SHEET 1 of 1

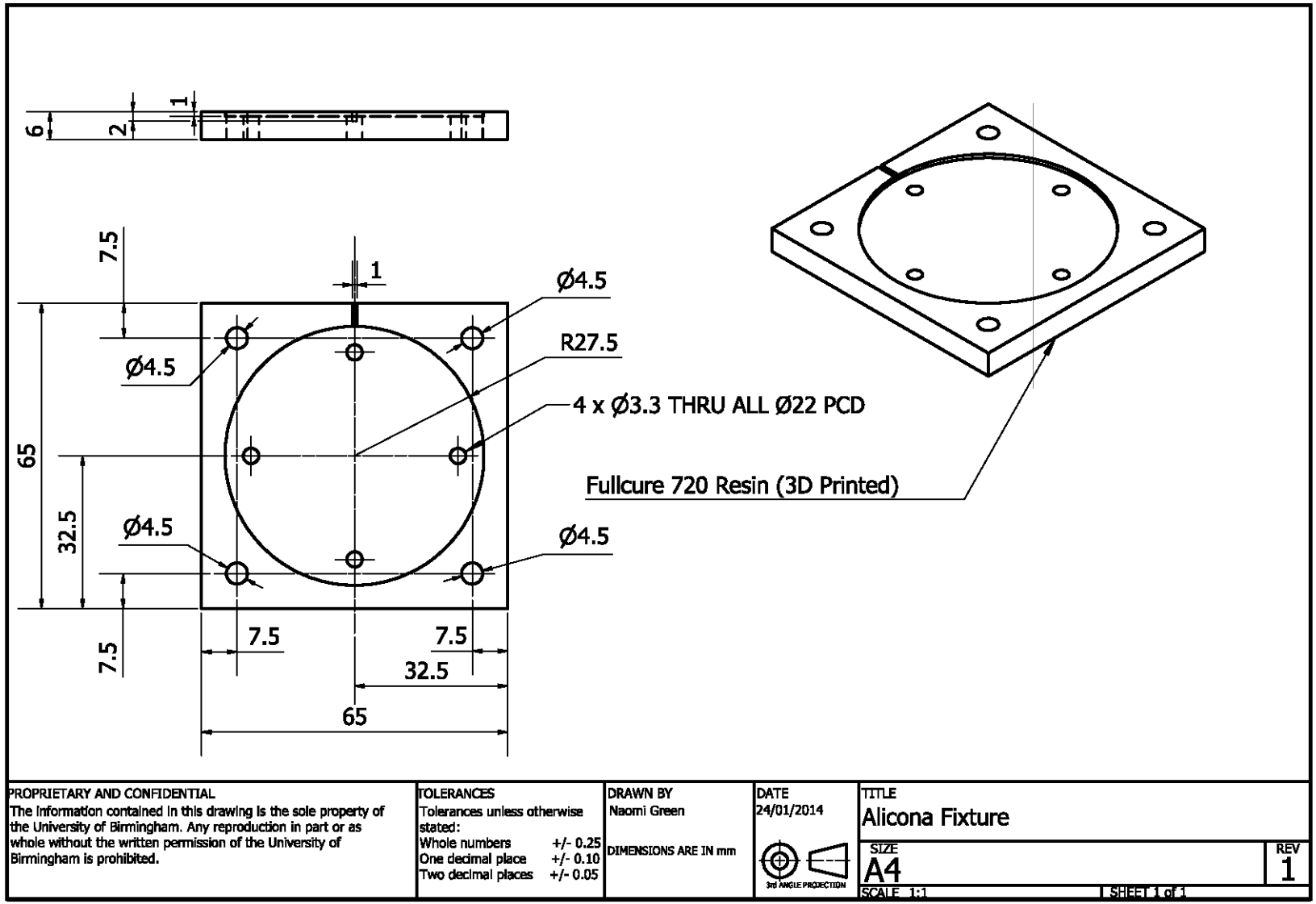

PROPRIETARY AND CONFIDENTIAL The information contained in this drawing is the sole property of the University of Birmingham. Any reproduction in part or as whole without the written permission of the University of Birmingham is prohibited.	TOLERANCES Tolerances unless otherwise stated: Whole numbers +/- 0.25 One decimal place +/- 0.10 Two decimal places +/- 0.05	DRAWN BY Naomi Green DIMENSIONS ARE IN mm	DATE 24/01/2014 3rd ANGLE PROJECTION	TITLE Alicona Fixture SIZE A4 REV 1 SCALE 1:1 SHEET 1 of 1

Appendix B

MATLAB Code

B.1. Dimensional_analysis.m

```
%% Crop scan to a sphere
[Run1Vol, struct] = genAliconaImport('LIO3Run1RawData.txt',
'findVolume', true, 'scale', 10^-6 );
xyz=struct.xyz;
x=xyz(:,:,1);
y=xyz(:,:,2);
z=xyz(:,:,3);
a=0.0049;
I=sqrt(x.^2+y.^2)<=a;
xSphere=x(I);
ySphere=y(I);
zSphere=z(I);
X=xSphere(:);
X(:,2)=ySphere(:);
X(:,3)=zSphere(:);
[Center,Radius, Maximum, Minimum] = sphereFit(X);
```

B.2. SphereFit.m

```
1.  function [Center,Radius, Maximum, Minimum] = sphereFit(X)
2.  %% this fits a sphere to a collection of data using a closed form
    for the
3.  %% solution (opposed to using an array the size of the data set).
4.  %% Minimizes Sum((x-xc)^2+(y-yc)^2+(z-zc)^2-r^2)^2
5.  %% x,y,z are the data, xc,yc,zc are the sphere's center, and r is
    the radius
6.
7.  %% Assumes that points are not in a singular configuration, real
    numbers, ...
8.  %% if you have coplanar data, use a circle fit with svd for
    determining the
9.  %% plane, recommended Circle Fit (Pratt method), by Nikolai
    Chernov
10. %% http://www.mathworks.com/matlabcentral/fileexchange/22643
11.
12. %% Input:
13. %% X: n x 3 matrix of cartesian data
14. %% Outputs:
15. %% Center: Center of sphere
16. %% Radius: Radius of sphere
17. %% Author:
18. %% Alan Jennings, University of Dayton
19.
20. A=[mean(X(:,1).*(X(:,1)-mean(X(:,1)))), ...
21.     2*mean(X(:,1).*(X(:,2)-mean(X(:,2)))), ...
22.     2*mean(X(:,1).*(X(:,3)-mean(X(:,3)))); ...
23.     0, ...
24.     mean(X(:,2).*(X(:,2)-mean(X(:,2)))), ...
25.     2*mean(X(:,2).*(X(:,3)-mean(X(:,3)))); ...
26.     0, ...
27.     0, ...
28.     mean(X(:,3).*(X(:,3)-mean(X(:,3))))];
29. A=A+A.';
30. B=[mean((X(:,1).^2+X(:,2).^2+X(:,3).^2).*(X(:,1)-
    mean(X(:,1))));...
31.     mean((X(:,1).^2+X(:,2).^2+X(:,3).^2).*(X(:,2)-
    mean(X(:,2))));...
32.     mean((X(:,1).^2+X(:,2).^2+X(:,3).^2).*(X(:,3)-
    mean(X(:,3))))];
33. Center=(A\B).';
34. Radius=sqrt(mean(sum([X(:,1)-Center(1),X(:,2)-Center(2),X(:,3)-
    Center(3)].^2,2)));
35.
36. %% adapted by Naomi Green to find Radial Separation
37. for ii=1:length(X);
38.     ra=sqrt((Center(1)-X(ii,1))^2+(Center(2)-
    X(ii,2))^2+(Center(3)-X(ii,3))^2);
39.     Rs(ii)=Radius-ra;
40. end
41. Minimum=min(Rs);
42. Maximum=max(Rs);
43. End
```

B.3. FormatData.m

```
1.  function [maxima, minima, frequency, cropdatarms] =
    fdatanalysis_ncg(filename, axis, minPeak, frequency, NoScans)
2.  %IMPORTFILE Import numeric data from a text file as column
    vectors.
3.  %   [TIME,ZMOMENT,XMOMENT,YMOMENT] = IMPORTFILE(FILENAME) Reads
    data from
4.  %   text file FILENAME for the default selection.
5.  %
6.  %       [TIME,ZMOMENT,XMOMENT,YMOMENT] = IMPORTFILE(FILENAME,
    STARTROW, ENDROW)
7.  %   Reads data from rows STARTROW through ENDROW of text file
    FILENAME.
8.  %
9.  % Example:
10. %   [time,Zmoment,Xmoment,Ymoment] =
11. %   importfile('0-5HzFrictionTestFlex001.CSV',12, 201170);
12. %
13. %   See also TEXTSCAN.
14. % Auto-generated by MATLAB on 2014/07/28 16:05:43
15.
16. %% Initialize variables.
17. delimiter = ',';
18. startRow = 12;
19. endRow = inf;
20.
21. %% Format string for each line of text:
22. %   column2: double (%f)
23. %     column9: double (%f)
24. %   column10: double (%f)
25. %     column11: double (%f)
26. % For more information, see the TEXTSCAN documentation.
27. formatSpec =
    '%*s%f%*s%*s%*s%*s%*s%f%f%f%*s%*s%*s%*s%*s%*s%*s%*s%*s%*s%*s%
    *s%*s%*s%*s%*s%*s%*s%*s%[^\n\r]';
28.
29. %% Open the text file.
30. fileID = fopen(filename,'r');
31.
32. %% Read columns of data according to format string.
33. textscan(fileID, '%[^\n\r]', startRow(1)-1, 'ReturnOnError',
    false);
34. dataArray = textscan(fileID, formatSpec, endRow(1)-
    startRow(1)+1, 'Delimiter', delimiter, 'ReturnOnError', false);
35. for block=2:length(startRow)
36.         frewind(fileID);
37.         textscan(fileID, '%[^\n\r]', startRow(block)-1,
            'ReturnOnError', false);
38.         dataArrayBlock = textscan(fileID, formatSpec,
            endRow(block)-startRow(block)+1, 'Delimiter', delimiter,
            'ReturnOnError', false);
39.         for col=1:length(dataArray)
40.         dataArray{col} = [dataArray{col};dataArrayBlock{col}];
41.         end
```

```
42.   end
43.
44.   %% Close the text file.
45.   fclose(fileID);
46.
47.   %% Allocate imported array to column variable names
48.   time = dataArray{:, 1};
49.   Zmoment = dataArray{:, 2};
50.   Xmoment = dataArray{:, 3};
51.   Ymoment = dataArray{:, 4};
52.
53.   %% Extract data for the required axial rotation defined in the
      function inputs
54.   if strcmp(axis, 'x') == 1
55.           data = Xmoment;
56.   elseif strcmp(axis, 'y') == 1
57.           data = Ymoment;
58.   elseif strcmp(axis, 'z') == 1
59.           data = Zmoment;
60.   else
61.           error('Invalid dimension')
62.   end
63.
64.   %% Crop data to the last 10 cycles
65.   cropAmount=((1/frequency)*10*NoScans);
66.   cropdata=data(end-cropAmount:end);
67.   croptime=time(end-cropAmount:end);
68.
69.   %% Calculate the Arithmetic mean of the last 10 cycles
70.   mu=mean(cropdata);
71.
72.   %% Find the maximum and minimum values of each of the last 10
      cycles
73.   minDist=((1/frequency)*NoScans);
74.   maxima     =findpeaks(cropdata,     'MINPEAKHEIGHT',     minPeak,
      'MINPEAKDISTANCE', minDist);
75.   InvData=cropdata.*(-1);
76.   minima=findpeaks(InvData,        'MINPEAKHEIGHT',        minPeak,
      'MINPEAKDISTANCE', minDist);
77.   minima = minima*-1;
78.
79.   %% Plot figure of the last 10 cycles
80.   figure, plot(croptime,cropdata, 'k')
81.   ylim([-8, 8])
82.   xlim([45, 50.1])
83.   title('Frictional Torque Lateral Bending Implant 2 2Hz Test 1')
84.   xlabel('Time, s')
85.   ylabel('Lateral Bending Moment, Nm')
86.   hline=refline([0, mu]);
87.   hline.Color = 'k';
88.   set(hline, 'LineStyle','--');
```

B.4. CalculateStribeck.m

```
%% Read the four input files for each test;
inputFiles={'0-25HzFrictionTestLat001.CSV'; '0-25HzFrictionTestLat002.CSV'; '0-25HzFrictionTestLat003.CSV'; '0-25HzFrictionTestLat004.CSV'};

%% Format input files and extract maxima and minima for each test;
for i=1:4;
        [maxima(i,:), minima(i,:), frequency]=FormatData(inputFiles{i}, 'x', 4, 0.25, 100);
end

%% Find mean and standard deviation of combined maxima and minima
Invminima=minima*-1;
CombTorq=[maxima Invminima];
meanCombTorq=mean(mean(CombTorq));
stdCombTorq=std(std(CombTorq));

%% Find Sommerfeld Number
% Inputs
rCup=0.00705; % Radius of cup
rBall=0.007; % Radius of ball
R=rBall;
viscosity=0.000713; % Viscosity of bovine serum
load=150; % Applied load
ang=6; % Maximum angular displacement
% Calculations
angVel=2*pi()*ang*frequency/180; % Calculate angular velocity
vEnt=angVel*R/2; % Calculate entraining velocity
SomNum025=(viscosity*R*vEnt)/load; % Calculate Sommerfeld Number

%% Find Friction Factors for different averages and standard deviations
FricNumComb025=(meanCombTorq/(R*load));
FricNumCombSD025=(stdCombTorq/(R*load));

%% Clear variables
clear('frequency', 'inputFiles', 'load', 'i', 'maxima', 'minima', 'rBall', 'rCup', 'vEnt', 'viscosity', 'frequency', 'ang', 'angVel', 'R', 'stdCombTorq', 'meanCombTorq', 'CombTorq', 'Invminima');
```

B.5. PlotStribeck.m

```
1.  %% Concatenate data
2.  SomNum=[SomNum025 SomNum05 SomNum075 SomNum1 SomNum125 SomNum15
    SomNum175 SomNum2];
3.  FricNumComb3=[FricNumComb025    FricNumComb05    FricNumComb075
    FricNumComb1   FricNumComb125   FricNumComb15   FricNumComb175
    FricNumComb2];
4.  FricNumCombSD3=[FricNumCombSD025                 FricNumCombSD05
    FricNumCombSD075 FricNumCombSD1 FricNumCombSD125 FricNumCombSD15
    FricNumCombSD175 FricNumCombSD2];
5.  save('combLatImpl3.mat');
6.
7.  %% Plot stribeck curve
8.  figure
9.  errorbar(SomNum, FricNumComb, FricNumCombSD, '.r')
10. title('Combined  Frictional  Torque  Flexion/Extension  Implant
    O3')
11. xlabel('Sommerfeld Number, Z')
12. ylabel('Friction Factor, f')
13. axis([0, 6.5e-11, 0, 8])
14. print -dpng stribeckCombFlexExImp3.png -r600
15. saveas(gcf, 'stribeckCombFlexExImp3.fig')
```

B.6. PlotAllStribeck.m

```
%% Plot all stribeck curves on one graph
figure
errorbar(SomNum, FricNumComb1, FricNumCombSD1, 'b')
hold on
errorbar(SomNum, FricNumComb2, FricNumCombSD2, 'r')
hold off
hold on
errorbar(SomNum, FricNumComb3, FricNumCombSD3, 'k')
hold off

title('Combined Frictional Torque Flexion/Extension All Implants')
xlabel('Sommerfeld Number, Z')
ylabel('Friction Factor, f')
legend ('Implant O1','Implant O2','Implant O3', 'location', 'southeast')
axis([0, 6.8e-11, 0, 8])
print -dpng stribeckCombFlexExAllLine.png -r600
saveas(gcf, 'stribeckCombFlexExAllLine.fig')
```

B.7. GenAliconaImport.m

```
1.  function [output, struct] = GenAliconaImport(filename, varargin)
2.
3.  % Import alicona data to matlab from a text file. It takes the form of
4.  %  [primary, struct] = genAliconaImport('path/to/file.txt', 'option1',
5.  % value1, ..., 'optionN', valueN);
6.
7.  %   This program will assume a single line header and footer on text files
8.  %  unless otherwise specified with the options:
9.  %  'startRow' & 'endRow'.
10.
11. %  To find the volume between the surface and the z plane, set
12. %  'findVolume' to true.
13.
14. %  To plot the data, set 'plot' to one of the following:
15. %  'contour', 'contourf', 'contour3', 'mesh', or 'surf'.
16.
17. %   To crop data, use 'crop' followed by [xmin,xmax,ymin,ymax]. N.B. these
18. %  must be scaled to the new size!
19. %
20.
21. % Author David Eckold
22. %% input argument parser
23. defaultStartRow = 2;
24. defaultEndRow = (numel(textread(filename,'%1c%*[^\n]')))-1;
25. defaultScale = 1;
26. defaultInterp = 'natural';
27. defaultFindVol = false;
28. defaultPlot = false;
29. defaultContourLayers = 20;
30. defaultCrop = false;
31. expectedInterp = {'nearest','linear','natural'};
32. expectedPlot = { 'contour', 'contourf', 'contour3', 'mesh', 'surf'};
33. err = 'Value must be a positive number.';
34. validationFunc = @(x) assert(isnumeric(x) && isscalar(x) && (x > 0), err);
35.
36. p = inputParser;
37. addRequired(p,'filename',@ischar);
38. addParamValue(p,'startRow',defaultStartRow,validationFunc);
39. addParamValue(p,'endRow',defaultEndRow,validationFunc);
40. addParamValue(p,'scale',defaultScale,validationFunc);
41. addParamValue(p,'interpolant',defaultInterp,@(x) any(validatestring(x,expectedInterp)));
42. addParamValue(p,'findVolume',defaultFindVol,@islogical);
43. addParamValue(p,'plot',defaultPlot,@(x) any(validatestring(x,expectedPlot)));
```

```
44.   addParamValue(p,'contourLayers',           defaultContourLayers,
      validationFunc);
45.   addParamValue(p,'crop', defaultCrop)
46.   parse(p,filename,varargin{:});
47.
48.   %% Import data from Alicona file to tuplets.
49.   startRow = p.Results.startRow;
50.   endRow = p.Results.endRow;
51.
52.   % Format string for each line of text:
53.   %   column1: double (%f)
54.   %   column2: double (%f)
55.   %   column3: double (%f)
56.   % For more information, see the TEXTSCAN documentation.
57.   formatSpec = '%13f%13f%f%[^\n\r]';
58.
59.   % Open the text file.
60.   fileID = fopen(filename,'r');
61.
62.   % Read columns of data according to format string.
63.   % This call is based on the structure of the file used to
      generate this
64.   % code. If an error occurs for a different file, try
      regenerating the code
65.   % from the Import Tool.
66.   dataArray    =    textscan(fileID,    formatSpec,    endRow(1)-
      startRow(1)+1, 'Delimiter', '', 'WhiteSpace', '', 'HeaderLines',
      startRow(1)-1, 'ReturnOnError', false);
67.   % for block=2:length(startRow)
68.   %     frewind(fileID);
69.   %             dataArrayBlock   =   textscan(fileID,   formatSpec,
      endRow(block)-startRow(block)+1, 'Delimiter', '', 'WhiteSpace',
      '', 'HeaderLines', startRow(block)-1, 'ReturnOnError', false);
70.   %     for col=1:length(dataArray)
71.   %         dataArray{col} = [dataArray{col};dataArrayBlock{col}];
72.   %     end
73.   % end
74.
75.   % Close the text file.
76.   fclose(fileID);
77.
78.   % Create output variable
79.   xyz = [dataArray{1:end-1}];
80.
81.   %% Convert Alicona tuplets to nxmx3 Mesh.
82.   scale = p.Results.scale;
83.
84.   x = xyz(:,1); y = xyz(:,2); z = xyz(:,3);
85.   x = x*scale; y = y*scale; z = z*scale;
86.   dx = abs(x(find(diff(x),1)+1)-x(1));
87.   dy = abs(y(find(diff(y),1)+1)-y(1));
88.
89.   if p.Results.crop == 0
90.             xvg = min(x):dx:max(x);
91.             yvg = min(y):dy:max(y);
92.   elseif length(p.Results.crop) == 4;
```

```
93.             xvg = p.Results.crop(1):dx:p.Results.crop(2);
94.             yvg = p.Results.crop(3):dy:p.Results.crop(4);
95.    else
96.             error ('Incorrect number of inputs'!')
97.    end
98.    F = scatteredInterpolant(x,y,z,p.Results.interpolant,'none');
99.    [vx,vy] = ndgrid(xvg,yvg);
100.   vz = F(vx,vy);
101.
102.   %% write outputs and plot graphs if called for
103.   if p.Results.findVolume == 1
104.             output = dx*dy*sum(vz(:));
105.             struct.xyz(:,:,1) = vx;
106.             struct.xyz(:,:,2) = vy;
107.             struct.xyz(:,:,3) = vz;
108.   else
109.             output(:,:,1) = vx;
110.             output(:,:,2) = vy;
111.             output(:,:,3) = vz;
112.   end
113.             struct.d = [dx dy];
114.             struct.F = F;
115.   if  p.Results.plot ~= 0
116.             figure
117.             if   any(strcmp(p.Results.plot,{'contour', ...
'contourf','contour3'})) == 1;
118.                  feval(p.Results.plot,                    vx,vy,vz,
      p.Results.contourLayers)
119.                  c = colorbar;
120.                  ylabel(c, 'z, m')
121.             else
122.             feval(p.Results.plot, vx,vy,vz);
123.             zlabel('z, m')
124.              end
125.              ylabel('y, m')
126.              xlabel('x, m')
127.              end
128.   end
```

B.8. FindVolume.m

```
%% Import data Run 1
[    ~,    struct]    =    GenAliconaImport('metalSpecimen1.txt', 'findVolume', true, 'crop', [-3500, 3500, -3500, 3500]);
xyz1=struct.xyz;
x1=xyz1(:,:,1);
y1=xyz1(:,:,2);
z1=xyz1(:,:,3);

%% Concatenate xyz data into one matrix
Run1=x1(:);
Run1(:,2)=y1(:);
Run1(:,3)=z1(:);

%% Crop data to obtain reference plane
a=2800 % Radius of cylinder
b=a+130;
I1=sqrt((x1).^2+(y1).^2)>=b;
zFlat1=z1.*(I1);
zFlat1(find(zFlat1==0))=NaN;

%% Plot image of reference plane
figure;
mesh(x1,y1,zFlat1)

%% Find mean and standard deviation of reference plane
meanFlat1=mean(zFlat1);
meanFlat1=meanFlat1(1,1);
stdFlat1=std(zFlat1);
stdFlat1=stdFlat1(1,1);

%% Crop data to size of specimen cylinder
I1=sqrt((x1).^2+(y1+75).^2)<=a;
zCylndr1=z1.*(I1);
zCylndr1(find(zCylndr1==0))=NaN;

%% Align the arbitrary z-plane with the reference plane by subtracting the mean of the reference plane from the z heights
zCylndrAlign1=zCylndr1-meanFlat1;

%% Plot image of specimen
figure;
mesh(x1,y1,zCylndrAlign1)

%% Calculate Volume
dx1 = x1(2,1)-x1(1,1);
dy1= y1(1,2)-y1(1,1);
SpecVol1=dx1*dy1*sum(zCylndrAlign1(find(zCylndrAlign1>0)))

%% Import data Run2
[    ~,    struct]    =    GenAliconaImport('metalSpecimen2.txt', 'findVolume', true, 'crop', [-3500, 3500, -3500, 3500]);
xyz2=struct.xyz;
x2=xyz2(:,:,1);
```

```
y2=xyz2(:,:,2);
z2=xyz2(:,:,3);

%% Concatenate xyz data into one matrix
Run2=x2(:);
Run2(:,2)=y2(:);
Run2(:,3)=z2(:);

%% Crop data to obtain reference plane
a=2800 % Radius of cylinder
b=a+130;
I2=sqrt((x2).^2+(y2).^2)>=b;
zFlat2=z2.*(I2);
zFlat2(find(zFlat2==0))=NaN;

%% Plot image of reference plane
figure;
mesh(x2,y2,zFlat2)

%% Find mean and standard deviation of reference plane
meanFlat2=mean(zFlat2);
meanFlat2=meanFlat2(1,1);
stdFlat2=std(zFlat2);
stdFlat2=stdFlat2(1,1);

%% Crop data to size of specimen cylinder
I2=sqrt((x2).^2+(y2).^2)<=a;
zCylndr2=z2.*(I2);
zCylndr2(find(zCylndr2==0))=NaN;

%% Align the arbitrary z-plane with the reference plane by
subtracting the mean of the reference plane from the z heights
zCylndrAlign2=zCylndr2-meanFlat2;

%% Plot image of specimen
figure;
mesh(x2,y2,zCylndrAlign2)

%% Calculate Volume
dx2 = x2(2,1)-x2(1,1);
dy2= y2(1,2)-y2(1,1);
SpecVol2=dx2*dy2*sum(zCylndrAlign2(find(zCylndrAlign2>0)))

%% Import data Run3
[    ~,    struct]    =    GenAliconaImport('metalSpecimen3.txt',
'findVolume', true, 'crop', [-3500, 3500, -3500, 3500]);
xyz3=struct.xyz;
x3=xyz3(:,:,1);
y3=xyz3(:,:,2);
z3=xyz3(:,:,3);

%% Concatenate xyz data into one matrix
Run3=x3(:);
Run3(:,2)=y3(:);
Run3(:,3)=z3(:);

```

```
104   %% Crop data to obtain reference plane
105   a=2800 % Radius of cylinder
106   b=a+130;
107   I3=sqrt((x3).^2+(y3).^2)>=b;
108   zFlat3=z3.*(I3);
109   zFlat3(find(zFlat3==0))=NaN;
110
111   %% Plot image of reference plane
112   figure;
113   mesh(x3,y3,zFlat3)
114
115   %% Find mean and standard deviation of reference plane
116   meanFlat3=mean(zFlat3);
117   meanFlat3=meanFlat3(1,1);
118   stdFlat3=std(zFlat3);
119   stdFlat3=stdFlat3(1,1);
120
121   %% Crop data to size of specimen cylinder
122   I3=sqrt((x3).^2+(y3).^2)<=a;
123   zCylndr3=z3.*(I3);
124   zCylndr3(find(zCylndr3==0))=NaN;
125
126   %% Align the arbitrary z-plane with the reference plane by
      subtracting the mean of the reference plane from the z heights
127   zCylndrAlign3=zCylndr3-meanFlat3;
128
129   %% Plot image of specimen
130   figure;
131   mesh(x3,y3,zCylndrAlign3)
132
133   %% Calculate Volume
134   dx3 = x3(2,1)-x3(1,1);
135   dy3= y3(1,2)-y3(1,1);
136   SpecVol3=dx3*dy3*sum(zCylndrAlign3(find(zCylndrAlign3>0)))
```

B.9. Trial1.m

```
%% Determine absolute volume for Runs 1, 2 and 3
run(FindVolume.m);

%% Align Run 2 to Run 1
DiffMean12=meanFlat1-meanFlat2; % Determine difference in z heights by subtracting the means of the reference surfaces.
Alignz12=zCylndr2+DiffMean12; % Align the z coordinates of Run 2 to Run 1
Alignz12=Alignz12-meanFlat1; % Subtract the mean of Run 1's reference surface to normalise the base of the specimen to zero
AlignVol12=dx2*dy2*sum(Alignz12(find(Alignz12>0))); % Calculate the volume of the aligned Run 2 data
DiffVol12=abs(AlignVol12-(SpecVol1)); % Compare the aligned volume of Run 2 to that of Run 1 to determine the absolute error

%% Align Run 3 to Run 1
DiffMean13=meanFlat1-meanFlat3; % Determine difference in z heights by subtracting the means of the reference surfaces.
Alignz13=zCylndr3+DiffMean13; % Align the z coordinates of Run 3 to Run 1
Alignz13=Alignz13-meanFlat1; % Subtract the mean of Run 1's reference surface to normalise the base of the specimen to zero
AlignVol13=dx3*dy3*sum(Alignz13(find(Alignz13>0))); % Calculate the volume of the aligned Run 3 data

DiffVol13=abs(AlignVol13-(SpecVol1)); % Compare the aligned volume of Run 3 to that of Run 1 to determine the absolute error

%% Align Run 1 to Run 2
DiffMean21=meanFlat2-meanFlat1; % Determine difference in z heights by subtracting the means of the reference surfaces.
Alignz21=zCylndr1+DiffMean21; % Align the z coordinates of Run 1 to Run 2
Alignz21=Alignz21-meanFlat2; % Subtract the mean of Run 2's reference surface to normalise the base of the specimen to zero
AlignVol21=dx1*dy1*sum(Alignz21(find(Alignz21>0))); % Calculate the volume of the aligned Run 1 data
DiffVol21=abs(AlignVol21-(SpecVol2)); % Compare the aligned volume of Run 2 to that of Run 2 to determine the absolute error

%% Align Run 3 to Run 2
DiffMean23=meanFlat2-meanFlat3; % Determine difference in z heights by subtracting the means of the reference surfaces.
Alignz23=zCylndr3+DiffMean23; % Align the z coordinates of Run 3 to Run 2
Alignz23=Alignz23-meanFlat2; % Subtract the mean of Run 2's reference surface to normalise the base of the specimen to zero
AlignVol23=dx3*dy3*sum(Alignz23(find(Alignz23>0))); % Calculate the volume of the aligned Run 3 data
DiffVol23=abs(AlignVol23-(SpecVol2)); % Compare the aligned volume of Run 3 to that of Run 2 to determine the absolute error

%% Align Run 1 to Run 3
```

```
34    DiffMean31=meanFlat3-meanFlat1; % Determine difference in z
      heights by subtracting the means of the reference surfaces.
35    Alignz31=zCylndr1+DiffMean31; % Align the z coordinates of Run 1
      to Run 3
36    Alignz31=Alignz31-meanFlat3; % Subtract the mean of Run 3's
      reference surface to normalise the base of the specimen to zero
37    AlignVol31=dx1*dy1*sum(Alignz31(find(Alignz31>0))); % Calculate
      the volume of the aligned Run 1 data
38     DiffVol31=abs(AlignVol31-(SpecVol3)); % Compare the aligned
      volume of Run 1 to that of Run 3 to determine the absolute error
39
40    %% Align Run 2 to Run 3
41     DiffMean32=meanFlat3-meanFlat32 % Determine difference in z
      heights by subtracting the means of the reference surfaces.
42     Alignz32=zCylndr2+DiffMean32; % Align the z coordinates of Run
      2 to Run 3
43     Alignz32=Alignz32-meanFlat3; % Subtract the mean of Run 3's
      reference surface to normalise the base of the specimen to zero
44     AlignVol32=dx2*dy2*sum(Alignz32(find(Alignz32>0))); % Calculate
      the volume of the aligned Run 2 data
45
46     DiffVol32=abs(AlignVol32-(SpecVol3)); % Compare the aligned
      volume of Run 2 to that of Run 3 to determine the absolute error
47
48     %% Determine Error in Alignment Method
49
      SumDiffVol=DiffVol12+DiffVol13+DiffVol21+DiffVol23+DiffVol31+Dif
      fVol32; %Sum the absolute errors between runs
50     MeanDiffVol=SumDiffVol/6; % Calculate the mean of the absolute
      volume errors between the all runs for this alignment method
51     SpecArea=pi*a*a; % Calculate the xy area of the specimen
52     ImpArea=pi*5000*5000; % Calculate the xy area of the implant
53     zHeightErr=MeanDiffVol/SpecArea; % Calculate the mean error in
      the z height  alignment for this alignment method
54     VolErrImp=zHeightErr*ImpArea; % Calculate the predicted mean
      error in volume for the implants using this alignment method
```

B.10. Trial2.m

```
%% Determine absolute volume for Runs 1, 2 and 3
run(FindVolume.m);

%% Import data and crop to patch in centre of specimen for Run 1
[    ~,    struct]    =    GenAliconaImport('metalSpecimen1.txt', 'findVolume', true, 'crop', [-1000, 1000, -1000, 1000]);
xyz1p=struct.xyz;
x1p=xyz1p(:,:,1);
y1p=xyz1p(:,:,2);
z1p=xyz1p(:,:,3);

%% Concatenate Run 1 patch xyz data into one matrix
Run1p=x1p(:);
Run1p(:,2)=y1p(:);
Run1p(:,3)=z1p(:);

%% Import data and crop to patch in centre of specimen for Run 2
[    ~,    struct]    =    GenAliconaImport    ('metalSpecimen2.txt', 'findVolume', true, 'crop', [-1000, 1000, -1000, 1000]);


xyz2p=struct.xyz;
x2p=xyz2p(:,:,1);
y2p=xyz2p(:,:,2);
z2p=xyz2p(:,:,3);

%% Concatenate Run 2 patch xyz data into one matrix
Run2p=x2p(:);
Run2p(:,2)=y2p(:);
Run2p(:,3)=z2p(:);

%% Import data and crop to patch in centre of specimen for Run 3
[    ~,    struct]    =    GenAliconaImport('metalSpecimen3.txt', 'findVolume', true, 'crop', [-1000, 1000, -1000, 1000]);
xyz3p=struct.xyz;
x3p=xyz3p(:,:,1);
y3p=xyz3p(:,:,2);
z3p=xyz3p(:,:,3);

%% Concatenate Run 3 patch xyz data into one matrix
Run3p=x3p(:);
Run3p(:,2)=y3p(:);
Run3p(:,3)=z3p(:);

%% Align Run 2 to Run 1
[TR12, TT12, ER12, t12] = icp(Run1p', Run2p', 10, 'Matching', 'Delaunay'); % Calculate the translation and rotation matrix required to move Run 2 to Run 1 using Closest Iterative Point Method
Alignz12=zCylndr2+TT12(3,1); % Align the z coordinates of Run 2 to Run 1 using only the translation matrix
Alignz12=Alignz12-meanFlat1; % Subtract the mean of Run 1's reference surface to normalise the base of the specimen to zero
```

```
46    AlignVol12=dx2*dy2*sum(Alignz12(find(Alignz12>0))); % Calculate
      the volume of the aligned Run 2 data
47    DiffVol12=abs(AlignVol12-(SpecVol1)); % Compare the aligned
      volume of Run 2 to that of Run 1 to determine the absolute error
48
49    %% Align Run 3 to Run 1
50    [TR13, TT13, ER13, t13] = icp(Run1p', Run3p', 10, 'Matching',
      'Delaunay'); % Calculate the translation and rotation matrix
      required to move Run 3 to Run 1 Using Closest Iterative Point
      Method
51    Alignz13=zCylndr3+TT13(3,1); % Align the z coordinates of Run 3
      to Run 1 using only the translation matrix
52    Alignz13=Alignz13-meanFlat1; % Subtract the mean of Run 1's
      reference surface to normalise the base of the specimen to zero
53    AlignVol13=dx3*dy3*sum(Alignz13(find(Alignz13>0))); % Calculate
      the volume of the aligned Run 3 data
54    DiffVol13=abs(AlignVol13-(SpecVol1)); % Compare the aligned
      volume of Run 3 to that of Run 1 to determine the absolute error
55
56    %% Align Run 1 to Run 2
57    [TR21, TT21, ER21, t21] = icp(Run2p', Run1p', 10, 'Matching',
      'Delaunay'); % Calculate the translation and rotation matrix
      required to move Run 1 to Run 2 Using Closest Iterative Point
      Method
58    Alignz21=zCylndr1+TT21(3,1); % Align the z coordinates of Run 1
      to Run 2 using only the translation matrix
59    Alignz21=Alignz21-meanFlat2; % Subtract the mean of Run 2's
      reference surface to normalise the base of the specimen to zero
60    AlignVol21=dx1*dy1*sum(Alignz12(find(Alignz12>0))); % Calculate
      the volume of the aligned Run 1 data
61    DiffVol21=abs(AlignVol21-(SpecVol2)); % Compare the aligned
      volume of Run 1 to that of Run 2 to determine the absolute error
62
63    %% Align Run 3 to Run 2
64    [TR23, TT23, ER23, t32] = icp(Run2p', Run3p', 10, 'Matching',
      'Delaunay'); % Calculate the translation and rotation matrix
      required to move Run 3 to Run 2 Using Closest Iterative Point
      Method
65    Alignz23=zCylndr3+TT23(3,1); % Align the z coordinates of Run 3
      to Run 1 using only the translation matrix
66    Alignz23=Alignz23-meanFlat2; % Subtract the mean of Run 2's
      reference surface to normalise the base of the specimen to zero
67    AlignVol23=dx3*dy3*sum(Alignz23(find(Alignz23>0))); % Calculate
      the volume of the aligned Run 3 data
68    DiffVol23=abs(AlignVol23-(SpecVol2)); % Compare the aligned
      volume of Run 3 to that of Run 2 to determine the absolute error
69
70    %% Align Run 1 to Run 3
71    [TR31, TT31, ER31, t31] = icp(Run3p', Run1p', 10, 'Matching',
      'Delaunay'); % Calculate the translation and rotation matrix
      required to move Run 1 to Run 3 Using Closest Iterative Point
      Method
72    Alignz31=zCylndr1+TT31(3,1); % Align the z coordinates of Run 1
      to Run 3 using only the translation matrix
73    Alignz31=Alignz31-meanFlat3; % Subtract the mean of Run 3's
      reference surface to normalise the base of the specimen to zero
```

```
74    AlignVol31=dx1*dy1*sum(Alignz31(find(Alignz31>0))); % Calculate
      the volume of the aligned Run 1 data
75    DiffVol31=abs(AlignVol31-(SpecVol3)); % Compare the aligned
      volume of Run 1 to that of Run 3 to determine the absolute error
76
77    %% Align Run 2 to Run 3
78    [TR32, TT32, ER32, t32] = icp(Run3p', Run2p', 10, 'Matching',
      'Delaunay'); % Calculate the translation and rotation matrix
      required to move Run 2 to Run 3 Using Closest Iterative Point
      Method
79    Alignz32=zCylndr2+TT32(3,1); % Align the z coordinates of Run 2
      to Run 3 using only the translation matrix
80    Alignz32=Alignz32-meanFlat3; % Subtract the mean of Run 3's
      reference surface to normalise the base of the specimen to zero
81    AlignVol32=dx2*dy2*sum(Alignz32(find(Alignz32>0))); % Calculate
      the volume of the aligned Run 2 data
82    DiffVol32=abs(AlignVol32-(SpecVol3)); % Compare the aligned
      volume of Run 2 to that of Run 3 to determine the absolute error
83
84    %% Determine Error in Alignment Method
85    SumDiffVol=DiffVol12+DiffVol13+DiffVol21+DiffVol23+DiffVol31+Dif
      fVol34; %Sum the absolute errors between runs
86    MeanDiffVol=SumDiffVol/6; % Calculate the mean of the absolute
      volume errors between the all runs for this alignment method
87    SpecArea=pi*a*a; % Calculate the xy area of the specimen
88    ImpArea=pi*5000*5000; % Calculate the xy area of the implant
89    zHeightErr=MeanDiffVol/SpecArea; % Calculate the mean error in
      the z height alignment for this alignment method
90    VolErrImp=zHeightErr*ImpArea; % Calculate the predicted mean
      error in volume for the implants using this alignment method
```

B.11. Trial5.m

```
%% Determine absolute volume for Runs 1, 2 and 3
run(FindVolume.m);

%% Align Run 2 to Run 1
[TR12, TT12, ER12, t12] = icp(Run1', Run2', 10, 'Matching', 'Delaunay'); % Calculate the translation and rotation matrix required to move Run 2 to Run 1 using Closest Iterative Point Method
AlignRun12=TR12*Run2'+repmat(TT12,1,length(Run2'));
AlignRun12=AlignRun12';
Alignz12=AlignRun12(:,3);
Alignz12=reshape(Alignz12,[1500,1500]);
Alignz12=Alignz12.*(I2); % Crop the data to the radius of the cylinder
Alignz12(find(Alignz12==0))=NaN;
Alignz12=Alignz12-meanFlat1; % Subtract the mean of Run 1's reference surface to normalise the base of the specimen to zero
AlignVol12=dx2*dy2*sum(Alignz12(find(Alignz12>0))); % Calculate the volume of the aligned Run 2 data
DiffVol12=abs(AlignVol12-(SpecVol1)); % Compare the aligned volume of Run 2 to that of Run 1 to determine the absolute error

%% Align Run 3 to Run 1
[TR13, TT13, ER13, t13] = icp(Run1', Run3', 10, 'Matching', 'Delaunay'); % Calculate the translation and rotation matrix required to move Run 3 to Run 1 Using Closest Iterative Point Method
AlignRun13=TR13*Run3'+repmat(TT13,1,length(Run3'));
AlignRun13=AlignRun13';
Alignz13=AlignRun13(:,3);
Alignz13=reshape(Alignz13,[1500,1500]);
Alignz13=Alignz13.*(I3); % Crop the data to the radius of the cylinder
Alignz13(find(Alignz13==0))=NaN;
Alignz13=Alignz13-meanFlat1; % Subtract the mean of Run 1's reference surface to normalise the base of the specimen to zero
AlignVol13=dx3*dy3*sum(Alignz13(find(Alignz13>0))); % Calculate the volume of the aligned Run 3 data
DiffVol13=abs(AlignVol13-(SpecVol1)); % Compare the aligned volume of Run 3 to that of Run 1 to determine the absolute error

%% Align Run 1 to Run 2
[TR21, TT21, ER21, t21] = icp(Run2', Run1', 10, 'Matching', 'Delaunay'); % Calculate the translation and rotation matrix required to move Run 1 to Run 2 Using Closest Iterative Point Method
AlignRun21=TR21*Run1'+repmat(TT21,1,length(Run1'));
AlignRun21=AlignRun21';
Alignz21=AlignRun21(:,3);
Alignz21=reshape(Alignz21,[1500,1500]);
Alignz21=Alignz21.*(I1); % Crop the data to the radius of the cylinder
Alignz21(find(Alig
```

```
36    nz21==0))=NaN;
37    Alignz21=Alignz21-meanFlat2; % Subtract the mean of Run 2's
      reference surface to normalise the base of the specimen to zero
38    AlignVol21=dx1*dy1*sum(Alignz12(find(Alignz12>0))); % Calculate
      the volume of the aligned Run 1 data
39    DiffVol21=abs(AlignVol21-(SpecVol2)); % Compare the aligned
      volume of Run 1 to that of Run 2 to determine the absolute error
40
41    %% Align Run 3 to Run 2
42    [TR23, TT23, ER23, t32] = icp(Run2', Run3', 10, 'Matching',
      'Delaunay'); % Calculate the translation and rotation matrix
      required to move Run 3 to Run 2 Using Closest Iterative Point
      Method
43    AlignRun23=TR23*Run3'+repmat(TT23,1,length(Run3'));
44    AlignRun23=AlignRun23';
45    Alignz23=AlignRun23(:,3);
46    Alignz23=reshape(Alignz23,[1500,1500]);
47    Alignz23=Alignz23.*(I3); % Crop the data to the radius of the
      cylinder
48    Alignz23(find(Alignz23==0))=NaN;
49    Alignz23=Alignz23-meanFlat2; % Subtract the mean of Run 2's
      reference surface to normalise the base of the specimen to zero
50    AlignVol23=dx3*dy3*sum(Alignz23(find(Alignz23>0))); % Calculate
      the volume of the aligned Run 3 data
51    DiffVol23=abs(AlignVol23-(SpecVol2)); % Compare the aligned
      volume of Run 3 to that of Run 2 to determine the absolute error
52
53    %% Align Run 1 to Run 3
54    [TR31, TT31, ER31, t31] = icp(Run3', Run1', 10, 'Matching',
      'Delaunay'); % Calculate the translation and rotation matrix
      required to move Run 1 to Run 3 Using Closest Iterative Point
      Method
55    AlignRun31=TR31*Run1'+repmat(TT31,1,length(Run1'));
56    AlignRun31=AlignRun31';
57    Alignz31=AlignRun31(:,3);
58    Alignz31=reshape(Alignz31,[1500,1500]);
59    Alignz31=Alignz31.*(I1); % Crop the data to the radius of the
      cylinder
60    Alignz31(find(Alignz31==0))=NaN;
61    Alignz31=Alignz31-meanFlat3; % Subtract the mean of Run 3's
      reference surface to normalise the base of the specimen to zero
62    AlignVol31=dx1*dy1*sum(Alignz31(find(Alignz31>0))); % Calculate
      the volume of the aligned Run 1 data
63    DiffVol31=abs(AlignVol31-(SpecVol3)); % Compare the aligned
      volume of Run 1 to that of Run 3 to determine the absolute error
64
65    %% Align Run 2 to Run 3
66    [TR32, TT32, ER32, t32] = icp(Run3', Run2', 10, 'Matching',
      'Delaunay'); % Calculate the translation and rotation matrix
      required to move Run 2 to Run 3 Using Closest Iterative Point
      Method
67    AlignRun32=TR32*Run2'+repmat(TT32,1,length(Run2'));
68    AlignRun32=AlignRun32';
69    Alignz32=AlignRun32(:,3);
70    Alignz32=reshape(Alignz32,[1500,1500]);
```

```
71    Alignz32=Alignz32.*(I2); % Crop the data to the radius of the
      cylinder
72    Alignz32(find(Alignz32==0))=NaN;
73    Alignz32=zCylndr2+TT32(3,1); % Align the z coordinates of Run 2
      to Run 3 using only the translation matrix
74    Alignz32=Alignz32-meanFlat3; % Subtract the mean of Run 3's
      reference surface to normalise the base of the specimen to zero
75    AlignVol32=dx2*dy2*sum(Alignz32(find(Alignz32>0))); % Calculate
      the volume of the aligned Run 2 data
76    DiffVol32=abs(AlignVol32-(SpecVol3)); % Compare the aligned
      volume of Run 2 to that of Run 3 to determine the absolute error
77
78    %% Determine Error in Alignment Method
79    SumDiffVol=DiffVol12+DiffVol13+DiffVol21+DiffVol23+DiffVol31+Dif
      fVol34; %Sum the absolute errors between runs
80    MeanDiffVol=SumDiffVol/6; % Calculate the mean of the absolute
      volume errors between the all runs for this alignment method
81    SpecArea=pi*a*a; % Calculate the xy area of the specimen
82    ImpArea=pi*5000*5000; % Calculate the xy area of the implant
83    zHeightErr=MeanDiffVol/SpecArea; % Calculate the mean error in
      the z height alignment for this alignment method
84    VolErrImp=zHeightErr*ImpArea; % Calculate the predicted mean
      error in volume for the implants using this alignment method
```

B.12. UpperImplantVolCalc.m

```
%% Import data Run 1
[Run1Vol, struct] = GenAliconaImport('UIO5Run1RawData.txt', 'findVolume', true , 'plot', 'mesh');
xyz=struct.xyz;
x=xyz(:,:,1);
y=xyz(:,:,2);
z=xyz(:,:,3);

%% Format figure
zlabel('z, \mum');
ylabel('y, \mum');
xlabel('x, \mum');
title ('Upper Implant O2, Zero Cycles');
axis([-5000, 5000, -5000, 5000, 10500, 14500]);
axis equal;
al=-37.5;
el=30;
view(al,el);
caxis manual
caxis ([10500 11600]);
colorbar;

%% Concatenate xyz data into one matrix
Run1=x(:);
Run1(:,2)=y(:);
Run1(:,3)=z(:);

%% Crop data to radius of upper implant
a=4000;
I=sqrt(x.^2+y.^2)<=a;
xSphere=x(I);
ySphere=y(I);
zSphere=z(I);

%% Plot Figure of Run1 Sphere
figure;
scatter3(xSphere,ySphere,zSphere,5,zSphere);
zlabel('z, \mum');
ylabel('y, \mum');
xlabel('x, \mum');
title ('Upper Implant O2, Zero Cycles');
axis([-5000, 5000, -5000, 5000, 10500, 14500]);
axis equal;
al=-37.5;
el=30;
view(al,el);
caxis manual
caxis ([10500 11600]);
colorbar;

%% Calculate Run1 Sphere Volume
dx = abs(xSphere(find(diff(xSphere),1)+1)-xSphere(1));
dy = abs(ySphere(find(diff(ySphere),1)+1)-ySphere(1));
```

```
53.   Run1VolSphere = dx*dy*sum(zSphere(:));
54.
55.   %% Crop Run1 to a Exclude Sphere and Wear and Obtain Reference
      Surface
56.   L=sqrt((x).^2+(y).^2)>(a+200);
57.   xFlat=x(L);
58.   yFlat=y(L);
59.   zFlat=z(L);
60.   Run1Flat=xFlat(:);
61.   Run1Flat(:,2)=yFlat(:);
62.   Run1Flat(:,3)=zFlat(:);
63.   Run1Flat=Run1Flat(~any(isnan(Run1Flat),2),:);
64.
65.   %% Plot Figure of Run1 Reference Surface
66.   figure;
67.   scatter3(xFlat,yFlat,zFlat,5,zFlat);
68.   zlabel('z, \mum');
69.   ylabel('y, \mum');
70.   xlabel('x, \mum');
71.   title ('Upper Implant O2, Zero Cycles');
72.   axis([-5000, 5000, -5000, 5000, 10500, 14500]);
73.   axis equal;
74.   al=-37.5;
75.   el=30;
76.   view(al,el);
77.   caxis manual
78.   caxis ([11000 11600]);
79.   colorbar;
80.
81.   %% Import data Run 2
82.   [Run2Vol,   struct]   =   GenAliconaImport('UI05Run2RawData.txt',
      'findVolume', true , 'plot', 'mesh');
83.   xyz2=struct.xyz;
84.   x2=xyz2(:,:,1);
85.   y2=xyz2(:,:,2);
86.   z2=xyz2(:,:,3);
87.
88.   %% Format figure
89.   zlabel('z, \mum');
90.   ylabel('y, \mum');
91.   xlabel('x, \mum');
92.   title ('Upper Implant O2, 0.25 Million Cycles');
93.   axis([-5000, 5000, -5000, 5000, 10500, 14500]);
94.   axis equal;
95.   al=-37.5;
96.   el=30;
97.   view(al,el);
98.   caxis manual
99.   caxis ([10500 11600]);
100.  colorbar;
101.
102.  %% Concatenate xyz data into one matrix
103.  Run2=x2(:);
104.  Run2(:,2)=y2(:);
105.  Run2(:,3)=z2(:);
106.
```

```
%% Crop data to radius of upper implant
a2=4000;
I2=sqrt((x2-50).^2+(y2+100).^2)<=a2;
xSphere2=x2(I);
ySphere2=y2(I);
zSphere2=z2(I);

%% Plot Figure of Run2 Sphere
figure;
scatter3(xSphere2,ySphere2,zSphere2,5,zSphere2);
zlabel('z, \mum');
ylabel('y, \mum');
xlabel('x, \mum');
title ('Upper Implant O2, 0.25 Million Cycles');
axis([-5000, 5000, -5000, 5000, 10500, 14500]);
axis equal;
al=-37.5;
el=30;
view(al,el);
caxis manual
caxis ([10500 11600]);
colorbar;

%% Calculate Run2 Sphere Volume
dx2 = abs(xSphere2(find(diff(xSphere2),1)+1)-xSphere2(1));
dy2 = abs(ySphere2(find(diff(ySphere2),1)+1)-ySphere2(1));
Run2VolSphere = dx*dy*sum(zSphere2(:));

%% Crop Run2 to a Exclude Sphere and Wear and Obtain Reference
Surface
L2=sqrt((x2-50).^2+(y2+100).^2)>(a+200);
xFlat2=x2(L2);
yFlat2=y2(L2);
zFlat2=z2(L2);
Run2Flat=xFlat2(:);
Run2Flat(:,2)=yFlat2(:);
Run2Flat(:,3)=zFlat2(:);
Run2Flat=Run2Flat(~any(isnan(Run2Flat),2),:);

%% Plot Figure of Run2 Reference Surface
figure;
scatter3(xFlat2,yFlat2,zFlat2,5,zFlat2);
zlabel('z, \mum');
ylabel('y, \mum');
xlabel('x, \mum');
title ('Upper Implant O2, 0.25 Million Cycles');
axis([-5000, 5000, -5000, 5000, 10500, 14500]);
axis equal;
al=-37.5;
el=30;
view(al,el);
caxis manual
caxis ([11000 11600]);
colorbar;

%% Import data Run 3
```

```
[Run3Vol, struct] = GenAliconaImport('UIO5Run3RawData.txt', 'findVolume', true, 'plot', 'mesh');
xyz3=struct.xyz;
x3=xyz3(:,:,1);
y3=xyz3(:,:,2);
z3=xyz3(:,:,3);

%% Format figure
zlabel('z, \mum');
ylabel('y, \mum');
xlabel('x, \mum');
title ('Upper Implant O2, 0.5 Million Cycles');
axis([-5000, 5000, -5000, 5000, 10500, 14500]);
axis equal;
al=-37.5;
el=30;
view(al,el);
caxis manual
caxis ([10500 11600]);
colorbar;

%% Concatenate xyz data into one matrix
Run3=x3(:);
Run3(:,2)=y3(:);
Run3(:,3)=z3(:);

%% Crop data to radius of upper implant
a3=4000;
I3=sqrt((x3).^2+(y3).^2)<=a3;
xSphere3=x3(I3);
ySphere3=y3(I3);
zSphere3=z3(I3);

%% Plot Figure of Run3 Sphere
figure;
scatter3(xSphere3,ySphere3,zSphere3,5,zSphere3);
zlabel('z, \mum');
ylabel('y, \mum');
xlabel('x, \mum');
title ('Upper Implant 2, 0.5 Million Cycles');
axis([-5000, 5000, -5000, 5000, 11000, 14500]);
axis equal;
al=-37.5;
el=30;
view(al,el);
caxis manual
caxis ([10500 11600]);
colorbar;

%% Calculate Run3 Sphere Volume
dx3 = abs(xSphere3(find(diff(xSphere3),1)+1)-xSphere3(1));
dy3 = abs(ySphere3(find(diff(ySphere3),1)+1)-ySphere3(1));
Run3VolSphere = dx3*dy3*sum(zSphere3(:));

%% Crop Run3 to a Exclude Sphere and Wear and Obtain Reference Surface
```

```
L3=sqrt((x3).^2+(y3).^2)>(a3+200);
xFlat3=x3(L3);
yFlat3=y3(L3);
zFlat3=z3(L3);
Run3Flat=xFlat3(:);
Run3Flat(:,2)=yFlat3(:);
Run3Flat(:,3)=zFlat3(:);
Run3Flat=Run3Flat(~any(isnan(Run3Flat),2),:);

%% Plot Figure of Run3 Reference Surface
figure;
scatter3(xFlat3,yFlat3,zFlat3,5,zFlat3);
zlabel('z, \mum');
ylabel('y, \mum');
xlabel('x, \mum');
title ('Upper Implant 2, 0.5 Million Cycles');
axis([-5000, 5000, -5000, 5000, 10500, 14500]);
axis equal;
al=-37.5;
el=30;
view(al,el);
caxis manual
caxis ([11000 11600]);
colorbar;

%% Import data Run 4
[Run4Vol,   struct]   =   GenAliconaImport('UI05Run4RawData.txt',
'findVolume', true, 'plot', 'mesh');
xyz4=struct.xyz;
x4=xyz4(:,:,1);
y4=xyz4(:,:,2);
z4=xyz4(:,:,3);

%% Format figure
zlabel('z, \mum');
ylabel('y, \mum');
xlabel('x, \mum');
title ('Upper Implant 02, 1 Million Cycles');
axis([-5000, 5000, -5000, 5000, 10500, 14500]);
axis equal;
al=-37.5;
el=30;
view(al,el);
caxis manual
caxis ([10500 11600]);
colorbar;

%% Concatenate xyz data into one matrix
Run4=x4(:);
Run4(:,2)=y4(:);
Run4(:,3)=z4(:);

%% Crop data to radius of upper implant
A4=4000;
I4=sqrt((x4).^2+(y4).^2)<=a4;
xSphere4=x4(I4);
```

```
ySphere4=y4(I4);
zSphere4=z4(I4);

%% Plot Figure of Run4 Sphere
figure;
scatter3(xSphere4,ySphere4,zSphere4,5,zSphere4);
zlabel('z, \mum');
ylabel('y, \mum');
xlabel('x, \mum');
title ('Upper Implant 2, 1 Million Cycles');
axis([-5000, 5000, -5000, 5000, 11000, 14500]);
axis equal;
al=-37.5;
el=30;
view(al,el);
caxis manual
caxis ([10500 11600]);
colorbar;

%% Calculate Run4 Sphere Volume
dx4 = abs(xSphere4(find(diff(xSphere4),1)+1)-xSphere4(1));
dy4 = abs(ySphere4(find(diff(ySphere4),1)+1)-ySphere4(1));
Run4VolSphere = dx4*dy4*sum(zSphere4(:));

%% Crop Run4 to a Exclude Sphere and Wear and Obtain Reference
Surface
L4=sqrt((x4).^2+(y4).^2)>(a4+200);
xFlat4=x4(L4);
yFlat4=y4(L4);
zFlat4=z4(L4);
Run4Flat=xFlat4(:);
Run4Flat(:,2)=yFlat4(:);
Run4Flat(:,3)=zFlat4(:);
Run4Flat=Run4Flat(~any(isnan(Run4Flat),2),:);

%% Plot Figure of Run4 Reference Surface
figure;
scatter3(xFlat4,yFlat4,zFlat4,5,zFlat4);
zlabel('z, \mum');
ylabel('y, \mum');
xlabel('x, \mum');
title ('Upper Implant 2, 1 Million Cycles');
axis([-5000, 5000, -5000, 5000, 10500, 14500]);
axis equal;
al=-37.5;
el=30;
view(al,el);
caxis manual
caxis ([11000 11600]);
colorbar;

%% Import data Run 5
[Run5Vol,   struct]   =   GenAliconaImport('UIO5Run5RawData.txt',
'findVolume', true, 'plot', 'mesh');
xyz5=struct.xyz;
x5=xyz5(:,:,1);
```

```
y5=xyz5(:,:,2);
z5=xyz5(:,:,3);

%% Format figure
zlabel('z, \mum');
ylabel('y, \mum');
xlabel('x, \mum');
title ('Upper Implant O2, 1.5 Million Cycles');
axis([-5000, 5000, -5000, 5000, 10500, 14500]);
axis equal;
al=-37.5;
el=30;
view(al,el);
caxis manual
caxis ([10500 11600]);
colorbar;

%% Concatenate xyz data into one matrix
Run5=x5(:);
Run5(:,2)=y5(:);
Run5(:,3)=z5(:);

%% Crop data to radius of upper implant
a5=4000;
I5=sqrt((x5).^2+(y5).^2)<=a5;
xSphere5=x5(I5);
ySphere5=y5(I5);
zSphere5=z5(I5);

%% Plot Figure of Run5 Sphere
figure;
scatter3(xSphere5,ySphere5,zSphere5,5,zSphere5);
zlabel('z, \mum');
ylabel('y, \mum');
xlabel('x, \mum');
title ('Upper Implant 2, 1.5 Million Cycles');
axis([-5000, 5000, -5000, 5000, 11000, 14500]);
axis equal;
al=-37.5;
el=30;
view(al,el);
caxis manual
caxis ([10500 11600]);
colorbar;

%% Calculate Run5 Sphere Volume
dx5 = abs(xSphere5(find(diff(xSphere5),1)+1)-xSphere5(1));
dy5 = abs(ySphere5(find(diff(ySphere5),1)+1)-ySphere5(1));
Run5VolSphere = dx5*dy5*sum(zSphere5(:));

%% Crop Run5 to a Exclude Sphere and Wear and Obtain Reference
Surface
L5=sqrt((x5).^2+(y5).^2)>(a5+200);
xFlat5=x5(L5);
yFlat5=y5(L5);
zFlat5=z5(L5);
```

```
Run5Flat=xFlat5(:);
Run5Flat(:,2)=yFlat5(:);
Run5Flat(:,3)=zFlat5(:);
Run5Flat=Run5Flat(~any(isnan(Run5Flat),2),:);

%% Plot Figure of Run5 Reference Surface
figure;
scatter3(xFlat5,yFlat5,zFlat5,5,zFlat5);
zlabel('z, \mum');
ylabel('y, \mum');
xlabel('x, \mum');
title ('Upper Implant 2, 1.5 Million Cycles');
axis([-5000, 5000, -5000, 5000, 10500, 14500]);
axis equal;
al=-37.5;
el=30;
view(al,el);
caxis manual
caxis ([11000 11600]);
colorbar;

%% Import data Run 6
[Run6Vol,   struct]   =   GenAliconaImport('UIO5Run6RawData.txt',
'findVolume', true, 'plot', 'mesh');
xyz6=struct.xyz;
x6=xyz6(:,:,1);
y6=xyz6(:,:,2);
z6=xyz6(:,:,3);

%% Format figure
zlabel('z, \mum');
ylabel('y, \mum');
xlabel('x, \mum');
title ('Upper Implant O2, 2 Million Cycles');
axis([-5000, 5000, -5000, 5000, 10500, 14500]);
axis equal;
al=-37.5;
el=30;
view(al,el);
caxis manual
caxis ([10500 11600]);
colorbar;

%% Concatenate xyz data into one matrix
Run6=x6(:);
Run6(:,2)=y6(:);
Run6(:,3)=z6(:);

%% Crop data to radius of upper implant
a6=4000;
I6=sqrt((x6).^2+(y6).^2)<=a5;
xSphere6=x6(I6);
ySphere6=y6(I6);
zSphere6=z6(I6);

%% Plot Figure of Run6 Sphere
```

```
435.  figure;
436.  scatter3(xSphere6,ySphere6,zSphere6,5,zSphere6);
437.  zlabel('z, \mum');
438.  ylabel('y, \mum');
439.  xlabel('x, \mum');
440.  title ('Upper Implant 2, 2 Million Cycles');
441.  axis([-5000, 5000, -5000, 5000, 11000, 14500]);
442.  axis equal;
443.  al=-37.5;
444.  el=30;
445.  view(al,el);
446.  caxis manual
447.  caxis ([10500 11600]);
448.  colorbar;
449.
450.  %% Calculate Run6 Sphere Volume
451.  dx6 = abs(xSphere6(find(diff(xSphere6),1)+1)-xSphere6(1));
452.  dy6 = abs(ySphere6(find(diff(ySphere6),1)+1)-ySphere6(1));
453.  Run6VolSphere = dx6*dy6*sum(zSphere6(:));
454.
455.  %% Crop Run6 to a Exclude Sphere and Wear and Obtain Reference
      Surface
456.  L6=sqrt((x6).^2+(y6).^2)>(a6+200);
457.  xFlat6=x6(L6);
458.  yFlat6=y6(L6);
459.  zFlat6=z6(L6);
460.  Run6Flat=xFlat6(:);
461.  Run6Flat(:,2)=yFlat6(:);
462.  Run6Flat(:,3)=zFlat6(:);
463.  Run6Flat=Run6Flat(~any(isnan(Run6Flat),2),:);
464.
465.  %% Plot Figure of Run6 Reference Surface
466.  figure;
467.  scatter3(xFlat6,yFlat6,zFlat6,5,zFlat6);
468.  zlabel('z, \mum');
469.  ylabel('y, \mum');
470.  xlabel('x, \mum');
471.  title ('Upper Implant 2, 2 Million Cycles');
472.  axis([-5000, 5000, -5000, 5000, 10500, 14500]);
473.  axis equal;
474.  al=-37.5;
475.  el=30;
476.  view(al,el);
477.  caxis manual
478.  caxis ([11000 11600]);
479.  colorbar;
480.
481.  %% Align the Run2 to Run1
482.  [TR12, TT12, ER12, t12] = icp(Run1Flat', Run2Flat');
483.  AlignRun12=TR12*Run2'+repmat(TT12,1,length(Run2')); % Align the
      coordinates of Run 2 to Run 1 using the rotation and translation
      matrices
484.  AlignRun12=AlignRun12'; % Invert the matrix
485.  Alignz12=AlignRun12(:,3); % Extract the z coordinates
486.  Alignz12=reshape(Alignz12,[2171,    1971]);%    Reshape    the    z
      coordinates to match the xy grid
```

```
487. Alignz12=Alignz12.*(I2); % Crop the data to the size of the
     implant
488. Alignz12(find(Alignz12==0))=NaN; % Make zero values to be "Not A
     Number" to remove from calculation
489. AlignVol12Sphere=dx2*dy2*sum(Alignz12(find(Alignz12>0))); %
     Calculate the volume of the aligned Run 2 data
490. DiffVol12=abs(AlignVol12Sphere-(Run1VolSphere));% Compare the
     aligned volume of Run 2 to that of Run 1 to determine the
     absolute error
491. save('Run12Results_ExtNone_12O215', 'AlignRun12',
     'AlignVol12Sphere', 'Alignz12', 'DiffVol12', 'ER12', 't12',
     'TR12', 'TT12'); %Save output variables to .mat file
492.
493. %% Align Run3 to Run1
494. [TR13, TT13, ER13, t13] = icp(Run1Flat', Run3Flat');
495. AlignRun13=TR13*Run3'+repmat(TT13,1,length(Run3')); % Align the
     coordinates of Run 3 to Run 1 using the rotation and translation
     matrices
496. AlignRun13=AlignRun13'; % Invert the matrix
497. Alignz13=AlignRun13(:,3); % Extract the z coordinates
498. Alignz13=reshape(Alignz13,[2182, 2175]);% Reshape the z
     coordinates to match the xy grid
499. Alignz13=Alignz13.*(I3); % Crop the data to the size of the
     implant
500. Alignz13(find(Alignz13==0))=NaN; % Make zero values to be "Not A
     Number" to remove from calculation
501. AlignVol13Sphere=dx3*dy3*sum(Alignz13(find(Alignz13>0))); %
     Calculate the volume of the aligned Run 3 data
502. DiffVol13=abs(AlignVol13Sphere-(Run1VolSphere));% Compare the
     aligned volume of Run 3 to that of Run 1 to determine the
     absolute error
503. save('Run13Results_ExtNone_12O215', 'AlignRun13',
     'AlignVol13Sphere', 'Alignz13', 'DiffVol13', 'ER13', 't13',
     'TR13', 'TT13'); %Save output variables to .mat file
504.
505. %% Align Run4 to Run1
506. [TR14, TT14, ER14, t14] = icp(Run1Flat', Run4Flat');
507. AlignRun14=TR14*Run4'+repmat(TT14,1,length(Run4')); % Align the
     coordinates of Run 4 to Run 1 using the rotation and translation
     matrices
508. AlignRun14=AlignRun14'; % Invert the matrix
509. Alignz14=AlignRun14(:,3); % Extract the z coordinates
510. Alignz14=reshape(Alignz14,[2451, 2175]);% Reshape the z
     coordinates to match the xy grid
511. Alignz14=Alignz14.*(I4); % Crop the data to the size of the
     implant
512. Alignz14(find(Alignz14==0))=NaN; % Make zero values to be "Not A
     Number" to remove from calculation
513. AlignVol14Sphere=dx4*dy4*sum(Alignz14(find(Alignz14>0))); %
     Calculate the volume of the aligned Run 4 data
514. DiffVol14=abs(AlignVol14Sphere-(Run1VolSphere));% Compare the
     aligned volume of Run 4 to that of Run 1 to determine the
     absolute error
515. save('Run14Results_ExtNone_12O215', 'AlignRun14',
     'AlignVol14Sphere', 'Alignz14', 'DiffVol14', 'ER14', 't14',
     'TR14', 'TT14'); %Save output variables to .mat file
```

```
516.
517.  %% Align Run5 to Run1
518.  [TR15, TT15, ER15, t15] = icp(Run1Flat', Run5Flat');
519.  AlignRun15=TR15*Run5'+repmat(TT15,1,length(Run5')); % Align the
      coordinates of Run 5 to Run 1 using the rotation and translation
      matrices
520.  AlignRun15=AlignRun15'; % Invert the matrix
521.  Alignz15=AlignRun15(:,3); % Extract the z coordinates
522.  Alignz15=reshape(Alignz15,[2451,   2175]);%   Reshape   the   z
      coordinates to match the xy grid
523.  Alignz15=Alignz15.*(I5); % Crop the data to the size of the
      implant
524.  Alignz15(find(Alignz15==0))=NaN; % Make zero values to be "Not A
      Number" to remove from calculation
525.  AlignVol15Sphere=dx5*dy5*sum(Alignz15(find(Alignz15>0)));      %
      Calculate the volume of the aligned Run 5 data
526.  DiffVol15=abs(AlignVol15Sphere-(Run1VolSphere));%  Compare  the
      aligned volume of Run 5 to that of Run 1 to determine the
      absolute error
527.  save('Run15Results_ExtNone_120215',                'AlignRun15',
      'AlignVol15Sphere',  'Alignz15',  'DiffVol15',  'ER15',  't15',
      'TR15', 'TT15'); %Save output variables to .mat file
528.
529.  %% Align Run6 to Run1
530.  [TR16, TT16, ER16, t16] = icp(Run1Flat', Run6Flat');
531.  AlignRun16=TR16*Run6'+repmat(TT16,1,length(Run6')); % Align the
      coordinates of Run 6 to Run 1 using the rotation and translation
      matrices
532.  AlignRun16=AlignRun16'; % Invert the matrix
533.  Alignz16=AlignRun16(:,3); % Extract the z coordinates
534.  Alignz16=reshape(Alignz16,[2451,   2175]);%   Reshape   the   z
      coordinates to match the xy grid
535.  Alignz16=Alignz16.*(I6); % Crop the data to the size of the
      implant
536.  Alignz16(find(Alignz16==0))=NaN; % Make zero values to be "Not A
      Number" to remove from calculation
537.  AlignVol16Sphere=dx6*dy6*sum(Alignz16(find(Alignz16>0)));      %
      Calculate the volume of the aligned Run 6 data
538.  DiffVol16=abs(AlignVol16Sphere-(Run1VolSphere));%  Compare  the
      aligned volume of Run 6 to that of Run 1 to determine the
      absolute error
539.  save('Run16Results_ExtNone_120215',                'AlignRun16',
      'AlignVol16Sphere',  'Alignz16',  'DiffVol16',  'ER16',  't16',
      'TR16', 'TT16');
540.
541.  %%Email to say the script has finished running
542.  props = java.lang.System.getProperties;
543.  props.setProperty('mail.smtp.auth', 'true');
544.  setpref('Internet', 'SMTP_Server', 'smtp.bham.ac.uk');
545.  setpref('Internet', 'E_mail', 'ncg937@bham.ac.uk');
546.  setpref('Internet', 'SMTP_Username', 'ncg937@bham.ac.uk');
547.  setpref('Internet', 'SMTP_Password', '*******');
548.  msg=num2str(DiffVol12,    DiffVol13,    DiffVol14,    DiffVol15,
      DiffVol16)
549.  sendmail('naomicharlottegreen@hotmail.com',  'It  has  finished',
      msg);
```

List of References

Adachi, K., Kato, K. and Chen N. (1997) Wear map of ceramics. **Wear**, 203-204: 291-301

Adachi, K. and Kato, K. (2000) Formation of smooth wear surfaces on alumina ceramics by embedding and tribo-sintering of fine wear particles. **Wear**, 245: 84–91

Adams, M. A. and Hutton, W. C. (1980) The effect of posture on the role of the apophysial joints in resisting intervertebral compressive forces. **Journal of Bone and Joint Surgery: British Volume**, 62 (3): 358-362

Adams, M. A., McNally, D. S. and Dolan, P (1996) 'Stress' distributions inside intervertebral discs. The effects of age and degeneration. **Journal of Bone and Joint Surgery: British Volume**, 78B (6): 965-972

Aiello, L., Dean, C. and Cameron, J. (2002) **An Introduction to Human Evolutionary Anatomy.** London: Academic Press

Anderson, P. A., Rouleau, J. P., Bryan, V. E. and Carlson, C. S. (2003) Wear analysis of the Bryan cervical disc prosthesis. **Spine**, 28 (20): S186-S194

Anderson, P. A., Kurtz, S. M. and Toth, J. M. (2006) Explant analysis of total disc replacement. **Seminars in Spine Surgery**, 18 (2): 109-116

ASTM International (2005) **F2423-05** Standard guide for functional, kinematic, and wear assessment of total disc prostheses. West Conshohocken: ASTM International

Bayer, R. G. (2004) **Mechanical Wear Fundamentals and Testing, Revised and Expanded.** Boca Raton: CRC Press

Bertagnoli, R., Duggal, N., Pickett, G. E., Wigfield, C., Gill, S., Karg, A. and Voigt, S. (2005) Cervical Total Disc Replacement, Part Two: Clinical results. **Orthopedic Clinics of North America,** 36 (3) 355-362

Bhushan, B. (2013) **Tribology in Practice Series: Introduction to Tribology (2).** Chichester: Wiley

Bifano, T. G., Dow, T. A. and Scattergood, R. O. (1991) Ductile-regime grinding: a new technology for machining brittle materials. **Journal of Engineering for Industry**, 113 (2): 184-189

Bills, P. J., Brown, L., Jiang, X. and Blunt, L. (2005) A metrology solution for the orthopaedic industry. **Journal of Physics Conference Series**, 13 (1): 316-319

Bills, P. J., Racasan, R. Underwood, R. J., Cann, P., Skinner, J., Hart, A. J., Jiang, X. and Blunt, L. (2012) Volumetric wear assessment of retrieved metal-on-metal hip prostheses and the impact of measurement uncertainty. **Wear**, 274: 212-219

Bland, J. M. and Altman, D. G. (1986) Statistical methods for assessing agreement between two methods of clinical measurement. **Lancet**, 1 (8476): 307-310

Bland, J. M. and Altman, D. G. (1999) Statistical methods in medical research. **Statistical Methods in Medical Research**, 8 (2): 135-160

Blomberg, A., Olsson, M. and Hogmark, S. (1994) Wear mechanisms and tribo mapping of Al_2O_3 and Sic in dry sliding. **Wear**, 171: 77-89

Blumenthal, S., McAfee, P. C., Guyer, R. D., Hochschuler, S. H., Geisler, F. H., Holt, R. T., Garcia, R., Regan, J. J. and Ohnmeiss, D. D. (2005) A prospective, randomized, multicenter Food and Drug Administration investigational device

exemptions study of lumbar total disc replacement with the CHARITÉ™ artificial disc versus lumbar fusion. Part I: Evaluation of clinical outcomes. **Spine**, 30 (14): 1565-1575

Blunt, L., Bills, P. J., Jiang, X-Q. and Chakrabarty, G. (2008) Improvement in the assessment of wear of total knee replacements using coordinate-measuring machine techniques. **Proceedings of the Institution of Mechanical Engineers. Part H, Journal of Engineering in Medicine**, 222 (3): 309-318

Blunt, L., Bills, P., Jiang, X., Hardacker, C. and Chakrararty, G. (2009) The role of tribology and metrology in the latest development of bio-materials. **Wear**, 266: 424-431

Bone, M. C., Sidaginamale, R. P., Lord, J. K., Scholes, S. C., Joyce, T. J., Nargol A. V. F. and Langton, D. J. (2015) Determining material loss from the femoral stem trunnion in hip arthroplasty using a coordinate measuring machine. **Proceedings of the Institution of Mechanical Engineers Part-H Journal of Engineering in Medicine**, 229 (1): 69-76

Boos, N., Weissbach, S., Rohrbach, H., Weiler, C., Spratt, K. F. and Nerlich, A. G. (2002) Classification of age-related changes in lumbar intervertebral discs - 2002 Volvo award in basic science. **Spine**, 27 (23): 2631–2644

Brandt, J. M., Brière, L .K., Marr, J., MacDonald, S. J., Bourne, R. B. and Medley, J. B. (2010) Biochemical comparisons of osteoarthritic human synovial fluid with calf sera used in knee simulator wear testing. **Journal of Biomedical Materials Research - Part A**, 94 (3): 961-971

Brinksmeier, E., Mutlugünes, Y., Klocke, F., Aurich, J. C., Shore, P. and Ohmori, H. (2010) Ultra-precision grinding. **CIRP Annals - Manufacturing Technology**, 59 (2): 652-671

British Standards Institution (1998a) **BS EN ISO 4287:1998+A1:2009** Geometrical product specification (GPS) — Surface texture: Profile method — Terms, definitions and surface texture parameters. London: BSI

British Standards Institution (1998b) **BS EN ISO 4288:1998** Geometric Product Specification (GPS) — Surface texture — Profile method: Rules and procedures for the assessment of surface texture. London: BSI

British Standards Institution (2000) **BS ISO 14242-2:2000** Implants for surgery: Wear of total hip joint prostheses Part 2: Methods of measurement. London: BSI

British Standards Institution (2009) **BS ISO 14243-1:2009** Implants for surgery. Wear of total knee-joint prostheses. Loading and displacement parameters for wear-testing machines with load control and corresponding environmental conditions for test. London: BSI

British Standards Institution (2011a) **BS ISO 18192-1:2011** Implants for surgery: Wear of total intervertebral spinal disc prostheses. Part 1: Loading and displacement parameters for wear testing and corresponding environmental conditions for test. London: BSI

British Standards Institution (2011b) **BS ISO 7206-2:2011** Implants for surgery — Partial and total hip joint prostheses Part 2: Articulating surfaces made of metallic, ceramic and plastics materials. London: BSI

British Standards Institution (2014) **BS ISO 14242-1:2014** Implants for surgery. Wear of total hip-joint prostheses. Loading and displacement parameters for wear-testing machines and corresponding environmental conditions for test. London: BSI

Brockett, C., Williams, S., Jin, Z., Isaac, G. and Fisher, J. (2007) Friction of total hip replacements with different bearings and loading conditions. **Journal of Biomedical Materials Research Part B: Applied Biomaterials**, 81 (2): 508-515

Bushelow, M., Nechtow, W., Hinter, M., Dressel, H. and Kaddick, C. (2008) Wear testing of a cervical Total Disc Replacement: effect of motion and load parameters on wear rate and particle morphology. **Transactions of the 54th Annual Meeting of the Orthopaedic Research Society**, San Francisco, CA

Carmignato, S., Spinelli, M., Affatato, S. and Savio, E. (2011) Uncertainty evaluation of volumetric wear assessment from coordinate measurements of ceramic hip joint prostheses. **Wear**, 270: 584-590

Clarke, I. C., Good, V., Williams, P., Schroeder, D., Anissian, L., Stark, A., Oonishi, H., Schuldies, J. and Gustafson, G. (2000) Ultra-low wear rates for rigid-on-rigid bearings in total hip replacements. **Proceedings of the Institution of Mechanical Engineers Part-H Journal of Engineering in Medicine**, 214 (4): 214-331

ClinicalTrials.gov (2016) **A Clinical Trial Evaluating a Total Disc Replacement in Patients with Cervical Disc Disease (CerPass)**. [online] Available from https://clinicaltrials.gov/ct2/show/NCT01433367 [Accessed 13th September 2016]

Cook, R. B., Shearwood-Porter, N. R., Latham, J. M. and Wood, R. J. K. (2015) Volumetric assessment of material loss from retrieved cemented metal hip replacement stems. **Tribology International,** 89: 105-108

Cramer, G. D. and Darby, S. A. (2013) **Clinical Anatomy of the Spine, Spinal Cord, and ANS.** Saint Louis: Mosby

Cui, C. (1995) **Experimental Investigation of Thermofluids in the Grinding Zone.** PhD Thesis. University of Connecticut

Denkena, B. and Friemuth, T. (2003) Potentials of different process kinematics in micro grinding. **CIRP Annals Manufacturing Technology**, 52 (1): 463-466

Denkena, B., Reichstein, M., van der Meer, M., Ostermeier, S. and Hurschler, C. (2008) Wear analysis and finishing of bioceramic implant surfaces. **Studies in Health Technology and Informatics**, 133 (1): 75-82

Dolan, P., Earley, M. and Adams, M. A. (1994) Bending and compressive stresses acting on the lumbar spine during lifting activities. **Journal of Biomechanics**, 27 (10): 1237-1248

Dynamic Ceramic (2014) **Material Properties** [online]. Available from http://www.dynacer.com/wp-content/themes/devvine/PDF/Material%20Properties%20datasheet.pdf [Accessed 22nd September 2014]

Eckold, D. G. (2016) **Spinal Implants—the Problems of Debris**. PhD Thesis. University of Birmingham

Enan, A., Abu-Hegazy, M., Abo-Hegy, M. and Al-Kerdany, A. (2011) Single level cervical arthroplasty with the Discocerv (R) prosthesis: a preliminary report. **Acta Orthopaedica Belgica**, 77 (2): 224-229

Feltrin, G. P., Macchi, V., Saccavini, C., Tosi, E., Dus, C., Fassina, A., Parenti, A. and De Caro, R. (2001) Fractal analysis of lumbar vertebral cancellous bone architecture. **Clinical Anatomy**, 14 (6): 414-417

Feng, H. S. and Li, H. (2002) Constant scallop-height tool path generation for three-axis sculptured surface generation. **Computer-Aided Design**, 34 (9): 647-654

Finn, M. A., Brodke, D. S., Daubs, M., Patel, A. and Bachus, K. N. (2009) Local and global subaxial cervical spine biomechanics after single-level fusion or cervical arthroplasty. **European Spine Journal**, 18 (10): 1520-1527

Fogh-Andersen, N., Altura, B. M., Altura, B. T. and Siggaard-Andersen, O. (1995) Composition of interstitial fluid. **Clinical Chemistry**, 41 (10): 1522-1525

Gallo, J., Goodman, S. B., Konttinen, Y. T., Wimmer, M. A. and Holinka, M. (2013). Osteolysis around total knee arthroplasty: a review of pathogenetic mechanisms. **Acta Biomaterialia**, 9 (9): 8046–8058

German, J. W. and Foley, K. T. (2005) Disc arthroplasty in the management of the painful lumbar motion segment. **Spine**, 30 (16S): S60–S67

Ghosh, S., Choudhury, D., Roy, T., Moradi, A., Masjuki, H. H. and Pingguan-Murphy, B. (2015) Tribological performance of the biological components of synovial fluid in artificial joint implants. **Science and Technology of Advanced Materials**, 16 (4): 045002

Gibson, J. N., Grant, I. C. and Waddell, G. (1999) The Cochrane review of surgery for lumbar disc prolapse and degenerative lumbar spondylosis. **Spine**, 24 (17): 1820–1832

Gibson, J. N. and Waddell, G. (2005) Surgery for degenerative lumbar spondylosis: updated Cochrane review. **Spine**, 30 (20): 2312–2320

Gray, H. (1918) **Anatomy of the Human Body**. Philadelphia: Lea and Febiger

Green, N. C., Keaveney, S., Shepherd, D. E. T., Ahearne, E. and Byrne, G. (2013) Articulating surfaces of ceramic Total Disc Replacements: requirements for surface finish and their production using grinding processes. In Byrne, G., Mullany, B., Ahearne, E. and Green, N. C. (eds.) **Proceedings of the 30th International Manufacturing Conference,** University College Dublin, Ireland ISBN 978-1-90-525475-0, pp 217-227

Green, N. C., Bowen J., Hukins D. W. L. and Shepherd D. E. T. (2015) Assessment of non-contacting optical methods to measure wear and surface roughness in ceramic total disc replacements. **Proceedings of the Institution of Mechanical Engineers Part-H Journal of Engineering in Medicine**, 229 (3): 245-254

Green, T. R., Fisher, J., Stone, M., Wroblewski, B. M. and Ingham, E. (1998) Polyethylene particles of a critical size are necessary for the induction of cytokines by macrophages in vitro. **Biomaterials**, 19 (24): 2297-2302

Green, T. R., Fisher, J., Matthews, J. B., Stone, M. H. and Ingham, E. (2000) Effect of size and dose on bone resorption activity of macrophages by *in vitro* clinically relevant ultra high molecular weight polyethylene particles. **Journal of Biomedical Materials Research**, 53 (3): 490-497

Grupp, T. M., Yue, J. J., Garcia, R., Basson, J., Schwiesau, J., Fritz, B. and Blomer, B. (2009) Biotribological evaluation of artificial disc arthroplasty devices: influence of loading and kinematic patterns during in vitro wear simulation. **European Spine Journal**, 18 (1): 98–108

Grupp, T. M., Meisel, H. J. Cotton, J. A., Schwiesau, J., Fritz, B., Blömer, B. and Jansson, V. (2010) Alternative bearing materials for intervertebral disc arthroplasty. **Biomaterials**, 31 (3): 523-531

Guerin, H. A. L. and Elliott, D. M. (2006) Structure and properties of soft tissues in the spine. In: Kurtz, S. M. and Edidin, A. A. (eds.) **Spine Technology Handbook.** Burlington: Academic Press, pp. 36-62

Guyer, R. D., McAfee, P. C., Banco, R. J., Bitan, F. D., Cappuccino, A., Geisler, F. H., Hochschuler, S. H., Holt, R. T., Jenis, L. G., Majd, M. E., Regan, J. J., Tromanhauser, S. G., Wong, D. C. and Blumenthal, S. L. (2009) Prospective, randomized, multicenter Food and Drug Administration investigational device exemption study of lumbar total disc replacement with the CHARITÉ artificial disc versus lumbar fusion: five-year follow-up. **The Spine Journal**, 9 (5): 374-386

Guyer, R. D., Thongtrangan, I. and Ohnmeiss, D. D. (2012) Outcomes of CHARITE lumbar artificial disk versus fusion: 5-year data. **Seminars in Spine Surgery**, 24 (1): 32–36

Hamrock, B. J. and Dowson, D. (1978) Elastohydrodynamic lubrication of elliptical contacts for materials of low elastic modulus. I. Fully flooded conjunction. **Journal of Lubrication Technology**, 100 (2): 236–245

Hsu, S. M., Wang, Y. S. and Munro, R. G. (1989) Quantitative wear maps as a visualization of wear mechanism transitions in ceramic materials. **Wear**, 134 (1): 1-11

Huang, H. and Liu, Y. C. (2003) Experimental investigations of machining characteristics and removal mechanisms of advanced ceramics in high speed deep grinding. **International Journal of Machine Tool Manufacturing**, 43 (8): 811–823

Hukins, D. W. L. (1988) Disc structure and function. In: Gosh, P. (ed.) **The Biology of the Intervertebral Disc, Vol. 1.** Boca Raton: CRC Press, pp. 1-37

Hukins, D. W. L. (1992) A simple model for the function of proteoglycans and collagen in the response to compression of the intervertebral disc. **Proceedings of the Royal Society Part B- Biological Sciences**, 249 (1326): 281-285

Hukins, D. W. L. and Aspden, R. M. (1985) Composition and properties of connective tissues. **Trends in Biochemical Sciences**, 10 (7): 260-264

Hukins, D. W. L. and Meakin, J. R. (2000) Relationship between structure and mechanical function of the tissues of the intervertebral joint. **American Zoology**, 40 (1): 42–52

Hwang, T. W., Evans, C. J. and Malkin, S. (2000) An investigation of high speed grinding with electroplated diamond wheels. **CIRP Annals Manufacturing Technology**, 49 (1): 245–248

Hyde, P. J., Fisher, J., Tipper, J. and Hall, R. M. (2015) Wear and biological effects of a semi-constrained total disc replacement subject to modified ISO

standard test conditions. **Journal of the Mechanical Behavior of Biomedical Materials**, 44: 43-52

Hyde, P. J., Fisher, J. and Hall, R. M. (2016) Wear simulation of a polyethylene-on- metal cervical total disc replacement under different concentrations of bovine serum lubricant. **Proceedings of the Institution of Mechanical Engineers Part-H Journal of Engineering in Medicine**, 230 (5): 481-488

Iatridis, J.C., Setton, L.A., Weidenbaum, M. and Mow, V. C. (1997) Alterations in the mechanical behavior of the human lumbar nucleus pulposus with degeneration and aging. **Journal of Orthopaedic Research**, 15 (2): 318-322

Ingham, E. and Fisher, J. (2000) Biological reactions to wear debris in total joint replacement. **Proceedings of the Institution of Mechanical Engineers Part-H Journal of Engineering in Medicine**, 214 (1): 21-37

Ingham, E. and Fisher, J. (2005) The role of macrophages in osteolysis of total joint replacement. **Biomaterials**, 26 (11): 1271–1286

International Standards Organisation (2008) **ISO/IEC Guide 98-3:2008 Ed 1**. Uncertainty of measurement. Guide to the expression of uncertainty in measurement. Switzerland: International Standards Organisation

Jacobs W. C. H., Van Der Gaag N. A., Kruyt M. C., Tuschel A., De Kleuver M., Peul W. C., Verbout A. J. and Oner F. C. (2013) Total disc replacement for chronic discogenic low back pain: A Cochrane review. **Spine**, 38 (1): 24-36

Jain, V. K. (2008) Abrasive-based nano-finishing techniques: an overview. **Machining Science and Technology**, 12 (3): 257–294

Janssen, M. E., Zigler, J. E., Spivak, J. M., Delamarter, R. B., Darden, B. V. and Kopjar, B. (2015) ProDisc-C total disc replacement versus anterior cervical discectomy and fusion for single-level symptomatic cervical disc disease. Seven-year follow-up of the prospective randomized US Food and Drug Administration investigational device exemption study. **Journal of Bone and Joint Surgery – American Volume**, 97A (21): 1738-1747

Jennings, A. (2013) **Sphere Fit (Least Squared)** [online] MATLAB Central File Exchange. Available from: https://www.mathworks.com/matlabcentral/fileexchange/34129-sphere-fit--least-squared- [Accessed 25th September, 2014]

Johannessen, W. and Elliott, D. M. (2005) Effects of degeneration on the biphasic material properties of human nucleus pulposus in confined compression. **Spine**, 30, (24): E724–E729

Kato, K. and Adachi, K. (2002) Wear of advanced ceramics. **Wear**, 253: 1097-1104

Kim, K. I. and Kim. K (1995) A new machine strategy for sculptured surfaces using offset surface. **International Journal of Production Research**, 33 (6): 1683-1693

Ku Leuven (2016) **Equipment - Department of Mechanical Engineering** [online]. Available from: http://www.mech.kuleuven.be/en/research/dm/equipment/facilities [Accessed on 7th March 2016]

Kurtz, S. M. and Edidin, A. A. (2006) The basic tools and terminology of spine treatment. In: Kurtz, S. M. and Edidin, A. A. (eds.) **Spine Technology Handbook.** Burlington: Academic Press, pp. 1-9

Kurtz, S. M., van Ooij, A., Ross, R., de Waal Malefijt, J., Peloza, J., Ciccarelli, L. and Villarraga, M. L. (2007) Polyethylene wear and rim fracture in total disc arthroplasty. **Spine Journal**, 7(1): 12–21

Kurtz, S. M., Toth, J. M., Siskey, R., Ciccarelli, L., Macdonald, D., Isaza, J., Lanman, T., Punt, I., Steinbeck, M., Goffin, J. and van Ooij, A. (2012a) The latest lessons learned from retrieval analyses of ultra-high molecular weight polyethylene, metal-on-metal, and alternative bearing total disc replacements. **Seminars in Spine Surgery**, 24 (1): 57–70

Kurtz, S. M., Ciccarelli, L., Harper, M. L., Siskey, R., Shorez, J. and Chan, F. W. (2012b) Comparison of in vivo and simulator-retrieved metal-on-metal cervical disc replacements. **International Journal of Spine Surgery,** 6: 145–156

Lancaster, J. G., Dowson, D., Isaac, G. H. and Fisher, J (1997) The wear of ultra-high molecular weight polyethylene sliding on metallic and ceramic counterfaces representative of current femoral surfaces in joint replacement. **Proceedings of the Institution of Mechanical Engineers Part-H Journal of Engineering in Medicine**, 211 (1): 17-24

Langton, D. J., Joyce, T. J., Mangat, N., Lord, J. K., Van Orsouw, M., De Smet, K. A. and Nargol, A. V. F., (2011) Reducing metal ion release following hip resurfacing arthroplasty. **Orthopaedic Clinics of North America**, 42 (2): 169–180

Langton, D. J., Sidaginamale, R., Lord, J. K., Nargol, A. V. F. and Joyce, T. J. (2012) Taper junction failure in large-diameter metal-on-metal bearings. **Bone and Joint Research**, 1 (4): 56-63

Langton, D. J., Sidaginamale, R. P., Holland, J. P., Deehan, D., Joyce, T. J., Nargol, A. V. F., Meek, R. D. and Lord, J. K. (2014) Practical considerations for volumetric wear analysis of explanted hip arthroplasties. **Bone and Joint Research**, 3 (3): 60–68

Lartigue, C., Duc, C. and Tournier, C. (1999) Machining of free-form surfaces and geometrical specifications. **Proceedings of the Institution of Mechanical Engineers, Part B: Journal of Engineering Manufacture**, 213 (1): 21-27

Lebl, D. R., Cammisa, F. P. Jr, Girardi, F. P., Wright, T. and Abjornson. C. (2012) The mechanical performance of cervical total disc replacements *in vivo*: prospective retrieval analysis of ProDisc-C devices. **Spine**, 37 (26): 2151-2160

Lee, S. W., Hsu, S. M. and Munro, R. G. (1990) Ceramic wear maps: SiC whisker reinforced alumina. In Rohatgi, P. K., Blau, P. J. and Yust, C. S. (eds.) **Tribology of Composite Materials**. Metals Park, OH: ASTM International, pp. 35-41

Lee, J. H., Jung, T. G., Kim, H. S., Jang, J. S. and Lee, S. H. (2010) Analysis of the incidence and clinical effect of the heterotopic ossification in a single-level cervical artificial disc replacement. **The Spine Journal,** 10 (8): 676–682

Leung, C., Casey, A. T., Goffin, J., Kehr, P., Liebig, K., Lind, B., Logroscino, C. and Pointillart, V. (2005) Clinical significance of heterotopic ossification in cervical disc replacement: a prospective multicenter clinical trial. **Neurosurgery**, 57 (4): 759-63

Li, K. and Liao, T. W. (1997) Modelling of ceramic grinding processes Part I. Number of cutting points and grinding forces per grit. **Journal of Materials Processing Technology**, 65 (1-3): 1-10

Liao, Y. S., Benya, P. D. and McKellop, H. A. (1999) Effect of protein lubrication on the wear properties of materials for prosthetic joints. **Journal of Biomedical Materials Research**, 48 (4): 465-473

Lord, J. K., Langton, D. J., Nargol, A. V. F. and Joyce, T. J. (2011) Volumetric wear assessment of failed metal-on-metal hip resurfacing prostheses. **Wear**, 272: 79-87

Lynch, P. J. and Jaffe, C. C. (2006) **Human Skeleton Diagrams, Lateral and Anterior Views.** [online] Available from https://commons.wikimedia.org/wiki/File:Skeleton_whole_body_ant_lat_views.svg [Accessed 7th September 2016]. Image used under a Creative Commons Attribution 2.5 License (https://creativecommons.org/licenses/by/2.5/legalcode)

Lyons, G., Eisenstein, S. M. and Sweet, M. B. E. (1981) Biochemical changes in intervertebral disc degeneration. **Biochimica et Biophysica Acta - General Subjects**, 673 (4): 443-453

Macdonald, N. and Bankes, M. (2014) Ceramic on ceramic hip prostheses: a review of past and modern materials. **Archives of Orthopaedic and Trauma Surgery**, 134 (9): 1325–1333

Malkin, S. (1989) **Grinding Technology: Theory and Applications of Machining with Abrasives.** Chichester: Ellis Horwood

Maniadakis, N. and Gray, A. (2000) The economic burden of back pain in the UK. **Pain**, 84 (1): 95-103

Mannion, A. F., Leivseth, G., Brox, J. I., Fritzell, P., Hagg, O. and Fairbank, J. C. (2014) ISSLS Prize winner: Long-term follow-up suggests spinal fusion is associated with increased adjacent segment disc degeneration but without influence on clinical outcome: results of a combined follow-up from 4 randomized controlled trials. **Spine**, 39 (17): 1373-1383

Marchand, F. and Ahmed, A. M. (1990) Investigation of the laminate structure of lumbar disc anulus fibrosus. **Spine**, 15 (5): 402-410

Marcolongo, M. S., Cannella, M. and Massey, C. J. (2006) Nucleus replacement of the intervertebral disc. In: Kurtz, S. M. and Edidin, A. A. (eds.) **Spine Technology Handbook.** Burlington: Academic Press, pp. 281-302

Maru, M. M., Amaral, M., Rodrigues, S. P., Santos, R., Gouvea, C. P., Archanjo, B. S., Trommer, R. M., Oliveira, F. J., Silva, R. F. and Achete, C. (2015) The high performance of nanocrystalline CVD diamond coated hip joints in wear simulator test. **Journal of the Mechanical Behavior of Biomedical Materials**, 49: 175-185

Mazzucco, D., Scott, R. and Spector, M. (2004) Composition of joint fluid in patients undergoing total knee replacement and revision arthroplasty: correlation with flow properties. **Biomaterials**, 25 (18): 4433-4445

McAfee, P. C., Cunningham, B., Holsapple, G., Adams, K., Blumenthal, S., Guyer, R. D., Dmietriev, A., Maxwell, J. H., Regan, J. J. and Isaza, J. (2005) A prospective, randomized, multicentre Food and Drug Administration investigational device exemption study of lumbar total disc replacement with

the CHARITÉ™ artificial disc versus lumbar fusion. Part II: Evaluation of radiographic outcomes and correlation of surgical technique accuracy with clinical outcomes. **Spine**, 30 (14): 1576-1583

McEwen, H. M. J., Barnett, P. I., Bell, C. J., Farrar, R., Auger, D. D., Stone, M. H. and Fisher, J. (2005) The influence of design, materials and kinematics on the in vitro wear of total knee replacements. **Journal of Biomechanics**, 38 (2): 357-365

McNally, D. S. and Adams, M. A. (1992) Interval intervertebral disc mechanics as revealed by stress profilometry. **Spine**, 17 (1): 66-73

McNally, D. S. and Arridge, R. G. C. (1995) An analytical model of intervertebral disc mechanics. **Journal of Biomechanics**, 28 (1): 53-68

Medtronic (2016) **Medtronic Receives FDA Approval for BRYAN® Cervical Disc System.** [online] Available from http://newsroom.medtronic.com/phoenix.zhtml?c=251324&p=irol-newsArticle&ID=1774173 [Accessed 15th September 2016]

Mercer, S. B. and Bogduk N. (1999) The ligaments and anulus fibrosus of human adult cervical intervertebral discs. **Spine**, 24 (7): 619-626

Moghadas, P. (2012) **Tribology of Ball-and-Socket Total Disc Arthroplasty.** PhD Thesis. University of Birmingham

Moghadas, P., Mahomed, A., Hukins, D. W. L. and Shepherd, D. E. T. (2012a) Friction in metal-on-metal total disc arthroplasty: effect of ball radius. **Journal of Biomechanics**, 45 (3): 504-509

Moghadas, P., Shepherd, D. E. T., Hukins, D. W. L. and Mahomed, A. (2012b) Polymer-on-metal or metal-on-polymer total disc arthroplasty. **Spine**, 37 (21): 1834-1838

Moghadas, P., Mahomed, A., Hukins, D. W. L. and Shepherd, D. E. T. (2013) Wear in metal-on-metal total disc arthroplasty. **Proceedings of the Institution of Mechanical Engineers Part-H Journal of Engineering in Medicine**, 227 (4): 356–361

Moghadas, P., Mahomed, A., Hukins, D. W. L. and Shepherd, D. E. T. (2015) Wear of the Charite (R) lumbar intervertebral disc replacement investigated using an electro-mechanical spine simulator. **Proceedings of the Institution of Mechanical Engineers Part-H Journal of Engineering in Medicine**, 229 (3): 264-268

Moreau, D., Stockslager, J. L., Cheli, R. and Haworth, K. (2002) **Anatomy and Physiology.** Philadelphia: Lippincott Williams & Wilkins

Murrey, D., Janssen, M., Delamarter, R., Goldstein, J., Zigler, J., Tay, B. and Darden, B. (2009) Results of the prospective, randomized, controlled multicenter Food and Drug Administration investigational device exemption study of the ProDisc-C total disc replacement versus anterior discectomy and fusion for the treatment of 1-level symptomatic cervical disc disease. **The Spine Journal**, 9 (4): 275-286

Nachemson, A. (1987) Lumbar intradiscal pressure. In: Jayson, M. I. V. (ed.) **The Lumbar Spine and Back Pain.** Churchill Livingstone: Edinburgh, pp. 191–203

National Institute for Health and Clinical Excellence (2009) Low back pain: early management of persistent non-specific low back pain. **Clinical Guideline 88**. Manchester: The National Collaborating Centre for Primary Care

National Joint Registry (2016) **13th Annual Report 2016**. [online] Available from http://www.njrcentre.org.uk/njrcentre/Portals/0/Documents/England/Reports/13th%20Annual%20Report/07950%20NJR%20Annual%20Report%202016%20ONLINE%20REPORT.pdf [Accessed 13th September 2016]

Nechtow, W., Bushelow, M., Hinter, M., Ochs, A. and Kaddick, C. (2008) Cervical disc prosthesis polyethylene wear following the ISO cervical test. **Transactions of the 54th Annual Meeting of the Orthopaedic Research Society**, San Francisco, CA

Neurosurgery Blog (2016) **Overview of Disc Arthroplasty – Past, Present and Future.** [online] Available from http://www.neurosurgery-blog.com/archives/656 [Accessed 15th September 2016]

Nevelos, J., Ingham, E., Doyle, C., Streicher, R., Nevelos, A., Walter, W. and Fisher, J. (2000) Microseparation of the centers of alumina-alumina artificial hip joints during simulator testing produces clinically relevant wear rates and patterns**. The Journal of Arthroplasty**, 15 (6): 793-795

O'Connell, G. D., Malhotra, N. R., Vresilovic, E. J. and Elliott, D. M. (2011) The effect of discectomy and the dependence on degeneration of human intervertebral disc strain in axial compression. **Spine**, 36 (21): 1765–1771

Olofsson, J., Bexell, U. and Jacobson, S. (2012) Tribofilm formation of lightly loaded self mated alumina contacts. **Wear**, 289: 39-45

OpenStax (2014) **Anatomy and Physiology** [online] Available from http://cnx.org/contents/14fb4ad7-39a1-4eee-ab6e-3ef2482e3e22@6.27 [Accessed 7th September 2016]. Images used under a Creative Commons Attribution 2.5 License (https://creativecommons.org/licenses/by/2.5/legalcode)

Pan, A., Hai, Y., Yang, J., Zhou, L., Chen, X. and Guo H. (2016) Adjacent segment degeneration after lumbar spinal fusion compared with motion-preservation procedures: a meta-analysis. **European Spine Journal**, 25 (5): 1522–1532

Patwardhan, A. G., Havey, R. M., Ghanayem, A. J., Diener, H., Meade, K. P., Dunlap, B. and Hodges, S. D. (2000) Load-carrying capacity of the human cervical spine in compression is increased under a follower load. **Spine**, 25 (12): 1548-1554

Pham, M. H., Mehta, V. A., Tuchman, A. and Hsieh, P. C. (2015) Material science in cervical total disc replacement. **Biomed Research International**, Article ID 719123, doi:10.1155/2015/719123

Phase Shift Technology Inc. (2014) **MicroXAM Surface Mapping Microscope** [online]. Available from https://cma.tcd.ie/misc/MicroXam.pdf, [Accessed 22nd September 2014]

Prokopovich, P., Perni, S., Fisher, J. and Hall, R. M. (2011) Spatial variation of wear on Charite lumbar discs. **Acta Biomaterialia**, 7 (11): 3914-3926

Przybyla, A. S., Skrzypiec, D., Pollintine, P., Dolan, P. and Adams, M. A. (2007) Strength of the cervical spine in compression and bending. **Spine**, 32 (15): 1612-1620

Punt, I. M., Visser, V. M., Van Rhijn, L. W., Kurtz, S. M., Antonis, J., Schurink, G. W. H. and van Ooij A. (2008) Complications and reoperations of the SB Charité lumbar disc prosthesis: experience in 75 patients. **European Spine Journal**, 17 (1): 36–43

Punt, I. M., Cleutjens, J. P., de Bruin, T., Willems, P. C., Kurtz, S. M., van Rhijn, L. W., Schurink, G. W. and van Ooij, A. (2009) Periprosthetic tissue reactions observed at revision of total intervertebral disc arthroplasty. **Biomaterials**, 30 (11): 2079-2084

Radcliff, K. E., Kepler, C. K., Jakoi, A., Sidhu, G. S., Rihn, J., Vaccaro, A. R., Albert, T. J. and Hilibrand, A. S. (2013) Adjacent segment disease in the lumbar spine following different treatment interventions. **The Spine Journal**, 13 (10): 1339-1349

Rieker, C., Konrad, R. and Schön, R. (2001) *In vitro* comparison of the two hard–hard articulations for total hip replacements. **Proceedings of the Institution of Mechanical Engineers Part-H Journal of Engineering in Medicine**, 215 (2): 153–160

Robinson, L. (2012) **Typical Properties 99.5% & 99.7% & 96% Alumina.** Data sheet received via personal communication from Lorraine Robinson, Goodfellow Cambridge Limited, 15th February 2012

Roy R. S., Guchhait, H., Chanda, A., Basu, D. and Mitra, M. K. (2007a) Improved sliding wear resistance of alumina with sub-micron grain size: A comparison with coarser grained material. **Journal of the European Ceramic Society**, 27 (16): 4737-3743

Roy, R. S., Mondal, A., Chanda, A., Basu, D. and Mitra, M. K. (2007b) Sliding wear behavior of submicron-grained alumina in biological environment. **Journal of Biomedical Materials Research Part A**, 83 (2): 257-262

Sagbas, B. and Durakbasa M. N. (2012) Measurement of wear in orthopaedic prosthesis. **Acta Physica Polonica A**, 121 (1): 131-134

Sartorius UK Ltd. (2014a) **Ultramicra and Micro Balances** [online]. Available from http://www.sartorius.co.uk/en/products/laboratory/laboratory-balances/ultramicro-micro-balances/ [Accessed 10th December 2014]

Sartorius UK Ltd. (2014b) **Analytical Balances** [online]. Available from http://www.sartorius.co.uk/en/products/laboratory/laboratory-balances/analytical-balances/ [Accessed 10th December 2014]

Sasso, R. C., Foulk, D.M. and Hahn, M. (2008) Prospective, randomized trial of metal-on-metal artificial lumbar disc replacement: Initial results for treatment of discogenic pain. **Spine**, 33 (2): 123–131

Savigny, P., Kuntze, S., Watson, P., Underwood, M., Ritchie, G., Cotterell, M., Hill, D., Browne, N., Buchanan, E., Coffey, P., Dixon, P., Drummond, C., Flanagan, M., Greenough, C., Griffiths, M., Halliday-Bell, J., Hettinga, D., Vogel, S. and Walsh, D. (2009) **Low Back Pain: Early Management of Persistent Non-Specific Low Back Pain.** London: National Collaborating Centre for Primary Care and Royal College of General Practitioners

Schmalzried, T. P., Jasty, M. and Harris, W. H. (1992) Periprosthetic bone loss in total hip arthroplasty. Polyethylene wear debris and the concept of the effective joint space. **Journal of Bone and Joint Surgery: American Edition**, 74 (6): 849 - 863

Scholes, S. C. and Joyce, T. J. (2013) *In vitro* tests of substitute lubricants for wear testing orthopaedic biomaterials. **Proceedings of the Institution of Mechanical Engineers Part-H Journal of Engineering in Medicine**, 227 (6): 693-703

Scholes, S. C. and Unsworth, A. (2000) Comparison of friction and lubrication of different hip prostheses. **Proceedings of the Institution of Mechanical Engineers Part-H Journal of Engineering in Medicine**, 214 (1): 49-57

Scholes, S. C. and Unsworth, A. (2006) The tribology of metal-on-metal total hip replacements. **Proceedings of the Institution of Mechanical Engineers Part-H Journal of Engineering in Medicine**, 220 (2): 183-194

Scholes, S. C., Unsworth, A., Hall, R. M. and Scott, R. (2000) The effects of material combination and lubricant on the friction of total hip prostheses. **Wear**, 241 (2): 209-213

Serra, E., Tucci, A., Esposito, L. and Piconi, C. (2002) Volumetric determination of the wear of ceramics for hip joints. **Biomaterials**, 23 (4): 1131–1137

Shaheen, A. and Shepherd, D. E. T. (2007) Lubrication regimes in lumbar total disc arthroplasty. **Proceedings of the Institution of Mechanical Engineers Part-H Journal of Engineering in Medicine**, 221 (6): 621-627

Siepe, C. J., Wiechert, K., Khattab, M. F., Korge, A. and Mayer, H. M. (2007) Total lumbar disc replacement in athletes: clinical results, return to sport and athletic performance. **European Spine Journal**, 16 (7): 1001–1013

Simon, S. R., Rose, R. M. and Radin, E. L. (1975) 'Stiction-friction' of total hip prostheses and its relationship to loosening. **Journal of Bone and Joint Surgery: American Edition**, 57 (2): 226–230

Siskey, R., Peck, J., Mehta, H., Kosydar, A., Kurtz, S. and Hill, G. (2016) Development of a clinically relevant impingement test method for a mobile bearing lumbar total disc replacement. **The Spine Journal**, advance online publication, http://dx.doi.org/10.1016/j.spinee.2016.05.004

Smit, T. H., Odgaard, A. and Schneider, E. (1997) Structure and function of vertebral trabecular bone. **Spine**, 22 (24): 2823-2833

Smith, A. M., Fleming, L., Wudebwe, U., Bowen, J. and Grover, L. M. (2014) Development of a synovial fluid analogue with bio-relevant rheology for wear testing of orthopaedic implants. **Journal of the Mechanical Behavior of Biomedical Materials**, 32; 177–184

Smith, S. L., Dowson, D. and Goldsmith, A. A. J. (2001) The lubrication of metal-on-metal total hip joints: a slide down the Stribeck curve. **Proceedings of the Institution of Mechanical Engineers, Part-J Journal of Engineering Tribology**, 215 (5): 483-493

Spikes, H. (1996) Mechanisms of boundary lubrication. **In Proceedings of the Tenth International Colloquium on Tribology—Solving Friction and Wear Problems**, Esslingen, Germany, 1737–1751

Spine Universe (2016) **Intervertebral Disc Replacement.** [online] Available from http://www.spineuniverse.com/treatments/emerging/artificial-discs/intervertebral-disc-replacement [Accessed 15h September 2016]

Stachowiak, G. W. and Batchelor, A. W. (2013) **Engineering Tribology.** Burlington: Butterworh-Heinemann

Stoner, K. E., Nassif, N. A., Wright, T. M. and Padgett, D.E. (2013) Laser scanning as a useful tool in implant retrieval analysis: a demonstration using rotating platform and fixed bearing tibial inserts. **The Journal of Arthroplasty**, 28 (1): 152-156

Stribeck, R. (1902) Die wesenlichen Eigenchalfen der Gleit- und Rollen-lager. **Zeitschrift des Vereines Deutscher Ingenieure**, 46 (37) 1341–1348

Taylor, J. (2012) **Ceramic Characteristics Data Sheet.** Received via personal communication from James Taylor, Goodfellows Ceramic and Glass Division, 2nd August 2012

The Burton Report (2016) **Artificial Disc.** [online] Available from http://www.burtonreport.com/infspine/surgartificialdiscs.htm [Accessed 7th September 2016]

Tournier, C. and Duc, C. (2002) A surface based approach for constant scallop height tool-path generation. **International Journal of Advanced Manufacturing Technology**, 19 (5): 318–324

Turger, A., Köhler, J., Denkena, B., Correa, T. A., Becher, C. and Hurschler C. (2013) Manufacturing conditioned roughness and wear of biomedical oxide ceramics for all-ceramic knee implants. **Biomedical Engineering Online**, 12:84

University of Leeds. **SOP01.6: Standard Operating Protocol for Spine Wear Simulator Studies.** Institute of Medical and Biological Engineering, University of Leeds, Leeds, UK.

Unsworth, A. (1978) The effects of lubrication in hip joint prostheses. **Physics in Medicine and Biology**, 23: 253-268

van den Eerenbeemt, K. D., Ostelo, R. W., van Royen, B. J., Peul, W. C. and van Tulder, M. W. (2010) Total disc replacement surgery for symptomatic degenerative lumbar disc disease: a systematic review of the literature. **European Spine Journal**, 19 (8): 1262-1280

van Ooij, A., Oner, F. C. and Verbout, A. J. (2003) Complications of artificial disc replacement: a report of 27 patients with the SB Charité disc. **Journal of Spinal Disorders and Technology**, 16 (4): 369–383

van Ooij, A., Kurtz, S. M., Stessels, F., Noten, H. and van Rhijn, L. (2007) Polyethylene wear debris and long-term clinical failure of the Charité disc prosthesis: a study of 4 patients. **Spine**, 32 (2): 223–229

Vicars, R., Fisher, J. and Hall, R. M. (2009) The accuracy and precision of a micro computer tomography volumetric measurement technique for the analysis of in-vitro tested total disc replacements. **Proceedings of the Institution of Mechanical Engineers Part-H Journal of Engineering in Medicine**, 223 (3): 383-388

Vicars, R., Hyde, P. J., Brown, T. D., Tipper, J. L., Ingham, E., Fisher J. and Hall, R. M. (2010) The effect of anterior-posterior shear load on the wear of ProDisc-L TDR. **European Spine Journal**, 19 (8): 1356-1362

Wang, A., Essner, A. and Schmidig, G. (2004) The effects of lubricant composition on in vitro wear testing of polymeric acetabular components. **Journal of Biomedical Materials Research. Part B, Applied Biomaterials,** 68 (1): 45-52

Warkentin, A. Bedi, S. and Ismail, F. (1996) Five-axis milling of spherical surfaces. **International Journal of Machine Tools Manufacture**, 36 (2): 229-243

Webster, J., Brinksmeier, E., Heinzel, C., Wittmann, M. and Thoens, K. (2002) Assessment of grinding fluid effectiveness in continuous-dress creep feed grinding. **CIRP Annals - Manufacturing Technology**, 51 (1): 235-240

Which Medical Device (2016) **Cadisc-L.** [online] Available from http://www.whichmedicaldevice.com/by-manufacturer/263/615/cadisc-l [Accessed 15th September 2016]

Willems, P., de Bie, R., Öner, C., Castelein, R. and de Kleuver, M. (2011) Clinical decision making in spinal fusion for chronic low back pain. Results of a nationwide survey among spine surgeons. **BMJ Open**, 1: e000391

Williams, S. R., Wu, J. J., Unsworth, A. and Khan, I. (2011) Wear and surface analysis of 38 mm ceramic-on-metal total hip replacements under standard and severe wear testing conditions. **Proceedings of the Institution of Mechanical Engineers Part-H Journal of Engineering in Medicine**, 225 (8): 783-796

Wilm, J. and Kjer, H. M. (2013) **Iterative Closest Point** [online] MATLAB Central File Exchange. Available from: http://uk.mathworks.com/matlabcentral/fileexchange/27804-iterative-closest-point [Accessed 25th Feburary, 2014]

Xin, H. (2013) **Evaluation of Poly-Ether-Ether-Ketone (PEEK) for Cervical Disc Replacement Devices.** PhD Thesis. University of Birmingham

Xin, H., Shepherd, D. E. T. and Dearn, K.D. (2013) A tribological assessment of a PEEK based self-mating total cervical disc replacement. **Wear**, 303: 473–479

Yin, L. and Huang, H. (2004) Ceramic response to high speed grinding. **Machining Science and Technology**, 8 (1): 21-37

Yoon, T. R., Rowe, S. M., Jung, S. T., Seon, K. J. and Maloney, W. J. (1998) Osteolysis in association with a total hip arthroplasty with ceramic bearing surfaces. **Journal of Bone and Joint Surgery: American Edition**, 80 (10): 1459-1468

Zigler J., Delamarter R., Spivak J. M., Linovitz R. J., Danielson III G. O., Haider T. T., Cammisa F., Zuchermann J., Balderston R., Kitchel S., Foley K., Watkins R., Bradford D., Yue J., Yuan H., Herkowitz H., Geiger D., Bendo J., Peppers T., Sachs B., Girardi F., Kropf M. and Goldstein J. (2007) Results of the prospective, randomized, multicenter Food and Drug Administration investigational device exemption study of the ProDisc-L total disc replacement versus circumferential fusion for the treatment of 1-level degenerative disc disease. **Spine**, 32 (11): 1155-1162

Zigler, J. E. and Delamarter, R. B. (2012) Five-year results of the prospective, randomized, multicenter, Food and Drug Administration investigational device exemption study of the ProDisc-L total disc replacement versus circumferential arthrodesis for the treatment of single-level degenerative disc disease. **Journal of Neurosurgery: Spine**, 17 (6): 493-501

Zigler, J. E., Delamarter, R., Murrey, D., Spivak, J. and Janssen M. (2013) ProDisc-C and anterior cervical discectomy and fusion as surgical treatment for single-level cervical symptomatic degenerative disc disease: five-year results of a Food and Drug Administration study. **Spine**, 38 (3): 203-209